THE UNIVERSITY *of* EDINBURGH

Modelling cosmological structure formation in the non-linear regime

Francesca Carina Lane

Doctor of Philosophy
The University of Edinburgh
August 2020

To my grandma for supporting me and for the endless supply of jelly tots that got me through sixth form

"Well, when I get it the only thing that does any good is to jump in a cab and go to Tiffany's. Calms me down right away. The quietness and the proud look of it; nothing very bad could happen to you there. If I could find a real-life place that'd make me feel like Tiffany's, then - then I'd buy some furniture and give the cat a name!"

– Holly Golightly, Breakfast at Tiffanys

Lay summary

In the past century, we have pieced together the puzzle of how our Universe formed. From the Big Bang theory to observing the oldest light in the Universe (the Cosmic Microwave Background) to detecting gravitational waves we have begun to answer the biggest questions in Astronomy. There remain some mysteries for us to solve like the nature of dark matter (the building blocks of the Universe) and dark energy (the force causing the accelerated expansion of the Universe). Perhaps the most important theory of the past century is that of Λ-CDM. This theory gives an approximation for both dark matter and dark energy. Dark energy is described by Einstein's cosmological constant and dark matter is a cold, collisionless fluid (does not interact via any forces other than gravity). Λ-CDM has been tested observationally for decades and performs incredibly well. However, cracks are beginning to form in the theory. Some recent late-time observations of objects, such as Type IA supernova, have suggested that new physics or a gravity theory other than Einstein's general relativity may govern the expansion of our Universe. We have also struggled to directly detect dark matter or rule out alternative forms.

In order to settle the dark energy and dark matter debate astronomers are building new instruments that will carry out the largest and most in-depth surveys of our Universe ever. This golden age of cosmology presents new challenges for theorists as our current tools for modelling how structures (like the complicated web of galaxies) are formed under the influence of gravity in our Universe are not accurate enough. This has led to us throwing away data on scales (small scales) we cannot model accurately without large, expensive numerical simulations but this data could be the key to the nature of the dark components.

In this thesis, we will introduce a new theoretical method that could be used to model astronomical observations (specifically dark matter) on small scales. Our aim is to develop a general theory that can be applied to a wide range of dark

matter, dark energy and modified gravity models. As the amount of data we will obtain from new surveys will be very large our method must be both economical time and cost-wise. It must also perform competitively with computer simulations and the most up-to-date theoretical techniques. We will calculate two observables that will be measured by upcoming surveys; the matter power spectrum and the correlation function. These observables can allow us to distinguish between dark energy, dark matter and structure formation models.

The next five years will bring the launch and collection of data from *Euclid*, the James Webb Space Telescope (*JWST*), the Dark Energy Spectroscopic Instrument (*DESI*), the Large Synoptic Survey Telescope (*LSST*) or the Rubin Observatory and the Wide Field Infrared Survey Telescope (*WFIRST*) plus many more. It is hoped that methods, such as the one presented in this thesis, will allow us to fully utilise these observations; hopefully shedding more light on the mysteries of our Universe.

Abstract

We are entering an age of precision cosmology with upcoming instruments and surveys such as *Euclid*, the Dark Energy Spectroscopic Instrument (*DESI*), the Large Synoptic Survey Telescope (*LSST*) or the Rubin Observatory and the James Webb Space Telescope (*JWST*). These will allow us to place even tighter statistical constraints on viable dark matter, dark energy and modified gravity theories. This could lead to discovering the answer to some of Astronomy's biggest questions about structure formation in the Universe. In order to test these theories, we must have theoretical predictions to compare to observations; some of the most powerful observables are 2-point statistics. These include the matter correlation function and its Fourier transform, the power spectrum. These simple statistics could allow us to distinguish between cosmological models and modified gravity theories.

Calculating these statistics on large-scales and in the linear regime is simple as we can apply the linear theory. However, on small scales ($r < 100$ Mpc), non-linear gravitational and baryonic effects become too important to ignore and our linear theories break down. The most successful theoretical technique, Standard Perturbation Theory (SPT), can be extended into the non-linear regime using techniques such as loop corrections and IR-resummation. Although these extensions have allowed us to compute the non-linear power spectrum on smaller scales, they can only push so far into the non-linear regime. This is especially the case for the correlation function where the most popular perturbation theory technique cannot accurately model even the mildly non-linear regime. Currently, the most accurate methods for calculating the non-linear regime are N-body and hydrodynamical simulations. These simulations must be run at high resolutions and with large box sizes to match the accuracy of upcoming observations. They are therefore very costly to run and if one wishes to test multiple dark matter theories, for example, a new simulation must usually be run for each theory. In

order to produce a wide variety of predictions for observations economically, we must return to our perturbative methods and search for ways to extend their reach further.

In this thesis, we will introduce a perturbative method for calculating the correlation function and power spectrum in the non-linear regime. We focus on these statistics as they are simplest to calculate and the most commonly used. This method is called the Cosmological Trajectories Method (CTM). We will present a formula for the power spectrum and show how an expanded version of the power spectrum can be calculated numerically. One of the main advantages of the CTM is that it can be applied to a wide range of cosmologies and redshifts. An approximation called Beyond Zel'dovich is then introduced and the CTM is used to compute its power spectrum and correlation function. This approximation aims to extend the Zel'dovich approximation (usually used to set the initial conditions of numerical simulations, study the non-linear regime and BAO reconstruction) into the non-linear regime. The Zel'dovich approximation can describe the formation of the cosmic web and is exact in 1D up until shell-crossing. In 3D the approximation performs well at high redshifts and mildly non-linear scales ($k \lesssim 0.1$ h Mpc^{-1}) until it breaks down due to shell-crossing and the formation of caustics.

We compare the Beyond Zel'dovich approximation to other methods including SPT 1-loop and Convolution Lagrangian Perturbation Theory (CLPT). We find that the Beyond Zel'dovich approximation breaks down at low redshifts and for scales $k > 0.1$ h Mpc^{-1}. This motivates the introduction of a Gaussian damped initial power spectrum in order to damp down this breakdown of the Beyond Zel'dovich approximation on small scales and at late times. With the introduction of a Gaussian cut-off, we conclude that the Beyond Zel'dovich approximation is best applied at redshifts $z \geq 2$. At these redshifts, it outperforms the Zel'dovich approximation and at redshifts $z \geq 4$ it also outperforms the Euclid Emulator.

The Beyond Zel'dovich approximation performs well on mildly non-linear scales and at redshifts above $z = 2$. This implies that this approximation could be also used to model redshift-space distortions in this regime and applied to BAO and Lyman-α observations. We, therefore, extend the CTM into redshift space. We compute the redshift-space power spectrum and correlation function using the Beyond Zel'dovich approximation for a range of redshifts. Finally, we compare these results to a range of other methods including the Kaiser formula and SPT 1-loop as we did for the real-space statistics.

Declaration

I declare that this thesis was composed by myself, that the work contained herein is my own except where explicitly stated otherwise in the text, and that this work has not been submitted for any other degree or professional qualification except as specified.

(*Francesca Carina Lane, August 2020*)

Acknowledgements

I would like to begin by thanking my supervisor Andy Taylor for his help and support in writing this thesis. I would also like to thank Daniele Sorini for stepping in as my second supervisor and providing much-appreciated guidance during the last year and a half of my PhD. Also a big thanks to Zvonimir Vlah, Marko Simonovic and Lucas Lombriser for making me feel welcome during my stay at CERN. I am also grateful for the extra funding awarded to me by SUPA and the IfA, that allowed me to complete my PhD and study abroad.

A big shout out to my office mates over the years particularly Dan, Joe and Rachel. I've missed your banter, advice and Joe's awful puns in my final year. To Niall, Dylan and Rohit all I can say is I hope that when you're in final year the third years are just as annoying. That said I'm sorry for being so grumpy and random chats in your office kept me going and cheered me up (please throw me a nice viva party). I'm also sorry for abandoning Ben in every office. I promise I won't do it again in our new office; I'd miss not knowing where to get the best crème brûlée or what the best new TV shows are? And of course, I have to thank my oldest friend Rachel for putting up with me for 15 years. We've both come so far since I was moved into your form class and hopefully, we can celebrate with some sangria in Madrid soon.

It goes without saying that I wouldn't be writing these acknowledgements without my parents and grandparents. I'm eternally grateful to my parents for the sacrifices they made to ensure I had the opportunities growing up that allowed me to go to university. A special thanks to my mum who watched countless orchestra performances and encouraged me to read (even if people were freaked out by a young child reading Wuthering Heights). And to my dad for all the pep talks, advice and for teaching me to believe in myself. I definitely learned perseverance dealing with your pranks and tricks growing up.

I dedicated this thesis to my Grandma who was always there for me whether it was buying me jelly tots or making me mince and dumplings and rice pudding. Words can't express the influence you and Grandad had on making me into the woman I've become and I will always look back fondly on our countless day trips and holidays to the Highlands.

Finally, thanks to Adam for always being there over the past four years. You've

been my rock and I genuinely couldn't have completed this thesis without you. We've had so many amazing adventures over the years (a surprising amount of them involving me being chased by an animal) and I can't wait to start our new adventure together.

Contents

Lay summary v

Abstract vii

Declaration ix

Acknowledgements xi

Contents xiii

List of Figures xix

1 Background 1

1.1 History 1

1.2 General relativity 2

1.2.1 Special Relativity 2

1.2.2 Curved spacetime 4

1.2.3 Geodesics, parallel transport and curvature 5

1.2.4 Einstein field equations 9

1.3 Cosmology 11

1.3.1 The geometry of the Universe 11

1.3.2 The hot dense Universe 16

1.3.3 The dark Universe 18

1.3.4 Λ-CDM 20

2 Cosmological Perturbation Theory 27

2.1 Relativistic Perturbation Theory 27

2.1.1 Background equations 27

2.1.2 Metric Perturbations 29

2.2 Scalar Perturbations 31

2.2.1 Scalar perturbation evolution equations 32

2.3 Scalar perturbations in our Universe 34

2.3.1 Matter dominated universe 35

2.4 Statistics of the density field 36

2.4.1 Linear matter power spectrum 36

2.4.2 Non-linear power spectrum 41

3 The Cosmological Trajectories Method: A trajectories approach to structure formation 45

3.1 Overview 45

3.2 Lagrangian Perturbation Theory 48

3.2.1 First-order LPT (Zel'dovich approximation) 48

3.2.2 Second-order LPT 50

3.2.3 The Zel'dovich power spectrum 51

3.2.4 Calculating the Zel'dovich power spectrum numerically 53

3.3 The Cosmological Trajectories Method 56

3.3.1 A general cosmological trajectory 59

3.4 Calculating the power spectrum for a general cosmological trajectory.... 62

3.4.1 Covariance matrix and correlation functions 62

3.4.2 The full power spectrum 65

3.4.3 Expansion of the power spectrum in ϵ 66

3.4.4 Calculating the full expanded power spectrum..... 68

3.5 Example I: A KFT trajectory 72

3.5.1 Previous results..... 72

3.5.2 The calculated power spectrum using the CTM 74

3.6 Conclusions 77

4 The Cosmological Trajectories Method: The Beyond Zel'dovich approximation and its applications in real space 79

4.1 The Beyond Zel'dovich approximation 80

4.2 Calculating the Beyond Zel'dovich power spectrum at different redshifts and investigating the free parameters..... 81

4.2.1 Different ϵ values..... 81

4.2.2 Different z_i values 84

4.3 Calculating a Gaussian damped Beyond Zel'dovich power spectrum at different redshifts 84

4.3.1 Testing the dependence of k_c on cosmology 92

4.4 An alternative time dependence example 93

4.5 Comparing Beyond Zel'dovich to other methods..... 95

4.5.1 SPT 1-loop 97

4.5.2 CLPT 100

4.5.3 KFT..... 103

4.6 Higher-order power spectrum 103

4.6.1 Deriving the higher-order power spectrum 105

4.6.2 Computing the higher-order power spectrum 108

4.7 Conclusions 111

5 The Cosmological Trajectories Method: The Beyond Zel'dovich approximation and its applications in redshift space 117

5.1 Overview 117

5.2 Redshift-space distortions (RSD) 119

5.2.1 Linear RSD Example - Kaiser formula 122

5.2.2 Non-linear RSD Example - TNS model 123

5.3 Calculating the Cosmological Trajectories Method power spectrum in redshift space 124

5.3.1 Calculating the redshift-space Zel'dovich power spectrum 124

5.3.2 Analytic computation of the CTM redshift-space power spectrum 126

5.4 Calculating the Beyond Zel'dovich redshift-space power spectrum at different redshifts and investigating the free parameters 131

5.4.1 Different ϵ values 131

5.4.2 Calculating a Gaussian damped Beyond Zel'dovich redshift-space power spectrum at different redshifts 134

5.5 Comparing Beyond Zel'dovich to other methods in redshift space 138

5.5.1 Kaiser 141

5.5.2 SPT 1-loop 145

5.6 Conclusions 151

6 Conclusions and future work 155

6.1 Conclusions 155

6.1.1 The Cosmological Trajectories Method 156

6.1.2 The Beyond Zel'dovich approximation in real space 157

6.1.3 The Beyond Zel'dovich approximation in redshift space 159

6.2 Future work 161

A Differential Geometry 163

A.1 Derivation of Lorentz tensor 163

A.2 Manifolds and tangent spaces 164

B Additional redshift-space figures 167

Bibliography 171

List of Figures

(1.1) A diagram of a Riemann sphere. A vector is parallel transported from A to N to B to A. The diagram shows that the vector is not conserved as it is transported. This is called holonomy and motives the introduction of affine connections and the Riemann tensor. 7

(1.2) Timeline of the evolution of the Universe from the Big Bang to today. 16

(1.3) Temperature map of the Cosmic Microwave Background taken by the ESA and *Planck* Collaboration in 2018 (Collaboration et al., 2018). The grey lines show the confidence mask..... 17

(1.4) A Planck TT angular power spectrum measured from the CMB taken from Collaboration et al. (2018). 21

(1.5) Figure taken from Verde et al. (2019) showing a range of early and late time measurements of H_0..... 25

(2.1) Figure from (Eisenstein et al., 2005) showing the correlation function measured by the SDSS survey compared to theoretical predictions. ... 40

(2.2) Figure from (Planck Collaboration et al., 2018) showing the matter power spectrum as measured by the *Planck*, *SDSS*, *BOSS* and *DES* surveys..... 41

(2.3) Figure showing the linear and one-loop power spectra for *Planck18* data produced using CLASS (Lesgourgues, 2011) and FASTPT (McEwen et al., 2016b). One can see the enhancement of growth on small-scales (large k-values) as expected from non-linear structure formation..... 44

(3.1) The top panel shows the functions X (purple solid line) and Y (orange dashed line) (3.25) versus q. The bottom panel shows the functions $\sigma_{\parallel}$ (purple solid line) and $\sigma_{\perp}$ (orange dashed line) (3.30) versus q for Planck18 (Collaboration et al., 2018) cosmology..... 57

(3.2) The q dependent functions defined in (3.73) and (3.76) are plotted above versus q for Planck18 (Collaboration et al., 2018) cosmology. .. 70

(3.3) The dimensionless power spectra for linear theory (black solid line), Zel'dovich approximation (orange dash-dashed line) and re-normalised KFT (blue dashed line) are shown in this figure for four different redshifts. The upper left panel is the result at $z = 0$, the upper right panel is the result at $z = 1$, the lower left panel is the result at $z = 2$ and the lower right panel is the result at $z = 3$..... 76

(4.1) In this figure the power spectrum in Equation (3.79) is shown calculated for the Beyond Zel'dovich time dependence with different ϵ values. The black solid lines show the linear power spectrum obtained from CLASS, the purple dashed lines show the computed Zel'dovich power spectrum, the orange dashed-dot lines show the Beyond Zel'dovich power spectrum and the pink dotted lines are the results from the emulator described above. 83

(4.2) The solid black line is the dimensionless linear power spectrum. The purple, orange and blue lines are the Beyond Zel'dovich power spectra with $\epsilon = 1$ and with $z_i = 50, 100$ and 150 respectively. The top panels from left to right are $z = 0, 1, 2$ and the bottom panels from left to right are $z = 3, 4, 5$..... 85

(4.3) Damped dimensionless Beyond Zel'dovich for three different k_c values: $k_c = 50$ h Mpc^{-1} is shown by the purple dashed lines, $k_c = 5$ h Mpc^{-1} is shown by the orange dashed-dot lines and $k_c = 0.5$ h Mpc^{-1} is shown by the blue dotted lines. The purple dashed line shows the emulator results for six redshifts and three ϵ values $\epsilon = 1, 0.1$ and 0.01 in the top, middle and lower rows respectively. 87

(4.4) Difference between the damped dimensionless Beyond Zel'dovich power spectra and the emulator results for a range of $k_c = 1 - 10$ h Mpc^{-1} with $\epsilon = 1$. The grey shaded area is $\Delta^2_{\rm diff} = \pm 0.05$ and the six panels are $z = 0$ (upper left) through to $z = 5$ (lower right)..... 88

(4.5) Figure showing cutoff values $k_c = 1{-}10$ h Mpc^{-1} versus the maximum k-value, $k_{\rm max}$, reached before the percentage difference between the Beyond Zel'dovich power spectra drop below the emulator results. The dotted horizontal lines show the maximum k-value reached by the undamped Beyond Zel'dovich power spectrum at that redshift. ... 90

(4.6) Zoomed in plot of the percentage difference between the damped Beyond Zel'dovich power spectra with $k_c = 6$ h Mpc^{-1} and $\epsilon = 1$ and the emulator results. These are shown in the solid lines with each colour representing a different redshift. The dashed lines are the percentage differences between the damped Zel'dovich approximation power spectra with $k_c = 6$ h Mpc^{-1} and the emulator results.The grey shaded region is again $\Delta^2_{\rm diff} = \pm 0.05$..... 91

(4.7) The top panel shows the maximum k-value before the percentage difference between Beyond Zel'dovich power spectra and the emulator results drop below 5% at six different redshifts. The orange circles are the results using *Planck18* and the purple diamonds are computed using the same cosmology with a different Ω_m value. The lower panel shows the ratio between the $k_{\rm max}$ values for the two cosmologies with the grey shaded region between the ratio between the two Ω_m values $\pm 5\%$..... 94

(4.8) The left-hand panel shows the percentage difference between the LPT-like dimensionless power spectra with $\epsilon = 10^{-4}$ (solid lines) and the Beyond Zel'dovich power spectra with $\epsilon = 1$ (dashed lines) and the emulator results. The right-hand panel shows the same as the left-hand but both approximations have been calculated with a damped initial power spectrum with $k_c = 6$ h Mpc^{-1}..... 96

(4.9) The correlation function, $\xi(r)$, scaled by r^2 for the linear theory (black solid line), Zel'dovich approximation (orange dashed line), damped Beyond Zel'dovich with $k_c = 6$ h Mpc^{-1} (blue dashed-dot) and the emulator in purple squares. The four panels are redshifts $z = 0,\ 1,\ 2$ and 3 with the upper left panel being $z = 0$ and the lower right panel being $z = 3$..... 98

(4.10) Figure showing the percentage difference between SPT-1 loop and emulator power spectra in dashed lines and the percentage difference between the Beyond Zel'dovich and emulator power spectra in solid lines for $z = 0,\ 1,\ 2,\ 3,\ 4$ and 5. The grey band is $\Delta^2_{\rm diff} = \pm 0.05$. 99

(4.11) The correlation function, $\xi(r)$, scaled by r^2 for the linear theory (black solid line), SPT 1-loop (orange dashed line), damped Beyond Zel'dovich with $k_c = 6$ h Mpc^{-1} (blue dashed-dot) and the emulator in purple squares. The four panels are redshifts $z = 0,\ 1,\ 2$ and 3 with the upper left panel being $z = 0$ and the lower right panel being $z = 3$..... 101

(4.12) Percentage difference between CLPT (dashed lines) and the Beyond Zel'dovich approximation (solid lines) power spectra and the emulator results. The percentage difference is shown for redshifts $z = 0,\ 1,\ 2,\ 3,\ 4$ and 5 and the grey shaded region is $\Delta^2_{\rm diff} = 0.05$..... 102

(4.13) The 2-point correlation function, $\xi(r)$, scaled by r^2 for linear theory (black solid line), Beyond Zel'dovich (blue dashed dot line), CLPT (orange dashed line) and the emulator in purple. The four panels are redshifts $z = 0,\ 1,\ 2$ and 3. 104

(4.14) Percentage difference between KFT approximation (dashed lines) and the Beyond Zel'dovich approximation (solid lines) with the emulator results for redshifts $z = 0,\ 1,\ 2,\ 3,\ 4$ and 5. The shaded grey band is $\Delta^2_{\rm calc}/\Delta^2_{\rm emu} - 1 = \pm 0.05$. 105

(4.15) In this Figure the dimensionless power spectra are shown for six redshifts. The black solid line is the linear dimensionless power spectrum, the orange dashed-dot line is the Beyond Zel'dovich approximation with $\epsilon = 1$ and $k_c = 6$ h Mpc^{-1}, the purple dashed line is the undamped higher-order Beyond Zel'dovich approximation with $\epsilon = 0.01, 0.1$ or 1 and finally the pink dotted line is the emulator result. 110

(4.16) The black solid line is the linear dimensionless power spectrum, the orange dashed-dot line is the Beyond Zel'dovich approximation with $\epsilon = 1$ and $k_c = 6$ h Mpc^{-1}, the purple dashed line is the full undamped higher-order Beyond Zel'dovich approximation with $\epsilon = 0.01, 0.1$ or 1 and finally the pink dotted line is the emulator result. 112

(4.17) The percentage difference between the full higher-order Beyond Zel'dovich (dotted lines), the higher-order Beyond Zel'dovich (dashed lines) power spectra and the emulator for $\epsilon = 0.01$ is shown in the left-hand panel and $\epsilon = 0.1$ in the right-hand panel. The solid lines are the percentage difference between the Beyond Zel'dovich power spectra with $\epsilon = 1$ and $k_c = 6$ h Mpc^{-1} and the emulator. 113

(4.18) The percentage difference between the full higher-order Beyond Zel'dovich (dotted lines), the higher-order Beyond Zel'dovich (dashed lines) power spectra and the emulator for $\epsilon = 0.01$ shown in the left-hand panel and $\epsilon = 0.1$ in the right-hand panel. Both of the higher-order power spectra have been calculated using a Gaussian damped initial power spectrum with $k_c = 6$ h Mpc^{-1}. The solid lines are the percentage difference between the Beyond Zel'dovich power spectra with $\epsilon = 1$ and $k_c = 5$ h Mpc^{-1} and the emulator..... 113

(5.1) Diagram showing how a spherical region with a central overdensity and objects at the solid red points appear in real space and redshift space. The top row of the diagram represents the largest scales and the lower row represents the smallest scales. 121

(5.2) In this figure the dimensionless linear real space (black solid line) and Beyond Zel'dovich power spectra are shown. The four panels are $z = 0$ (upper left), $z = 1$ (upper right), $z = 2$ (lower left) and $z = 3$ (lower right). The Beyond Zel'dovich redshift-space power spectra are calculated for three μ_k values: $\mu_k = 0$ in purple, $\mu_k = 0.4$ in orange and $\mu_k = 1$ in blue and three ϵ values: $\epsilon = 0.01$ in dotted lines, $\epsilon = 0.1$ in dashed lines and $\epsilon = 1$ in solid lines. 132

(5.3) Figure demonstrating the convergence of the Beyond Zel'dovich (dotted lines) redshift space to the Zel'dovich (dashed lines) redshift-space power spectrum for small ϵ values. Again three μ_k values are shown $\mu_k = 0$ in purple, $\mu_k = 0.4$ in orange and $\mu_k = 1$ in blue and the four panels are redshifts $z = 0,\ 1,\ 2$ and 3 from upper left to lower right. 133

(5.4) Figure showing the maximum k-value, $k_{\rm max}$, reached before the percentage difference between the damped Beyond Zel'dovich and the simulation data becomes larger than $\pm 5\%$ versus a range of cutoff values. The black dots show the $k_{\rm max}$ for the undamped Zel'dovich approximation, the orange crosses show the $k_{\rm max}$ for the Beyond Zel'dovich approximation with $k_c = 0.5$ h Mpc^{-1}, the purple diamonds show the $k_{\rm max}$ for the Beyond Zel'dovich approximation with $k_c = 5$ h Mpc^{-1} and the blue plus signs show the $k_{\rm max}$ for the Beyond Zel'dovich approximation with $k_c = 50$ h Mpc^{-1}. 136

(5.5) Figure showing the maximum k-value, $k_{\rm max}$, reached before the percentage difference between the damped Beyond Zel'dovich and the simulation data becomes larger than $\Delta^2_{\rm diff} = \pm 5\%$ versus a range of cutoff values. The results for $z = 0$ are shown in blue dots, $z = 1$ in orange downward pointing triangles, $z = 2$ in green squares, $z = 3$ in red upward pointing triangles, $z = 4$ in purple stars and $z = 5$ in pink diamonds. 137

(5.6) The dimensionless real space linear (solid black lines), Zel'dovich (dashed lines), Beyond Zel'dovich (solid lines) power spectra in redshift space for three $\mu_k = 0,\ 0.5,\ 1$ values in purple, orange and blue respectively. The panels show six redshifts ($z = 0,\ 1,\ 2,\ 3,\ 4$ and 5) with the upper left panel being $z = 0$ and the lower right panel being $z = 5$. 139

(5.7) Figure shown the percentage difference (4.4) between the Beyond Zel'dovich and simulation power spectra in solid lines and the Zel'dovich and simulation power spectra in dashed lines. The three panels are $\mu_k = 0$, $\mu_k = 0.5$ and $\mu_k = 1$. The dark grey shaded region is $\Delta^2_{\rm diff} = \pm 0.05$ and the light grey shaded region is $\Delta^2_{\rm diff} = \pm 0.1$. 140

(5.8) The 2-point correlation function, $r^2\xi(r)$ at $z = 0$ is shown for linear linear in real space (black solid lines), Zel'dovich redshift space (purple dashed lines) and Beyond Zel'dovich redshift space (orange dot-dashed lines). The three panels are $\mu_k = 0$, $\mu_k = 0.5$ and $\mu_k = 1$... 141

(5.9) The ratio between $\mathrm{P_{RSD}}(k, \mu_k)$ and $\mathrm{P_L}(k)$ in real space is shown for three $\mu_k = 0,\ 0.5$ and 1. The rows are the redshifts $z = 0 - 3$ respectively and the grey lines in left-hand column show $\mathrm{P_{Kaiser}/P_L}$ and the right-hand column show $\mathrm{P_{SPT}/P_L}$..... 143

(5.10) Percentage difference between Beyond Zel'dovich (solid lines) and the simulation power spectra and Kaiser (dashed lines) and the simulation power spectra for $\mu_k = 0,\ 0.5$ and 1. The dark grey shaded region is $\Delta^2_{\rm diff} = \pm 0.05$ and the light grey shaded region is $\Delta^2_{\rm diff} = \pm 0.1$. 144

(5.11) Pre-reconstructed power spectrum measured by *BOSS* in Alam et al. (2017) for $0.5 < 5 < 0.75$ for the NGC (Northern Galactic Caps) sample. The contours show the best fit model and the colour scale shows the data..... 145

(5.12) Contour plot showing the power spectrum $\log_{10} \mathrm{P}(k_\parallel, k_\perp)$ at $z = 0$ for the Kaiser formula, damped Zel'dovich approximation and Beyond Zel'dovich approximation..... 146

(5.13) The 2-point correlation function, $r^2\xi(r)$ at $z = 0$ is shown for linear linear in real space (black solid lines), Kaiser (purple dashed lines) and Beyond Zel'dovich redshift space (orange dot-dashed lines). The three panels are $\mu_k = 0$, $\mu_k = 0.5$ and $\mu_k = 1$..... 147

(5.14) Contour plot showing the two-point correlation function $r^2\xi(r_\parallel, r_\perp)$ at $z = 0$ for the Kaiser formula, damped Zel'dovich approximation and Beyond Zel'dovich approximation. 148

(5.15) Percentage difference between Beyond Zel'dovich (solid lines) and the simulation power spectra and SPT 1-loop (dashed lines) and the simulation power spectra for $\mu_k = 0,\ 0.5$ and 1. The dark grey shaded region is $\Delta^2_{\rm diff} = \pm 0.05$ and the light grey shaded region is $\Delta^2_{\rm diff} = \pm 0.1$. 149

(5.16) Contour plot showing the power spectrum $\log_{10} \mathrm{P}(k_\parallel, k_\perp)$ at $z = 0$ for SPT 1-loop, damped Zel'dovich approximation and Beyond Zel'dovich approximation..... 150

(5.17) The 2-point correlation function, $r^2\xi(r)$ at $z = 0$ is shown for linear linear in real space (black solid lines), SPT 1-loop (purple dashed lines) and Beyond Zel'dovich redshift space (orange dot-dashed lines). The three panels are $\mu_k = 0$, $\mu_k = 0.5$ and $\mu_k = 1$. 151

(5.18) Contour plot showing the two-point correlation function $r^2\xi(r_\parallel, r_\perp)$ at $z = 0$ for SPT 1-loop, damped Zel'dovich approximation and Beyond Zel'dovich approximation. 152

(A.1) Diagram of a manifold where O is an open set containing some point p. This point can be mapped onto a point in $\mathbb{R}^n$ with a chart called ϕ.165

(B.1) Contour plot showing the power spectrum $\log_{10} \mathrm{P}(k_\parallel, k_\perp)$ at $z = 0$ for Kaiser, damped Zel'dovich approximation and Beyond Zel'dovich approximation. The grey dashed lines show the contours produced from the simulation data described in Section 5.5..... 168

(B.2) Contour plot showing the power spectrum $\log_{10} \mathrm{P}(k_\parallel, k_\perp)$ at $z = 0$ for SPT 1-loop, damped Zel'dovich approximation and Beyond Zel'dovich approximation. The grey dashed lines show the contours produced from the simulation data described in Section 5.5..... 169

Chapter 1

Background

> Scientists have calculated that the chances of something so patently absurd actually existing are millions to one. But magicians have calculated that million-to-one chances crop up nine times out of ten.
>
> *Terry Pratchett*

1.1 History

Astronomy has been a prevalent topic since prehistoric humans began studying the sky. At first celestial objects were attributed to gods and other spiritual beings. This lead to the study of constellations so that Egyptian Pharaohs could look at the night sky in the afterlife and monuments like Stonehenge being erected. Astronomy was also studied to create accurate calendars that could be used to grow crops and celebrate religious festivals. For example, in the 7th century, Bede of Jarrow wrote a book, *De temporibus*, that allowed an accurate calculation of the date of Easter.

Philosophers in Ancient Greece combined philosophy, mathematics and physics to study the world around them. Hipparchus of Nicea produced the first-star

catalogue using an apparent magnitude system that is a precursor to the one used today. Euclid wrote the *Elements*, a series of 13 books, written in 300 B.C. which was a collection of mathematical postulates and proofs that are the basis of mathematics. The philosophers of the ancient world lay down the foundations of modern astronomy, physics and mathematics and observed and recorded astronomical events like supernovae (185 A.D. in China) for the first time.

Nicolaus Copernicus in 1543 postulated that the planets in our solar system revolved around the Sun. This idea inspired Johannes Kepler to write down the laws that govern the motion of the planets in 1624 and are still used today. Modern Astronomy truly began in this era when Galileo Galilei used a telescope (the first telescope being used by Hans Lippershey in 1608) to observe the solar system in 1610.

Mathematics set down by Sir Isaac Newton, Gottfried Leibniz, Leonhard Euler, Joseph-Luis Lagrange and James Clerk Maxwell in the 17th-19th centuries describing electromagnetism, gravity and fluid dynamics allowed Max Planck, Erwin Schroedinger, Werner Heisenberg and Max Born among others to theorise quantum mechanics and Albert Einstein to write down his theory of general relativity. Quantum mechanics and general relativity are the basis for our current cosmological model. As such these two topics have allowed us to postulate theories of the origin and evolution of our Universe. In this chapter, we will briefly introduce general relativity and cosmology. The theories and concepts in this background chapter will provide the motivation and basis for the original work in later chapters.

1.2 General relativity

1.2.1 Special Relativity

In 1905 Albert Einstein wrote a paper entitled "*On the electrodynamics of moving bodies*" in which he developed special relativity. There are two postulates in special relativity:

- **Principle of relativity**: The results of any experiment performed by an observer do not depend on their speed relative to other observers who are not involved in the experiment.
- **Constancy of the speed of light**: The speed of light (measured to be $c \approx 3 \times 10^8$ ms^{-1}) is the same in all inertial frames of reference and it does not depend on the motion of the observer or source.

The first postulate says that the equations describing the laws of physics are of the same form in all inertial frames of reference. The second postulate, introduced by Einstein, transformed the theory into what we now know as special relativity. Anyone moving uniformly with respect to another at rest is entitled to believe that they are stationary and the other person is moving, encapsulates the relativity part. Einstein noticed that the electromagnetism equations (Maxwell's equations) were included in the laws of physics and therefore when combined with the first postulate implied that there must be something subtly incorrect about our conception of velocity and hence space and time.

One feature of special relativity is that one can define an inertial coordinate system in which the geometry is Lorentzian, i.e. particles move in a straight line with constant velocity. In this frame of reference, Newton's laws of inertia apply, i.e. a stationary object will not move on a table unless the reader moves it with the reader's hand. An inertial coordinate system or an inertial reference frame satisfies the following criteria:

1. The distance between two points is fixed.
2. There is a standard clock at every point.
3. The geometry of space is Euclidean.

The ability to write down an inertial reference frame allows us to measure positions and times which are presented in the form of a 4-vector. A 4-vector has an extra component, a time coordinate which represents a complex time direction. In 4D spacetime, we adopt the convention of Roman letters running through indices (1,3) and Greek letters running through indices (0,4). Since we are combining time with space in relativity, one can choose to measure time in units of length (treat it as another space coordinate). However, all factors of the speed of light, c, will be dropped in the rest of this section.

1.2.2 Curved spacetime

Einstein postulated that gravity relates to the relative acceleration of particles and acceleration can exist in special relativity. However, accelerating and stationary frames are treated differently in special relativity. For the acceleration of particles to be caused by the curved nature of spacetime, we must upgrade special relativity to general relativity. In general relativity, our postulates are upgraded to:

- **Principle of relativity**: The results of any experiment performed by an observer do not depend on their speed relative to other observers who are not involved in the experiment.
- **Constancy of the speed of light**: The speed of light (measured to be $c \approx 3 \times 10^8$ ms^{-1}) is the same in all frames of reference and it does not depend on the motion of the observer or source.

Lorentz invariance

There are multiple frames of reference in the Universe. For example, somebody on a rocket ship has a different coordinate system to somebody stationery on Earth. A concept that would allow one to change coordinate systems is, therefore, a good idea. A Lorentz transformation does just that. Let us begin with the infinitesimal distance between two points in Euclidean space before generalising to curved spacetime. Imagine two points in $\mathbb{R}^3$ one at (x, y, z) and the other at $(x + dx, y + dy, z + dz)$. The distance between the two points is given by the usual formula

$$ds^2 = dx^2 + dy^2 + dz^2 = dx^i dx^j \delta_{ij} \tag{1.1}$$

which is called the line element. Throughout this thesis, we will use the Einstein summation convention, i.e. two identical indices imply summation. In general relativity, we require a line element that is valid no matter the curvature and coordinate system. This involves the introduction of the metric tensor, which is

the generalisation of the Newtonian potential and contains information about the geometry of spacetime.

Consider a change of coordinates $x^i = F^i(y)$ then its derivative is $dx^i = \frac{\partial F^i}{\partial y^k} dy^k$ by the chain rule. Substituting this into the line element equation (1.1) above gives

$$\begin{aligned} ds^2 &= \frac{\partial F^\alpha}{\partial y^\gamma} dy^\gamma \frac{\partial F^\beta}{\partial y^\sigma} dy^\sigma \delta_{\alpha\beta} \\ &= \left(\frac{\partial F^\alpha}{\partial y^\gamma} \frac{\partial F^\beta}{\partial y^\sigma} \delta_{\alpha\beta} \right) dy^\gamma dy^\sigma \\ \implies ds^2 &= g_{\gamma\sigma} dy^\gamma dy^\sigma . \end{aligned} \tag{1.2}$$

This is the general form of the line element where $g_{\gamma\sigma}$ is the metric tensor. We will use the Misner, Thorne and Wheeler (MTW, Misner et al. (1973)) sign convention for our metric throughout resulting in $ds^2 = -dt^2 + dx^2 + dy^2 + dz^2$ for called Minkowski or flat spacetime. One final definition before moving on from the line element is that of proper time or the time measured by a clock in its rest frame, $ds^2 = -d\tau^2$.

A Lorentz transformation transforms one frame of reference into another that is moving at a constant velocity relative to the first. The invariance of this transformation only applies to inertial frames of reference and not to accelerating frames of reference, we will meet a metric in Section 1.3 that is not Lorentz invariant. In Appendix A.1 we prove that a Lorentz transformation is the most general transformation that preserves the line element.

The equivalence principle tells us that one cannot distinguish between motion under gravity and acceleration, which implies that one can think of replacing gravity with acceleration. General relativity allows one to think of all motion as relative and can be applied no matter the reader's coordinate system, i.e. the fundamental equations of physics always hold.

1.2.3 Geodesics, parallel transport and curvature

Our ultimate goal is to derive the Einstein field equations which will tell us how matter behaves under the influence of gravity. Or in other words how space (the metric tensor) is deformed by mass. Spacetime is defined as a mathematical

object called a manifold, for a detailed explanation of manifolds and tensors see Appendix A.2. If we have two events that occur at different places in curved spacetime (the manifold) we require a method to compare the vectors and tensors at the two events. The method used to do this is called parallel transport, crudely it transports the two events to a common-event, where comparisons can be made.

Before we elaborate on the idea of parallel transport it is useful for us to define how different objects transform. A covariant vector is a vector $V_\mu(x)$ that transforms like

$$V'_\mu(x') = V_\nu(x)\frac{\partial x^\nu}{\partial x'^\mu} \tag{1.3}$$

and a contravariant vector $V^\mu(x)$ is defined to transform like

$$V'^\mu(x') = \frac{\partial x'^\mu}{\partial x^\nu}V^\nu(x)\,. \tag{1.4}$$

Finally a general tensor is defined as something that transforms like

$$T^{\mu_1,\ldots,\mu_r}{}_{\nu_1,\ldots,\nu_s}(x') = \left(\frac{\partial x'^{\mu_1}}{\partial x^{\alpha_1}}\cdots\frac{\partial x'^{\mu_r}}{\partial x^{\alpha_r}}\right)\left(\frac{\partial x^{\beta_1}}{\partial x'^{\nu_1}}\cdots\frac{\partial x^{\beta_s}}{\partial x'^{\nu_s}}\right)T^{\alpha_1,\ldots,\alpha_r}{}_{\beta_1,\ldots,\beta_s}(x)\,. \tag{1.5}$$

Parallel transport

An affine connection connects tangent spaces (defined in A.2) to allow parallel transport along a curve; therefore allowing us to compare vectors at different points in spacetime. In Figure 1.1 a Riemann sphere is shown. A vector is parallel transported from A to N to B to A. The reader can see that the vector is not conserved. This is the motivation for introducing the Riemann tensor or curvature tensor in the next section.

To describe curvature or acceleration we require a way to differentiate vectors. The covariant derivative allows one to differentiate tangent vectors along a manifold. A covariant derivative will be represented by $\nabla_\mu V^\nu = V^\nu{}_{;\,\mu}$ and

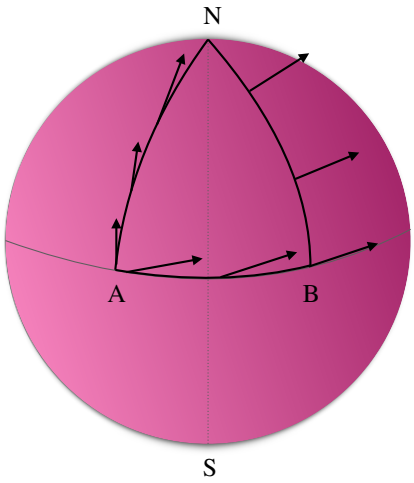

Figure 1.1 *A diagram of a Riemann sphere. A vector is parallel transported from A to N to B to A. The diagram shows that the vector is not conserved as it is transported. This is called holonomy and motives the introduction of affine connections and the Riemann tensor.*

$\partial_\mu f = f_{,\mu}$ is a contravariant derivative. The covariant derivative is defined as

$$\nabla_\nu V_\mu = \partial_\nu V_\mu - \Gamma^\lambda_{\mu\nu} V^\lambda \tag{1.6}$$

where $\Gamma^\lambda_{\mu\nu}$ is an affine connection. A final word on the covariant derivative is that $g_{\mu\nu;\alpha} = 0$ to preserve the raising and lowering of indices. The Christoffel symbol in (1.7) is the coefficients of the affine connection. This part of the derivative (1.6) that is accounting for the curvature of space (deformation of the metric tensor) as it involves contravariant derivatives of the metric tensor.

Christoffel symbols are defined as

$$\Gamma^\rho_{\mu\nu} = \frac{1}{2} g^{\rho\lambda} \left(g_{\mu\lambda,\ \nu} + g_{\lambda\nu,\ \mu} - g_{\mu\nu,\ \lambda} \right). \tag{1.7}$$

Now we must derive an equation that can describe the motion of particles through spacetime.

Geodesic equation

A geodesic is the idea of a straight line but generalised to curved spacetime. The geodesic equation tells us how free particles are moving on worldlines through spacetime. Massless particles, like photons, travel along null geodesics (straight worldlines in a radial direction). Consider a worldline $x^\mu(s)$ of a particle. The tangent vector to such a curve is $u^\mu = \frac{dx^\mu}{ds}$ and the curve is geodesic if $u^\mu{}_{;\nu} = 0$. This is the analogue of asking how much a vector $\mathbf{u}$ changes. Now we wish to know how much the vector $\mathbf{u}$ changes in the direction of $\mathbf{u}$. In our new language this leads to $u^\mu{}_{;\nu}u^\nu = 0$. Inserting the expression for the covariant derivative (1.6) and re-writing in terms of s yields the geodesic equation

$$\frac{d^2x^\mu}{ds^2} + \Gamma^\mu_{\nu\lambda}\frac{dx^\lambda}{ds}\frac{dx^\nu}{ds} = 0. \tag{1.8}$$

Riemann tensor

The curvature tensor or the Riemann tensor relies on the non-commutative nature of the covariant derivative i.e. $V_{\lambda;\,\mu\nu} - V_{\lambda;\,\nu\mu}$. Thus measuring the curvature of the surface and accounting for the holonomy of the surface (the fact a vector is not preserved on a sphere when it is parallel transported). The Riemann tensor is defined as

$$R^\rho{}_{\lambda\mu\nu} = \Gamma^\rho_{\lambda\nu,\,\mu} - \Gamma^\rho_{\lambda\mu,\,\nu} + \Gamma^\rho_{\mu\sigma}\Gamma^\sigma_{\lambda\nu} - \Gamma^\rho_{\nu\sigma}\Gamma^\sigma_{\lambda\mu}. \tag{1.9}$$

If one contracts two of the indices on the Riemann tensor, the Ricci tensor would be obtained, and after contracting both indices on the Ricci tensor the scalar curvature or Ricci scalar would be obtained. The Ricci tensor encodes how different the Riemann geometry is to flat space; it also tells us how the metric changes as a function of position. These are the curvature tensors that will appear in the Einstein field equations. As a side note, the Riemann tensor also satisfies

the Bianchi identity

$$R_{\rho\mu\sigma\nu;\,\tau} + R_{\rho\mu\nu\tau;\,\sigma} + R_{\rho\mu\tau\sigma;\,\nu} = 0. \tag{1.10}$$

There is one more tensor we must define before deriving the Einstein field equations. This tensor combines the Ricci tensor and scalar to provide all information needed about the curvature of spacetime to calculate the connection between gravity and curvature. It is given by

$$G_{\mu\nu} = R_{\mu\nu} - \frac{1}{2} R g_{\mu\nu}. \tag{1.11}$$

This is the Einstein tensor.

1.2.4 Einstein field equations

The Einstein field equations aim to relate spacetime curvature to matter content. These equations must be the same for all observers in any set of coordinates motivating the choice of tensors. Before we begin deriving these equations, we must define a tensor that describes the matter in general relativity.

Stress-energy momentum tensor

The stress-energy momentum tensor, $T^{\mu\nu}$, describes the matter content of general relativity. It is symmetric, and its covariant derivative is zero to conserve energy and momentum. Its components in the rest frame are $T^{00} = \rho$ and $T^{ij} = p\delta^{ij}$ where ρ is mass density and p is pressure. Using the value of the stress-energy momentum tensor in the rest frame, we can write its general form as

$$T^{\mu\nu} = (\rho + p)\, u^{\mu} u^{\nu} + p g_{\mu\nu}. \tag{1.12}$$

The derivatives of the stress-energy momentum tensor lead to the continuity and

equations of motion for a perfect fluid in thermodynamic equilibrium. We will use this tensor in Section 1.3 to derive key equations that describe the matter in our Universe.

Derivation of the Einstein field equations

We can write down the form we wish the Einstein equations to take based on the goal stated at the beginning of this subsection

$$C^{\mu\nu} = \kappa T^{\mu\nu} \tag{1.13}$$

where $C^{\mu\nu}$ is symmetric and κ is a constant. The tensor $C^{\mu\nu}$ represents curvature and $T^{\mu\nu}$ is the stress-energy momentum tensor representing matter. In the Newtonian limit, we must still be able to reproduce Newtonian gravity. We will therefore say that we want $C^{\mu\nu}$ to have no more than second derivatives. The second derivative of curvature is the Ricci tensor so we can assume that

$$C^{\mu\nu} = R^{\mu\nu} + \lambda\left(x\right) g^{\mu\nu} = \kappa T^{\mu\nu}. \tag{1.14}$$

We also know that energy and momentum are conserved so $C^{\mu\nu;\ \nu} = 0$. This leads to

$$R^{\mu\nu;\nu} + \lambda^{;\nu} g^{\mu\nu} = 0 \tag{1.15}$$

and we can express the covariant derivative of the Ricci tensor in terms of the Ricci scalar using the Bianchi identity (1.10). Substituting this into (1.15) allows us to write down a form for the function $\lambda\left(x\right)$

$$\lambda\left(x\right) = -\frac{1}{2}R + \Lambda \tag{1.16}$$

where Λ is a constant. The two constants κ and Λ must be determined so that we have a complete expression for the field equations. The Einstein field equations must return Newtonian gravity in the Newtonian limit as we know this description to be true under certain constraints. This implies that $\kappa = 8\pi G$ and Λ appears to be zero. We will meet Λ later on as the cosmological constant. One can prove that these are the values for the two constants by using gravitational redshift and perturbing the metric tensor. Our final form for the Einstein field equations is

$$R_{\mu\nu} + \left(\Lambda - \frac{1}{2}R\right) g_{\mu\nu} = 8\pi G T_{\mu\nu}. \tag{1.17}$$

If an object with some mass is placed in spacetime, it will deform the metric tensor, this, in turn, will alter the curvature of space and determine the gravitational effect. We refer the reader to Schutz (1985), Misner et al. (1973), Hobson et al. (2006) and Weinberg (1972) for more information on general relativity.

1.3 Cosmology

1.3.1 The geometry of the Universe

In this section the mathematics used to describe the background cosmology will be introduced.

FRW metric and redshift

If we accept general relativity to be the correct theory of gravity in our Universe, we require a metric that to describe the curvature of the Universe. The Cosmological Principle tells us that on large scales and at any fixed time, the Universe is isotropic and homogeneous. We also know that the Universe is expanding (at an accelerated rate). The metric of a 3D sphere embedded in

4D spacetime (Robertson Walker spacetime metric in spherical coordinates) is

$$ds^2 = -c^2 dt^2 + \frac{dr^2}{1 - Kr^2} + r^2 \left[d\theta^2 + \sin^2 \theta d\phi^2 \right]. \tag{1.18}$$

We can alter this metric so that it describes the expanding Universe by replacing the time-dependent curvature K with $\frac{k}{a^2(t)}$ and $r = a(t)\, x$. The new coordinates x are called co-moving coordinates and $a(t)$ is the scale factor. Co-moving coordinates ensure that the isotropic Universe characteristics only depend on time. The Friedmann-Robertson Walker (FRW) metric used to describe our expanding Universe is

$$ds^2 = -c^2 dt^2 + a^2(t) \left[\frac{dr^2}{1 - kr^2} + r^2 \left(d\theta^2 + \sin^2 \theta d\phi^2 \right) \right] \tag{1.19}$$

where r is now the co-moving radial distance. The curvature parameter can have the following values;

- flat space, $k = 0$
- positive curvature (closed universe), $k = 1$
- negative curvature (open universe), $k = -1$.

The FRW metric is not Lorentz invariant, and the CMB tells us that the Universe has a preferred frame of rest due to the initial conditions. We will set the value of the scale factor today to be $a(t_0) = 1$. Note that in the later chapters we will normalise all calculations to this. We have defined a new coordinate system that allows us to account for the expansion of space which results in our physical velocity changing. We now have

$$\mathbf{v}_{\text{phy}} = H(t)\, \mathbf{x}_{\text{phy}} + \mathbf{v}_{\text{pec}} \tag{1.20}$$

where $H = \frac{\dot{a}}{a}$ is the Hubble parameter and $\mathbf{v}_{\text{pec}}$ is the peculiar velocity which describes the inherent motion of the object relative to the cosmological frame.

Today's value of the Hubble parameter is called the Hubble constant and is denoted by H_0.

The physical size of the Universe is

$$d_{\text{phy}} = a \int_0^{r_{\max}} \frac{dr'}{\sqrt{1 - kr'^2}}, \tag{1.21}$$

where $r_{\max}$ is the distance that light has travelled since the Big Bang. This distance is called the particle horizon, and nothing outside of this horizon can affect us today. We desire a way to measure the age of and distance, to the objects we are observing. The observational data travels towards us in light waves which we learned in Section 1.2 travel along null geodesics and in a radial direction. This means that

$$cdt = \frac{\pm a \ dr}{\sqrt{1 - kr'^2}} \tag{1.22}$$

where the light is travelling towards us if its sign is negative and away from us with its sign is positive. Suppose that some distant object at r_1 emits light at some time t_1 and we observe the signal at $r = 0$ and time t_0

$$c \int_{t_1}^{t_0} \frac{dt}{a} = \int_0^{r_1} \frac{dr}{\sqrt{1 - kr'^2}}. \tag{1.23}$$

Now a second galaxy emits light at time $t_1 + \delta t_1$ and it is observed at $t_0 + \delta t_0$ then

$$c \int_{t_1+\delta t_1}^{t_0+\delta t_0} \frac{dt}{a} = \int_0^{r_1} \frac{dr}{\sqrt{1 - kr'^2}}. \tag{1.24}$$

The RHS of (1.23) and (1.24) are the same therefore

$$\int_{t_1+\delta t_1}^{t_0+\delta t_0} \frac{dt}{a} - \int_{t_1}^{t_0} \frac{dt}{a} = 0 \tag{1.25}$$

and the difference in time is $\delta t_0 = \frac{\delta t_1}{a(t_1)}$. We can relate this difference in time to the wavelength of the light emitted by $\lambda = c\delta t$. Redshift is hence defined as

$$z = \frac{\lambda_0 - \lambda_1}{\lambda_1} = \frac{1}{a} - 1. \tag{1.26}$$

This means that when $z = 1$ the Universe was half its current size and that light is being stretched by the expansion of space. Cosmological redshift is a very useful method of measuring how light travels towards us from distant galaxies. We can use its definition to define the luminosity distance which is given by

$$d_L = c\,(1+z) \int_0^z \frac{dz'}{H\,(z')}, \tag{1.27}$$

and is usually measured in Parsecs in astronomy. A Parsec is defined as the distance at which a star will exhibit one arcsecond of parallax and 1pc $\approx 3.086 \times 10^{16}$m. Some examples of distances are: 8 kiloparsecs to the centre of the Milky Way and 1 megaparsecs to the nearest galaxy.

Friedmann equations

In Section 1.2.4 we introduced the Einstein field equations which allow us to connect matter and the curvature of space. We have the FRW metric (1.19) which describes the geometry of the Universe encoding the ideas of homogeneity and isotropy. The next ingredient we need to calculate the Einstein field equations for our Universe is the stress-energy momentum tensor. When one computes the Ricci tensor components for the FRW metric only diagonal components remain, e.g. $R_{tt} \neq 0$, therefore, the stress-energy momentum tensor also only has non-zero diagonal terms. On large scales the Universe does appear to be homogeneous and

isotropic, it, therefore, makes sense to use the stress-energy momentum tensor for a perfect fluid whose components are $T^{00} = \rho g^{00}$ and $T^{ii} = p g^{ii}$.

Substituting the Ricci tensor, scalar and the stress-energy momentum tensor into the Einstein equations yields the Friedmann equations (Friedman, 1922). These equations can also be derived using a Newtonian method. The first Friedmann equation is

$$H^2 = \left(\frac{\dot{a}}{a}\right)^2 = \frac{8\pi G}{3}\rho - \frac{k^2}{a^2} + \frac{\Lambda}{3} \tag{1.28}$$

and the second equation (the acceleration equation) is

$$\frac{\ddot{a}}{a} = -4\pi G\left(\frac{1}{3}\rho + p\right) + \frac{\Lambda}{3}. \tag{1.29}$$

These Equations (1.28) and (1.29) inform us how the scale factor, a, evolves which in turn tells us how quickly the Universe is expanding. Measuring the mass density, ρ, of the Universe is difficult to imagine leading us to re-write (1.28) in terms of more digestible variables. We can define the critical density to be $\rho_{\text{crit}} = \frac{3H^2}{8\pi G}$ and the define the ratio of the mass density and the critical density as $\Omega = \frac{\rho}{\rho_{\text{crit}}}$. The mass density ρ is the total mass density this means we can write $\rho = \rho_m + \rho_r + \rho_v$ representing the three species of matter in the Universe. ρ_m is the mass density of non-relativistic matter including baryonic and dark matter, ρ_r is the mass density of radiation in the Universe, and ρ_v is the mass density for empty space, i.e. dark energy. We can measure the values of these parameters today observationally, to write ρ_m in terms of its present-day value we have to solve the continuity equation

$$\dot{\rho} + 3H(\rho + p) = 0. \tag{1.30}$$

The pressure can be related to the density using the equation of state $p = w\rho$ where $w = 0$ for matter, $w = 1/3$ for radiation and $w = -1$ for empty space. This allows us to solve Equation (1.30) for each species; the matter density is given by

$\rho^m = \rho_0^m a^{-3}$ for example. We can now rewrite the Friedmann equation as

$$H^2 = H_0^2 \left(\frac{\Omega_{m,0}}{a^3} + \frac{\Omega_{r,0}}{a^4} + \Omega_{v,0} \right) \tag{1.31}$$

where we have set the curvature constant $k = 0$ as this matches current observations and the cosmological constant has been absorbed into the $\Omega_{v,0}$ term. If the curvature constant is zero then this implies that $\Omega = \sum_\alpha \Omega_\alpha = 1$ which matches current observations of our Universe. We will use this in later chapters and it will be assumed to be true. In Chapter 2 we will expand on the equations defined in this section and show how we can determine theoretical predictions of observations.

1.3.2 The hot dense Universe

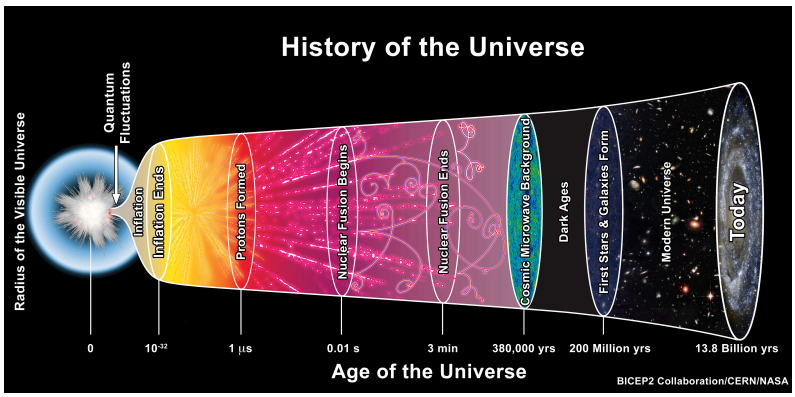

Figure 1.2 *Timeline of the evolution of the Universe from the Big Bang to today.*

Our current theory of the beginning of the Universe is called the Big Bang, we do not know what happened before this event or indeed if anything happened before. The Cosmological Principle tells us that "*Viewed on a sufficiently large scale at any fixed time, the properties of the Universe are the same for all observers*". The Big Bang model has some problems including the horizon problem (why does everything look the same in every direction?) and the flatness problem (why is the density of matter in the Universe comparable to the critical density needed for a flat Universe?). These problems can be solved with the introduction of cosmic inflation (Starobinskii, 1979, Guth, 1981). Cosmic inflation is the theory that between 10^{-36} seconds to 10^{-32} seconds after the Big Bang there was an exponential expansion of space.

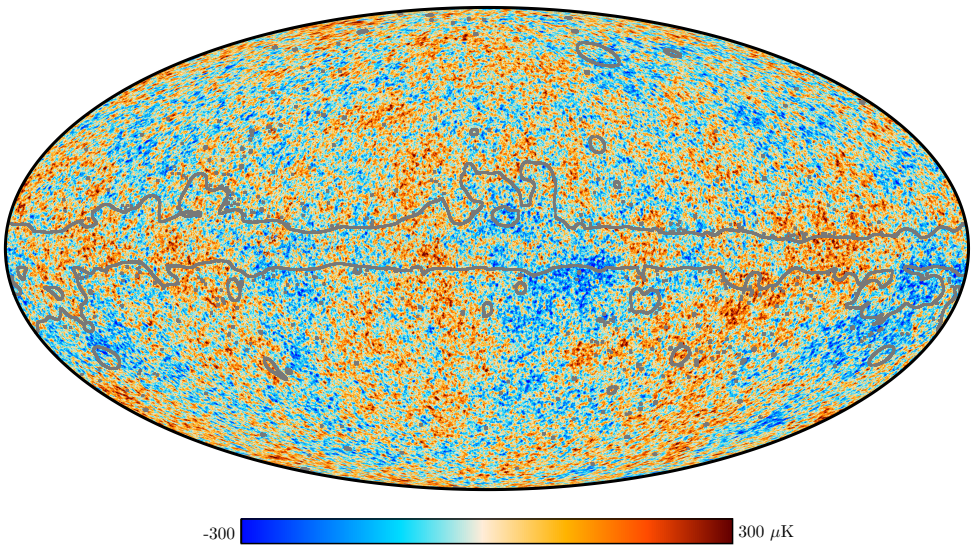

Figure 1.3 *Temperature map of the Cosmic Microwave Background taken by the ESA and Planck Collaboration in 2018 (Collaboration et al., 2018). The grey lines show the confidence mask.*

We know very little about this era of the Universe as our theory of general relativity breaks down due to quantum effects. We believe the quantum fluctuations that existed at the very beginning of our Universe were stretched out during inflation and became the seeds for the growth of structure today. There are many theories of inflation including single field, multi-field and eternal (We refer the reader to Kolb & Turner (1990), Liddle & Lyth (1993), Liddle (1999) for an introduction to inflation). Current efforts are turning to string theory and quantum gravity in order to better describe the physics of the early universe by unifying general relativity and quantum mechanics.

Around 1 second after the Big Bang neutrinos decoupled from matter and subatomic particles such as protons and neutrons were formed. The decoupling of the neutrinos is called the Cosmic Neutrino Background (CNB) which is very difficult to observe directly. A few minutes later the Universe was cool enough for Big Bang Nucleosynthesis (BBN) to occur and for elements such as deuterium to form. This process of cooling down continued until around 377,000 years ($z \approx 1100$) after the Big Bang when recombination occurred or when neutral atoms were formed. Then at 380,000 years ($z \approx 1089$) after the Big Bang matter decoupled from light resulting in the Cosmic Microwave Background (CMB). This is called the epoch of last scattering.

The CMB is the oldest object we can currently observe in our Universe. In 2009 a space instrument was launched by ESA (European Space Agency) called *Planck*

that measured the CMB temperature anisotropies until it was decommissioned in 2013. In Figure 1.3 a *Planck* 2018 map of the temperature anisotropies of the CMB (the current temperature of the CMB is 2.725 K and it is almost isotropic) is shown. We expected the CMB to have a Black-Body spectrum (requires thermal equilibrium) and early measurements in the 1960s by Penzias and Wilson confirmed this (Penzias & Wilson, 1965). However, as our instruments for observing the CMB have improved we have begun to see there are small anisotropies ($\Delta T = 5.4$mK). These have lead us to believe that the early Universe was not as smooth as we originally thought motivating the introduction of non-baryonic matter (matter made of particles other than protons and neutrons). CMB measurements have ruled out other theories about the beginning of our Universe and seem to favour the Big Bang and inflation model. We will go into more detail about what the CMB tells us about the evolution of the Universe in Section 1.3.4.

1.3.3 The dark Universe

After matter decoupled from light and the CMB was produced we entered the dark ages of the Universe which lasted until about 1 billion years after the Big Bang. In the dark ages, star formation began and, the structures that would eventually form the galaxies and clusters we observe today formed. There are three key components of the Universe as we know it today; baryonic matter, dark matter and dark energy. The nature of the dark components is still an unanswered question in cosmology.

Dark matter (25% of today's Universe)

In 1884 Lord Kelvin presented a talk in which he estimated the abundance of dark structures in our Universe from the velocity dispersion of the stars orbiting the centre of our galaxy. The phrase "dark matter" was coined later in 1906 by Henri Poincaré. In the 1930s the first modern evidence of dark matter's existence was presented by Fritz Zwicky (Zwicky, 1937) after he used observations of the Coma cluster to show that the galaxy rotation curves did not match what was predicted if only visible matter existed. In the 1970s Vera Rubin, Kent Ford and Ken Freeman (Rubin & Ford, 1970) provided even more strong evidence again using galaxy rotation curves and by the 1980s dark matter had been accepted as

a fundamental part of the theory of our Universe.

The currently favoured theory of dark matter is Cold Dark Matter (CDM). It is cold as its velocity is much less than that of light at matter-radiation equality. It is collisionless as it only reacts with itself and other particles through gravity and it is non-baryonic. Dark matter collapses under gravity to form walls, filaments and nodes. These structures are the building blocks of the Universe as the baryonic matter is attracted to their mass. The combination of this structure is known as the cosmic web. The formation and appearance of the cosmic web will provide motivation for the work carried out in Chapter 3.

As mentioned before the nature of dark matter has not yet been discovered. There are many alternatives to CDM including fuzzy (extremely light bosonic dark matter), self-interacting, axion-like, sterile neutrinos, Weakly Interacting Massive Particles (WIMPs) and even primordial blackholes have been proposed as candidates (Schneider et al., 2017). The current evidence for CDM will be discussed in Section 1.3.4.

Dark energy (75% of today's Universe)

In Section 1.3.2 the theory of inflation was introduced. During this period the Universe expanded exponentially due to the negative pressure properties of a scalar field. The Universe is still expanding today, and the force causing the accelerated expansion is called dark energy. This does not mean that the objects in the Universe are getting larger but that they are getting further apart. Evidence for the accelerated expansion of the Universe was detected in 1988 and Perlmutter, Schmidt and Riess (Riess et al., 1998) won the Nobel prize for the discovery in 2011.

Recall in Section 1.2.4 in Equation (1.17) a constant Λ had to be introduced into the Einstein field equations. This constant is called the cosmological constant and is the most popular explanation for dark energy. There are alternative dark energy theories including quintessence, united dark matter and dark energy and modified gravity (see Clifton et al. (2012) for a review). The combined cosmological theory of CDM and the cosmological constant is called Λ-CDM. This theory accounts for the CMB, cosmic web and the accelerating expansion of our Universe amongst other observable properties. In Section 1.3.1 we will describe the parameters of this model and controversies surrounding evidence for it.

The cosmological constant can also be estimated using Quantum Field Theory (QFT). The value estimated using QFT is 10^{60} times larger than the cosmological measurement, and this value would not make sense in a cosmological context. This is known as the cosmological constant problem. Solutions to the cosmological constant problem include the multiverse (Weinberg, 2005), string theory (Polchinski, 2006, Bousso, 2007) and IR-modifications to gravity (Dvali, 2004). See Padilla (2015) for a more in-depth overview of the cosmological constant problem.

1.3.4 Λ-CDM

Current observational evidence is in favour of Λ-CDM being a good approximation to describe our Universe (Del Popolo & Le Delliou, 2017). Let us focus on four observations that provide evidence for the theory.

Cosmic Microwave Background (CMB)

The CMB introduced in Section 1.3.2 can be described using linear theory, hence we understand the physics of it very well (Sunyaev & Zeldovich, 1980a). However, it is only a 2D image, therefore, information can be erased on small scales meaning we must combine it with other probes to tightly constrain our models.

The temperature anisotropies in the CMB can be decomposed into spherical harmonics which allows us to define the angular power spectrum. We use a Gaussian random field as the initial conditions for our Universe. This can cause issues since we can only observe one CMB, ours, which is a single realisation of a random field. This means that the error on our measurements is dominated by cosmic variance on large scales.

Photons are polarised due to Thomson scattering off free electrons in the surface of last scattering which leads to us being able to also have polarisation anisotropies. The polarisation field is usually decomposed into E modes and B modes. The E modes are parallel or perpendicular to the plane wave (curl-free part of the polarisation field) and can only be produced by scalar perturbations (density fluctuations). The B modes are at 45° to the polarisation field and can be produced by scalar and tensor perturbations (gravitational waves).

The signals of the anisotropies in the CMB are affected on the large scales by cosmic variance. They are also affected by the Integrated Sachs-Wolfe (ISW,

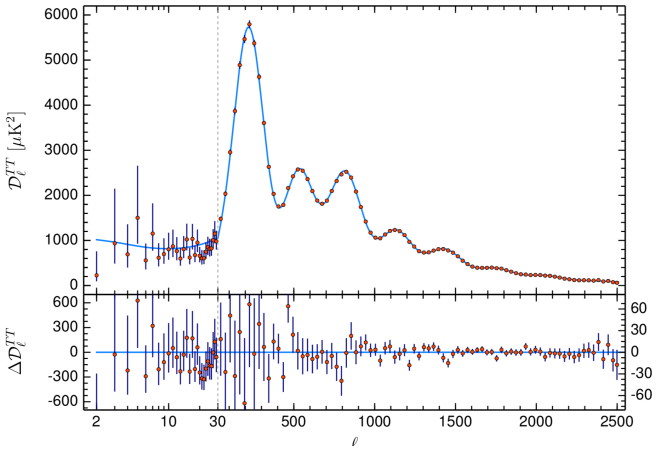

Figure 1.4 *A Planck TT angular power spectrum measured from the CMB taken from Collaboration et al. (2018).*

Sachs & Wolfe (1967)) which redshifts the photons from the surface of last scattering (points in the Universe where decoupling occurred). The Sunyaev-Zel'dovich (Sunyaev & Zeldovich, 1970, 1972, 1980b) effect also scatters the photons through their contact with hot gas (this occurs at later times). Primordial gravitational waves can also distort the signal although they have not been detected. Taking these effects into account we can measure four power spectra: T-T, E-E, B-B and E-T. We cannot measure B-T as the B mode has opposite parity.

In Figure 1.4 a *Planck* collaboration temperature-temperature power spectrum is shown versus the angular scale ℓ. The large scales are given by small values of ℓ which are dominated by cosmic variance. One can clearly see that for values of $\ell < 30$ the errors on the measurement are far greater than on small scales. The small increase in power on large scales is due to reionization (when Hydrogen was reionized at around $z = 1089$). The first largest peak is a strong probe of the curvature of our Universe because it occurs at around $\ell = 200$ it suggests that we live in a flat universe. This can be used to constrain Ω_m which in turn allows us to constrain the non-baryonic matter.

Standard Candles

The CMB gave us evidence for the Big Bang, inflation and non-baryonic matter. Standard candles were some of the first observational evidence for the accelerated expansion of the Universe in the 1990s (Riess et al., 1998). These are objects

whose intrinsic brightness can be measured by means other than the luminosity distance. The luminosity distance defined in (1.27) depends on the Hubble parameter. Therefore if one could measure the apparent brightness of an object without using the luminosity distance, the value of the Hubble parameter could be measured. Some examples of standard candles are cepheids (bright pulsing stars originally used by Hubble) and type Ia supernova (white dwarves collapsing). The measurement of the brightness of standard candles has allowed teams to measure the value of the Hubble constant. In Section 1.3.4 we will discuss the tension between these late-time measurements and early-time measurements.

Baryon Acoustic Oscillations (BAO)

In the early Universe, baryons and photons were coupled together in a primordial plasma. Consider a small point-like perturbation early in the Universe and that all species have been perturbed by the same amount (this is an adiabatic perturbation). The neutrinos from the Cosmic Neutrino Background have streamed away and the dark matter only interacts gravitationally. As the baryonic matter and photons are dense they attract the dark matter and it falls into the centre of the sphere. As it is the early Universe, the gas is extremely hot, which, results in the photons being unable to travel far. It is this trapping of the photons that creates radiation pressure. The sphere continues to attract matter from its surroundings resulting in an expanding sphere with dark matter clumped in the centre. Eventually, when the Universe cools the photons can escape the gas (this is called Silk damping (Silk, 1968)). The resulting object, that is no longer subject to radiation pressure, is a sphere with a clump of dark matter in the centre and a shell of gas at a radius of around 150 Mpc. Eventually, the shell of gas will imprint on the dark matter via gravitational interaction, this imprint is called the acoustic scale.

In Figure 1.4 the largest peak appears at approximately $\ell = 200$ this tells us the scale at which galaxies are correlated, this is precisely the acoustic scale. We can measure this scale at different redshifts and build a picture of how the Universe is expanding. In Chapter 4 the difficulties modelling BAO features are discussed.

Gravitational lensing

The theory of general relativity tells us that massive objects will bend the light emitted from sources behind them, which results in galaxies appearing distorted. The reader can demonstrate strong gravitational lensing by placing the bottom of a wine glass over an image. We can measure and quantify the distortion of galaxies and use this to map out the underlying dark matter distribution.

In practice, it is difficult to estimate the distortion of one galaxy as they usually occupy only a few pixels of an image. Gravitational lensers, therefore, average over many galaxies and measure how elliptical these galaxies are on average. Thus allowing them to probe dark matter and dark energy. Recent surveys such as *KiDS* (Hildebrandt et al., 2017) and *DES* (Abbott et al., 2018) have combined their predictions with the CMB and placed even tighter constraints on the Λ-CDM model. In the near future *Euclid* (Laureijs et al., 2011, Amendola et al., 2013), a space-based lensing instrument, will be launched and will observe around 10 billion sources. It is hoped, that this will help shed light on dark matter, the formation of cosmic structures and the other dark component, dark energy.

Parameters of Λ-CDM

The Λ-CDM model has six independent parameters these are:

- $\Omega_b h^2$, the physical baryon density
- $\Omega_c h^2$, the physical non-baryonic matter density
- t_0, the age of the Universe
- n_s, scalar spectral index
- Δ^2_R, curvature fluctuation amplitude
- τ, reionisation optical depth.

We have met the physical baryon and non-baryonic matter densities in Section 1.3.1 where they have now been multiplied by $h = \frac{H}{100}$. The scalar spectral index describes how the density fluctuations vary with scale and is used in the definition of the primordial power spectrum. The curvature fluctuation

amplitude tells us how different the Universe is from a flat universe. From these parameters, we can calculate all others including Ω_Λ and H_0. Measurements of these parameters using the above methods and more match the theoretical predictions of Λ-CDM. However, there are still issues with the dark matter model including the too big to fail problem and the missing satellite problem (Klypin et al., 1999, Moore et al., 1999, Boylan-Kolchin et al., 2011, Weinberg et al., 2015, Papastergis & Shankar, 2016, Schneider et al., 2017, Popolo & Delliou, 2017). Λ-CDM also does not tell us how dark matter and dark energy formed or what they are made of.

H_0 tension

In this section we have summarised some of the observational methods that allow us to measure cosmological parameters. Although measurements of the parameters in the Λ-CDM model have matched predictions there is currently a tension between H_0 measurements (Bernal et al., 2016, Verde et al., 2019). The early Universe measurements of the CMB (Planck Collaboration et al., 2016a,b, Collaboration et al., 2018), BAO (Alam et al., 2017) and BBN give a value of around $H_0 = 67$ kms^{-1}Mpc^{-1}. The late Universe measurements using standard candles (Riess et al., 2016, Wong et al., 2019) give a value of around $H_0 = 73$ kms^{-1}Mpc^{-1}. The difference between the early and late time measurements ranges from 4σ to 6σ.

In Figure 1.5 the measured value of H_0 is shown for a range of early and late time surveys. One thing to note is that the early-time measurements have far smaller error bars because there are not many standard candles. However, the early Universe measurements rely on having a model and therefore are not model-independent. This tension is one of the most significant controversies in modern cosmology. The solution could be that there is some statistical flaw in the measurements, or it could indicate that we need new physics. Gravitational waves can provide an independent measurement of H_0, and are called standard sirens. It is hoped, that with future surveys and more gravitational wave measurements we can solve the tension.

For a more in depth overview of cosmology we refer the reader to Peacock (1999), Dodelson (2003), Mukhanov (2005) and Weinberg (2008).

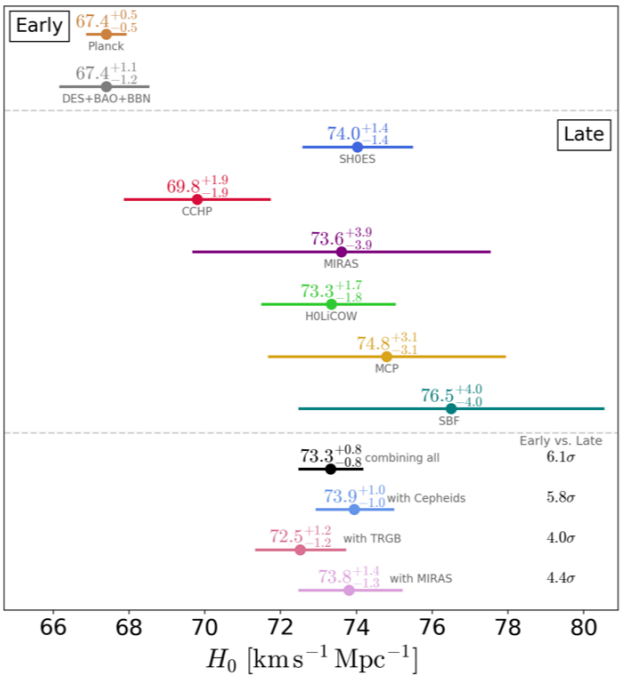

Figure 1.5 *Figure taken from Verde et al. (2019) showing a range of early and late time measurements of H_0.*

Chapter 2

Cosmological Perturbation Theory

> The definition of a good mathematical problem is the mathematics it generates rather than the problem itself.
>
> *Andrew Wiles*

2.1 Relativistic Perturbation Theory

We will derive standard cosmological perturbation theory relativistically in this chapter. For more in depth discussion we refer the reader to Peebles (1980, 1987), Peebles & Harrison (1994) and Coles & Lucchin (1996).

2.1.1 Background equations

In Section 1.3.1 we introduced the FRW metric (2.1). We will begin by defining the background evolution equations in a flat universe with $c = 1$ resulting in

$$ds^2 = -dt^2 + a^2(t)\,\delta_{ij}dx^i dx^j \tag{2.1}$$

it is useful to write this in terms of conformal time, $d\eta = \frac{dt}{a}$

$$ds^2 = a^2(\eta)\left[-d\eta^2 + \delta_{ij}dx^i dx^j\right]. \tag{2.2}$$

The background Friedmann equations are (1.28)

$$\mathcal{H}^2 = \frac{8\pi G}{3}\bar{\rho}a^2 \tag{2.3a}$$

$$\mathcal{H}' = -\frac{4\pi G}{3}(\bar{\rho} + 3\bar{p})a^2 \tag{2.3b}$$

where $\mathcal{H} = aH$ and a prime denotes differentiation by η. It is also useful to define the continuity equation, the background equation of state and the sound speed

$$\bar{\rho}' = -3\mathcal{H}(1+w)\bar{\rho} \quad , \quad w = \frac{\bar{p}}{\bar{\rho}} \quad \text{and} \quad c_s^2 = \frac{\bar{p}'}{\bar{\rho}'}. \tag{2.4}$$

Before moving on we will define three more useful expressions

$$\mathcal{H}' = -\frac{1}{2}\mathcal{H}^2(1+3w) \tag{2.5a}$$

$$\frac{w'}{1+w} = 3\mathcal{H}\left(w - c_s^2\right) \tag{2.5b}$$

$$\bar{p}' = -3\mathcal{H}c_s^2(1+w)\bar{\rho}. \tag{2.5c}$$

When $w < -1$ there is phantom energy for this reason is always taken to be $w \leq -1$ in the rest of this thesis. Dark matter is usually described as a pressure-

less perfect fluid, hence $w = 0$ is used. The values of $w = 1/3$ and $w = -1$ are used for radiation and dark energy respectively. See Section 1.3.1 for more details.

2.1.2 Metric Perturbations

The perturbed metric is $g_{\mu\nu} = \bar{g}_{\mu\nu} + \delta g_{\mu\nu} = a^2 \left(\eta_{\mu\nu} + h_{\mu\nu}\right)$ where $h_{\mu\nu}$ is not a tensor. We will only consider perturbations to order h and will define $h^{\mu\nu} = \eta^{\mu\rho}\eta^{\nu\sigma}h_{\rho\sigma}$. The components of the metric perturbation are

$$[h_{\mu\nu}] = \begin{bmatrix} -2A & -B_i \\ -B_i & -2D\delta_{ij} + 2E_{ij} \end{bmatrix}, \tag{2.6}$$

where $D = -\frac{1}{6}h$ and $E_{ii} = 0$ (Bertschinger, 1995, Ma & Bertschinger, 1995). The line element for our perturbed metric is therefore

$$ds^2 = a^2 \left[-(1+2A)\, d\eta^2 - 2B_i d\eta dx^i + \left((1-2D)\,\delta_{ij} + 2E_{ij}\right) dx^i dx^j \right] \tag{2.7}$$

where $A\left(\eta, x^i\right)$ is called the lapse function and $B_i\left(\eta, x^i\right)$ is called the shift vector.

Two types of coordinate transforms can be considered. The first is called a gauge transformation which is when the background coordinates are fixed, and the coordinates in the perturbed spacetime are changed. There are multiple suitable coordinate choices in the perturbed spacetime. Let us introduce two gauges to demonstrate how such transformations are performed.

Synchronous gauge

One popular gauge choice is the synchronous gauge. In this gauge the g_{00} and g_{0i} components are unperturbed. The line element is therefore

$$ds^2 = a^2(\eta) \left[-d\eta^2 + \left(\delta_{ij} + h_{ij}\right) dx^i dx^j \right]. \tag{2.8}$$

There are, however, issues with this gauge as the gauge degrees of freedom are not fixed. Coordinate singularities can also arise when two free-falling observers trajectories cross each other. This motivates the introduction of another gauge.

Conformal Newtonian Gauge

The line element for this gauge is

$$ds^2 = a^2(\eta)\left[-(1+2\psi)\,d\eta^2 + (1-2\phi)\,dx^i dx_i\right] \tag{2.9}$$

where ψ can be related the the gravitational potential in the Newtonian limit. We will eventually use this gauge to study scalar perturbations later in this chapter (note that only scalar perturbations can be studied in this gauge). For now, we will use these two gauges to demonstrate gauge transformations.

A general coordinate transform is $\hat{x}^\mu + d^\mu(x^\nu)$ which when split into time and space components is

$$\hat{x}^0 = x^0 + \alpha(\mathbf{x}, \eta) \tag{2.10}$$

$$\hat{\mathbf{x}} = \mathbf{x} + \nabla\beta(\mathbf{x}, \eta) + \epsilon(\mathbf{x}, \eta)\,. \tag{2.11}$$

where β is the longitudinal component (along the propagation direction) of d and ϵ is the transverse component (perpendicular to the propagation direction). Using these rules (2.10) one can show that the transformed metric is

$$\hat{g}_{\mu\nu} = g_{\mu\nu} - g_{\mu\beta}\partial_\nu x^\beta - g_{\alpha\nu}\partial_\mu x^\alpha - d^\alpha \partial_\alpha g_{\mu\nu} \tag{2.12}$$

which can then be applied to determine $(\hat{A},\ \hat{B}_i,\ \hat{D},\ \hat{E}_{ij})$. These are

$$\hat{A}(\mathbf{x},\eta) = A(\mathbf{x},\eta) - \alpha'(\mathbf{x},\eta) - \frac{a'}{a}\alpha(\mathbf{x},\eta) \tag{2.13}$$

$$\hat{B}_i(\mathbf{x},\eta) = B_i(\mathbf{x},\eta) - \frac{1}{2}\partial_i\alpha(\mathbf{x},\eta) + \frac{1}{2}\left(\beta'_{,i}(\mathbf{x},\eta) + \epsilon'_i(\mathbf{x},\eta)\right) \tag{2.14}$$

$$\hat{D}(\mathbf{x},\eta) = D(\mathbf{x},\eta) + \frac{1}{3}\nabla^2\beta(\mathbf{x},\eta) + \frac{a'}{a}\alpha(\mathbf{x},\eta) \tag{2.15}$$

$$\hat{E}_{ij}(\mathbf{x},\eta) = E_{ij}(\mathbf{x},\eta) - \left(\partial_i\partial_j - \frac{1}{3}\delta_{ij}\nabla^2\right)\beta(\mathbf{x},\eta) - \frac{1}{2}\left(\partial_i\epsilon_j(\mathbf{x},\eta) + \partial_j\epsilon_i(\mathbf{x},\eta)\right). \tag{2.16}$$

These equations (2.13) can be used to define A and D in terms of the function β. These, in turn, can be implemented to switch between the synchronous and conformal gauges, for example. Note that one usually ignores the arbitrary time coordinate change $\hat{x}^0 = x^0 + \psi(\eta)$ by setting $\psi(\eta) = 0$.

2.2 Scalar Perturbations

Let us focus on scalar perturbations as they are responsible for structure formation in the Universe, which is the main motivation for the work in this thesis. Recall that $g^S_{\mu\nu} = a^2\eta_{\mu\nu} + \delta^S g_{\mu\nu}$ and $ds^2 = g^S_{\mu\nu}dx^\mu dx^\nu$ for the scalar perturbations. We will work in the conformal Newtonian gauge for the rest of this chapter, results for the synchronous gauge can be found in Ma & Bertschinger (1995). We will also define the Bardeen potentials (Bardeen, 1980) which are gauge invariant

$$\Phi = -\phi \tag{2.17}$$

$$\Psi = \psi. \tag{2.18}$$

the conformal Newtonian gauge (2.9) is now given by

$$ds^2 = a^2(\eta)\left[-(1+2\Phi)\,d\eta^2 + (1-2\Psi)\,\delta_{ij}dx^i dx^j\right] \tag{2.19}$$

with

$$g_{\mu\nu} = a^2(\eta)\begin{bmatrix} -1-2\Psi & 0 \\ 0 & (1-2\Phi)\,\delta_{ij} \end{bmatrix} \tag{2.20}$$

and

$$g^{\mu\nu} = a^{-2}(\eta)\begin{bmatrix} -1+2\Psi & 0 \\ 0 & (1+2\Phi)\,\delta_{ij} \end{bmatrix}. \tag{2.21}$$

2.2.1 Scalar perturbation evolution equations

In Chapter 1 we introduced the Einstein equations as a method used to link the curvature of space with matter. To investigate structure formation in the Universe, we will need to calculate these equations in the conformal Newtonian gauge. We will therefore need the Einstein tensor. To derive this let us first state the non-zero Christoffel symbols in the conformal Newtonian gauge

$$\Gamma^0_{00} = \mathcal{H} + \Psi',\ \Gamma^0_{0k} = \Psi_{,\,k},\ \Gamma^0_{ij} = \mathcal{H}\delta_{ij} - \left[2\mathcal{H}(\Psi+\Phi) + \Phi'\right]\delta_{ij},\ \Gamma^i_{00} = \Psi_{,\,i}$$
$$\Gamma^i_{0j} = \mathcal{H}\delta^i_j - \Phi'\delta^i_j,\ \Gamma^i_{kl} = -\left(\Phi_{,\,l}\delta^i_k + \Phi_{,\,k}\delta^i_l\right) + \Phi_{,\,i}\delta_{kl}.$$

The non-zero components of the Ricci tensor are

$$R_{00} = -3\mathcal{H} + 3\Phi'' + \nabla^2\Psi + 3\mathcal{H}(\Psi'+\Phi')$$
$$R_{0i} = 2\left(\Phi' + \mathcal{H}\Psi\right)_{,\,i}$$
$$R_{ij} = \left(\mathcal{H}' + 2\mathcal{H}^2\right)\delta_{ij} + \left[-\Phi'' + \nabla\Phi^2 - \mathcal{H}\left(\Psi' + 5\Phi' 4\mathcal{H}^2\right)(\Psi+\Phi)\right]\delta_{ij} + (\Phi-\Psi)_{,\,ij}$$

and the Ricci scalar is

$$R = 6a^{-2}\left(\mathcal{H}' + \mathcal{H}^2\right) + a^{-2}\left[-\Phi'' + 2\nabla^2\left(2\Phi - \Psi\right) - 6\mathcal{H}\left(\Psi' + 3\Phi'\right) - 12\left(\mathcal{H}' + \mathcal{H}^2\right)\Psi\right]. \tag{2.22}$$

Finally the components of the Einstein tensor are

$$\begin{aligned}
G^0_0 &= -3a^{-2}\mathcal{H}^2 + a^{-2}\left[-2\nabla^2\Phi + 6\mathcal{H}\Phi' + 6\mathcal{H}^2\Psi\right] \\
G^0_i &= R^0_i \\
G^i_0 &= -G^0_i \\
G^i_k &= a^{-2}\left(-2\mathcal{H}' - \mathcal{H}^2\right)\delta^i_j + a^{-2}\left[2\Phi'' + \nabla^2\left(\Psi - \Phi\right) + \mathcal{H}\left(2\Psi' + 4\Phi'\right)\right. \\
&\quad \left. + \left(4\mathcal{H}' + 2\mathcal{H}^2\right)\Psi\right]\delta^i_j + a^{-2}\left(\Phi - \Psi\right)_{,\,ij}.
\end{aligned}$$

We now know what the perturbations to the Einstein tensor are. By calculating the perturbations to the stress-energy momentum tensor we can also use its conservation to simplify the Einstein equations. In the conformal Newtonian gauge, the stress-energy momentum tensor is

$$\delta T^\mu_\nu = \begin{bmatrix} -\delta\rho & -\left(\bar{\rho} + \bar{p}\right)\mathbf{v} \\ \left(\bar{\rho} + \bar{p}\right)\mathbf{v} & \delta p\delta^i_j + \bar{p}\left(\Pi_{,\,ij} - \frac{1}{3}\delta_{ij}\nabla^2\Pi\right) \end{bmatrix}, \tag{2.23}$$

where $\Pi_{ij} = \Sigma_{ij}/\bar{p}$ and $\Sigma_{ij} = \delta T^i_j - 1/3\delta^i_j\delta T^k_k$ and Σ_{ij} is called anisotropic stress. The full set of perturbed Einstein equations are therefore

$$3\mathcal{H}\left(\Phi' + \mathcal{H}\Psi\right) - \nabla^2\Phi = -4\pi G a^2 \delta\rho \tag{2.24}$$

$$\left(\Phi' + \mathcal{H}\Psi\right)_{,\,i} = 4\pi G a^2 \left(\bar{\rho} + \bar{p}\right) \mathbf{v} \tag{2.25}$$

$$\Phi'' + \mathcal{H}\left(\Psi' + 2\Phi'\right) + \left(2\mathcal{H}' + \mathcal{H}^2\right)\Psi + \frac{1}{3}\nabla^2\left(\Psi - \Phi\right) = 4\pi G a^2 \delta p \tag{2.26}$$

$$\left(\partial_i\partial_j - \frac{1}{3}\delta^i_j\nabla^2\right)\left(\Phi - \Psi\right) = 8\pi G a^2 \left(\partial_i\partial_j - \frac{1}{3}\delta^i_j\right)\Pi \tag{2.27}$$

2.3 Scalar perturbations in our Universe

We will use the perfect fluid description of the matter in our Universe. There are perturbation theory results for models that are not perfect fluids (Blas et al., 2015, 2018, Anand et al., 2017, Floerchinger et al., 2016). If we have a perfect fluid then $\Pi = 0$ and $\Psi = \Phi$ resulting in

$$\nabla^2\Psi = \frac{3}{2}\mathcal{H}^2\left[\delta + 3\mathcal{H}\left(1 + w\right)\mathbf{v}\right] \tag{2.28}$$

$$\Psi' + \mathcal{H}\Psi = \frac{3}{2}\mathcal{H}^2\left(1 + w\right)\mathbf{v} \tag{2.29}$$

$$\Psi'' + 3\mathcal{H}\Psi' + \left(2\mathcal{H}' + \mathcal{H}^2\right)\Psi' = \frac{3}{2}\mathcal{H}^2\frac{\delta p}{\bar{\rho}} \tag{2.30}$$

being our set of Einstein equations.

Adiabatic perturbations

The total energy budget of our Universe can be split into baryonic and dark matter, dark energy and radiation. Recall that dark matter is usually described as a pressureless perfect fluid, i.e. $w = 0$. However, if one sets $\delta p = \bar{p} = w = c_s^2 = 0$ then entropy is not defined. Therefore one sets $\delta p = c_s^2\delta\rho$ as this quantity is conserved when considering a pressureless fluid. Perturbations of this type are called adiabatic. Although they are adiabatic initially, they may not remain so over time. Considering initially adiabatic perturbations means our Einstein

equations are

$$\nabla^2\Psi = \frac{3}{2}\mathcal{H}^2\left[\delta + 3\mathcal{H}\left(1+w\right)\mathbf{v}\right], \tag{2.31}$$

$$\Psi' + \mathcal{H}\Psi = \frac{3}{2}\mathcal{H}^2\left(1+w\right)\mathbf{v}, \tag{2.32}$$

$$\Psi'' + 3\mathcal{H}\Psi' + \left(2\mathcal{H}' + \mathcal{H}^2\right)\Psi' = \frac{3}{2}c_s^2\mathcal{H}^2\delta. \tag{2.33}$$

where $\delta = \frac{\delta\rho}{\bar{\rho}}$ is the overdensity field, $\mathbf{v}$ is the velocity perturbation and δp is the pressure perturbation. The conservation of the stress-energy momentum tensor also provides us with evolution equations for δ and $\mathbf{v}$

$$\delta' = 3\mathcal{H}\delta\left(w - c_s^2\right) + \left(1+w\right)\left(\nabla^2\mathbf{v} + 3\Psi'\right), \tag{2.34}$$

$$\mathbf{v}' = -\mathcal{H}\left(1-3w\right)\mathbf{v} - \frac{w'}{1+w}\mathbf{v} + \frac{c_s^2\delta\rho}{\bar{\rho}+\bar{p}} + \Psi. \tag{2.35}$$

2.3.1 Matter dominated universe

In perturbation theory matter is described as a pressureless fluid called dust. If we ignore pressure perturbations then we can solve the structure formation equations. These solutions are only valid for a matter-dominated universe and in the conformal Newtonian gauge. If one wanted to consider a radiation dominated universe then the pressure perturbations can no longer be ignored.

The first step to exploring structure formation in the matter dominated era is to solve the background evolution equations. Recall that $\bar{\rho} \propto a^{-3(1+w)}$ and $w = 0$ for matter therefore for an Einstein-de Sitter (EdS, Einstein & de Sitter (1932)) model

$$a \propto \eta^2, \qquad \mathcal{H} \propto \frac{2}{\eta} \qquad , \qquad \frac{3}{2}\mathcal{H} = \frac{6}{\eta^2}. \tag{2.36}$$

Our perturbation equations for dust are (2.31, 2.32, 2.33)

$$\nabla^2\Psi = \frac{3}{2}\mathcal{H}^2\left(\delta + 3\mathcal{H}\mathbf{v}\right), \tag{2.37}$$

$$\Psi' + \mathcal{H}\Psi = \frac{3}{2}\mathcal{H}^2\mathbf{v}, \tag{2.38}$$

$$\Psi'' + 3\mathcal{H}\Psi + \left(2\mathcal{H}' + \mathcal{H}^2\right)\Psi = 0. \tag{2.39}$$

The third perturbation equation (2.39) can be solved to show that $\Psi\left(\mathbf{x}, \eta\right) = \Psi\left(\mathbf{x}\right)$ therefore the Bardeen potential is constant over time. Then Equation (2.37) can be solved and Fourier transformed to give

$$\delta\left(\mathbf{k}\right) = -\left[2 + \frac{2}{3}\left(\frac{k}{\mathcal{H}}\right)^2\right]\Psi\left(\mathbf{k}\right). \tag{2.40}$$

There are two scales on which cosmological perturbations are usually considered. The Hubble scale $\mathcal{H}^{-1}$ evolves over time, therefore scales which are much less than $\mathcal{H}$ are called super-horizon and they will eventually become sub-horizon when the Hubble scale grows. Considering Equation (2.40) for super-horizon scales ($k \ll \mathcal{H}$) gives $\delta\left(\mathbf{k}\right) = \text{cnst}$ and for sub-horizon scales ($k \gg \mathcal{H}$) gives $\delta\left(\mathbf{k}\right) \propto a$. Therefore the density perturbations grow as they enter the horizon.

2.4 Statistics of the density field

We have described in the previous section how the matter perturbations can be determined using relativistic arguments. In this section, we will take the Newtonian limit of the evolution equations for δ and $\mathbf{v}$ and introduce the correlation function and power spectrum statistics. We will then show how theoretical predictions match observations and validate the Λ–CDM theory.

2.4.1 Linear matter power spectrum

By either taking the Newtonian limit of the equations derived in Section 2.3 or by beginning with the picture of our Universe being a sphere of fluid that is expanding and obeys Hubble's law (1.20) where the peculiar velocity is ignored;

we can write down equations that describe non-relativistic matter (where pressure is negligible) but the description is only valid well within the Hubble radius (or super-horizon scales). The evolution equations are

$$\frac{\partial \delta(\mathbf{x},\eta)}{\partial \eta} + \nabla \cdot [(1+\delta(\mathbf{x},\eta))\,\mathbf{v}] = 0, \tag{2.41}$$

$$\frac{\partial \mathbf{v}(\mathbf{x},\eta)}{\partial \eta} + [\mathbf{v}(\mathbf{x},\eta)\cdot\nabla]\,\mathbf{v}(\mathbf{x},\eta) = -\mathcal{H}(\eta)\,\mathbf{v}(\mathbf{x},\eta) - \nabla\phi(\mathbf{x},\eta), \tag{2.42}$$

$$\nabla^2\phi(\mathbf{x},\eta) = \frac{3}{2}\mathcal{H}^2(\eta)\,\Omega_m(\eta)\,\delta(\mathbf{x},\eta). \tag{2.43}$$

If we consider $\mathbf{v}$ to have no vorticity we can set $\theta = \nabla\cdot\mathbf{v}$ and Fourier transform Equations (2.41, 2.42) and (2.43)

$$\frac{\partial \delta_k}{\partial \eta} + \theta_k = -\int \frac{d^3k_1}{(2\pi)^3}\int d^3k_2\,\delta_{\mathrm{D}}(\mathbf{k}_1+\mathbf{k}_2-\mathbf{k})\,\alpha(\mathbf{k},\mathbf{k}_1)\,\theta_{k_1}\delta_{k_2} \tag{2.44}$$

$$\frac{\partial \theta_k}{\partial \eta} + \mathcal{H}\theta_k + \frac{3}{2}\mathcal{H}^2(\eta)\,\Omega_m(\eta)\,\delta_k \tag{2.45}$$
$$= -\int \frac{d^3k_1}{(2\pi)^3}\int d^3k_2\,\delta_{\mathrm{D}}(\mathbf{k}_1+\mathbf{k}_2-\mathbf{k})\,\beta(\mathbf{k},\mathbf{k}_1,\mathbf{k}_2)\,\theta_{k_1}\theta_{k_2}$$

where $\alpha(\mathbf{k},\mathbf{k}_1) = \frac{\mathbf{k}\cdot\mathbf{k}_1}{k_1^2}$ and $\beta(\mathbf{k},\mathbf{k}_1,\mathbf{k}_2) = \frac{k^2(\mathbf{k}_1\cdot\mathbf{k}_2)}{2k_1^2k_2^2}$. Now all of the non-linear evolution is on the RHS of the above equations. Therefore in the linear regime (where δ and $\mathbf{v}$ are small) we can ignore the RHS and solve to find the evolution of the perturbations. If one does this then the linear perturbative solutions are

$$\delta_1(\mathbf{k},\eta) = \frac{D_1(\eta)}{D_1(\eta_0)}\delta_1(\mathbf{k},\eta_0) \tag{2.46}$$

$$\theta_1(\mathbf{k},\eta) = -\frac{d\ln D_1(a)}{d\ln a}\mathcal{H}(\eta)\,\delta_1(\mathbf{k},\eta) = -f(\eta)\,\mathcal{H}(\eta)\,\delta_1(\mathbf{k},\eta) \tag{2.47}$$

where D_1 is the linear growth factor and f is the logarithmic growth factor.

Transfer functions

Initially, our perturbations are Gaussian and adiabatic, but how do we go from these initial conditions to what we observe in the Universe today? In the above formulae we require $\delta_1(\mathbf{k}, \eta_0)$ to understand the evolution of the density perturbations today. We can introduce a function called the transfer function, $T(k)$, which takes the initial perturbations (which we understand the behaviour of) and evolves them to today. Hence one can write

$$\delta(\mathbf{k}, \eta_0) = T(k)\,\delta(\mathbf{k}, \eta_i) \tag{2.48}$$

where η_i is some initial time (usually around inflation) and η_0 is today.

As seen in the previous section, we are concerned with the time when a perturbation crosses the co-moving horizon scale. If we call k_{eq} the wavenumber at matter-radiation equality then when $k < k_{eq}$ the perturbation is outside of the horizon during radiation domination and will enter during matter domination. When $k > k_{eq}$ the perturbation will enter the horizon during radiation domination. By solving the Newtonian equations of motion for matter and radiation dominated eras

$$\delta(\mathbf{k}, \eta) = \left(\frac{a_{eq}}{a_i}\right)^2 \frac{a_0}{a_{eq}} \delta(\mathbf{k}, \eta_i) \;\;,\;\; k < k_{eq} \tag{2.49}$$

$$\delta(\mathbf{k}, \eta) = \left(\frac{a_{ent}}{a_i}\right)^2 \left[\left(\frac{a_{eq}}{a_i}\right)^2 \frac{a_0}{a_{eq}}\right] \delta(\mathbf{k}, \eta_i) \;\;,\;\; k > k_{eq} \tag{2.50}$$

where a_{ent} is the scale factor when the perturbation enters the horizon, a_0 is the scale factor today, a_i is the initial scale factor and a_{eq} is the scale factor at matter radiation equality. The perturbations for $k > k_{eq}$ are damped as the radiation pressure is halting the growth of structure. It can be shown that $a_{ent}^{-1} \propto k^{-1}$, therefore the transfer function is

$$T(k) \approx \text{ cnst} \begin{cases} 1 & , \; k < k_{eq} \\ k^{-2} & , \; k > k_{eq} \end{cases} . \tag{2.51}$$

More complex transfer functions can be used to describe more advanced physics. Examples are the BBKS (Bardeen et al., 1986a) and Eisenstein and Hu transfer functions (Eisenstein & Hu, 1998). Codes such as CLASS (Lesgourgues, 2011) and CAMB (Lewis et al., 2000, Howlett et al., 2012, Lewis, Lewis) calculate the transfer function accurately through matter-radiation equality and the last scattering of CMB. Finally our linear overdensity field solution is

$$\delta_1(\mathbf{k},\eta) = \frac{D_1(\eta)}{D_1(\eta_0)} T(k)\,\delta(\mathbf{k},\eta_i)\,. \tag{2.52}$$

Linear correlation function and power spectrum

Now that we have a way of evolving the overdensity field from the initial conditions to today, we wish to have an observable that is easy to measure. The statistic usually measured in galaxy surveys is the 2-point correlation function which can allow us to test our cosmological theories. The 2-point correlation function is defined as

$$\xi_1(|\mathbf{x}-\mathbf{y}|,\eta) = \langle \delta_1(\mathbf{x},\eta)\,\delta_1(\mathbf{y},\eta)\rangle. \tag{2.53}$$

The fact that the left-hand side only depends on the distance between the two positions is a reflection of statistical homogeneity. In observational terms ξ is calculated by binning the Universe into small volumes and then calculating the probability two bins separated by a distance r both contain galaxies, which are biased discrete tracers of the underlying overdensity field.

Another commonly used statistic is the Fourier transform of the correlation function called the power spectrum $\mathrm{P}(k)$ which is defined as $\langle \delta(\mathbf{k}_1,\eta)\,\delta(\mathbf{k}_2,\eta)\rangle = (2\pi)^3\,\delta_{\mathrm{D}}(\mathbf{k}_1+\mathbf{k}_2)\,\mathrm{P}(k)$ where $k = |\mathbf{k}_1+\mathbf{k}_2|$. It is this statistic we will focus on calculating in later chapters. We know from the CMB and the Gaussian initial adiabatic conditions that the primordial power spectrum is a power law $\mathrm{P}(k) \propto k^{n_s}$ where n_s is the spectral index measured to be $n_s = 0.96$. Combining

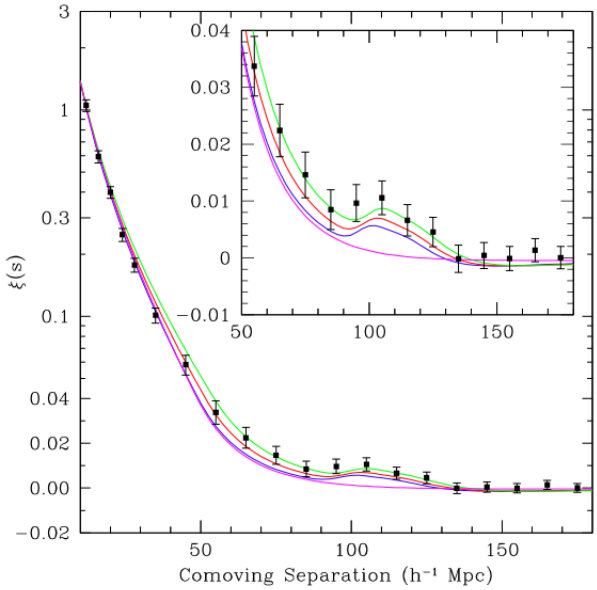

Figure 2.1 *Figure from (Eisenstein et al., 2005) showing the correlation function measured by the SDSS survey compared to theoretical predictions.*

this primordial power spectrum with the transfer function in (2.51) leads to

$$\mathrm{P}(k) = T^2(k)\,\frac{D_1^2(\eta)}{D_1^2(\eta_0)}\mathrm{P}^{\mathrm{prim}}(k) \propto \frac{D_1^2(\eta)}{D_1^2(\eta_0)}\begin{cases} k^{n_s} & , k < k_{eq} \\ k^{n_s-4} & , k > k_{eq} \end{cases} . \tag{2.54}$$

In Figure 2.1 the correlation function (2.53) as predicted theoretically and measured by the *SDSS* survey is shown. One can see the BAO peak clearly at around 100 h^{-1}Mpc. In Figure 2.2 the theoretical linear power spectrum (2.54) is shown as measured by a range of current surveys.

In this section, we have only considered the linear correlation and power spectrum. However, on small-scales (large k-values) the assumptions that we used during our perturbative expansions are no longer valid. These so-called non-linear scales are an issue as a lot of our observational data is in that regime and we do not wish to have to throw away data on those scales. Soon when new telescopes and surveys are launched our observational measurements will become extremely accurate. We currently mismatch observations theoretically by around 1%, this could increase on all scales leading to a reduction in certainty on the cosmological parameters we extract from the data.

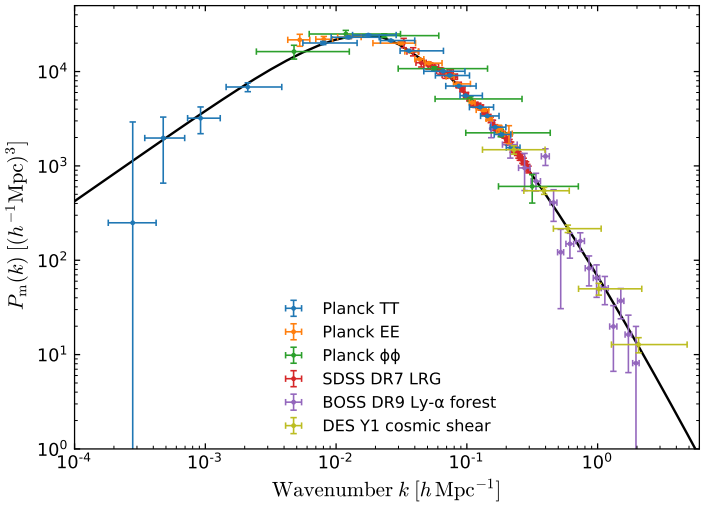

Figure 2.2 *Figure from (Planck Collaboration et al., 2018) showing the matter power spectrum as measured by the Planck, SDSS, BOSS and DES surveys.*

In the remaining chapters of this thesis, this mismatch between linear theory and observations on small-scales will motivate our work. For now, let us investigate other techniques that can be employed to calculate the power spectrum in the non-linear regime.

2.4.2 Non-linear power spectrum

If we consider an Einstein-de Sitter (EdS) universe with $\Omega_m = 1$ then we can write the overdensity field and velocity fields as sums following (Goroff et al., 1986, Jain & Bertschinger, 1994, Bernardeau, 2000)

$$\delta(\mathbf{k},\eta) = \sum_{n=1}^{\infty} a^n(\eta)\,\delta_n(\mathbf{k}) \quad \text{and} \quad \theta(\mathbf{k},\eta) = \sum_{n=1}^{\infty} a'(\eta)\,a^{n-1}(\eta)\,\theta_n(\mathbf{k})\,. \tag{2.55}$$

If we substitute these into Equations (2.44) and (2.45) then for $n > 1$

$$\delta_n(\mathbf{k}) = \int d^3q_1 \cdots \int d^3q_n \delta_{\mathrm{D}}(\mathbf{q}_1 + \cdots + \mathbf{q}_n - \mathbf{k}) F_n(\mathbf{q}_1, ..., \mathbf{q}_n) \delta_1(\mathbf{q}_1) \cdots \delta_n(\mathbf{q}_1) \tag{2.56}$$

$$\theta_n(\mathbf{k}) = -\int d^3q_1 \cdots \int d^3q_n \delta_{\mathrm{D}}(\mathbf{q}_1 + \cdots + \mathbf{q}_n - \mathbf{k}) G_n(\mathbf{q}_1, ..., \mathbf{q}_n) \delta_1(\mathbf{q}_1) \cdots \delta_n(\mathbf{q}_1) \tag{2.57}$$

with initial values of δ_1 and $\theta_1 = -\delta_1$. The functions F_n and G_n are called kernels and are given by recursion relations

$$\begin{aligned} F_n(\mathbf{q}_1, ..., \mathbf{q}_n) = \sum_{m=1}^{n-1} \frac{G_m(\mathbf{q}_1, ..., \mathbf{q}_m)}{(2n+3)(n-1)} [(1+2n)\alpha(\mathbf{k}, \mathbf{k}_1) F_{n-m}(\mathbf{q}_{m+1}, ..., \mathbf{q}_n) \\ +\beta(\mathbf{k}, \mathbf{k}_1, \mathbf{k}_2) G_{n-m}(\mathbf{q}_{m+1}, ..., \mathbf{q}_n)] \end{aligned} \tag{2.58}$$

$$\begin{aligned} G_n(\mathbf{q}_1, ..., \mathbf{q}_n) = \sum_{m=1}^{n-1} \frac{G_m(\mathbf{q}_1, ..., \mathbf{q}_m)}{(2n+3)(n-1)} [3\alpha(\mathbf{k}, \mathbf{k}_1) F_{n-m}(\mathbf{q}_{m+1}, ..., \mathbf{q}_n) \\ +n\beta(\mathbf{k}, \mathbf{k}_1, \mathbf{k}_2) G_{n-m}(\mathbf{q}_{m+1}, ..., \mathbf{q}_n)] \end{aligned} \tag{2.59}$$

with $\mathbf{k}_1 = \mathbf{q}_1 + \cdots + \mathbf{q}_m$, $\mathbf{k}_2 = \mathbf{q}_{m+1} + \cdots + \mathbf{q}_n$, $\mathbf{k} = \mathbf{k}_1 + \mathbf{k}_2$ and $F_1 = G_1 = 1$.

We now wish to calculate the first non-linear correction to the linear power spectrum. These corrections are called loop corrections and we will demonstrate how to calculate $\mathrm{P}_{1-\mathrm{loop}}$. In order to do this we require symmetrised versions of F_2, F_3 and G_2 these are given by

$$F_2^{(s)}(\mathbf{k}_1, \mathbf{k}_2) = \frac{5}{7} + \frac{2}{7}\frac{(\mathbf{k}_1 \cdot \mathbf{k_2})^2}{k_1^2 k_2^2} + \frac{(\mathbf{k}_1 \cdot \mathbf{k}_2)}{2}\left(\frac{1}{k_1^2} + \frac{1}{k_2^2}\right), \tag{2.60}$$

$$G_2^{(s)}(\mathbf{k}_1, \mathbf{k}_2) = \frac{3}{7} + \frac{4}{7}\frac{(\mathbf{k}_1 \cdot \mathbf{k}_2)^2}{k_1^2 k_2^2} + \frac{(\mathbf{k}_1 \cdot \mathbf{k}_2)}{2}\left(\frac{1}{k_1^2} + \frac{1}{k_2^2}\right), \tag{2.61}$$

$$\begin{aligned} F_3^{(s)}(\mathbf{k}_1, \mathbf{k}_2, \mathbf{k}_3) = {} & \frac{2k^2}{54}\left[\frac{\mathbf{k}_1 \cdot (\mathbf{k}_2 + \mathbf{k}_3)}{k_1^2 |\mathbf{k}_2 + \mathbf{k}_3|^2} G_2^{(s)}(\mathbf{k}_2, \mathbf{k}_3) + (2 \text{ cyclic})\right] \\ & + \frac{7}{54}\mathbf{k} \cdot \left[\frac{\mathbf{k}_1 + \mathbf{k}_2}{|\mathbf{k}_1 + \mathbf{k}_2|^2} G_2^{(s)}(\mathbf{k}_1, \mathbf{k}_2) + (2 \text{ cyclic})\right] \\ & + \frac{7}{54}\mathbf{k} \cdot \left[\frac{\mathbf{k}_1}{k_1^2} F_2^{(s)}(\mathbf{k}_2, \mathbf{k}_3) + (2 \text{ cyclic})\right]. \end{aligned} \tag{2.62}$$

The contributions to the power spectrum are determined by $\langle \delta_m(\mathbf{k}_1)\, \delta_{n-m}(\mathbf{k}_2) \rangle = \mathrm{P}_{m,\, n-m}(k)\, \delta_{\mathrm{D}}(\mathbf{k}_1 + \mathbf{k}_2)$ and the one-loop power spectrum is

$$\mathrm{P}_{1-\mathrm{loop}}(k, z) = \mathrm{P}_{11}(k, z) + \mathrm{P}_{22}(k, z) + 2\mathrm{P}_{13}(k, z) \tag{2.63}$$

where

$$\mathrm{P}_{22}(k, z) = 2\int d^3q\ \mathrm{P}_{11}(q)\, \mathrm{P}_{11}(|\mathrm{k} - \mathrm{q}|)\left[F_2^{(s)}(\mathbf{q}, \mathbf{k} - \mathbf{q})\right]^2, \tag{2.64}$$

$$\mathrm{P}_{13}(k, z) = 3\mathrm{P}_{11}(k)\int d^3q\ \mathrm{P}_{11}(q)\, F_3^{(s)}(\mathbf{q}, -\mathbf{q}, \mathbf{k})\,. \tag{2.65}$$

Techniques like loop corrections allow us to push into the non-linear regime, however, a variety of other techniques also exist including (Effective Field Theory of Large-Scale Structure and IR-resummation). We have only discussed Eulerian perturbation theory in this chapter and the next chapter will introduce Lagrangian perturbation theory. For references of alternative perturbation theory techniques and more detail about Lagrangian perturbation theory please see Chapter 3.

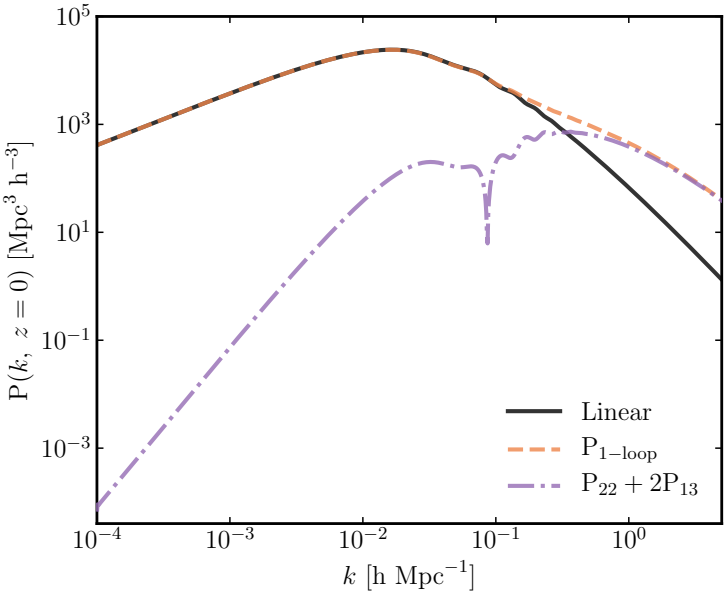

Figure 2.3 *Figure showing the linear and one-loop power spectra for Planck18 data produced using* CLASS *(Lesgourgues, 2011) and* FASTPT *(McEwen et al., 2016b). One can see the enhancement of growth on small-scales (large k-values) as expected from non-linear structure formation.*

Chapter 3

The Cosmological Trajectories Method: A trajectories approach to structure formation

> We will always have STEM with us. Some things will drop out of the public eye and will go away, but there will always be science, engineering, and technology. And there will always, always be mathematics.
>
> *Katherine Johnson*

3.1 Overview

Understanding how the cosmic web and large-scale structure (galaxy clusters etc.) is formed in our Universe is an essential part of understanding cosmology. Better knowledge of large-scale structure formation will allow us to extract more information from current observations of our Universe (e.g. Planck Collaboration et al., 2016a, Hildebrandt et al., 2017, Abbott et al., 2018). Gathering more

statistical information from current and upcoming surveys (*DESI*[1], the Vera Rubin Observatory [2], *Euclid*[3], etc.) will lead to tighter constraints on viable cosmological models, gravity models and structure formation models.

Modelling the cosmic web involves knowing how structures form under the influence of gravity. Describing the formation of structure on large scales can be achieved using linear methods as one can apply the Newtonian limit. However, on small scales, ($k > 0.1$ hMpc^{-1}), non-linear effects, such as gravitational instability (overdense regions collapsing and underdense regions expanding) and baryonic effects (such as feedback from AGN and supernova explosions) must be taken into account.

The current preferred method for investigating this non-linear regime is to run large cosmological simulations. Although if one wishes to test multiple theories of gravity and cosmological models a new simulation typically must be run for each instance. Upcoming instruments, such as *Euclid*, will survey larger volumes and produce more data than ever before. We, therefore, require larger simulations and for the simulations to model structure formation on all scales more accurately. This can be computationally and time-intensive, leading the community to search for alternative methods.

One technique that does not require the running of simulations is perturbation theory (see Chapter 2 for an introduction to perturbation theory). Standard Perturbation Theory (SPT) or Eulerian Perturbation Theory (EPT) can reproduce cosmological observations up to scales of around $k \sim 0.01$ h Mpc^{-1}, where non-linear gravitational and baryonic effects become important (Peebles, 1980, Bertschinger, 1995, Bouchet, 1996, Bernardeau et al., 2002, Carlson et al., 2009, Bernardeau, 2013). SPT can be extended to model smaller scales using IR-resummation (accounting for the physical effects of bulk flows) and loop corrections (next to leading order corrections), as demonstrated in Crocce & Scoccimarro (2006a,b), Taruya & Hiramatsu (2008), Bernardeau et al. (2008, 2012, 2014) and Blas et al. (2014). Lagrangian Perturbation Theory (LPT) is another technique that can be used to model the formation of structure. LPT, unlike SPT, follows the motion of particles through a system and has been found to be more accurate at equal orders than SPT (Matsubara, 2008a,b, Bouchet et al., 1995, Carlson et al., 2013, White, 2014, Catelan, 1995). The Zel'dovich

[1] `https://www.desi.lbl.gov`
[2] `https://www.lsst.org`
[3] `https://www.euclid-ec.org`

approximation (first-order LPT) is unique in that in 1D it is exact up until shell-crossing occurs. In 3D it behaves competitively with EPT, higher- order LPT. It is an intuitive method for describing how particles form the structures we see in the cosmic web (McQuinn & White, 2016).

As discussed in McQuinn & White (2016), although techniques that aim to address the breakdown of perturbation theory on small scales have made an improvement, fundamental failings on these scales still remain. For example, it is well known that when the overdensity field becomes large ($\delta \gg 1$) these schemes are no longer valid. The point at which streams of matter from different directions intersect is called shell-crossing. However, we know that virialised structures in our Universe, such as dark matter haloes, are formed after shell-crossing occurs.

The Effective Field Theory of Large Scale Structure (EFTofLSS) is a method that aims to fix these issues by integrating out small wavelengths (Carrasco et al., 2012, 2014a,b, Carroll et al., 2014, Porto et al., 2014, Senatore & Zaldarriaga, 2015, Vlah et al., 2015a,b, 2016a,b), to reduce the uncontrolled small-scale perturbative effects affecting large scales. EFTofLSS generally requires either data from simulations or observations to fix free parameters in the theory. Other methods for extending perturbation theory into the non-linear regime including semi-classical propagators and methods based on field theory have been suggested in Seljak & Vlah (2015), Taruya & Colombi (2017), McDonald & Vlah (2018), Prokopec & Friedrich (2017), Friedrich & Prokopec (2018), Uhlemann et al. (2019), Friedrich & Prokopec (2019) and Halle et al. (2020).

A statistical mechanics approach to modelling gravitational interaction and therefore the non-linear regime was introduced in Bartelmann et al. (2014a,b), Fabis et al. (2014), Kozlikin et al. (2014), Viermann et al. (2015), Bartelmann et al. (2017), Sorini (2017), Lilow et al. (2019) and Bartelmann et al. (2019). This method is called Kinetic Field Theory (KFT). The method was re-derived using particle trajectories in Ali-Haïmoud (2015). We will focus on this implementation of the technique. The trajectories approach to structure formation uses ideas from LPT and can be thought of as carrying out an N-body simulation on paper. The initial results for the matter power spectrum (Bartelmann et al., 2014a) hinted that the method could match current simulations. Another advantage of this method is that it has the potential to be easily adapted to multiple cosmological models, therefore allowing predictions to be made without running numerous simulations.

In this chapter, we will investigate the trajectories approach to modelling structure formation in more detail building on the results from Ali-Haïmoud (2015) and generalizing them. In Section 3.2 we will re-derive Lagrangian Perturbation Theory, the Zel'dovich power spectrum and methods used to calculate the latter numerically. Then in Section 3.3 we will summarise previous results and introduce the Cosmological Trajectories Method (CTM). The power spectrum for the CTM is calculated in Section 3.4 and is applied to the KFT formalism in Section 3.5.

3.2 Lagrangian Perturbation Theory

First let us introduce Lagrangian Perturbation Theory (LPT), the Zel'dovich power spectrum and methods used to calculate it. These techniques will be useful when we introduce the trajectories approach in Section 3.3. For a more in depth derivation of LPT see Moutarde et al. (1991), Catelan (1995), Buchert (1992), Buchert & Ehlers (1993), Bouchet (1996), Tatekawa (2004) and Rampf & Buchert (2012).

3.2.1 First-order LPT (Zel'dovich approximation)

A one-to-one mapping between the Eulerian spatial coordinate $\mathbf{x}$ and the Lagrangian spatial coordinate $\mathbf{q}$ can be expressed as,

$$\mathbf{x}(\mathbf{q}, t) = \mathbf{q} + \mathbf{\Psi}(\mathbf{q}, t) . \tag{3.1}$$

The positions $\mathbf{q}$ can be thought of as the initial particle positions and $\mathbf{\Psi}$ as the displacement field. As Equation (3.1) is a one-to-one mapping the Jacobian of the transformation is,

$$J(\mathbf{q}, t) = \det\left(\frac{\partial \mathbf{x}}{\partial \mathbf{q}}\right) \neq 0, \tag{3.2}$$

which can be used to define the overdensity field as we know mass must be

conserved

$$1 + \delta \left[\mathbf{x} \left(\mathbf{q}, t \right), t \right] = J \left(\mathbf{q}, t \right)^{-1} . \tag{3.3}$$

The Eulerian Perturbation Theory (EPT) description for the overdensity field is only valid for $\delta \ll 1$ where caustics (regions of infinite density) do not arise. Caustics can occur in LPT when the Jacobian vanishes i.e. when particles different initial positions end up at the same Eulerian position. The equation of motion for the Eulerian positions is,

$$\frac{\partial \mathbf{u}}{\partial t} + \mathrm{H} \left(t \right) \mathbf{u} = -\frac{1}{a} \nabla_{\mathbf{x}} \phi, \tag{3.4}$$

where $\mathbf{u}$ is the peculiar velocity, $\nabla^2 \phi = -4\pi G \rho_b \delta$ and H is the Hubble parameter. Taking the divergence of Equation (3.4) and multiplying by the Jacobian results in,

$$J \left(\mathbf{q}, t \right) \nabla_{\mathbf{x}} \cdot \left[\frac{\partial^2 \mathbf{\Psi}}{\partial t^2} + 2\mathrm{H} \frac{\partial \mathbf{\Psi}}{\partial t} \right] = \frac{3}{2} \Omega_m \mathrm{H}^2 \left[J \left(\mathbf{q}, t \right) - 1 \right], \tag{3.5}$$

note that the gradient depends on the Eulerian coordinate. Instead of expanding in the overdensity field as is the case in SPT we wish to expand in terms of the displacement field such that,

$$\mathbf{x} \left(\mathbf{q}, t \right) = \mathbf{q} + \mathbf{\Psi}^{(0)} \left(\mathbf{q}, t \right) + \mathbf{\Psi}^{(1)} \left(\mathbf{q}, t \right) + \mathbf{\Psi}^{(2)} \left(\mathbf{q}, t \right) + \ldots . \tag{3.6}$$

Truncating the above expression at first-order, noting that $J \left(\mathbf{q}, \tau \right) \nabla_{\mathbf{x}} \approx \nabla_{\mathbf{q}}$ and to first-order $J \left(\mathbf{q}, \tau \right) \approx 1 + \nabla_{\mathbf{q}} \cdot \mathbf{\Psi}$. The equation of motion (3.5) can be solved to obtain the Zel'dovich approximation (Zel'dovich, 1970, Shandarin & Zeldovich,

1989),

$$\nabla_q \cdot \mathbf{\Psi}^{(0)}(\mathbf{q}, t) = -\frac{D_1(t)}{D_1(t_i)}\delta^{(0)}(\mathbf{q}, t_i)\,. \tag{3.7}$$

D_1 is the linear growth factor and $\delta^{(0)}$ is the initial overdensity field. The Zel'dovich approximation is exact in 1D until shell crossing (White, 2014, McQuinn & White, 2016) and is often used as the initial condition for simulations. The Zel'dovich approximation can describe the formation of walls and filaments under gravitational collapse (Hahn et al., 2007a,b).

3.2.2 Second-order LPT

Using Bouchet (1996) and beginning with the trajectory

$$\mathbf{x}(\mathbf{q}, t) = \mathbf{q} + D_1(t)\mathbf{\Psi}^{(0)}(\mathbf{q}, t_i) + D_2(t)\,\mathbf{\Psi}^{(1)}(\mathbf{q}, t_i) \tag{3.8}$$

one can rearrange Equation (3.3) to obtain $\delta(\mathbf{x}, t) = \det(\mathbf{I} + \mathbf{D})^{-1} - 1$, where $\mathbf{D} = \partial\mathbf{\Psi}/\partial\mathbf{q}$. Here D_2 is some unknown second-order time dependent function. The determinant can be expanded as

$$\det(\mathbf{I} + \mathbf{D}) \approx 1 + \Psi_{ii} + \frac{1}{2}\sum_{i\neq j}\Psi_{ii}\Psi_{jj} - \Psi_{ij}\Psi_{ji}, \tag{3.9}$$

where $\Psi_{ii} = \frac{\partial\Psi_i}{\partial q_i}$. Then using the binomial theorem

$$\det(\mathbf{I} + \mathbf{D})^{-1} \approx 1 - \Psi_{ii} + (\Psi_{ii})^2 - \frac{1}{2}\sum_{i\neq j}\Psi_{ii}\Psi_{jj} - \Psi_{ij}\Psi_{ji}. \tag{3.10}$$

We have the following information from the Zel'dovich approximation $\Psi^{(0)}_{ii} \approx -D_1\delta^{(0)}(\mathbf{q})$ and $\Psi^{(1)}_{ii} \approx D_1^2\sum_{i\neq j}\Psi^{(0)}_{ii}\Psi^{(0)}_{jj} - \Psi^{(0)}_{ij}\Psi^{(0)}_{ji}(\mathbf{q})$. The overdensity field is

then

$$\delta\left(\mathbf{x},t\right) \approx D_1\delta^{(0)}\left(\mathbf{q}\right) + D_1^2\left(\delta^{(0)}\left(\mathbf{q}\right)\right)^2 - \frac{1}{2}\left(D_2 + D_1^2\right)\nabla_q^i.\Psi_i^{(1)} \tag{3.11}$$

We want to express the above expression in terms of the Eulerian coordinate $\mathbf{x}$. Recall that $\mathbf{x} = \mathbf{q} + \mathbf{\Psi}$ and set,

$$\eta \cdot \mathbf{g} \approx \nabla\delta^{(0)}\left(\mathbf{x}\right) \cdot \nabla\phi\left(\mathbf{x}\right) \tag{3.12a}$$

and

$$E_{ij} = \nabla_i\nabla_j\nabla^{-2}\delta^{(0)}\left(\mathbf{x}\right) - \frac{1}{3}\delta^{(0)}\left(\mathbf{x}\right)\delta_{ij}. \tag{3.12b}$$

The overdensity field (3.11) can finally be written as

$$\delta\left(\mathbf{x},t\right) \approx D_1\delta^{(0)}\left(\mathbf{x}\right) + \frac{1}{3}D_1^2\left(2-\kappa\right)\left(\delta^{(0)}\left(\mathbf{x}\right)\right)^2 - D_1^2\eta\cdot\mathbf{g} + \frac{1}{2}D_1^2\left(1+\kappa\right)E^2, \tag{3.13}$$

with $\kappa = D_2/D_1^2$. For a flat Λ-CDM cosmology $D_2 \approx \frac{-3}{7}D_1^2\Omega_m^{-1/143}$ (Bouchet et al., 1995). As was mentioned above, second-order LPT involves integrals over the whole field; these are included in terms three and four in the above Equation (3.13). This implies that the growth of density perturbations is influenced by their environment. The third term represents the flow of matter from void regions. Hence its appearance with a negative sign and a gradient of the gravitational field. The final term, the tidal field, represents the deformation of the density perturbations due to the surrounding matter.

3.2.3 The Zel'dovich power spectrum

Now let us calculate the Zel'dovich power spectrum following Taylor (1993), Schneider & Bartelmann (1995) and Taylor & Hamilton (1996), White (2014),

Vlah et al. (2015a). This calculation will be useful when we calculate the power spectrum for a general cosmological trajectory. The overdensity field is given by

$$1 + \delta(\mathbf{x}) = \int d^3q \; \delta_D(\mathbf{x} - \mathbf{q} - \mathbf{\Psi}) \tag{3.14}$$

and its Fourier transform [1] is

$$(2\pi)^3 \delta_D(\mathbf{k}) + \delta(\mathbf{k}) = \int d^3q \; \mathrm{e}^{i\mathbf{k}\cdot\mathbf{q}} \mathrm{e}^{i\mathbf{k}\cdot\mathbf{\Psi}}. \tag{3.15}$$

Recall that the power spectrum is given by $(2\pi)^3 \mathrm{P}(k) \delta_D(\mathbf{k}_1 + \mathbf{k}_2) = \langle \delta(\mathbf{k}_1) \delta(\mathbf{k}_2) \rangle$ implying that

$$(2\pi)^3 \delta_D(\mathbf{k}) + \mathrm{P}(k, z) = \int d^3q \; \mathrm{e}^{i\mathbf{k}\cdot\mathbf{q}} \langle \mathrm{e}^{-i\mathbf{k}\cdot\Delta} \rangle \tag{3.16}$$

where $\Delta = \mathbf{\Psi}(\mathbf{q}_2, z) - \mathbf{\Psi}(\mathbf{q}_1, z)$. The $\langle \cdots \rangle$ term can be expanded using the cumulant expansion since $\mathbf{\Psi}$ is initially Gaussian. The first term in the cumulant expansion is zero and the second term allows us to write

$$\mathrm{P}(k) = \int d^3q \; \mathrm{e}^{i\mathbf{k}\cdot\mathbf{q}} \left[\mathrm{e}^{-\frac{1}{2} k_i k_j A_{ij}(\mathbf{q})} - 1 \right] \tag{3.17}$$

[1] Our Fourier transform convention is $f(\mathbf{k}) = \int d^3x \; \mathrm{e}^{i\mathbf{k}\cdot\mathbf{x}} f(\mathbf{x})$ and $f(\mathbf{x}) = \frac{1}{(2\pi)^3} \int d^3k \; \mathrm{e}^{-i\mathbf{k}\cdot\mathbf{x}} f(\mathbf{k})$.

with $A_{ij}(\mathbf{q}) = \langle \Delta_i \Delta_j \rangle$. We can calculate $A_{ij}(\mathbf{q})$

$$
\begin{aligned}
A_{ij} &= \langle (\Psi_i(\mathbf{q}_2, z) - \Psi_i(\mathbf{q}_1, z)) \left(\Psi_j(\mathbf{q}_2, z) - \Psi_j(\mathbf{q}_1, z)\right) \rangle \\
&= \langle \Psi_i(\mathbf{q}_2, z) \Psi_j(\mathbf{q}_2, z) \rangle + \langle \Psi_i(\mathbf{q}_1, z) \Psi_j(\mathbf{q}_1, z) \rangle \\
&- \langle \Psi_i(\mathbf{q}_2, z) \Psi_j(\mathbf{q}_1, z) \rangle - \langle \Psi_i(\mathbf{q}_1, z) \Psi_j(\mathbf{q}_2, z) \rangle \\
&= 2\langle \Psi_i(\mathbf{q}_2, z) \Psi_j(\mathbf{q}_2, z) \rangle - 2\langle \Psi_i(\mathbf{q}_2, z) \Psi_j(\mathbf{q}_1, z) \rangle \\
&= 2\left[\sigma_{ij}(\mathbf{0}, z) - \sigma_{ij}(\mathbf{q}, z)\right]
\end{aligned}
\tag{3.18}
$$

therefore the final Zel'dovich power spectrum is given by,

$$
\mathrm{P}(k, z) = \int d^3q \, \mathrm{e}^{i\mathbf{k}\cdot\mathbf{q}} \left[\mathrm{e}^{-k_i k_j \left[\sigma_{ij}(\mathbf{0}, z) - \sigma_{ij}(\mathbf{q}, z)\right]} - 1\right]. \tag{3.19}
$$

The variances σ_{ij} are defined as

$$
\sigma_{ij}(\mathbf{0}, z) = \sigma_\psi^2 \delta_{ij} = \frac{1}{3}\delta_{ij} \int \frac{d^3k}{(2\pi)^3} \frac{\mathrm{P_L}(k, z)}{k^2}, \tag{3.20a}
$$

$$
\sigma_{ij}(\mathbf{q}, z) = \int \frac{d^3k}{(2\pi)^3} \, \mathrm{e}^{-i\mathbf{k}\cdot\mathbf{q}} \frac{k_i k_j}{k^4} \mathrm{P_L}(k, z) \tag{3.20b}
$$

with $\mathbf{q} = \mathbf{q}_2 - \mathbf{q}_1$.

3.2.4 Calculating the Zel'dovich power spectrum numerically

Method I: Splitting A_{ij}

Using the methods described in Schneider & Bartelmann (1995), Carlson et al. (2013), Sugiyama (2014) and Vlah et al. (2015a) the covariance matrix A_{ij} can

be split as

$$A_{ij}(\mathbf{q}, z) = X(q, z)\,\delta_{ij} + Y(q, z)\,\hat{q}_i\hat{q}_j. \tag{3.21}$$

Contracting A_{ij} with δ_{ij} and $\hat{q}_i\hat{q}_j$ gives two expressions for calculating the functions X and Y with $\mu = \hat{\mathbf{k}} \cdot \hat{\mathbf{q}}$

$$A_{ij}\delta_{ij} = 3X(q, z) + Y(q, z) \text{ and } A_{ij}\hat{q}_i\hat{q}_j = X(q, z) + Y(q, z). \tag{3.22}$$

We previously defined A_{ij} in (3.18) and can use this definition to calculate X and Y. For example

$$\begin{aligned} A_{ij}\delta_{ij} &= 2\left[\sigma_{ii}(\mathbf{0}, z) - \sigma_{ii}(\mathbf{q}, z)\right] \\ &= 2\int \frac{d^3k}{(2\pi)^3}\frac{\mathrm{P_L}(k, z)}{k^2} - 2\int \frac{d^3k}{(2\pi)^3}\mathrm{e}^{i\mathbf{k}\cdot\mathbf{q}}\frac{\mathrm{P_L}(k, z)}{k^2} \\ &= \frac{4\pi}{(2\pi)^3}\int_0^\infty dk \int_{-1}^1 d\mu\ \mathrm{P_L}(k, z) \\ &- \frac{4\pi}{(2\pi)^3}\int_0^\infty dk \int_{-1}^1 d\mu\ \mathrm{e}^{i\mathbf{k}\cdot\mathbf{q}}\mathrm{P_L}(k, z) \\ &= \frac{1}{\pi^2}\int_0^\infty dk\ \left[1 - j_0(kq)\right]\mathrm{P_L}(k, z) \end{aligned} \tag{3.23}$$

and

$$A_{ij}\hat{q}_i\hat{q}_j = \frac{1}{\pi^2}\int_0^\infty dk\ \left[\frac{1}{3} - j_0(kq) + 2\frac{j_1(kq)}{kq}\right]\mathrm{P_L}(k, z). \tag{3.24}$$

Therefore solving Equations (3.22) for X and Y yields

$$\begin{aligned} X(q,z) &= \frac{1}{2\pi^2}\int_0^\infty dk\ \left[\frac{2}{3} - 2\frac{j_1(kq)}{kq}\right] \mathrm{P_L}(k,z) \\ Y(q,z) &= \frac{1}{2\pi^2}\int_0^\infty dk\ \left[6\frac{j_1(kq)}{kq} - 2j_0(kq)\right] \mathrm{P_L}(k,z)\,. \end{aligned} \tag{3.25}$$

$\mathrm{P_L}(k)$ is the linear power spectrum and the exponent in (3.17) can now be written in terms of X and Y. We then split the integral into the angular and spatial parts and use the k-th moment of the integral to calculate the angular integral

$$I_k = \int_{-1}^{1} d\mu\ \mu^k \mathrm{e}^{ia\mu}\mathrm{e}^{b^2\mu^2} \tag{3.26}$$

which can be solved using the general prescription (Schneider & Bartelmann, 1995, Vlah et al., 2015a)

$$I_k = 2(-i)^k\,\mathrm{e}^b \sum_{n=0}^{\infty} (-2b)^n \left(\frac{d}{dk}\right)^k a^{-n} j_n(a)\,. \tag{3.27}$$

The angular parts of (3.17) are calculated using an identity resulting in

$$\mathrm{P}(k,z) = 4\pi \int_0^\infty dq\ q^2 \mathrm{e}^{-\frac{1}{2}k^2(X+Y)} \sum_{n=0}^{\infty} \left(\frac{kY}{q}\right)^n j_n(kq) \tag{3.28}$$

where j_n is a spherical Bessel function. In order to minimize the oscillatory nature of the power spectrum integral we will subtract $\mathrm{e}^{-k^2\sigma_\psi^2}$ from the $n = 0$ term as in Schneider & Bartelmann (1995). We will also use a low-k approximation (Vlah et al., 2015a) to the Zel'dovich power spectrum which is obtained by expanding in small k

$$\mathrm{P}\left(k,z\right)=\left[1-k^{2}\sigma_{\psi}^{2}\left(z\right)+\frac{1}{2}k^{4}\sigma_{\psi}^{4}\left(z\right)\right]\mathrm{P}_{\mathrm{L}}\left(k,z\right)+\frac{k^{4}}{20\pi^{2}}\int_{k_{\mathrm{min}}}^{k_{\mathrm{max}}}dq\ \left(\frac{\mathrm{P}_{\mathrm{L}}\left(q,z\right)}{q}\right)^{2}. \tag{3.29}$$

Method II: Splitting σ_{ij}

In Taylor & Hamilton (1996) the Zel'dovich power spectrum is calculated numerically by splitting only the correlation function of the displacement field at two positions into a parallel and perpendicular component (Gorski, 1988)

$$\sigma_{ij}\left(\mathbf{q},z\right)=\sigma_{\parallel}\left(q,z\right)\hat{q}_{i}\hat{q}_{j}+\sigma_{\perp}\left(q,z\right)\left(\delta_{ij}-\hat{q}_{i}\hat{q}_{j}\right). \tag{3.30}$$

These can be written in terms of X and Y

$$\sigma_{\parallel}\left(q,z\right)=\sigma_{\psi}^{2}\left(z\right)-\frac{1}{2}\left(X+Y\right)\ \text{ and }\sigma_{\perp}\left(q,z\right)=\sigma_{\psi}^{2}\left(z\right)-\frac{1}{2}X \tag{3.31}$$

proving that the two methods are equal. $\sigma_{\parallel}$ and $\sigma_{\perp}$ provide a physical interpretation of the functions X and Y. In Figure 3.1 the functions X and Y are plotted alongside $\sigma_{\parallel}$ and $\sigma_{\perp}$. Only $\sigma_{\parallel}$ is negative due to the particle positions being a large distance apart and being affected by a gravitational potential.

3.3 The Cosmological Trajectories Method

We begin by recapping the method introduced in Bartelmann et al. (2014a) and Ali-Haïmoud (2015). Throughout the remainder of this thesis these papers will be referred to as B14 and AH15.

The Zel'dovich approximation (Section 3.2.1) is valid and performs well until a late time when it begins to break down due to non-linear effects. The concept in B14 and AH15 is that until some time z_{*} the particles follow a Zel'dovich trajectory, then at the time z_{*} a new trajectory takes precedence. This new

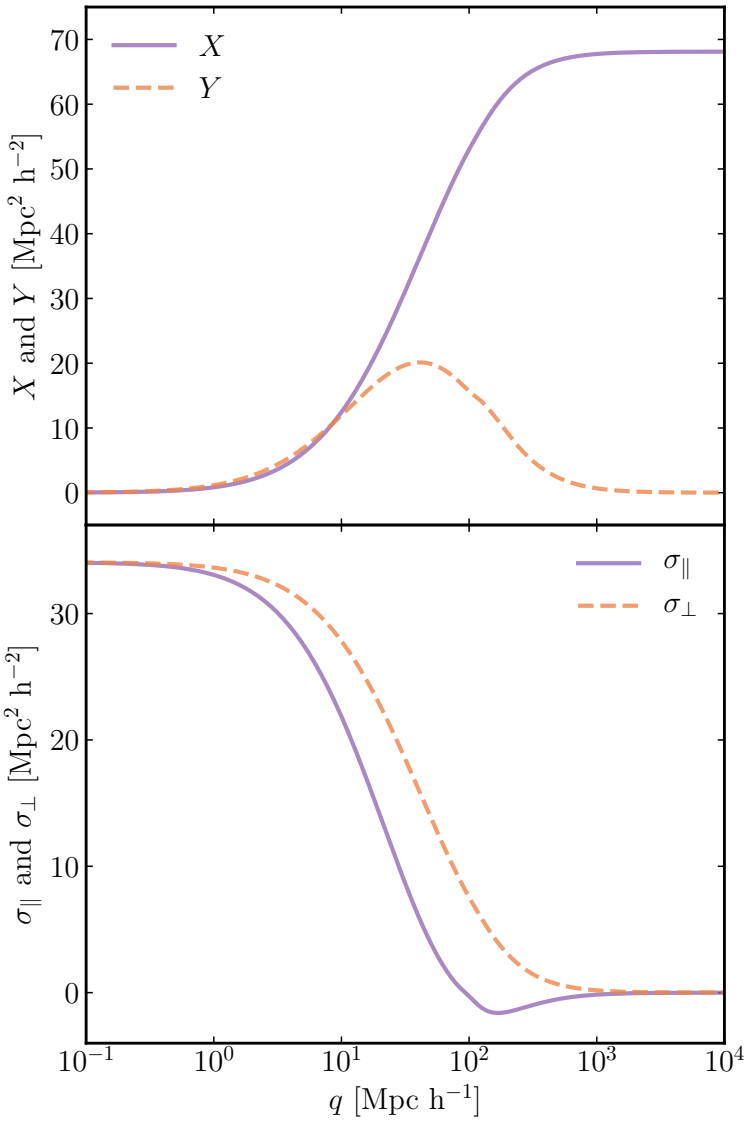

Figure 3.1 *The top panel shows the functions X (purple solid line) and Y (orange dashed line) (3.25) versus q. The bottom panel shows the functions $\sigma_\parallel$ (purple solid line) and $\sigma_\perp$ (orange dashed line) (3.30) versus q for Planck18 (Collaboration et al., 2018) cosmology.*

trajectory will include non-linear effects such as gravitational interaction. It can therefore be thought of as "switching on" higher-order effects, like in an N-body simulation, at some redshift. We begin by defining the equations of motion for point particles as

$$\frac{d\mathbf{x}}{dt} = \frac{\mathbf{u}}{a^2}, \tag{3.32a}$$

$$\frac{d\mathbf{u}}{dt} = -\nabla_{\mathbf{x}}\phi\left(\mathbf{x}, t\right). \tag{3.32b}$$

Here t is proper time, $\mathbf{u} = a\mathbf{v}$ where $\mathbf{v}$ is the proper velocity and a is the scale factor. Equations (3.32) can be solved implicitly to obtain a particle trajectory,

$$\mathbf{x}\left(t\right) = \mathbf{x}\left(t_*\right) + \mathbf{u}\left(t_*\right)\int_{t_*}^{t}\frac{dt'}{a'^2} - \epsilon\int_{t_*}^{t'}\frac{dt''}{a''^2}\int_{t_*}^{t}dt'\nabla\phi\left(\mathbf{x}\left(t'\right), t'\right). \tag{3.33}$$

The time t_* is the time at which this trajectory is "switched on" and ϵ is a book-keeping or expansion parameter. In AH15 ϵ is used to represent the order of gravitational interaction being considered. It can also be thought of as a way to control the size of the non-linear effects. This is discussed more in Chapter 4. The trajectories have been set up such that the Zel'dovich approximation is used until t_*, so this is what we shall choose to fix the initial conditions. Equation (3.33) then becomes

$$\mathbf{x}\left(t\right) = \mathbf{q} + \alpha\left(t\right)\boldsymbol{\Psi}\left(\mathbf{q}, t_*\right) - \epsilon\int_{t_*}^{t'}\frac{dt''}{a''^2}\int_{t_*}^{t}dt'\nabla\phi\left(\mathbf{x}\left(t'\right), t'\right). \tag{3.34}$$

where $\alpha\left(t\right) = 1 + a_*\frac{\dot{D}_1(t_*)}{D_1(t_*)}\int_{t_*}^{t}\frac{dt'}{a'^2}$. Following AH15 the trajectory can be split into $\mathbf{x}_0$, containing the initial positions and velocity terms and $\mathbf{x}_1$ containing the

gravitational terms. This translates to;

$$\mathbf{x}_0(t) = \mathbf{q} + \alpha(t)\,\boldsymbol{\Psi}(\mathbf{q}, t_*) \tag{3.35a}$$

$$\mathbf{x}_1(t) = -\epsilon \int_{t_*}^{t'} \frac{dt''}{a''^2} \int_{t_*}^{t} dt' \nabla\phi\left(\mathbf{x}(t'), t'\right). \tag{3.35b}$$

We will generalise this approach and show how it can be related back to the trajectory in this section in 3.3.1. In Section 3.5 we will calculate the power spectrum for this method using our approach.

3.3.1 A general cosmological trajectory

In Section 3.4 we will calculate the power spectrum for a general trajectory to second-order in the initial overdensity field $\delta^{(0)}$. The method requires us to have a general expression for such a trajectory, which will be calculated in this subsection.The equations of motion for point particles are

$$\frac{d\mathbf{x}}{dt} = \frac{\mathbf{u}}{a^2} \qquad \text{and} \qquad \frac{d\mathbf{u}}{dt} = -\nabla_{\mathbf{x}}\phi(\mathbf{x}, t). \tag{3.36}$$

In the above equations a is the scale factor, t is cosmic time and $\mathbf{u} = a\mathbf{v}$ where $\mathbf{v}$ is the proper velocity. The equations of motion (3.36) can be solved to give

$$\mathbf{x}(\mathbf{q}, t) = \mathbf{x}(\mathbf{q}, t_i) + \mathbf{u}(\mathbf{q}, t_i) \int_{t_i}^{t} \frac{dt'}{a'^2} - \epsilon \int_{t'}^{t} \frac{dt''}{a''^2} \int_{t_i}^{t} dt' \nabla_{\mathbf{x}}\phi\left(\mathbf{x}(\mathbf{q}, t'), t'\right) \tag{3.37}$$

where $\mathbf{x}(\mathbf{q})$ is the initial trajectory, $\mathbf{u}(\mathbf{q}, t_i)$ is the initial velocity and ϵ is an expansion parameter used to control the size of the higher-order gravitational term. We will replace the initial trajectory and velocity by the Zel'dovich approximation. Our trajectory will therefore describe a particle moving under free motion (Zel'dovich approximation) with a gravitational correction term.

Defining $\mathbf{g} = -\nabla\phi$ we can write the trajectory (3.37) as

$$\mathbf{x}(\mathbf{q}, t) = \mathbf{q} + \mathbf{x}_0(\mathbf{q}, t) + \mathbf{x}_1(\mathbf{q}, t) \tag{3.38}$$

with

$$\mathbf{x}_0(\mathbf{q}, t) = \frac{D_1(t)}{D_1(t_i)}\boldsymbol{\Psi}^{(0)}(\mathbf{q}, t_i) = A(t)\,\boldsymbol{\Psi}^{(0)}(\mathbf{q}, t_i), \tag{3.39}$$

$$\mathbf{x}_1(\mathbf{q}, t) = \epsilon \int_{t'}^{t} \frac{dt''}{a''^2} \int_{t_i}^{t} dt' \mathbf{g}(\mathbf{x}(\mathbf{q}, t'), t') \tag{3.40}$$

where t_i is some suitably early time. The overdensity field is given by

$$\delta(\mathbf{x}, t) = \int d^3q\ \delta_D(\mathbf{x} - \mathbf{q} - \mathbf{x}_0 - \mathbf{x}_1) - 1 \tag{3.41}$$

and its Fourier transform is

$$(2\pi)^3 \delta_D(\mathbf{k}) + \delta(\mathbf{k}, t) = \int d^3q\ \mathrm{e}^{i\mathbf{k}\cdot\mathbf{q}} \mathrm{e}^{i\mathbf{k}\cdot(\mathbf{x}_0 + \mathbf{x}_1)}. \tag{3.42}$$

Via the Poisson equation, $\nabla^2\phi = \frac{3}{2}H_0^2\Omega_m a^{-1}\delta = \frac{3}{2}\omega_0^2 a^{-1}\delta$, the gravitational field $\mathbf{g}(\mathbf{x}, t)$ can be written as

$$\mathbf{g}(\mathbf{x}, t) = i\omega_0^2 a^{-1} \int \frac{d^3k}{(2\pi)^3}\ \mathrm{e}^{-i\mathbf{k}\cdot\mathbf{x}} \frac{\mathbf{k}}{k^2} \delta(\mathbf{k}, t) \tag{3.43}$$

where $\delta(\mathbf{k}, t)$ is the instantaneous non-linear overdensity field. As $\mathbf{g}$ also depends on the particle trajectory we are following we are calculating the non-linear growth of matter density field due to the particles' motion which depends on the non-linear overdensity field.

If we assume the overdensity field is fully specified by the initial velocity of the particles then

$$\delta\left(\mathbf{x},t\right)=\int d^{3}q\ \delta_{D}\left(\mathbf{x}-\mathbf{q}-\mathbf{x}_{0}\right) \tag{3.44}$$

and the gravitational field (3.43) can be expanded as

$$\begin{aligned}
\mathbf{g}\left(\mathbf{x},t'\right) &= i\omega_{0}^{2}\frac{1}{a'}\int\frac{d^{3}k}{\left(2\pi\right)^{3}}\ \frac{\mathbf{k}}{k^{2}}\int d^{3}q'\ \mathrm{e}^{-i\mathbf{k}\cdot\left(\mathbf{x}-\mathbf{q}'-\mathbf{x}_{0}\left(\mathbf{q}',t'\right)\right)}-i\omega_{0}^{2}\frac{1}{a'}\int d^{3}k\ \frac{\mathbf{k}}{k^{2}}\delta_{D}\left(\mathbf{k}\right)\\
&= i\omega_{0}^{2}\frac{1}{a'}\int\frac{d^{3}k}{\left(2\pi\right)^{3}}\ \frac{\mathbf{k}}{k^{2}}\int d^{3}q'\ \mathrm{e}^{-i\mathbf{k}\cdot\left(\mathbf{q}-\mathbf{q}'+\mathbf{x}_{0}\left(\mathbf{q},t'\right)-\mathbf{x}_{0}\left(\mathbf{q}',t'\right)\right)}-i\omega_{0}^{2}\frac{1}{a'}\int d^{3}k\ \frac{\mathbf{k}}{k^{2}}\delta_{D}\left(\mathbf{k}\right)\\
&= i\omega_{0}^{2}\frac{1}{a'}\int\frac{d^{3}k}{\left(2\pi\right)^{3}}\ \frac{\mathbf{k}}{k^{2}}\int d^{3}q'\ \mathrm{e}^{-i\mathbf{k}\cdot\left(\mathbf{q}-\mathbf{q}'\right)}\sum_{n=1}^{\infty}\frac{1}{n!}\left[-i\mathbf{k}\cdot\left(\mathbf{x}_{0}\left(\mathbf{q},t'\right)-\mathbf{x}_{0}\left(\mathbf{q}',t'\right)\right)\right]^{n}\\
&\approx i\omega_{0}^{2}\frac{1}{a'}\int\frac{d^{3}k}{\left(2\pi\right)^{3}}\ \frac{\mathbf{k}}{k^{2}}\int d^{3}q'\ \mathrm{e}^{-i\mathbf{k}\cdot\left(\mathbf{q}-\mathbf{q}'\right)}\left[-i\mathbf{k}\cdot\left[\mathbf{x}_{0}\left(\mathbf{q},t'\right)-\mathbf{x}_{0}\left(\mathbf{q}',t'\right)\right]\right.\\
&\left.+\frac{1}{2}\left[\mathbf{k}\cdot\left(\mathbf{x}_{0}\left(\mathbf{q},t'\right)-\mathbf{x}_{0}\left(\mathbf{q}',t'\right)\right)\right]^{2}\right]\\
&\approx \omega_{0}^{2}\frac{1}{a'}A\left(t'\right)\left[\mathbf{\Psi}^{(0)}\left(\mathbf{q},t_{i}\right)-A\left(t'\right)\mathbf{\Psi}^{(0)}\left(\mathbf{q},t'\right)\nabla\cdot\mathbf{\Psi}^{(0)}\left(\mathbf{q},t_{i}\right)\right]\\
&\approx -\omega_{0}^{2}\frac{1}{a'}A\left(t'\right)^{2}\mathbf{\Psi}^{(0)}\left(\mathbf{q},t'\right)\nabla\cdot\mathbf{\Psi}^{(0)}\left(\mathbf{q},t_{i}\right).
\end{aligned} \tag{3.45}$$

where we have ignored the $n=1$ term ($\mathbf{\Psi}^{(0)}$) as it is already captured by the Zel'dovich approximation and we wish to avoid double counting. Therefore, the CTM trajectory to second-order is given by

$$\mathbf{x}\left(\mathbf{q},t\right)=\mathbf{q}+\Psi_{i}\left(\mathbf{q},t_{i}\right)\left[A\left(t\right)\delta_{ij}+B\left(t\right)\bar{E}_{ij}\left(\mathbf{q},t_{i}\right)\right] \tag{3.46}$$

where the tidal tensor is $\bar{E}_{ij}\left(\mathbf{q},t\right)=\nabla_{i}\nabla_{j}\nabla^{-2}\delta^{(0)}\left(\mathbf{q},t\right)$ with $\delta^{(0)}$ being the linear overdensity field. This tidal term describes the effects of gravitational scattering and deflection.

Finally, we will define the tidal tensor as $E_{ij}=\bar{E}_{ij}-\frac{1}{3}\delta^{(0)}\delta_{ij}$ resulting in

$$x_i(z) = q_i + \Psi_j(\mathbf{q}, z_i)\left[A(z)\,\delta_{ij} + B(z)\left(E_{ij}(\mathbf{q}, z_i) + \frac{1}{3}\delta^{(0)}(\mathbf{q}, z_i)\,\delta_{ij}\right)\right], \tag{3.47}$$

where $\delta^{(0)}$ is the linear overdensity field and $A(z) = \frac{D_1(z)}{D_1(z_i)}$. The time dependence factor $B(t)$ is

$$B(t) = -\epsilon\omega_0^2 \int_{t'}^{t} \frac{dt''}{a''^2} \int_{t_i}^{t} \frac{dt'}{a'} A(t')^2 \tag{3.48}$$

which after using $dt = -\frac{a}{H}dz$ can be written as

$$B(t) = -\epsilon\omega_0^2 \int_{z'}^{z} \frac{dz''}{a''H(z'')} \int_{z_i}^{z} \frac{dz'}{H(z')} A(z')^2 . \tag{3.49}$$

We no longer have t_* but some early time t_i this parameter can be chosen freely and we will investigate it later in Chapter 4. This general cosmological trajectory (3.47) will be used in Section 3.4 to calculate an analytic expression for the power spectrum.

3.4 Calculating the power spectrum for a general cosmological trajectory

3.4.1 Covariance matrix and correlation functions

Using the methods (Bardeen et al., 1986b, van de Weygaert & Bertschinger, 1996) and results from Taylor & Watts (2000) we can derive the correlation of the fields that appear in the general trajectory (3.47). These fields are Ψ_i, E_{ij} and $\delta^{(0)}$ as defined in Section 3.3.1.

We need to calculate the correlation of the fields with each other at the same and different points i.e. $\mathbf{q}_1$ and $\mathbf{q}_2$ at z_i. Let us calculate the correlation between the displacement field at two points to demonstrate the method used in Taylor

& Watts (2000)

$$\begin{aligned}\sigma_{ij}\left(\mathbf{q}, z_i\right) &= \left\langle \Psi_i\left(\mathbf{q}_1, z_i\right) \Psi_j\left(\mathbf{q}_2, z_i\right)\right\rangle \\ &= \int \frac{d^3k_1}{(2\pi)^3} \int \frac{d^3k_2}{(2\pi)^3}\, \mathrm{e}^{-i\mathbf{k}_1\cdot\mathbf{q}_1 - i\mathbf{k}_2\cdot\mathbf{q}_2} \frac{k_i^1 k_j^2}{k_1^2 k_2^2} \langle \delta_1^{(0)} \delta_2^{(0)} \rangle \\ &= \int \frac{d^3k_1}{(2\pi)^3}\, \mathrm{e}^{i\mathbf{k}_1\cdot(\mathbf{q}_2-\mathbf{q}_1)} \frac{k_i^1 k_j^1}{k_1^4} \mathrm{P}_{\mathrm{L}}\left(k, z_i\right) \\ &= \int \frac{d^3k}{(2\pi)^3}\, \mathrm{e}^{i\mathbf{k}\cdot\mathbf{q}} \frac{k_i k_j}{k^4} \mathrm{P}_{\mathrm{L}}\left(k, z_i\right).\end{aligned} \tag{3.50}$$

Carrying out a similar calculation for the other correlations allows us to write

$$\mathbf{C} = \begin{bmatrix} \sigma_\psi^2 \delta_{ij} & \sigma_{ij}\left(\mathbf{q}\right) & 0 & \Phi_{ijk}\left(\mathbf{q}\right) & 0 & \Pi_i\left(\mathbf{q}\right) \\ \sigma_{ij}\left(\mathbf{q}\right) & \sigma_\psi^2 \delta_{ij} & \Phi_{ijk}\left(\mathbf{q}\right) & 0 & \Pi_i\left(\mathbf{q}\right) & 0 \\ 0 & \Phi_{ijk}\left(\mathbf{q}\right) & \eta_{ijkl}\left(\mathbf{0}\right) & \eta_{ijkl}\left(\mathbf{q}\right) & \Sigma_{ij}\left(\mathbf{0}\right) & \Sigma_{ij}\left(\mathbf{q}\right) \\ \Phi_{ijk}\left(\mathbf{q}\right) & 0 & \eta_{ijkl}\left(\mathbf{q}\right) & \eta_{ijkl}\left(\mathbf{0}\right) & \Sigma_{ij}\left(\mathbf{q}\right) & \Sigma_{ij}\left(\mathbf{0}\right) \\ 0 & \Pi_i\left(\mathbf{q}\right) & \Sigma_{ij}\left(\mathbf{0}\right) & \Sigma_{ij}\left(\mathbf{q}\right) & \sigma_0^2\left(\mathbf{0}\right) & \sigma_0^2\left(\mathbf{q}\right) \\ \Pi_i\left(\mathbf{q}\right) & 0 & \Sigma_{ij}\left(\mathbf{q}\right) & \Sigma_{ij}\left(\mathbf{0}\right) & \sigma_0^2\left(\mathbf{q}\right) & \sigma_0^2\left(\mathbf{0}\right) \end{bmatrix}, \tag{3.51}$$

.

with

$$\sigma_{ij}\left(\mathbf{q}\right) = \left\langle \Psi_i\left(\mathbf{q}_1\right) \Psi_j\left(\mathbf{q}_2\right)\right\rangle \tag{3.52a}$$

$$\Phi_{ijk}\left(\mathbf{q}\right) = \left\langle E_{ij}\left(\mathbf{q}_1\right) \Psi_k\left(\mathbf{q}_2\right)\right\rangle, \tag{3.52b}$$

$$\eta_{ijkl}\left(\mathbf{q}\right) = \left\langle E_{ij}\left(\mathbf{q}_1\right) E_{kl}\left(\mathbf{q}_2\right)\right\rangle, \tag{3.52c}$$

$$\Sigma_{ij}\left(\mathbf{q}\right) = \left\langle E_{ij}\left(\mathbf{q}_1\right) \delta^{(0)}\left(\mathbf{q}_2\right)\right\rangle, \tag{3.52d}$$

$$\Pi_i\left(\mathbf{q}\right) = \left\langle \delta^{(0)}\left(\mathbf{q}_1\right) \Psi_i\left(\mathbf{q}_2\right)\right\rangle, \tag{3.52e}$$

$$\sigma_0^2\left(\mathbf{q}\right) = \left\langle \delta^{(0)}\left(\mathbf{q}_1\right) \delta^{(0)}\left(\mathbf{q}_2\right)\right\rangle, \tag{3.52f}$$

and $\mathbf{q} = \mathbf{q}_2 - \mathbf{q}_1$. We have also defined

$$\sigma_{ij}\left(\mathbf{q}, z_i\right) = \int \frac{d^3k}{\left(2\pi\right)^3} \mathrm{e}^{i\mathbf{k}\cdot\mathbf{q}} \frac{k_i k_j}{k^4} \mathrm{P}_{\mathrm{L}}\left(k, z_i\right), \tag{3.53a}$$

$$\sigma_{ij}\left(\mathbf{0}, z_i\right) = \sigma_\psi^2 \delta_{ij} = \sigma_\psi^2 \delta_{ij} = \frac{1}{3}\delta_{ij} \int \frac{d^3k}{\left(2\pi\right)^3} \frac{\mathrm{P}_{\mathrm{L}}\left(k, z_i\right)}{k^2} \delta_{ij}. \tag{3.53b}$$

For ease, we can define the following correlations for $\bar{E}_{ij} = \nabla_i \nabla_j \nabla^{-2} \delta^{(0)}$,

$$\bar{\Phi}_{ijk}\left(\mathbf{q}\right) = \langle \bar{E}_{ij}\left(\mathbf{q}_1\right) \Psi_k\left(\mathbf{q}_2\right) \rangle = i \int \frac{d^3k}{\left(2\pi\right)^3} \mathrm{e}^{i\mathbf{k}\cdot\mathbf{q}} \frac{k_i k_j k_k}{k^4} \mathrm{P}_{\mathrm{L}}\left(k, z_i\right), \tag{3.54a}$$

$$\bar{\eta}_{ijkl}\left(\mathbf{q}\right) = \langle \bar{E}_{ij}\left(\mathbf{q}_1\right) \bar{E}_{kl}\left(\mathbf{q}_2\right) \rangle = \int \frac{d^3k}{\left(2\pi\right)^3} \mathrm{e}^{i\mathbf{k}\cdot\mathbf{q}} \frac{k_i k_j k_k k_l}{k^4} \mathrm{P}_{\mathrm{L}}\left(k, z_i\right), \tag{3.54b}$$

$$\Pi_i\left(\mathbf{q}\right) = i \int \frac{d^3k}{\left(2\pi\right)^3} \mathrm{e}^{i\mathbf{k}\cdot\mathbf{q}} \frac{k_i}{k^2} \mathrm{P}_{\mathrm{L}}\left(k, z_i\right). \tag{3.54c}$$

The correlations containing E_{ij} defined in Equations (3.52a, 3.52b, 3.52c, 3.52d, 3.52e, 3.52f) can be re-expressed in terms correlations of $\bar{E}_{ij}$ defined in Equations (3.54a, 3.54b, 3.54c).

$$\Phi_{ijk}\left(\mathbf{q}\right) = \bar{\Phi}_{ijk}\left(\mathbf{q}\right) - \frac{1}{3}\pi_k\left(\mathbf{q}\right)\delta_{ij}, \tag{3.55}$$

$$\eta_{ijkl}\left(\mathbf{q}\right) = \bar{\eta}_{ijkl}\left(\mathbf{q}\right) + \frac{1}{9}\sigma_0^2\left(\mathbf{q}\right)\delta_{ij}\delta_{kl} - \frac{1}{3}\left(\bar{\eta}_{ijmm}\left(\mathbf{q}\right)\delta_{kl} + \bar{\eta}_{mmkl}\left(\mathbf{q}\right)\delta_{ij}\right), \tag{3.56}$$

$$\Sigma_{ij}\left(\mathbf{q}\right) = \bar{\eta}_{ijnn}\left(\mathbf{q}\right) - \frac{1}{3}\sigma_0^2\left(\mathbf{q}\right)\delta_{ij}. \tag{3.57}$$

3.4.2 The full power spectrum

The power spectrum for the general cosmological trajectory (3.47) is given by

$$\mathrm{P}(k,z) = \int d^3q\ \mathrm{e}^{i\mathbf{k}\cdot\mathbf{q}} \Big[\langle \mathrm{e}^{ik_i\Psi_j(\mathbf{q}_1,z_i)\left(A(z)\delta_{ij}+B(z)E_{ij}(\mathbf{q}_1,z_i)+\frac{1}{3}B(z)\delta^{(0)}(\mathbf{q}_1,z_i)\right)} \mathrm{e}^{-ik_i\Psi_j(\mathbf{q}_2,z_i)\left(A(z)\delta_{ij}+B(z)E_{ij}(\mathbf{q}_2,z_i)+\frac{1}{3}B(z)\delta^{(0)}(\mathbf{q}_2,z_i)\right)} \rangle - 1 \Big]. \tag{3.58}$$

Our aim is to calculate the $\langle \cdots \rangle$ term. If we assume that all of our fields are initially Gaussian we can write

$$\begin{aligned} &\langle \mathrm{e}^{ik_i\Psi_j(\mathbf{q}_1)\left(A\delta_{ij}+BE_{ij}(\mathbf{q}_1)+\frac{1}{3}B\delta^{(0)}(\mathbf{q}_1)\right)-ik_i\Psi_j(\mathbf{q}_2)\left(A\delta_{ij}+BE_{ij}(\mathbf{q}_2)+\frac{1}{3}B\delta^{(0)}(\mathbf{q}_2)\right)} \rangle \\ &= \frac{1}{(2\pi)^{10}} \int d\mathbf{X}\ (|\det \mathbf{C}|)^{-1/2}\ \mathrm{e}^{-\frac{1}{2}X_jC^{-1}_{ij}X_i} \mathrm{e}^{ik_i\Psi^1_j\left(A\delta_{ij}+BE^1_{ij}+\frac{1}{3}B\delta^{(0)}_1\right)-ik_i\Psi^2_j\left(A\delta_{ij}+BE^2_{ij}+\frac{1}{3}B\delta^{(0)}_2\right)} \end{aligned} \tag{3.59}$$

where the fields Ψ, $\delta^{(0)}$ and E_{ij} are evaluated at z_i and the functions A and B are evaluated at z for the rest of this thesis. We have defined $X_i = \left(\Psi^1_\alpha\ ,\Psi^2_\alpha\ ,E^1_{\alpha\beta}\ ,E^2_{\alpha\beta},\delta^{(0)}_1,\delta^{(0)}_2\right)$ and $\mathbf{C}$ is the covariance matrix calculated in Section 3.4.1. The Roman indices run through $i,j = \Psi_1,\Psi_2,E^1,E^2,\delta^1,\delta^2$ and the Greek indices run through 1 to 3 in the above and following expressions.

If we introduce $K_i = (Ak_\alpha, -Ak_\alpha, 0, 0, 0, 0)$ and a matrix $\mathbf{M}$

$$\mathbf{M} = \begin{bmatrix} 0 & 0 & -iBk_\alpha\delta_{\beta\gamma} & 0 & -\frac{1}{3}iBk_\alpha & 0 \\ 0 & 0 & 0 & iBk_\alpha\delta_{\beta\gamma} & 0 & \frac{1}{3}iBk_\alpha \\ -iBk_\alpha\delta_{\beta\gamma} & 0 & 0 & 0 & 0 & 0 \\ 0 & iBk_\alpha\delta_{\beta\gamma} & 0 & 0 & 0 & 0 \\ -\frac{1}{3}iBk_\alpha & 0 & 0 & 0 & 0 & 0 \\ 0 & \frac{1}{3}iBk_\alpha & 0 & 0 & 0 & 0 \end{bmatrix}, \tag{3.60}$$

Equation (3.59) can be rewritten as a more explicit multivariate Gaussian

$$\langle e^{ik_i\Psi_j(\mathbf{q}_1)\left(A\delta_{ij}+BE_{ij}(\mathbf{q}_1)\right)-ik_i\Psi_j(\mathbf{q}_2)\left(A\delta_{ij}+BE_{ij}(\mathbf{q}_2)\right)}\rangle$$
$$= \frac{1}{(2\pi)^{10}}\int d\mathbf{X}\,(|\det \mathbf{C}|)^{-1/2}\, e^{-\frac{1}{2}X_jC_{ij}^{-1}X_i} e^{iK_iX_i} e^{-\frac{1}{2}X_jM_{ij}X_i} \quad (3.61)$$

which can be integrated and evaluated as

$$\langle e^{ik_i\Psi_j(\mathbf{q}_1)\left(A\delta_{ij}+BE_{ij}(\mathbf{q}_1)\right)-ik_i\Psi_j(\mathbf{q}_2)\left(A\delta_{ij}+BE_{ij}(\mathbf{q}_2)\right)}\rangle$$
$$= (|\det 1+\mathbf{MC}|)^{-1/2}\, e^{-\frac{1}{2}\mathbf{K}^T\mathbf{C}[1+\mathbf{MC}]^{-1}\mathbf{K}} \quad (3.62)$$

dropping index notation for ease. The power spectrum for a general trajectory is thereby

$$\mathrm{P}(k,z) = \int d^3q\; e^{i\mathbf{k}\cdot\mathbf{q}}\left[(|\det 1+\mathbf{MC}|)^{-1/2}\, e^{-\frac{1}{2}\mathbf{K}^T\mathbf{C}[1+\mathbf{MC}]^{-1}\mathbf{K}} - 1\right]. \quad (3.63)$$

This is the key new result of this thesis. In the next Section 3.4.3 we will focus on calculating this result numerically.

3.4.3 Expansion of the power spectrum in ϵ

Our goal is to calculate (3.63) numerically. Expanding $\mathrm{P}(k,z)$ in orders of ϵ will allow for easier computation of the power spectrum and comparison to other methods. The argument of the exponential in Equation (3.63) can be expanded using the binomial theorem,

$$\mathbf{K}^T\mathbf{C}\,[1+\mathbf{MC}]^{-1}\,\mathbf{K} \approx \mathbf{K}^T\mathbf{CK} - \mathbf{K}^T\mathbf{CMCK}, \quad (3.64)$$

The first term in the exponent expansion is

$$\mathbf{K}^T\mathbf{C}\mathbf{K} = 2A^2(z)\left[k^2\sigma_\psi^2(z_i) - k_i k_j \sigma_{ij}(\mathbf{q}, z_i)\right] \tag{3.65}$$

which is simply the Zel'dovich power spectrum with a general time dependence function $A(z)$. The second term in the exponent expansion is

$$\mathbf{K}^T\mathbf{C}\mathbf{M}\mathbf{C}\mathbf{K} = 0 \tag{3.66}$$

Since Equation (3.66) is zero this suggests we may have to go to a higher-order in the exponent to include higher-order effects. The determinant of a matrix can be expressed in terms of an exponential i.e. $\det\mathbf{A} = \exp[\mathrm{tr}(\ln\mathbf{A})]$. Applying this to the determinant in (3.63) and expanding the logarithm gives

$$\begin{aligned}(|\det 1 + \mathbf{MC}|)^{-1/2} &= \mathrm{e}^{-\frac{1}{2}\mathrm{tr}[\ln(1+\mathbf{MC})]} \\ &\approx \mathrm{e}^{-\frac{1}{2}\mathrm{tr}(\mathbf{MC})}\mathrm{e}^{\frac{1}{4}\mathrm{tr}(\mathbf{MCMC})}.\end{aligned} \tag{3.67}$$

The trace of $\mathbf{MC}$ is

$$\begin{aligned}\mathrm{tr}(\mathbf{MC}) = {} & M_{\Psi^1 E^1} C_{E^1\Psi^1} + M_{\Psi^2 E^2} C_{E^2\Psi^2} + M_{E^1\Psi^1} C_{\Psi^1 E^1} + M_{E^2\Psi^2} C_{\Psi^2 E^2} \\ & + M_{\delta^1\Psi^1} C_{\Psi^1\delta^1} + M_{\delta^2\Psi^2} C_{\Psi^2\delta^2} = 0\end{aligned} \tag{3.68}$$

and the trace of $\mathbf{MCMC}$ is

$$\begin{aligned}\mathrm{tr}(\mathbf{MCMC}) = {} & 4B^2(z)\, k_i k_j \left[\bar{\Phi}_{nni}(\mathbf{q})\,\bar{\Phi}_{mmj}(\mathbf{q}) + \frac{2}{9}\sigma_0^2(\mathbf{q})\,\sigma_{ij}(\mathbf{q})\right. \\ & + \frac{2}{3}\sigma_{ni}(\mathbf{q})\,\bar{\eta}_{njmm}(\mathbf{q}) - \frac{1}{3}\bar{\eta}_{nnmm}(\mathbf{q})\,\sigma_{ij}(\mathbf{q}) + \frac{4}{9}\Pi_i(\mathbf{q})\,\Pi_j(\mathbf{q}) \\ & \left. - \frac{4}{3}\Pi_i(\mathbf{q})\,\bar{\Phi}_{jmm}(\mathbf{q}) - \frac{1}{3}\sigma_\psi^2\eta_E^2\delta_{ij}\right],\end{aligned} \tag{3.69}$$

After noting that $\bar{\eta}_{ijkk}(\mathbf{0}) = \eta_E^2 \delta_{ij}$ and $\sigma_0^2(\mathbf{0}) = 3\eta_E^2$ where

$$\eta_E^2 = \frac{1}{6\pi^2} \int_0^\infty dk \; k^2 \mathrm{P_L}(k, z_i) \,. \tag{3.70}$$

3.4.4 Calculating the full expanded power spectrum

Calculating $\bar{\Phi}_{ijk}$ and $\bar{\eta}_{ijkl}$

The correlations σ_{ij}, $\bar{\Phi}_{ijk}$ and $\bar{\eta}_{ijkl}$ can be split into irreducible components (Vlah et al., 2015a, Catelan et al., 2000, Crittenden et al., 2001). The splitting of σ_{ij} is calculated in Section 3.2.3. The correlations $\bar{\Phi}_{ijk}$ can be expanded as

$$\bar{\Phi}_{ijk}(q) = F(q)\left[\hat{q}_i\delta_{jk} + \hat{q}_j\delta_{ik} + \hat{q}_k\delta_{ij}\right] + D(q)\,\hat{q}_i\hat{q}_j\hat{q}_k \tag{3.71}$$

Setting $P_0 = \bar{\Phi}_{ijk}(q)\,\hat{q}_i\delta_{jk}$ and $\bar{P} = \bar{\Phi}_{ijk}(q)\,\hat{q}_i\hat{q}_j\hat{q}_k$ gives

$$P_0 = 5F(q) + D(q) \;\text{ and }\; \bar{P} = 3F(q) + D(q) \,. \tag{3.72}$$

Using Equations (3.72) to solve for the functions F and D results in

$$D(q) = \frac{1}{2\pi^2} \int_0^\infty dk \; j_3(kq)\, k \; \mathrm{P_L}(k, z_i) \,. \tag{3.73a}$$

$$F(q) = -\frac{1}{10\pi^2} \int_0^\infty dk \;\; [j_1(kq) + j_3(kq)]\, k \; \mathrm{P_L}(k, z_i) \tag{3.73b}$$

In Catelan et al. (2000) and Crittenden et al. (2001) the correlation η_{ijkl} is calculated by writing,

$$\bar{\eta}_{ijkl}(q) = \frac{1}{2\pi^2} \int_0^\infty \frac{dk}{k^2} \; \mathrm{P_L}(k, z_i)\, \nabla_i\nabla_j\nabla_k\nabla_l j_0(kq) \tag{3.74}$$

which implies that

$$\bar{\eta}_{ijkl}(q) = G(q)\,\hat{q}_i\hat{q}_j\hat{q}_k\hat{q}_l + I(q)\left(\delta_{ij}\delta_{kl} + \delta_{il}\delta_{jk} + \delta_{jl}\delta_{ik}\right) + H(q)\left(\hat{q}_i\hat{q}_k\delta_{jl} + \hat{q}_k\hat{q}_l\delta_{ij} + \hat{q}_i\hat{q}_l\delta_{jk} + \hat{q}_l\hat{q}_j\delta_{ik} + \hat{q}_i\hat{q}_j\delta_{kl} + \hat{q}_k\hat{q}_j\delta_{il}\right). \quad (3.75)$$

The functions G, H and I are defined as

$$G(q) = \frac{1}{2\pi^2}\int_0^\infty dk\ k^2 j_4(kq)\,\mathrm{P_L}(k, z_i), \quad (3.76a)$$

$$H(q) = -\frac{1}{14\pi^2}\int_0^\infty dk\ k^2\left[j_2(kq) + j_4(kq)\right]\mathrm{P_L}(k, z_i), \quad (3.76b)$$

$$I(q) = \frac{1}{210\pi^2}\int_0^\infty dk\ k^2\left[7j_0(kq) + 10j_2(kq) + 3j_4(kq)\right]\mathrm{P_L}(k, z_i). \quad (3.76c)$$

The functions D, F, G, H and I are defined in (3.73) and (3.76) are plotted in Figure 3.2.

The covariance $\mathbf{\Pi}_i$ can be easily calculated following the above methods

$$\mathbf{\Pi}_i(\mathbf{q}) = \bar{\Pi}(q)\,\hat{q}_i = -\frac{1}{2\pi^2}\int_0^\infty dk\ k\mathrm{P_L}(k)\,j_1(kq)\,\hat{q}_i. \quad (3.77)$$

Substituting (3.75), (3.71) and (3.77) into (3.69) then splitting the integral into k^2 and $k^2\mu^2$ parts using the method for numerically calculating the Zel'dovich power spectrum described in Section 3.2.3. The power spectrum (3.63) becomes,

$$\mathrm{P}(k, z) \approx 2\pi\int_0^\infty dq\ q^2\int_{-1}^1 d\mu\ \mathrm{e}^{ikq\mu}\left[\mathrm{e}^{-\frac{1}{2}k^2A^2\left(X'+\mu^2Y'\right)}\mathrm{e}^{B^2k^2\left(W'+\mu^2Z'\right)} - \mathrm{e}^{-k^2\sigma_\psi^2\left(A^2+\frac{1}{3}B^2\eta_E^2\right)}\right]. \quad (3.78)$$

where the second exponential term has been added to cancel oscillations as described in Schneider & Bartelmann (1995). The functions X' and Y' are equal

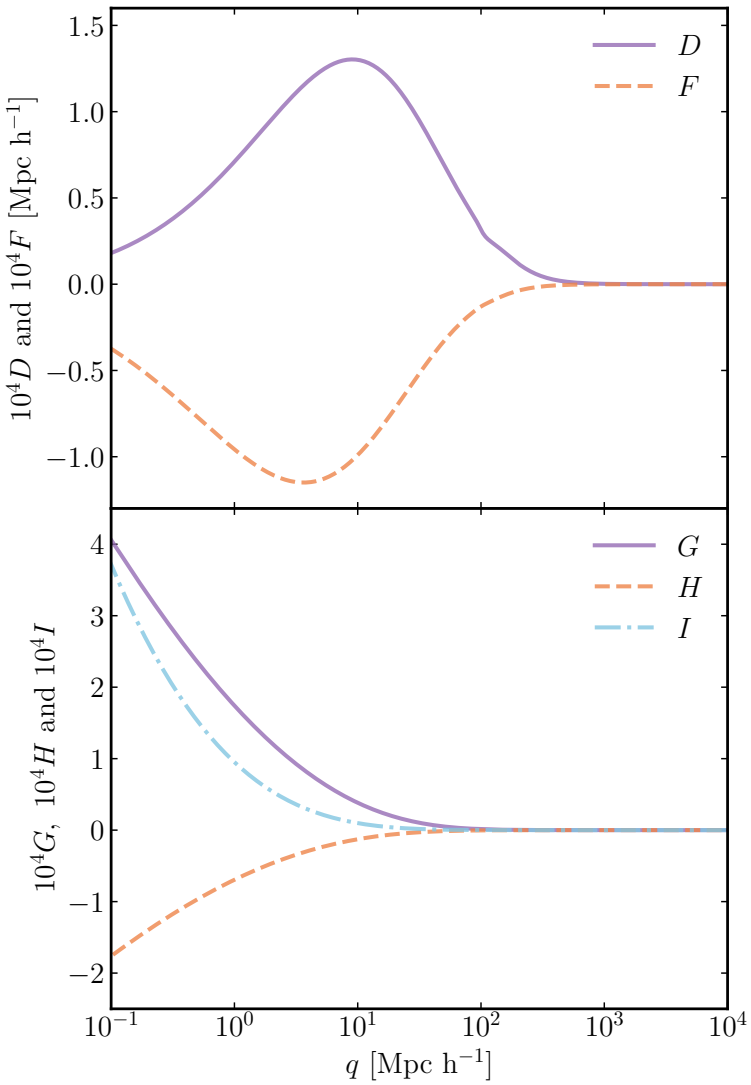

Figure 3.2 *The q dependent functions defined in (3.73) and (3.76) are plotted above versus q for Planck18 (Collaboration et al., 2018) cosmology.*

to those defined in (3.25) with the linear power spectrum evaluated at z_i rather than $z = 0$.

The power spectrum to second-order in ϵ is finally given by

$$\mathrm{P}(k,z) = 4\pi \int_0^\infty dq\; q^2 \mathrm{e}^{-\frac{1}{2}k^2\left[A^2(X'+Y')-2B^2(W'+Z')\right]} \sum_{n=0}^{\infty} \left[\frac{k\left(A^2Y' - 2B^2Z'\right)}{q}\right]^n j_n(kq) \tag{3.79}$$

where

$$W'(q) = -\frac{1}{3}\sigma_\psi^2\eta_E^2 - \frac{1}{3}\left(\sigma_\psi^2 - \frac{1}{2}X'(q)\right)\left(5I(q) + 8H(q) + G(q) - \frac{2}{3}\sigma_0^2(q)\right), \tag{3.80a}$$

$$\begin{aligned} Z'(q) = {} & (5F(q) + D(q))^2 + \frac{4}{9}\bar{\Pi}(q)^2 - \frac{4}{3}\bar{\Pi}(q)(5F(q) + D(q)) \\ & + \frac{2}{3}\left(\sigma_\psi^2 - \frac{1}{2}X'(q)\right)(G(q) + 7H(q)) \\ & - \frac{1}{3}Y'(q)\left(-\frac{5}{2}I(q) + 3H(q) + \frac{1}{2}G(q) + \frac{1}{3}\sigma_0^2(q)\right). \end{aligned} \tag{3.80b}$$

Expansion of power spectrum in $\mathrm{P_L}$

We can further expand (3.78) in $\mathrm{P_L}$ so that we may compare our method more directly to B14's

$$\begin{aligned} \mathrm{P}(k,z) \approx {} & A^2(z)\left[1 - A^2(z)\,k^2\sigma_\psi^2 - B^2(z)\,k^2\sigma_\psi^2\eta_E^2\right]\mathrm{P_L}(k,z_i) \\ & + A^4(z)\,\mathrm{P_{1-loop}}(k,z_i) + B^2(z)\left[1 - A^2(z)\,k^2\sigma_\psi^2\right]\left[\mathrm{P}_2(k,z_i) - \mathrm{P}_1(k,z_i)\right] \\ & + A^2(z)\,B^2(z)\left[\mathrm{P}_4(k,z_i) - \mathrm{P}_3(k,z_i)\right]. \end{aligned} \tag{3.81}$$

with

$$\mathrm{P}_1(k) = \int \frac{d^3k'}{(2\pi)^3} \frac{\mathrm{P_L}(k')\,\mathrm{P_L}(k'')}{k'^4 k''^4} (\mathbf{k}\cdot\mathbf{k}')(\mathbf{k}\cdot\mathbf{k}'')(\mathbf{k}'\cdot\mathbf{k}'')^2 \tag{3.82a}$$

$$\mathrm{P}_2(k) = \int \frac{d^3k'}{(2\pi)^3} \frac{\mathrm{P_L}(k')\,\mathrm{P_L}(k'')}{k'^4 k''^4} (\mathbf{k}\cdot\mathbf{k}'')^2(\mathbf{k}'\cdot\mathbf{k}'')^2 \tag{3.82b}$$

$$\mathrm{P}_3(k) = \int \frac{d^3k'}{(2\pi)^3} \int \frac{d^3k'''}{(2\pi)^3} \frac{\mathrm{P_L}(k')\,\mathrm{P_L}(k''')\,\mathrm{P_L}(k'''')}{k'^4 k'''^4 k''''^4} \times (\mathbf{k}\cdot\mathbf{k}''')(\mathbf{k}\cdot\mathbf{k}')(\mathbf{k}\cdot\mathbf{k}'''')(\mathbf{k}''\cdot\mathbf{k}'''')^2 \tag{3.82c}$$

$$\mathrm{P}_4(k) = \int \frac{d^3k'}{(2\pi)^3} \int \frac{d^3k'''}{(2\pi)^3} \frac{\mathrm{P_L}(k')\,\mathrm{P_L}(k''')\,\mathrm{P_L}(k'''')}{k'^4 k'''^4 k''''^4} \times (\mathbf{k}\cdot\mathbf{k}'''')^2(\mathbf{k}\cdot\mathbf{k}''')^2(\mathbf{k}'\cdot\mathbf{k}'''')^2 \tag{3.82d}$$

and $\mathbf{k}'' = \mathbf{k} - \mathbf{k}'$,$\mathbf{k}'''' = \mathbf{k} - \mathbf{k}' - \mathbf{k}'''$.

3.5 Example I: A KFT trajectory

3.5.1 Previous results

In AH15 a more detailed computation of the power spectrum to first-order in the gravitational interaction is given. The computation is also described in B14 from the statistical mechanics perspective. We will simply summarise the results here so that we may compare our power spectrum to B14's. Using the definition of the overdensity field (3.14) the Dirac delta can be expanded such that

$$1 + \delta^{(0)}(\mathbf{x}) = \int \delta_{\mathrm{D}}(\mathbf{x} - \mathbf{x}_0)\, d^3q, \tag{3.83a}$$

$$\delta^{(1)}(\mathbf{x}) = -\int \mathbf{x}_1(\mathbf{q}) \cdot \nabla \delta_{\mathrm{D}}(\mathbf{x} - \mathbf{x}_0)\, d^3q. \tag{3.83b}$$

To first-order in the gravitational interaction (with $\mathrm{P}^{(00)} \propto \langle \delta^{(0)}\delta^{(0)} \rangle$ and $\mathrm{P}^{(01)} \propto$

$\langle \delta^{(0)} \delta^{(1)} \rangle$) the power spectrum is given by,

$$\mathrm{P}(k) \approx \mathrm{P}^{(00)}(k) + 2\epsilon \mathrm{P}^{(01)}(k) . \tag{3.84}$$

It is then noted that $\mathbf{x}_0$ is equal to the Zel'dovich approximation with the exception of the time dependent function $\alpha(t)$. Therefore the power spectrum to zeroth order in the interaction is,

$$\mathrm{P}^{(00)}(k) = \int d^3q \; \mathrm{e}^{i\mathbf{k}\cdot\mathbf{q}} \left[\mathrm{e}^{-k^2\alpha^2\sigma_\psi^2 + k_i k_j \alpha^2 \sigma_{ij}(\mathbf{q})} - 1 \right] . \tag{3.85}$$

Calculating $\mathrm{P}^{(01)}$ is more involved as it requires taking the correlation of $\delta^{(0)}$ and $\delta^{(1)}$. It is calculated in full in AH15 and B14. However, let us focus on the result obtained if one expands in P_L

$$\mathrm{P}_\mathrm{L}^{(00)}(k, z) = \alpha^2(z) \, \mathrm{P}_\mathrm{L}(k, z_*) , \tag{3.86a}$$

$$\mathrm{P}_\mathrm{L}^{(01)}(k, z) = \omega_0^2 \alpha(z) \int_{t'}^{t} \frac{dt''}{a''^2} \int_{t_*}^{t} \frac{dt'}{a'} \alpha(z') \, \mathrm{P}_\mathrm{L}(k, z_*) , \tag{3.86b}$$

where $\omega_0^2 = \frac{3}{2} H_0^2 \Omega_m$.

There are a number of issues raised in AH15 concerning the results presented in B14. One such issue is with the expansion carried out to calculate the power spectrum. Expanding Equation (3.19) in the usual way gives (Crocce & Scoccimarro, 2006a)

$$\mathrm{P}_\mathrm{zel}(k) \approx \mathrm{P}_\mathrm{L}(k) - k^2 \sigma_\psi^2 \mathrm{P}_\mathrm{L}(k) + \mathrm{P}_{1-\mathrm{loop}}(k) \tag{3.87}$$

with

$$\mathrm{P}_{1-\mathrm{loop}}(k) = \frac{1}{2}\int \frac{d^3k'}{(2\pi)^3}\frac{\mathrm{P}_{\mathrm{L}}(k')\,\mathrm{P}_{\mathrm{L}}(k'')}{k'^4k''^4}(\mathbf{k}\cdot\mathbf{k}')^2(\mathbf{k}\cdot\mathbf{k}'')^2\,. \tag{3.88}$$

The following expansion however, is chosen in B14

$$\mathrm{P}_{\mathrm{zel,B14}}(k) \approx \mathrm{P}_{\mathrm{L}}(k) + \frac{\mathrm{P}_{1-\mathrm{loop}}}{1+k^2\sigma_\psi^2}. \tag{3.89}$$

This may lead to enhancement of power on small scales, which is what one would expect from the non-linear power spectrum. Note that there are two free parameters in this approach. There is the time at which the new trajectory is "switched on", z_* and there is the book-keeping parameter, ϵ. In AH15 z_* is chosen to be $z_* = 99$ and $\epsilon = 1$ to match B14's results.

3.5.2 The calculated power spectrum using the CTM

The time dependent functions $A(z)$ and $B(z)$

In the method described in AH15 the trajectory follows the Zel'dovich approximation until some time z_* when the new trajectory is switched on. The time dependent factors using our notation (with t_i being some initial time) would be

$$A(t) = \alpha(t) + \epsilon\omega_0^2\beta(t)\,, \tag{3.90a}$$
$$B(t) = -\epsilon\omega_0^2\gamma(t)\,. \tag{3.90b}$$

with

$$\alpha(t) = 1 + a_i^2\frac{\dot{D}_1(t_i)}{D_1(t_i)}\int_{t_i}^{t}\frac{dt'}{a'^2} = 1 + a_iH(z_i)\frac{D_1'(z_i)}{D_1(z_i)}\int_{z_i}^{z}\frac{dz'}{a'H(z')}, \tag{3.91a}$$

$$\beta(t) = \int_{t'}^{t} \frac{dt''}{a''^2} \int_{t_i}^{t} \frac{dt'}{a'} \frac{D_1(t')}{D_1(t_i)} = \int_{z'}^{z} \frac{dz''}{a''H(z'')} \int_{z_i}^{z} \frac{dz'}{H(z')} \frac{D_1(z')}{D_1(z_i)}, \tag{3.91b}$$

$$\gamma(t) = \int_{t'}^{t} \frac{dt''}{a''^2} \int_{t_i}^{t} \frac{dt'}{a'} \frac{D_1(t')}{D_1(t_i)} \alpha(t') = \int_{z'}^{z} \frac{dz''}{a''H(z'')} \int_{z_i}^{z} \frac{dz'}{H(z')} \frac{D_1(z')}{D_1(z_i)} \alpha(z'). \tag{3.91c}$$

We will calculate an initial power spectrum using CLASS (Lesgourgues, 2011), we will use CLASSYLSS[4] to calculate the linear growth factor and use the code MCFIT[5] to carry out the power spectrum integrals. In the general trajectory equation we will set $z_i = 99$ and $\epsilon = 1$ to match B14 unless stated otherwise.

Re-normalisation

Let us return to the low-k expansion of the expanded power spectrum (3.29). To lowest order the power spectrum should be proportional to $\mathrm{P_L}(k, z)$. Our power spectrum is proportional to

$$\mathrm{P}^A(k, z = 0) = A^2(z = 0)\, \mathrm{P_L}(k, z = z_i) \tag{3.92}$$

therefore to obtain the linear power on large we must re-normalise by $A^{-2}(z = 0) \left(\frac{D_1(z=z_i)}{D_1(z=0)}\right)^2$. In Figure 3.3 the re-normalised B14 dimensionless power spectrum is shown with the linear and Zel'dovich power spectra for different redshifts. One can now see that this method never outperforms the Zel'dovich approximation even at high redshifts. This could be due to the acceleration term causing destruction of structure on small scales. This re-normalisation feels unnatural and in the next Chapter 4 we will seek an expansion that does not require re-normalisation on large.

[4] https://github.com/nickhand/classylss
[5] https://github.com/eelregit/mcfit

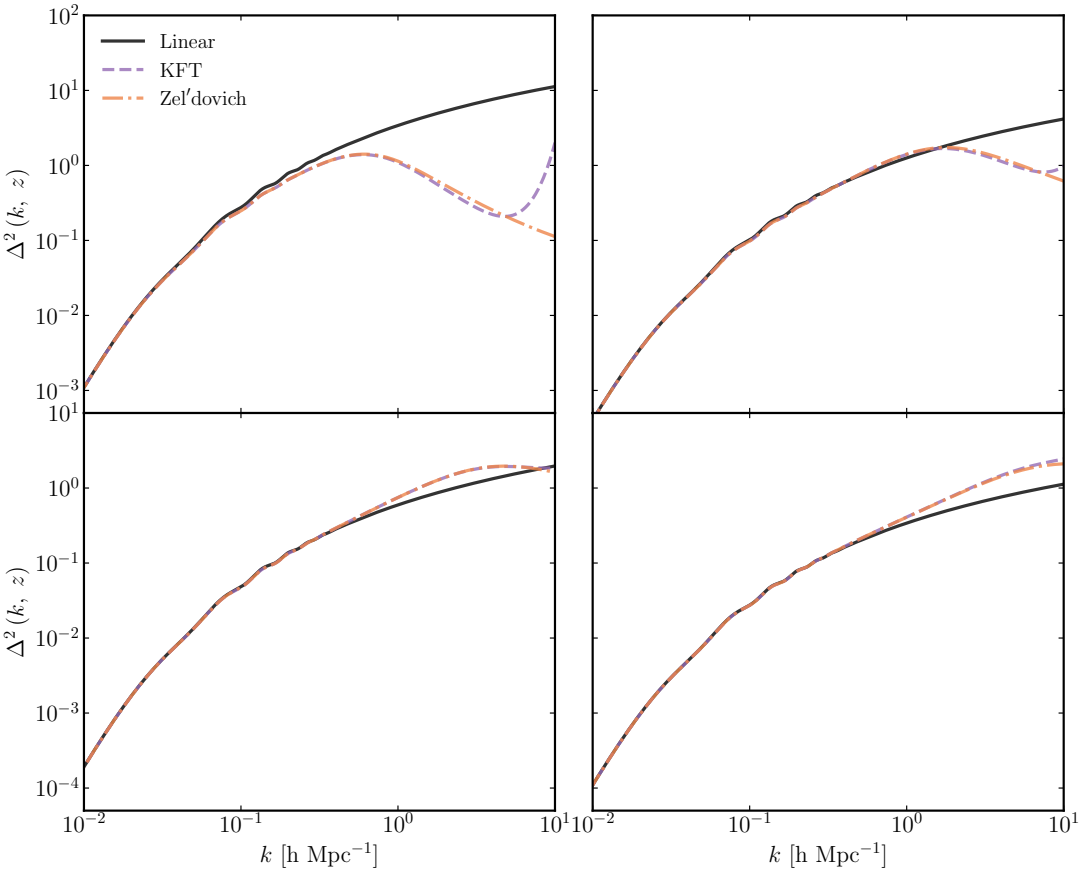

Figure 3.3 *The dimensionless power spectra for linear theory (black solid line), Zel'dovich approximation (orange dash-dashed line) and renormalised KFT (blue dashed line) are shown in this figure for four different redshifts. The upper left panel is the result at $z = 0$, the upper right panel is the result at $z = 1$, the lower left panel is the result at $z = 2$ and the lower right panel is the result at $z = 3$.*

3.6 Conclusions

In this chapter we have revised Lagrangian Perturbation Theory (LPT) and its first-order solution the Zel'dovich approximation. We have seen that this perturbation theory performs better than Eulerian Perturbation Theory (EPT) but still begins to break down after shell crossing occurs. We also introduced a method called Kinetic Field Theory (KFT) which is described in detail in Bartelmann et al. (2014a,b, 2017) and Bartelmann et al. (2019). In these papers field theory techniques are applied to model the interaction of particles in the Universe and it is claimed that this method can model the non-linear regime of the power spectrum more accurately than SPT. We focused on the trajectories re-derivation of this method presented in Ali-Haïmoud (2015). In this re-derivation the equations of motion for point particles are solved and the Zel'dovich approximation is used as the initial condition. The physical picture of this method is that until some time z_* the Zel'dovich approximation describes the motion of particles and then higher-order gravitational effects are "switched on" like in a simulation. As shown in Section 3.5.2 the power spectrum result for this method, although exact, is difficult to compute and requires careful evolution or re-normalisation.

Our goal was to use the trajectories derivation of KFT to obtain an analytical expression for the power spectrum that can be calculated numerically and does not require re-normalisation. This method is called the Cosmological Trajectories Method (CTM). We began by solving the equations of motion of point particles with the Zel'dovich approximation as the initial condition but instead of retaining the gravitational interaction term to full order we expanded it. This resulted in a trajectory that could be generalised to contain two fields: a linear displacement field and a tidal field (3.47) which gives rise to gravitational scattering. This general cosmological trajectory can be related back to the result obtained in Ali-Haïmoud (2015) by choosing the two time dependent functions $A(z)$ and $B(z)$ carefully. There are two main advantages to the CTM: the time dependent functions can be calculated for a range of cosmologies and approximations and the trajectory only contains linear fields evaluated at some initial time.

As the trajectory contains linear fields evaluated at some initial time the power spectrum can be written down as a multivariate Gaussian and an analytical expression can be found as shown in Section 3.4. This full power spectrum cannot be calculated numerically with current computational methods. However

expanding the power spectrum to first-order in the gravitational interaction terms results in a power spectrum that looks similar to the Zel'dovich approximation power spectrum. We applied techniques used to calculate the Zel'dovich power spectrum to calculate the correlation functions for the fields and the expanded power spectrum itself.

In the last section of this chapter we showed that we could apply the CTM to the KFT formalism by choosing the time-dependent functions to be (3.91). The power spectrum calculated is not as exact as the power spectrum calculated in Bartelmann et al. (2019) however it demonstrates that our method can be applied to other approximations. One issue with KFT is that the resulting power spectrum must be multiplied by a normalisation factor in order to obtain linear power on large. This is the motivation for the approximation introduced in Chapter 4. In that chapter we will also investigate the free parameters in the CTM, calculate the power spectrum at different redshifts and present a method to combat the breakdown of methods based on the Zel'dovich approximation on small scales at low redshifts as seen in Figure 3.3.

Chapter 4

The Cosmological Trajectories Method: The Beyond Zel'dovich approximation and its applications in real space

> I am no bird; and no net ensnares me; I am a free human being with an independent will.
>
> *Jane Eyre, Charlotte Brontë*

In Chapter 3 we introduced the Cosmological Trajectories Method (CTM). The power spectrum up to order $\sim \epsilon^2$ was derived for a general trajectory and it was applied to KFT introduced in Bartelmann et al. (2014b) and Ali-Haïmoud (2015). In this chapter we will introduce our approximation, Beyond Zel'dovich, and calculate the power spectrum for a range of redshifts in Sections 4.1 and 4.2. We will also demonstrate how the CTM can be applied to another approximation and compare results for the Beyond Zel'dovich approximation to other methods. Finally, we will explore a higher-order expansion of the power spectrum in Section 4.6.

4.1 The Beyond Zel'dovich approximation

If we assume a Zel'dovich approximation trajectory as the initial trajectory then $A(z) = \frac{D_1(z)}{D_1(z_i)}$ where D_1 is the linear growth factor. Then the time dependent factors are $A(z)$ and $B(z)$ in (3.91) are

$$A(z) = \frac{D_1(z)}{D_1(z_i)} \tag{4.1a}$$

$$B(z) = -\epsilon\omega_0^2\zeta(z) \tag{4.1b}$$

with

$$\zeta(z) = \int_{t'}^{t} \frac{dt''}{a''^2} \int_{t_i}^{t} \frac{dt'}{a'} \left(\frac{D_1(t')}{D_1(t_i)}\right)^2 = \int_{z'}^{z} \frac{dz''}{a''H(z'')} \int_{z_i}^{z} \frac{dz'}{H(z')} \left(\frac{D_1(z')}{D_1(z_i)}\right)^2. \tag{4.2}$$

Motivation behind the Beyond Zel'dovich approximation

In the overview of Chapter 3 the break down of perturbative techniques was discussed. Techniques such as EPT and LPT are single-stream approximations. It is well known that when the overdensity field becomes large ($\delta \gg 1$) these schemes are no longer valid. The point at which streams of matter from different directions intersect (at a node etc.) is called shell-crossing. This is when most perturbative schemes breakdown and are no longer accurate. However, we know that virialised structures (particles that are gravitationally interacting but stable i.e. not expanding or collapsing) in our Universe are formed after shell-crossing occurs. This is why we must improve our theoretical models in order to understand the formation of important virialised structures like dark matter haloes. Although this behaviour is modelled more accurately in N-body simulations the problem does not disappear entirely and caustics (areas of infinite density) can also inhibit the modelling of virialised objects.

Returning to the Zel'dovich approximation it is unique in that in 1D it is exact up until shell-crossing occurs. In 3D it behaves competitively with EPT, higher-order LPT and other methods cited in Section 3.1. It is an intuitive method

for describing how particles form the structures we see in the cosmic web. We therefore hope that the Zel'dovich approximation with the addition of the tidal field will capture the non-linear gravitational effects, such as gravitational interaction, discussed in Section 3.1. The acceleration term that should be included exaggerates the destruction that occurs at shell-crossing. The choice of time dependence in the Beyond Zel'dovich approximation will also allow us to recover the linear power spectrum on large-scales, remove the need for re-normalisation and remove the destructive effect of the acceleration term.

4.2 Calculating the Beyond Zel'dovich power spectrum at different redshifts and investigating the free parameters

In this section all power spectra shown are calculated using *Planck18* (Collaboration et al., 2018) cosmology ($\Omega_m = 0.3123,\ h = 0.6737,\ n_s = 0.9665$ and $\sigma_8 = 0.8102$) and with $z_i = 99$ unless stated otherwise. The CTM power spectrum code is run summing over 32 spherical Bessel functions and the initial power spectrum is computed using CLASS as described in Section 3.5.2. The numerical code used to compute the power spectrum has been tested for convergence extensively and we will use 5000 k-values with minimum and maximum k-values of 10^{-5} and 10 h Mpc^{-1}. We found that a sparser sampling of k-values resulted in the power spectrum not converging but more than 5000 values did not provide any improvement. Due to the highly oscillatory nature of the integrals computed any results obtained above $k = 0.9$ h Mpc^{-1} will be ignored as they are not reliable at low redshifts. We will compute the Beyond Zel'dovich power spectrum for a range of redshifts and ϵ values in order to establish the applicability of the method.

4.2.1 Different ϵ values

In the definition of a general cosmological trajectory in (3.47) there is an expansion parameter ϵ. This parameter controls the size of the higher-order gravitational terms. If one considers ϵ as a mathematical perturbative parameter then by definition it should be small ($\epsilon \ll 1$). This parameter can also be interpreted in a physical sense as controlling the size of the gradient of the gravitational potential

or in other words how large the over and under densities are. This parameter is therefore controlling how large the non-linear structures being modelled are. We would expect that larger ϵ values will increase the impact the higher-order gravitational terms have on non-linear structure formation.

In Figure 4.1 the dimensionless Beyond Zel'dovich power spectrum is shown for redshifts $z = 0,\ 1,\ 2,\ 3,\ 4$ and 5 and three ϵ values $\epsilon = 0.01,\ 0.1$ and 1. The calculated power spectra are compared to results obtained from the EUCLID EMULATOR[1] (Euclid Collaboration et al., 2019). In Euclid Collaboration et al. (2019) the emulator is found to be $\sim 1\%$ accurate compared to simulations up to $k = 6$ h Mpc^{-1} at $z = 0$ and $\sim 1\%$ up to $k = 1$ h Mpc^{-1} at $z = 1$. Above $z = 1$ it is around $\sim 3\%$ accurate. The first row shows the results with $\epsilon = 1$, the middle row shows $\epsilon = 0.1$ and the bottom row is with $\epsilon = 0.01$. As expected the lower the ϵ value the smaller the effect of the tidal term and at high redshifts the Beyond Zel'dovich result converges to the Zel'dovich result. This is evidence that the method and the numerics are robust.

One very noticeable feature is that for high ϵ values and at low redshifts there is excessive damping of the power spectrum. This indicates that this feature is a wave of destruction caused by the breaking down of the Zel'dovich approximation. On small-scales at low redshifts it is well known that the Zel'dovich approximation breaks down due to shell crossing and other destructive non-linear small-scale effects (discussed above in 4.1 and Vlah et al. (2015a)). These non-linear effects are damped down by the smaller ϵ values but appear to be amplified by the larger ϵ values at low redshifts. We also encounter numerical issues with large ϵ values at low redshifts due to the size of the higher-order gravitational term.

Although the Beyond Zel'dovich method performs poorly on small-scales at low redshifts for $\epsilon = 1$ there is no improvement over the Zel'dovich approximation at high redshifts for smaller values. We want the non-destructive non-linear gravitational effects, which will hopefully lead to more power on small-scales, to still be present. Choosing a value of $\epsilon = 1$ allows one to obtain the maximum effect of the non-linear gravitational terms on structure formation at high redshifts. At $z = 4$ and $z = 5$ the Beyond Zel'dovich approximation with $\epsilon = 1$ outperforms the Zel'dovich approximation and the emulator at $z = 5$. This is more motivation that the choice of $\epsilon = 1$ will produce the best results.

Finally, the breakdown of the Beyond Zel'dovich method at low redshifts could

[1] https://github.com/miknab/EuclidEmulator/wiki/III)-Usage

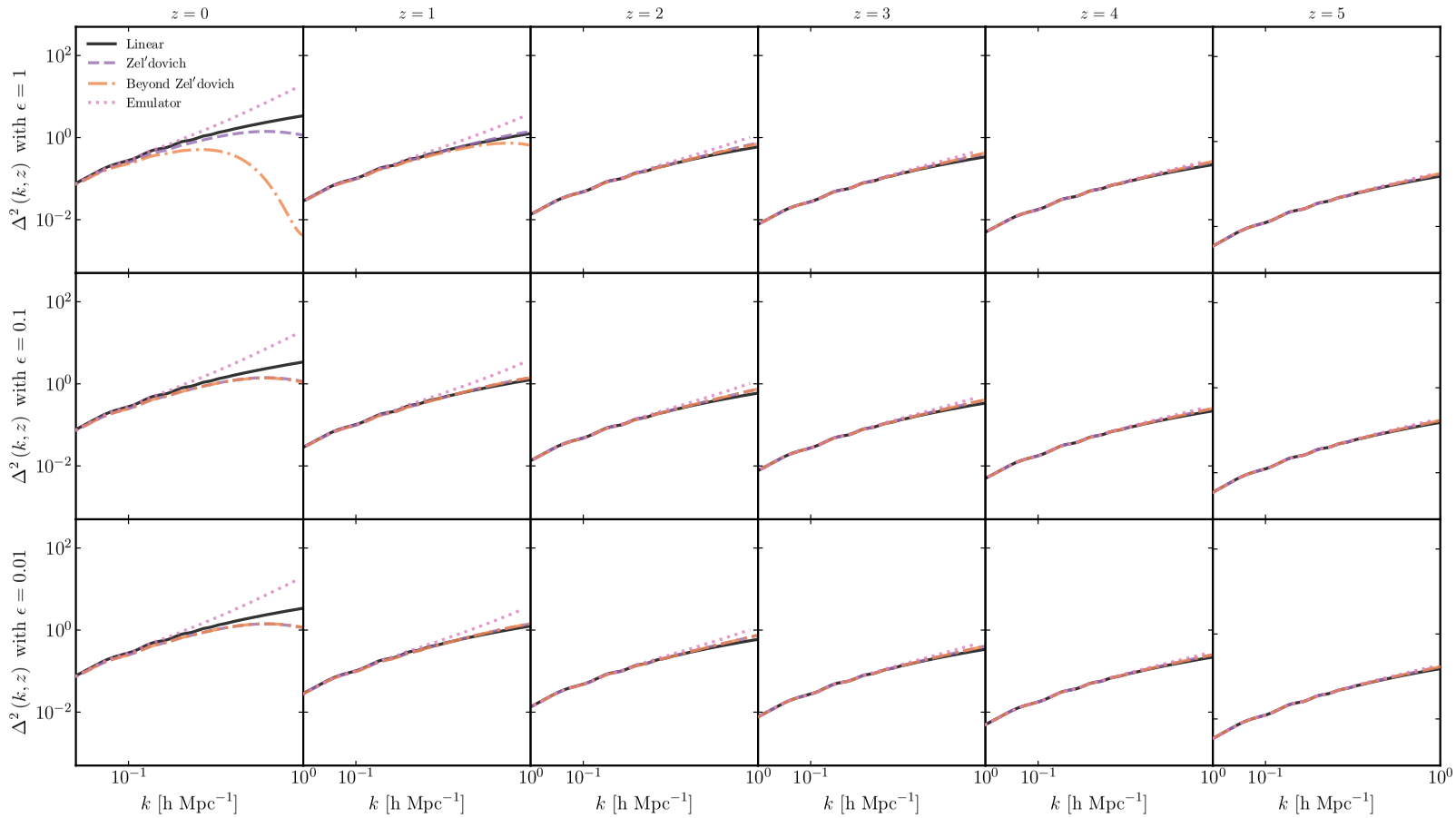

Figure 4.1 *In this figure the power spectrum in Equation (3.79) is shown calculated for the Beyond Zel'dovich time dependence with different ϵ values. The black solid lines show the linear power spectrum obtained from* CLASS*, the purple dashed lines show the computed Zel'dovich power spectrum, the orange dashed-dot lines show the Beyond Zel'dovich power spectrum and the pink dotted lines are the results from the emulator described above.*

suggest that the method is not applicable in that regime. This method is a first-order gravitational extension of the Zel'dovich approximation which as we have discussed performs very well at high redshifts before shell-crossing. Pushing the Beyond Zel'dovich method to $z = 0$ may have been optimistic. Our main goal now is to use the tidal part of our trajectory to improve structure formation on small-scales at redshifts $z = 2$ and above. In Section 4.3 we investigate introducing a cutoff to reduce the impact of the small-scale breakdown of the Zel'dovich approximation in this redshift range.

4.2.2 Different z_i values

There is another free parameter in the CTM, the initial redshift z_i. This parameter is generally set to be $z_i = 100$ throughout this thesis in order to match the results obtained in Bartelmann et al. (2014a) and Ali-Haïmoud (2015). In AH15 it was suggested that a value of $z_i = 10$ had also been used to obtain results in B14.

In Figure 4.2 the dimensionless linear power spectra (solid black line) and the dimensionless Beyond Zel'dovich power spectrum with $\epsilon = 1$ and three initial redshifts $z_i = 150$ (blue dotted line), $z_i = 100$ (orange dashed-dot line) and $z_i = 50$ (purple dashed line) are plotted. There are again six redshifts ($z = 0, 1, 2, 3, 4$ and 5) shown with the upper left panel being $z = 0$ and the bottom right panel is $z = 5$. The choice of $z_i = 50$ is an extreme one to demonstrate that the choice of initial redshift can have an effect on the power spectrum calculated. The initial redshift is the point at which the time dependence, i.e. the growth function, is integrated from. An approach similar to that taken by those running cosmological simulations should be adopted and a suitably large initial redshift should be chosen. We will hence continue to use the value of $z_i = 100$.

4.3 Calculating a Gaussian damped Beyond Zel'dovich power spectrum at different redshifts

As discussed in Section 4.2.1 the breakdown of the Beyond Zel'dovich approximation on small-scales creates a wave of destruction that affects scales of between

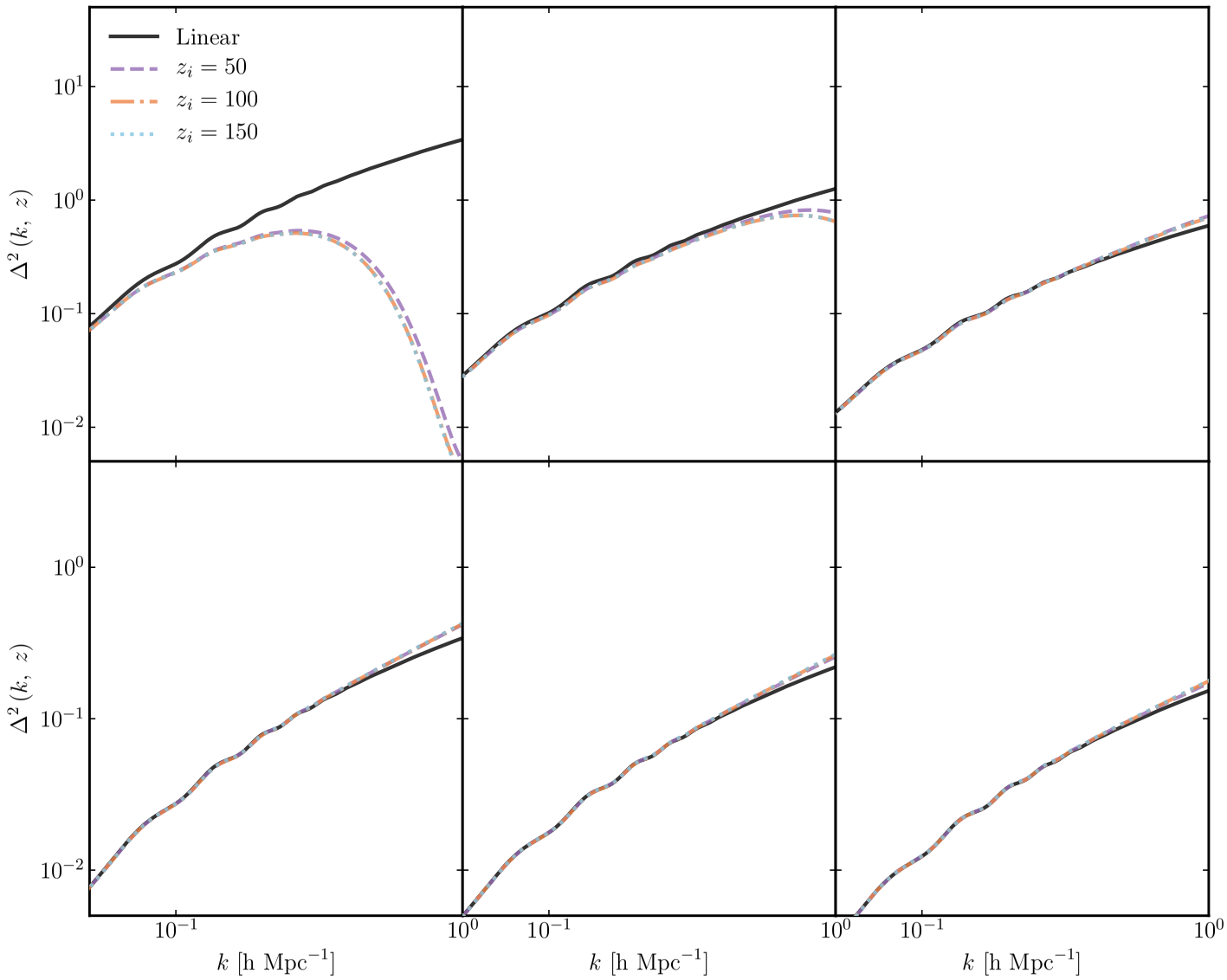

Figure 4.2 *The solid black line is the dimensionless linear power spectrum. The purple, orange and blue lines are the Beyond Zel'dovich power spectra with* $\epsilon = 1$ *and with* $z_i = 50, 100$ *and* 150 *respectively. The top panels from left to right are* $z = 0, 1, 2$ *and the bottom panels from left to right are* $z = 3, 4, 5$.

$k = 0.01$ h Mpc^{-1} and $k = 0.5$ h Mpc^{-1} at low redshifts. In order to combat this effect on small-scales we will introduce a Gaussian cutoff in the initial power spectrum. This will stop scales below a cutoff value, k_c , affecting larger scales. The damped Beyond Zel'dovich initial power spectrum is

$$\mathrm{P}_{\mathrm{damped}}\left(k, z_i\right) = \mathrm{e}^{-\left(\frac{k}{k_c}\right)^2} \mathrm{P}_{\mathrm{lin}}\left(k, z_i\right). \tag{4.3}$$

In Figure 4.3 the effect of different cutoff values ($k_c = 50,\ 5$ and 0.5 h Mpc^{-1}) is shown for redshifts $z = 0,\ 1,\ 2,\ 3,\ 4$ and 5 and three ϵ values ($\epsilon = 1$, 0.1 and 0.01). The smaller ϵ values in combination with a damped initial power spectrum more effectively removes the wave behaviour from all redshifts compared to $\epsilon = 1$. However, the non-linear behaviour we wish to capture is also removed and we do not match or beat the emulator at any redshift.

Focusing on the value of $\epsilon = 1$, a cutoff value of $k_c = 50$ h Mpc^{-1} does not damp down any of the wave-like behaviour until around redshift $z = 3$. On the other hand a value of $k_c = 0.5$ h Mpc^{-1} is too stringent a cutoff. It works very well at low redshifts removing all signatures of the breakdown on small-scales but at high redshifts it fails to capture even the linear power on mid-scales. These two extreme cutoff values can be summarised with 50 h Mpc^{-1} being too large a scale to remove the effects and 0.5 h Mpc^{-1} being too small a scale and removing all information from the small scales at high redshifts.

The main conclusion to be drawn from Figure 4.3 is that $k_c = 5$ h Mpc^{-1} is a suitable cutoff value when combined with $\epsilon = 1$. The small-scale information is not completely erased at high redshifts but the destructive behaviour is damped down effectively at all redshifts. This cutoff is also motivated physically as it corresponds to galaxy cluster scales which is when most perturbative schemes, including the Zel'dovich approximation, will breakdown at the redshifts we are interested in.

Now that we have settled on the value of $\epsilon = 1$ for the Beyond Zel'dovich trajectory in the redshift range we are focusing on we should investigate a wider range of k_c values of order 5 h Mpc^{-1}. In Figure 4.4 the difference between the dimensionless calculated Beyond Zel'dovich power spectra and the Euclid

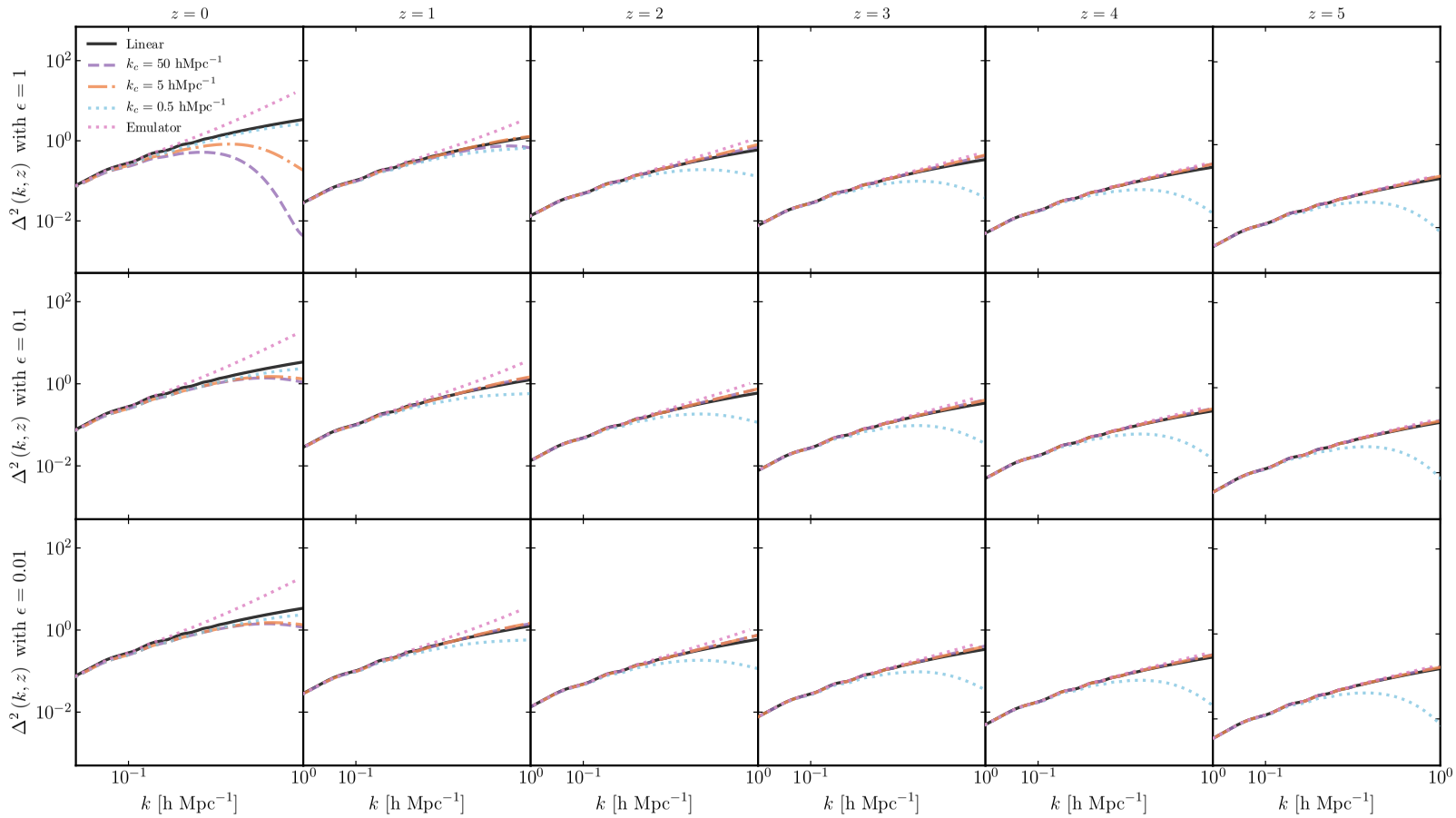

Figure 4.3 *Damped dimensionless Beyond Zel'dovich for three different k_c values: $k_c = 50$ h Mpc^{-1} is shown by the purple dashed lines, $k_c = 5$ h Mpc^{-1} is shown by the orange dashed-dot lines and $k_c = 0.5$ h Mpc^{-1} is shown by the blue dotted lines. The purple dashed line shows the emulator results for six redshifts and three ϵ values $\epsilon = 1, 0.1$ and 0.01 in the top, middle and lower rows respectively.*

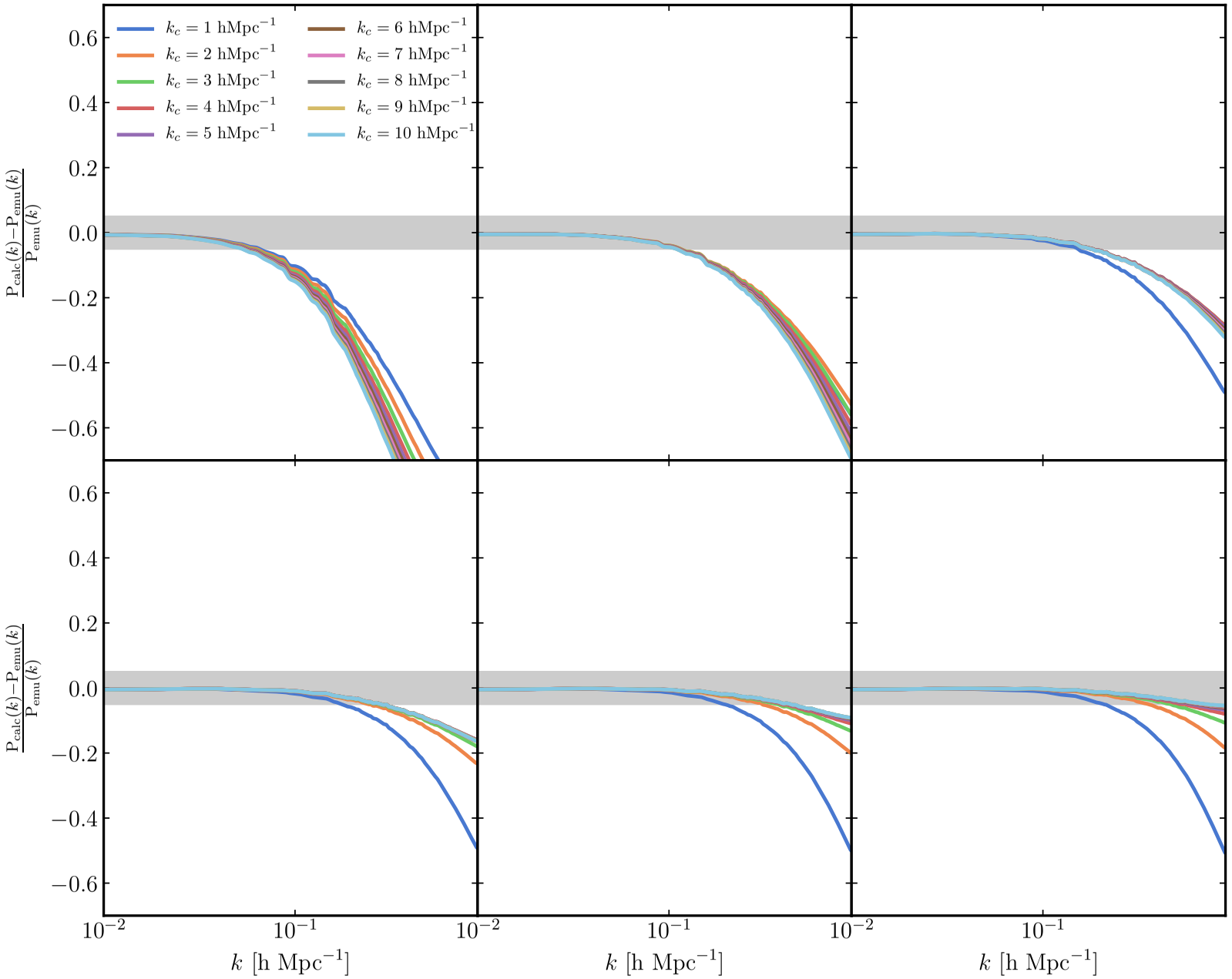

Figure 4.4 *Difference between the damped dimensionless Beyond Zel'dovich power spectra and the emulator results for a range of* $k_c = 1 - 10$ h Mpc^{-1} *with* $\epsilon = 1$. *The grey shaded area is* $\Delta^2_{\text{diff}} = \pm 0.05$ *and the six panels are* $z = 0$ *(upper left) through to* $z = 5$ *(lower right).*

EMULATOR results are shown. The difference is defined as

$$\Delta^2_{\text{diff}} = \frac{\Delta^2_{\text{calculated}} - \Delta^2_{\text{emu}}}{\Delta^2_{\text{emu}}} \tag{4.4}$$

this will be described as the percentage difference throughout the rest of this thesis. The grey band shown in Figure 4.4 is $\Delta^2_{\text{diff}} = \pm 0.05$ and the panels are the redshifts $z = 0,\ 1,\ 2,\ 3,\ 4$ and 5 with the upper left panel being $z = 0$ and the lower right panel being $z = 5$. The values of k_c lower than 6 h Mpc^{-1} have an improving effect at redshifts lower than $z = 2$ but a detrimental effect on higher redshifts. Any value of k_c above 6 h Mpc^{-1} performs as well as another.

This is demonstrated more clearly in Figure 4.5 where the range of k_c values are plotted versus the maximum k-value, k_{max}, reached before the percentage difference between the damped Beyond Zel'dovich power spectrum and the emulator result drops below 5%. It can be seen in this figure that for cutoff values of $k_c < 4$ h Mpc^{-1} the maximum k-value reached at redshifts $z = 4$ and 5 is lower. This indicates that these cutoff values are too powerful and we are erasing too much structure on these scales. For values of $k_c > 4$ h Mpc^{-1} there is very little improvement between different cutoff values at the high redshifts. Therefore we will choose $k_c = 6$ h Mpc^{-1} for maximum effect at all redshifts.

In later sections power spectra that are labelled as Beyond Zel'dovich are computed using the initial power spectrum defined in (4.3). The cutoff value chosen is $k_c = 6$ h Mpc^{-1} and the value of ϵ is 1. Figure 4.6 shows the percentage difference between the Beyond Zel'dovich power spectra and the emulator results in solid lines for different redshifts. The percentage difference between Zel'dovich approximation power spectra computed with the same damped initial power spectrum is also shown in dashed lines for comparison. The Beyond Zel'dovich approximation outperforms the Zel'dovich approximation after about $z = 2$.

Lyman-α forest- an application for Beyond Zel'dovich

The intergalactic medium (IGM) can be defined as "anything outside of the virial radius of galaxies and clusters" as in the review McQuinn (2016). Observations of the IGM can be used to probe cosmological parameters, structure formation and the epoch of reionisation. Between the redshifts of $z = 2$ and $z = 5$ hydrogen

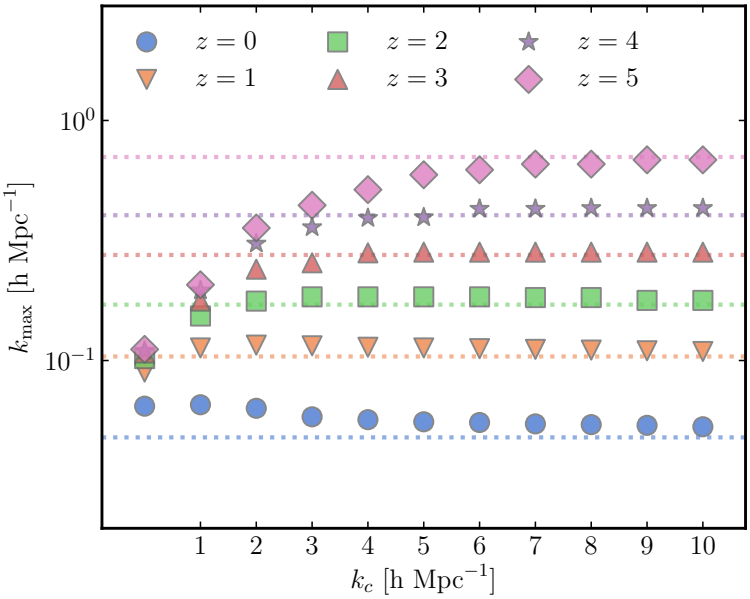

Figure 4.5 *Figure showing cutoff values $k_c = 1 - 10$ h Mpc^{-1} versus the maximum k-value, $k_{\max}$, reached before the percentage difference between the Beyond Zel'dovich power spectra drop below the emulator results. The dotted horizontal lines show the maximum k-value reached by the undamped Beyond Zel'dovich power spectrum at that redshift.*

emission and absorption lines called Lyman-α can be observed using ground based telescopes. These Lyman-α lines are most commonly seen in the spectra of distant quasars. Quasars are Active Galactic Nuclei (AGN), when material from the galactic disk falls towards the supermassive blackhole at the centre of the galaxy it increases in temperature emitting electromagnetic waves allowing us to observe these high redshift objects. This environment allows a Lyman-α transition to occur in the hydrogen. This means that an electron is demoted from the $n = 2$ state to the $n = 1$ state producing a photon. The Lyman-α emission line occurs at $\lambda = 1216$Å under laboratory conditions. Our Universe is expanding resulting in the redshifting of this emission line. Not only is the Lyman-α emission line from the quasar being redshifted but the photons that are travelling towards us are passing through clouds of neutral gas in the IGM. The photons ionize the neutral gas allowing an electron to jump from the $n = 1$ to the $n = 2$ state. Hence, a Lyman-α absorption line is shifted blueward of Lyman-α emission line due to redshifting. The subsequent redshifting and intersection of photons with neutral gas produces the Lyman-α forest.

Observations of the Lyman-α forest can tell us about the underlying density field of the Universe and therefore dark matter and structure formation in the

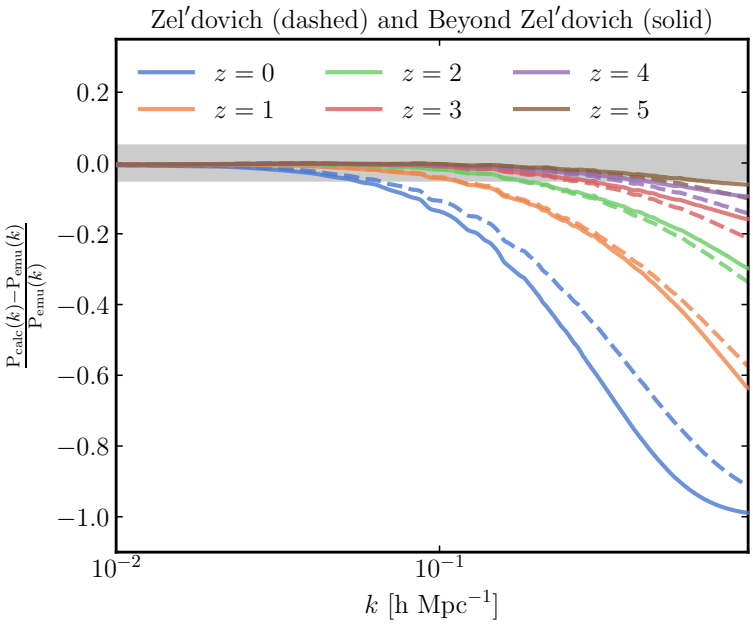

Figure 4.6 *Zoomed in plot of the percentage difference between the damped Beyond Zel'dovich power spectra with* $k_c = 6$ h Mpc^{-1} *and* $\epsilon = 1$ *and the emulator results. These are shown in the solid lines with each colour representing a different redshift. The dashed lines are the percentage differences between the damped Zel'dovich approximation power spectra with* $k_c = 6$ h Mpc^{-1} *and the emulator results. The grey shaded region is again* $\Delta^2_{\text{diff}} = \pm 0.05$.

Universe. The regime in which we observe the Lyman-α forest is also quasi-linear allowing for application of perturbative schemes and accurate simulations. The redshifting of the Lyman-α lines is related to the expansion of the Universe which can provide more observational constraints on dark energy models. As our telescopes improve we are able to gather more high redshift observations of Lyman-α emitters. These observations could therefore be an invaluable tool in cosmology. We refer the reader to the following articles as examples of how Lyman-α can be used in cosmology: Weinberg (2003), Viel et al. (2004), Croft (2004), Viel et al. (2005), Viel (2005), Seljak et al. (2005b), Zaroubi et al. (2006), Meiksin (2009), Bird et al. (2012), Font-Ribera & SDSS-III Collaboration (2015) and Brax & Valageas (2019).

As the Beyond Zel'dovich approximation outperforms the emulator for redshifts in the range $z = 4 - 5$ and the Zel'dovich approximation for redshifts in the range $z = 1 - 5$ it could be used in conjunction with Lyman-α observations to constrain cosmological parameters and modified gravity models among other new physics. Although hydrodynamical simulations can compute the matter power spectrum to high accuracy at these redshifts as it lies within the mildly non-linear range. The requirement of running a new simulation for every cosmological, modified gravity or dark matter model one wishes to test is still present and is even greater as hydrodynamical simulations are more expensive than N-body simulations. As Lyman-α observations could detect the presence of new physics (like modified gravity) and non-cold dark matter (hot dark matter). The flexibility of the CTM could provide a viable alternative to simulations in this redshift range.

4.3.1 Testing the dependence of k_c on cosmology

One concern with the Gaussian damped initial power spectrum is that it may give very different results for different cosmologies. An advantage of the CTM is that it is easily applied to any flat cosmological model. If the initial linear power spectrum can be computed accurately and it has no non-standard components e.g. modified gravity, dynamical dark energy then the CTM can be applied. The method could be extended to include physics like modified gravity and dynamical dark energy.

We have tested the dependence of the maximum k-value, $k_{\max}$, one can reach using two cosmologies when the damped initial power spectrum is used. The results from this test are shown in Figure 4.7. The alternate Beyond Zel'dovich

power spectra computed to produce this figure have the same h, σ_8, w and n_s as the *Planck18* cosmology but the Ω_m value has been changed slightly. The cutoff value for both cosmologies is $k_c = 6$ h Mpc^{-1}. In *Planck18* $\Omega_m = 0.3123$ and in the alternate cosmology $\Omega_m = 0.3365$. The lower panel shows the fractional difference between the $k_{\max}$ values at each redshift.

There is a difference between the results for all redshifts, indicating that there is a weak dependence on the cosmological chosen and redshift. As we are only considering *Planck18* cosmology in this thesis we will leave the full investigation of this dependence to future work when applying the CTM to modified gravity theories, for example. One caveat is that the EUCLID EMULATOR does not allow for a wide enough range of values of Ω_m to see whether there would be a larger difference for a larger difference between the Ω_m values. A future test would be to obtain N-body results for the range of redshifts we are interested in for a wide range of cosmologies.

4.4 An alternative time dependence example

In this section, we will demonstrate the applicability of the CTM to other approximations. As well as the Beyond Zel'dovich approximation we also explored a time dependence based on second-order Lagrangian Perturbation Theory (2LPT). For a review of 2LPT see Section 3.2. The time dependence ansatz for this approximation is

$$A(z) = \frac{D_1(z)}{D_1(z_i)} \tag{4.5a}$$

$$B(z) = -\epsilon\omega_0^2 \left(\frac{D_1(z)}{D_1(z_i)}\right)^2 . \tag{4.5b}$$

We will refer to this approximation as LPT-like. Second-order Lagrangian Perturbation Theory outperforms second-order Eulerian Perturbation Theory. The higher-order gravitational terms having a time dependence proportional to the second-order terms in 2LPT could result in us capturing non-linear growth and it may perform better than Beyond Zel'dovich. A drawback of this approximation is that the time dependent function, $B(z)$, is very large. This causes issues numerically and the largest ϵ value one can choose is $\epsilon = 10^{-4}$.

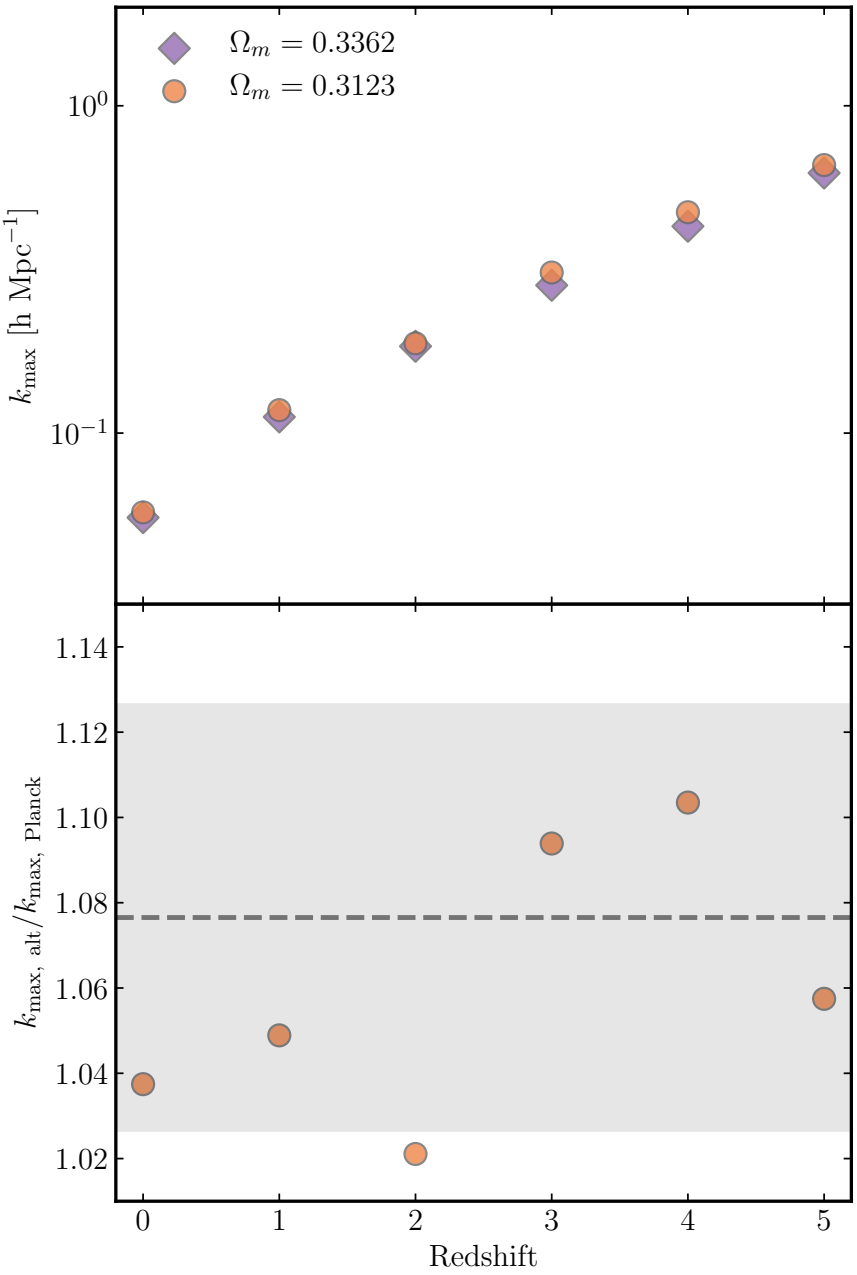

Figure 4.7 *The top panel shows the maximum k-value before the percentage difference between Beyond Zel'dovich power spectra and the emulator results drop below 5% at six different redshifts. The orange circles are the results using Planck18 and the purple diamonds are computed using the same cosmology with a different* Ω_m *value. The lower panel shows the ratio between the* $k_{\max}$ *values for the two cosmologies with the grey shaded region between the ratio between the two* Ω_m *values* ±5%.

In Figure 4.8 the percentage difference between the LPT-like (with $\epsilon = 10^{-4}$) and Beyond Zel'dovich power spectra (with $\epsilon = 1$) and the emulator results is shown. The right-hand panel of Figure 4.8 shows the percentage difference between the damped LPT-like and Beyond Zel'dovich power spectra both with $k_c = 6$ h Mpc^{-1} and the emulator. The damped LPT-like time approximation beats the Beyond Zel'dovich approximation up until $z = 2$.

As LPT-like time dependence does not outperform the emulator for as many redshifts as Beyond Zel'dovich we will not pursue it any further. However, we have demonstrated how easily the CTM can be applied to other approximations. Another example of an alternative time dependence would be any modified gravity model that does not have a screening mechanism.

4.5 Comparing Beyond Zel'dovich to other methods

In this section we will compare the Beyond Zel'dovich approximation calculated with $\epsilon = 1$ and $k_c = 6$ h Mpc^{-1} to other methods. In Section 2.4.1 the correlation function was introduced as being the inverse Fourier transform of the power spectrum. The BAO peak appears in the correlation function as a bump at around 100 Mpch^{-1}. This feature has been used to constrain the Λ-CDM model (see Section 1.3.4). In particular, the acoustic scale is used as a standard ruler and can therefore tell us about dark energy. If this scale is not as expected then it could be evidence of new physics or that our perturbative methods are under-performing.

As the BAO feature appears at around $r = 100$ h^{-1}Mpc one would expect perturbative methods to capture it well. A scale of this size corresponds to $k \sim 0.01$ h Mpc^{-1} which lies in the mildly non-linear regime. However as demonstrated in Figure 4.11 linear theory and even Standard Perturbation Theory (SPT) with 1-loop fails to capture the BAO peak. In linear theory and SPT it is assumed that the early universe imprint of the BAO remains the same spatially but increases in amplitude overtime. This is not the true picture as the BAO peak does evolve spatially resulting in it appearing smeared. This is because bulk flows as well as gravitational instability, which are non-linear effects, change the spatial shape of the imprint.

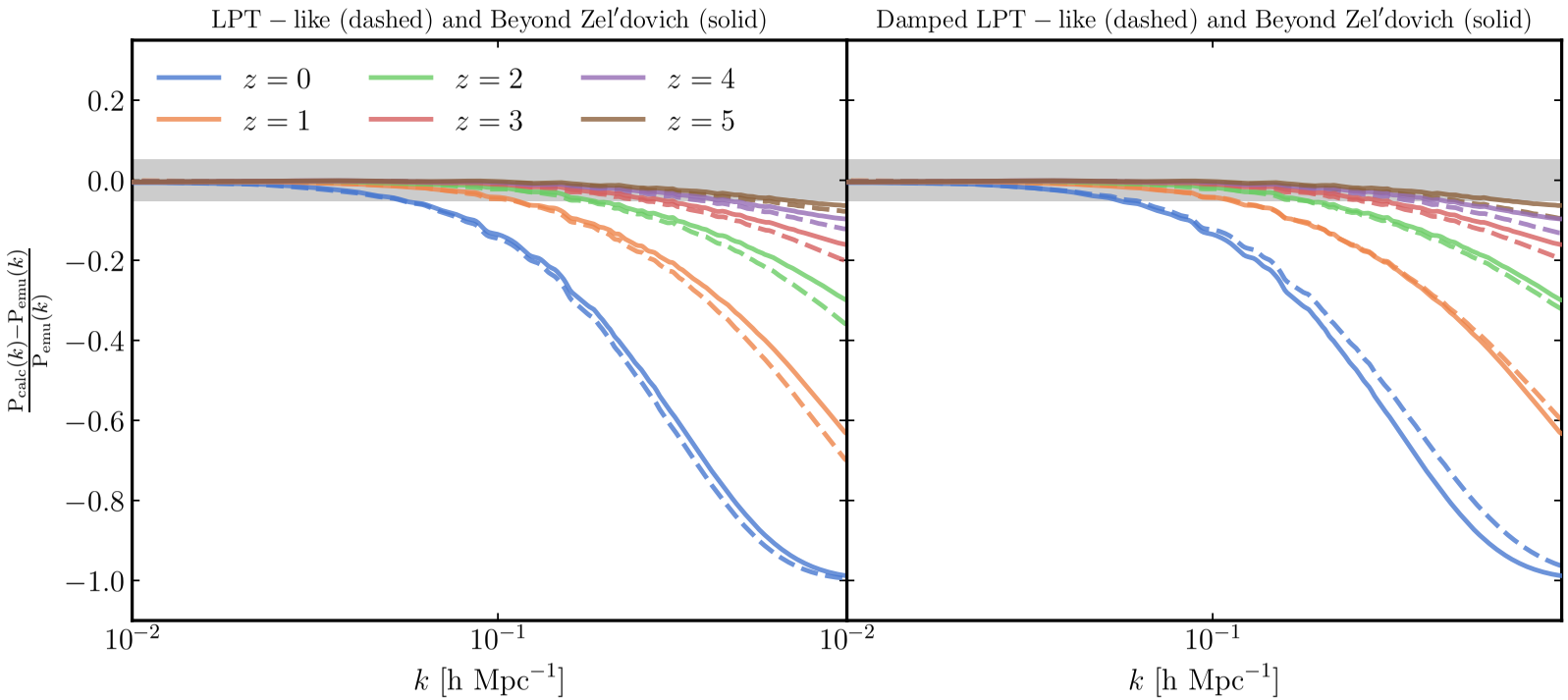

Figure 4.8 *The left-hand panel shows the percentage difference between the LPT-like dimensionless power spectra with* $\epsilon = 10^{-4}$ *(solid lines) and the Beyond Zel'dovich power spectra with* $\epsilon = 1$ *(dashed lines) and the emulator results. The right-hand panel shows the same as the left-hand but both approximations have been calculated with a damped initial power spectrum with* $k_c = 6$ h Mpc^{-1}.

Accurately modelling the BAO feature in the correlation function is as important as modelling the power spectrum in the non-linear regime. Although N-body simulations can capture the non-linear smearing of the BAO peak a theoretical model that does not require large computing power and is more malleable would be desirable. LPT can reconstruct the BAO feature more accurately than SPT for the same reasons LPT can model the power spectrum on small-scales more accurately. A wide range of methods are available based on LPT and commonly involve the IR-resummation of LPT to capture the non-linear BAO features have been proposed. These resummation schemes aim to capture the coupling between short and long wavelength modes (how the perturbations behave over short and long distances). We will compare our method to one such scheme Convolved Lagrangian Perturbation Theory (CLPT) in Section 4.5.2. Some other notable works are Eisenstein et al. (2007b,a), Crocce & Scoccimarro (2008), Baldauf et al. (2015a) and Blas et al. (2015).

The correlation function, $\xi(r)$, is shown in Figure 4.9 scaled by r^2 for linear theory (solid black line), the Zel'dovich approximation (orange dashed line), the Beyond Zel'dovich approximation (blue dashed-dot line) and the emulator (purple squares points) for four redshifts $z = 0,\ 1,\ 2$ and 3. Again the top left panel is $z = 0$ and the lower right panel is $z = 3$. At high redshifts there is no noticeable difference between the methods. This is to be expected as the non-linear effects that cause the smearing of the BAO feature will not be large enough to have an effect. From redshift $z = 2$ the mismatch between linear theory and the emulator results can be seen. The smearing of the BAO peak is captured by the emulator, Zel'dovich approximation and the Beyond Zel'dovich approximation. This is promising news as it is more evidence that the Beyond Zel'dovich approximation has inherited the good features of the Zel'dovich approximation. However, for scales $r = 5\ \mathrm{h}^{-1}$Mpc the small-scale breakdown of both the Zel'dovich and Beyond Zel'dovich approximations takes effect and causes a mismatch with the emulator results.

4.5.1 SPT 1-loop

Recall that, the 1-loop correction to SPT is given by

$$\mathrm{P}_{1-\mathrm{loop}}(k, z) = \mathrm{P}_{\mathrm{L}}(k, z) + \mathrm{P}_{22}(k, z) + 2\mathrm{P}_{13}(k, z) \tag{4.6}$$

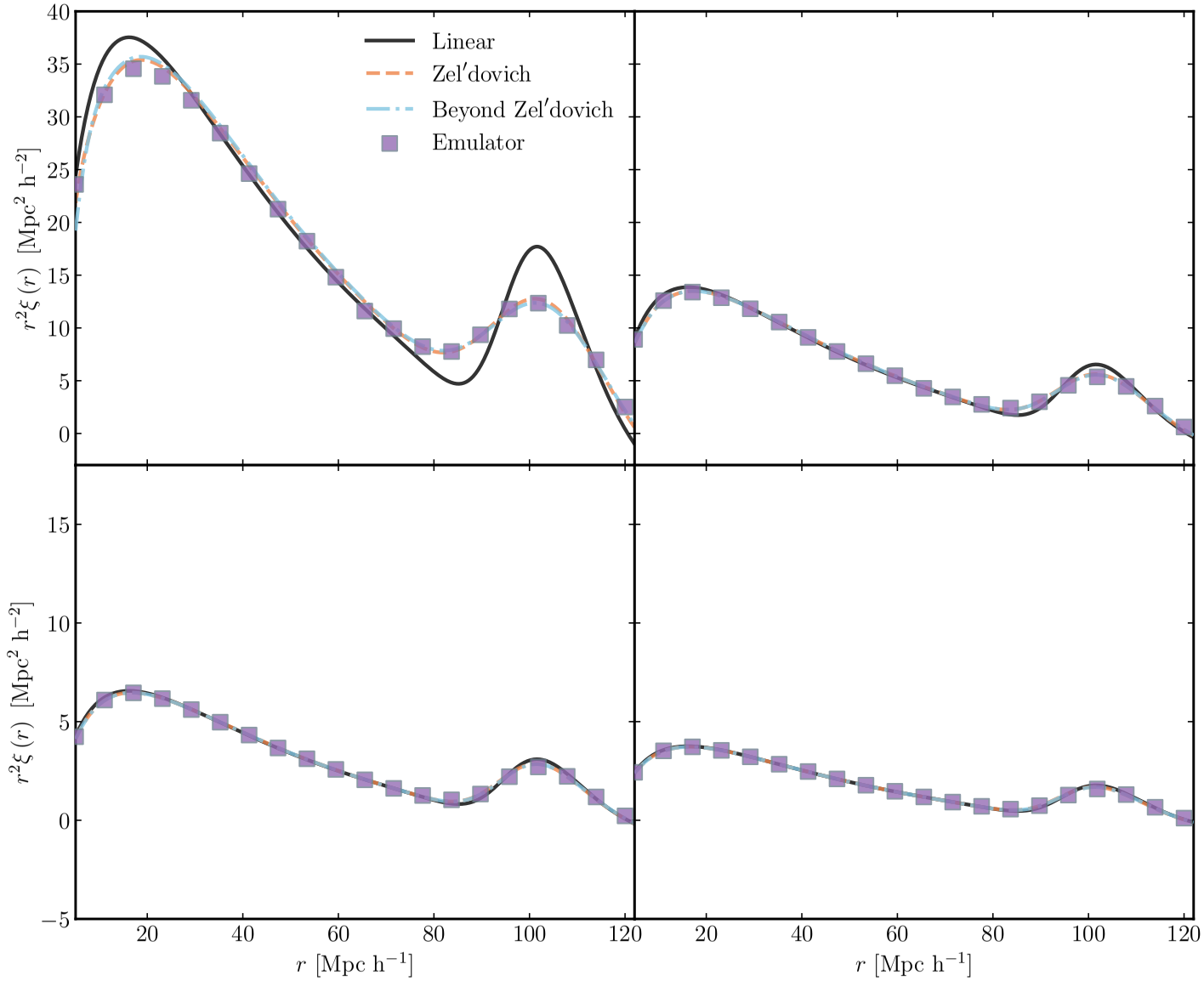

Figure 4.9 *The correlation function, $\xi(r)$, scaled by r^2 for the linear theory (black solid line), Zel'dovich approximation (orange dashed line), damped Beyond Zel'dovich with $k_c = 6$ h Mpc^{-1} (blue dashed-dot) and the emulator in purple squares. The four panels are redshifts $z = 0,\ 1,\ 2$ and 3 with the upper left panel being $z = 0$ and the lower right panel being $z = 3$.*

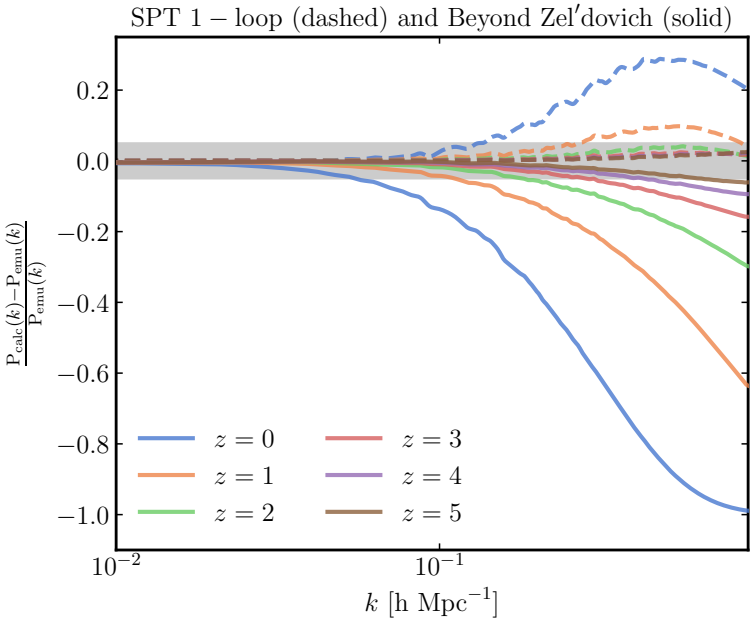

Figure 4.10 *Figure showing the percentage difference between SPT-1 loop and emulator power spectra in dashed lines and the percentage difference between the Beyond Zel'dovich and emulator power spectra in solid lines for $z = 0,\ 1,\ 2,\ 3,\ 4$ and 5. The grey band is $\Delta^2_{\rm diff} = \pm 0.05$.*

where

$$\mathrm{P}_{22}\left(k,z\right) = 2\int d^3q\ \mathrm{P}_{\mathrm{L}}\left(q\right)\mathrm{P}_{\mathrm{L}}\left(|\mathrm{k}-\mathrm{q}|\right)\left[F_2^{(s)}\left(\mathbf{q},\mathbf{k}-\mathbf{q}\right)\right]^2, \tag{4.7}$$

$$\mathrm{P}_{13}\left(k,z\right) = 3\mathrm{P}_{\mathrm{L}}\left(k\right)\int d^3q\ \mathrm{P}_{\mathrm{L}}\left(q\right)F_3^{(s)}\left(\mathbf{q},-\mathbf{q},\mathbf{k}\right). \tag{4.8}$$

The kernels $F_3^{(s)}$ and $F_2^{(s)}$ are given in Equation (2.60). In this Section the 1-loop SPT power spectrum has been calculated again using *Planck18* cosmology. The 1-loop integrals (4.7) were calculated using FAST-PT [2] using Fast Fourier Transforms (FFTs). For more details on the code and method please see McEwen et al. (2016a) and Fang et al. (2017).

In Figure 4.10 the percentage difference between the SPT 1-loop (dashed lines) and the Beyond Zel'dovich approximation (solid lines) power spectra and the emulator results are shown for the six redshifts $z = 0$ through to $z = 5$. The SPT 1-loop outperforms the Beyond Zel'dovich approximation at all redshifts. These are the redshifts in which there is a boost of power on small scales. This

[2] https://github.com/JoeMcEwen/FAST-PT

is due to the loop corrections becoming very small at large redshifts and the 1-loop SPT converges to linear SPT. The results obtained qualitatively match those from McEwen et al. (2016a) but there is no explicit quotation of how accurate FAST-PT is compared to the emulator. Therefore we cannot comment on its performance in more depth.

The correlation functions for linear theory (black line), SPT 1-loop (orange dashed line), Beyond Zel'dovich (blue dashed dot) and the emulator (purple squares) are shown in Figure 4.11. Again the six panels are the redshifts $z = 0$ through to $z = 5$. As we observed in Figure 4.9 the correlation functions lie on top of one another at high redshifts. At the present day a clear mismatch between 1-loop SPT and the emulator results is present. As explained in Section 4.5 SPT fails to capture the linear spatial evolution of the BAO peak that is caused by bulk flows and gravitational interaction. Although 1-loop SPT matches the emulator power spectrum on small-scales more consistently than the Beyond Zel'dovich approximation it does not model the BAO peak well. This demonstrates that our method incorporates gravitational instability at BAO scales more effectively than SPT 1-loop.

4.5.2 CLPT

In Carlson et al. (2013) and Wang et al. (2014) a method called Convolution Lagrangian Perturbation Theory (CLPT) was proposed. CLPT is an extension of the resummation scheme from Matsubara (2008a) and Matsubara (2008b) and to lowest order the Zel'dovich approximation is obtained. We rely on large-scale structure tracers to determine the underlying dark matter field. These tracers can be bias as the overdense regions today are directly related to overdensities in the initial field. CLPT is one method that can incorporate these biases and accurately model the correlation function and redshift space distortions. An introduction to redshift space distortions is given in Chapter 5. An effective field theory version of CLPT, CLEFT (Vlah et al., 2016b), has also been posited as an extension.

All CLPT results have been produced using the CLEFT-CODE[3] which is publicly available. In Vlah et al. (2016b) the one-loop CLPT correlation function is investigated and it is shown that above $r = 30$ Mpch^{-1} the CLPT method outperforms the Zel'dovich approximation but below this scale it does not perform

[3]https://github.com/alejandroaviles/CLEFT

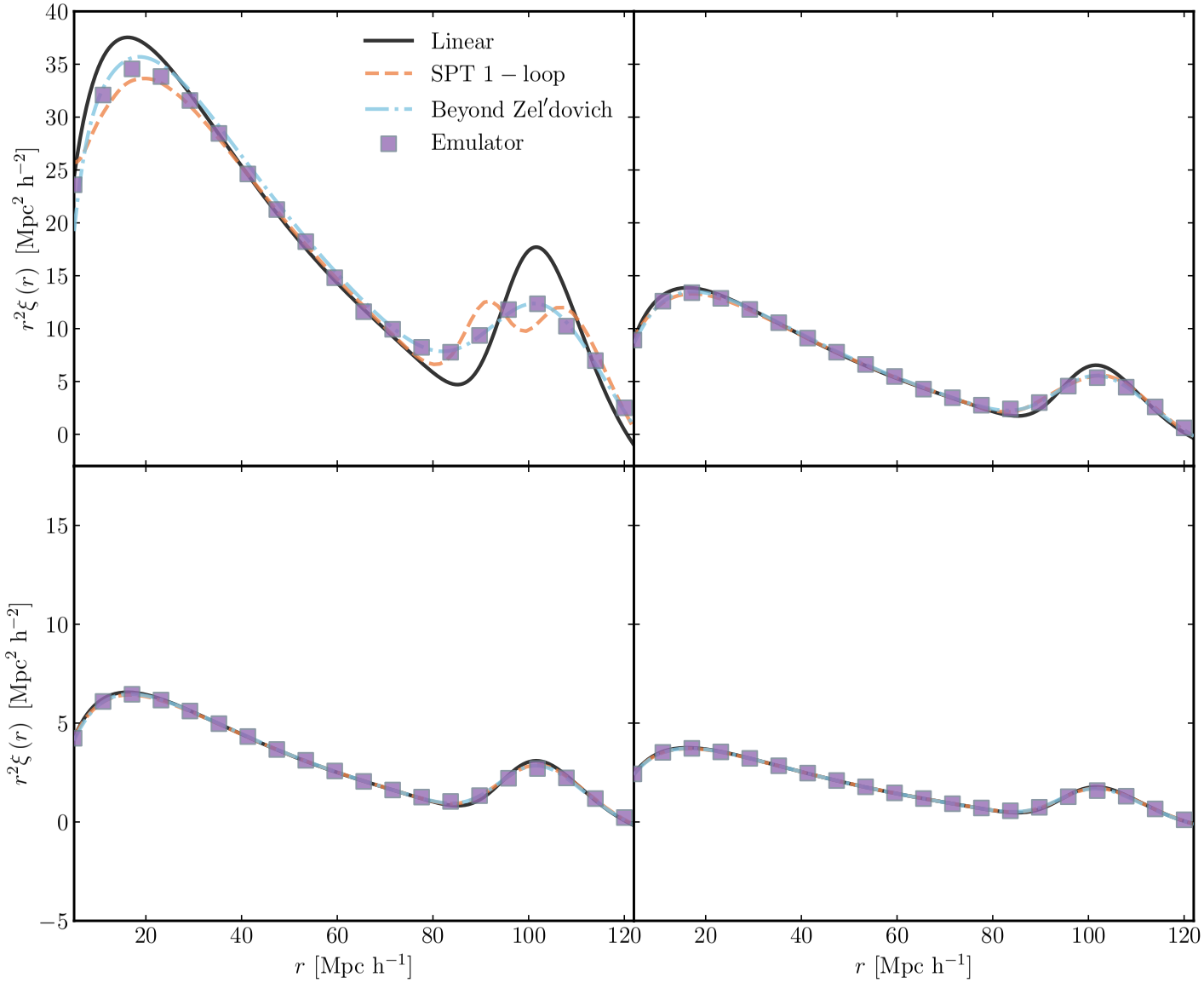

Figure 4.11 *The correlation function, $\xi(r)$, scaled by r^2 for the linear theory (black solid line), SPT 1-loop (orange dashed line), damped Beyond Zel'dovich with $k_c = 6$ h Mpc^{-1} (blue dashed-dot) and the emulator in purple squares. The four panels are redshifts $z = 0,\ 1,\ 2$ and 3 with the upper left panel being $z = 0$ and the lower right panel being $z = 3$.*

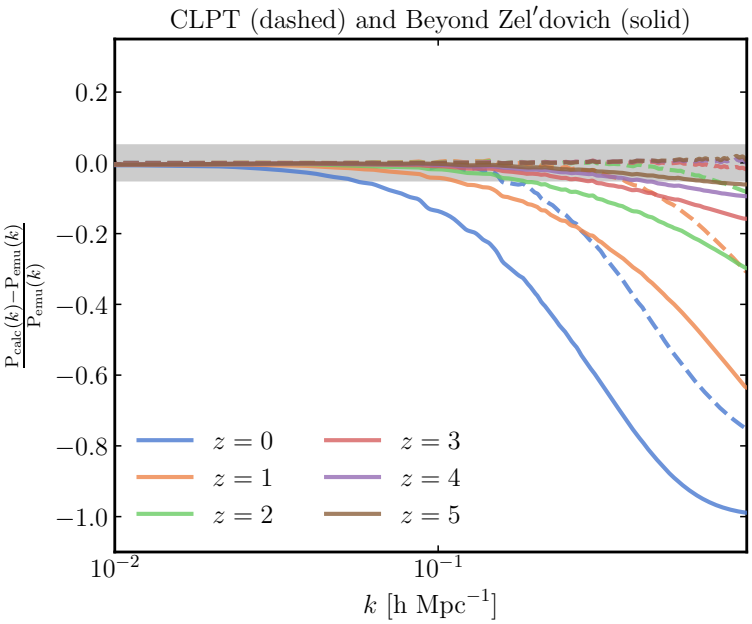

Figure 4.12 *Percentage difference between CLPT (dashed lines) and the Beyond Zel'dovich approximation (solid lines) power spectra and the emulator results. The percentage difference is shown for redshifts* $z = 0,\ 1,\ 2,\ 3,\ 4$ *and* 5 *and the grey shaded region is* $\Delta^2_{\text{diff}} = 0.05$.

well. The CLEFT-CODE output is the 2-point correlation function therefore the CLPT power spectrum has been obtained using MCFIT. This Fourier transform and interpolation is accountable for the oscillations seen in Figure 4.12.

The percentage difference between three-loop CLPT (see Vlah et al. (2016a) for more details on its computation) and Beyond Zel'dovich approximation power spectra and emulator results are shown for $z = 0,\ 1,\ 2,\ 3,\ 4$ and 5. At the four redshifts the CLPT method matches the emulator results more closely than the Beyond Zel'dovich approximation. However, the Beyond Zel'dovich approximation can be applied more easily at higher redshifts which can be seen as one advantage over the CLPT method.

Finally the 2-point correlation functions for linear perturbation theory (black solid line), three-loop CLPT (blue dashed line), Beyond Zel'dovich (orange dashed-dot line) and the emulator (yellow squares) are shown in Figure 4.13. The four panels are redshifts $z = 0,\ 1,\ 2$ and 3 with the upper left panel being $z = 0$ and the lower right panel being $z = 3$. As we have seen before there is a smaller difference between linear theory and the other methods at higher redshifts. At redshift $z = 0$ where there is a marginal difference between CLPT and Beyond Zel'dovich at BAO scales. The Beyond Zel'dovich approximation matches the

emulator results at these scales as accurately than CLPT. This suggests that the Beyond Zel'dovich approximation is modelling the non-linear BAO peak as well as CLPT. On small-scales below $r = 30$ h^{-1}Mpc both CLPT and Beyond Zel'dovich breakdown.

4.5.3 KFT

In Section 3.5.2 the functions $A(z)$ and $B(z)$ are given for an approximation that is based on the Kinetic Field Theory (KFT) method presented in Bartelmann et al. (2019) and re-derived in Ali-Haïmoud (2015). Our method is of a lower order as we have expanded the gravitational interaction term to first-order. In this subsection we will calculate the KFT approximation and the Beyond Zel'dovich approximation with $z_i = 100$. In Bartelmann et al. (2019) an initial value of $z_i = 1100$ is used, however we have shown that there is little difference between early initial redshifts.

The results for Beyond Zel'dovich and KFT time dependence are shown in Figure 4.14. The power spectrum we have calculated in this chapter does not reach as high an order or accuracy as in Bartelmann et al. (2019). However, it is still interesting to see how the KFT method can be calculated using our CTM. This also serves as another example of the flexibility of the method and how easily it can be applied to a variety of approximations.

The quantity shown in Figure 4.14 is $\Delta^2_{\rm calc}/\Delta^2_{\rm emu} - 1$ in order to match comparison figures in Bartelmann et al. (2019). The Beyond Zel'dovich approximation matches the emulator results at all redshifts above $z = 1$ more consistently than the KFT approximation.

4.6 Higher-order power spectrum

Computing the Beyond Zel'dovich approximation with a Gaussian damped initial power spectrum results in more power on small-scales compared to results from the emulator at high redshifts. The ability to push Beyond Zel'dovich to lower redshifts would increase the range of scenarios the method can be applied to. For example, observational evidence of modified gravity is concentrated at low redshifts. Therefore if one wishes to apply this method to model these theories we

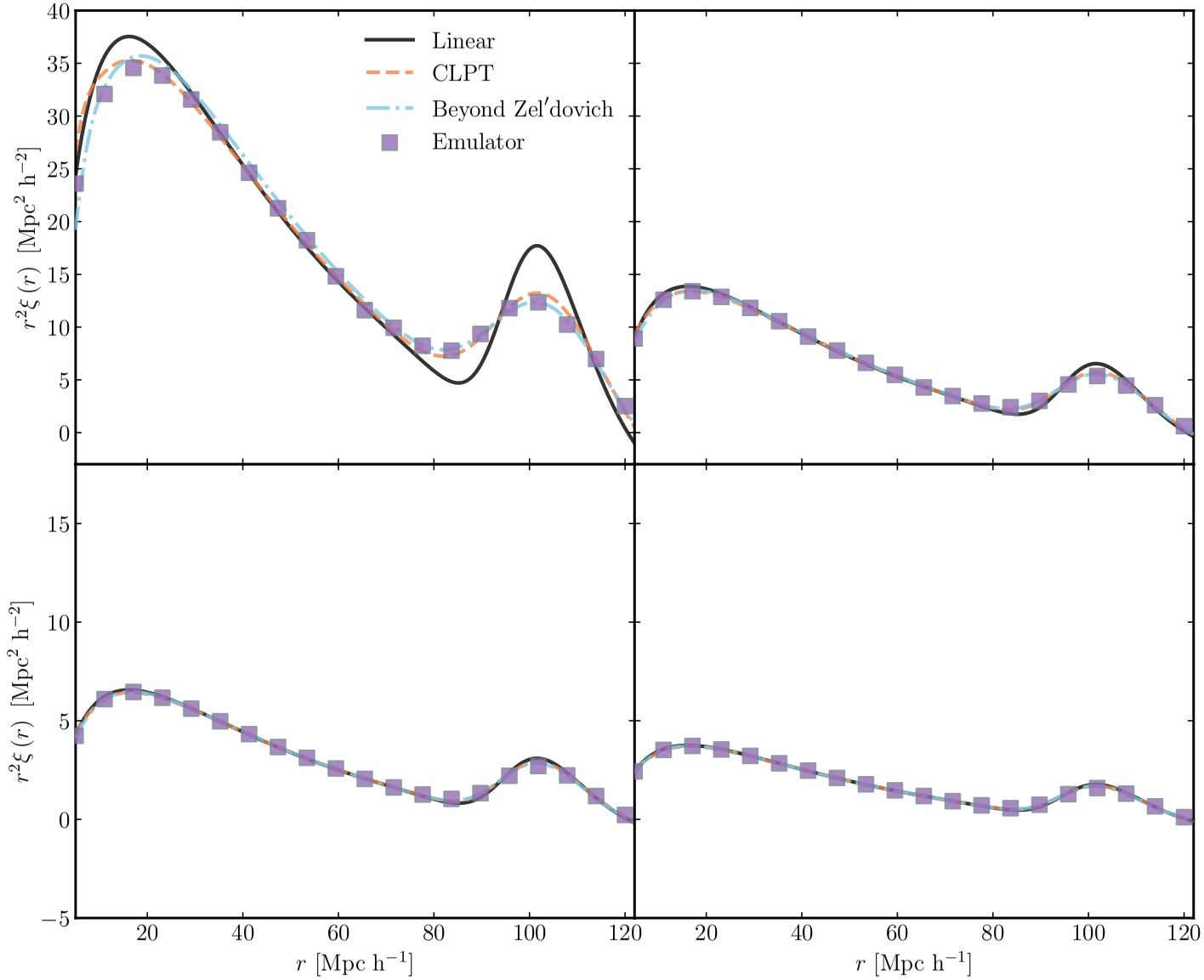

Figure 4.13 *The 2-point correlation function, $\xi(r)$, scaled by r^2 for linear theory (black solid line), Beyond Zel'dovich (blue dashed dot line), CLPT (orange dashed line) and the emulator in purple. The four panels are redshifts $z = 0,\ 1,\ 2$ and 3.*

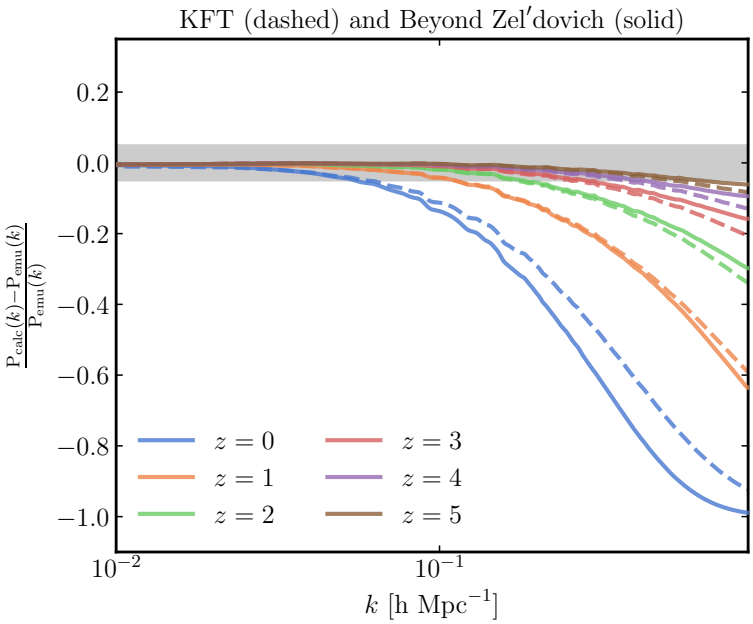

Figure 4.14 *Percentage difference between KFT approximation (dashed lines) and the Beyond Zel'dovich approximation (solid lines) with the emulator results for redshifts* $z = 0,\ 1,\ 2,\ 3,\ 4$ *and* 5. *The shaded grey band is* $\Delta^2_{\rm calc}/\Delta^2_{\rm emu} - 1 = \pm 0.05$.

must attempt to halt the effect the breakdown of the Zel'dovich approximation has on our low redshift power spectra. In this section we will expand the Beyond Zel'dovich power spectrum one order further in an attempt to reach lower redshifts.

4.6.1 Deriving the higher-order power spectrum

Recall, the general power spectrum is given by

$$\mathrm{P}\left(k,z\right) = \int d^3q\ \mathrm{e}^{i\mathbf{k}\cdot\mathbf{q}}\left[\left(\det\left(1+\mathbf{MC}\right)\right)^{-1/2}\mathrm{e}^{-\frac{1}{2}\mathbf{K}^T\mathbf{C}\left(1+\mathbf{MC}\right)^{-1}\mathbf{K}} - 1\right] \tag{4.9}$$

we have expanded the determinant and the exponent to second-order in $\mathbf{K}$ so far.

The exponent is expanded as

$$\begin{aligned} -\frac{1}{2}\mathbf{K}^T\mathbf{C}\left(1+\mathbf{MC}\right)^{-1}\mathbf{K} &\approx -\frac{1}{2}\mathbf{K}^T\mathbf{C}\left(1-\mathbf{MC}+\mathbf{MCMC}\right)\mathbf{K} \\ &= -\frac{1}{2}\mathbf{K}^T\mathbf{CK}+\frac{1}{2}\mathbf{K}^T\mathbf{CMCK}-\frac{1}{2}\mathbf{K}^T\mathbf{CMCMCK} \end{aligned} \tag{4.10}$$

where the first term gives (3.65), the second term was shown to be zero in (3.66) and the third term is the higher-order term we will calculate. The determinant was expanded as

$$\left(\det\left(1+\mathbf{MC}\right)\right)^{-1/2} = \mathrm{e}^{-\frac{1}{2}\mathrm{tr}(\ln 1+\mathbf{MC})} \approx \mathrm{e}^{-\frac{1}{2}\mathrm{tr}\left(\mathbf{MC}-\frac{1}{2}\mathbf{MCMC}+\frac{1}{3}\mathbf{MCMCMC}\right)} \tag{4.11}$$

where $\mathrm{tr}\left(\mathbf{MC}\right)=0$, $\mathrm{tr}\left(\mathbf{MCMC}\right)$ is given in (3.69) and $\mathrm{tr}\left(\mathbf{MCMCMC}\right)$ is also zero. Therefore in order to calculate a higher-order expansion of the power spectrum we only need to compute $-\frac{1}{2}\mathbf{K}^T\mathbf{CMCMCK}$. This calculation is lengthy we will summarise the final result of the calculation.

$$\begin{aligned} -\frac{1}{2}\mathbf{K}^T\mathbf{CMCMCK} \approx -\frac{1}{2}A^2\left(z\right)B^2\left(z\right)k_ik_jk_kk_l\Big[&P\left(q\right)\hat{q}_i\hat{q}_j\hat{q}_k\hat{q}_l+Q\left(q\right)\delta_{ij}\delta_{kl} \\ &+O\left(q\right)\hat{q}_i\hat{q}_j\delta_{kl}\Big] \end{aligned} \tag{4.12}$$

with

$$
\begin{aligned}
P(q) &= \frac{2}{9}\left[X\left(9D^2+45DF+\frac{9}{2}D\bar{\pi}\right)+Y\left(\frac{27}{2}D^2+108DF+9\bar{\pi}D+\frac{405}{2}F^2+\frac{63}{2}F\bar{\pi}+\frac{3}{2}\bar{\pi}^2\right)\right.\\
&\quad\left.-\frac{3}{2}XY(2G+7H)-Y^2\left(\frac{9}{4}G+\frac{39}{2}H-\frac{15}{4}I+\frac{3}{4}\sigma_0^2\right)-3\sigma_\psi^2\left(6D^2+30DF+2D\bar{\pi}\right)\right],\\
Q(q) &= \frac{2}{9}\left[X^2\left(-\frac{3}{4}G-9H+\frac{15}{4}I-\frac{3}{4}\sigma_0^2\right)+12\eta_E^2\left(\sigma_\psi^4-X\sigma_\psi^2\right)+4\sigma_0^2\left(\sigma_\psi^2X-\sigma_\psi^4\right)\right],\\
O(q) &= \frac{2}{9}\left[X\left(\frac{9}{2}D^2+\frac{495}{2}F^2+36F\bar{\pi}+\frac{3}{2}\bar{\pi}^2+\frac{9}{2}D\bar{\pi}+72DF\right)-\frac{3}{2}X^2(G+7H)\right.\\
&\quad+Y\left(45F^2+\frac{9}{2}F\bar{\pi}+9DF\right)-XY\left(3G+\frac{57}{2}H-\frac{15}{2}I+\frac{3}{2}\sigma_0^2\right)\\
&\quad\left.+\sigma_\psi^2\left(-54DF-270F^2-6D\bar{\pi}-48F\bar{\pi}-2\bar{\pi}^2+Y\sigma_0^2-3Y\eta_E^2\right)\right].
\end{aligned}
\tag{4.13}
$$

The expanded power spectrum is now

$$
\begin{aligned}
\mathrm{P}(k,z) \approx 2\pi\int_0^\infty dq\; q^2\int_{-1}^{1}d\mu\; \mathrm{e}^{ikq\mu}\Big[&\mathrm{e}^{-\frac{1}{2}k^2A^2\left(X'+\mu^2Y'\right)}\mathrm{e}^{B^2k^2\left(W'+\mu^2Z'\right)}\\
&\mathrm{e}^{-\frac{1}{2}A^2B^2\left(k^4\mu^4P+k^4Q+k^2\mu^2O\right)}-\mathrm{e}^{-k^2\sigma_\psi^2\left(A^2+\frac{1}{3}B^2\eta_E^2-A^2B^2\sigma_\psi^2\eta_E^2\right)}\Big].
\end{aligned}
\tag{4.14}
$$

Focusing on the angular integral we can apply the identities (3.26) and (3.27). Let us first define

$$
\begin{aligned}
E_1 &= A^2X'-2B^2W'\\
E_2 &= A^2B^2Q\\
E_3 &= A^2Y'-2B^2Z'+A^2B^2O'\\
E_4 &= A^2B^2P
\end{aligned}
\tag{4.15}
$$

allowing us to re-write (4.14) as

$$\mathrm{P}\left(k,z\right) \approx 2\pi \int_0^\infty dq\ q^2 \int_{-1}^{1} d\mu\ \mathrm{e}^{ikq\mu}\left[\mathrm{e}^{-\frac{1}{2}k^2E_1-\frac{1}{2}k^4E_2}\mathrm{e}^{-\frac{1}{2}k^2\mu^2E_3-\frac{1}{2}k^4\mu^4E_4} - \mathrm{e}^{-k^2\sigma_\psi^2\left(A^2+\frac{1}{3}B^2\eta_E^2-A^2B^2\sigma_\psi^2\eta_E^2\right)}\right]. \quad (4.16)$$

The angular integral is then calculated to be

$$\begin{aligned}\int_{-1}^{1} d\mu\ \mathrm{e}^{ikq\mu}\mathrm{e}^{-\frac{1}{2}k^2\mu^2E_3}\mathrm{e}^{-\frac{1}{2}k^4\mu^4E_4} &= \int_{-1}^{1} d\mu\ \mathrm{e}^{ikq\mu}\mathrm{e}^{-\frac{1}{2}k^2\mu^2E_3}\sum_{m=0}^{\infty}\frac{\left(-\frac{1}{2}k^4\mu^4E_4\right)^m}{m!} \\ &\approx \int_{-1}^{1} d\mu\ \mathrm{e}^{ikq\mu}\mathrm{e}^{-\frac{1}{2}k^2\mu^2E_3} - \frac{1}{2}k^4E_4\int_{-1}^{1} d\mu\ \mu^4\mathrm{e}^{ikq\mu}\mathrm{e}^{-\frac{1}{2}k^2\mu^2E_3} \\ &\approx 2\mathrm{e}^{-\frac{1}{2}k^2E_3}\left[\sum_{n=0}^{\infty}\left(\frac{kE_3}{q}\right)^n\left(j_n\left(kq\right)-\frac{1}{2}k^4E_4j_{n+4}\left(kq\right)\right)\right].\end{aligned} \quad (4.17)$$

Hence the higher-order power spectrum is

$$\mathrm{P}\left(k,z\right) \approx 4\pi \int_0^\infty dq\ q^2\mathrm{e}^{-\frac{1}{2}k^2(E_1+E_3)}\mathrm{e}^{-\frac{1}{2}k^4E_2}\left[\sum_{n=0}^{\infty}\left(\frac{kE_3}{q}\right)^n\left(j_n\left(kq\right)-\frac{1}{2}k^4E_4j_{n+4}\left(kq\right)\right) - \mathrm{e}^{-k^2\sigma_\psi^2\left(A^2+\frac{1}{3}B^2\eta_E^2-A^2B^2\sigma_\psi^2\eta_E^2\right)}\right]. \quad (4.18)$$

4.6.2 Computing the higher-order power spectrum

We have calculated two forms of the higher-order power spectrum for the Beyond Zel'dovich approximation. The first only contains new terms that are of order k^2 in (4.18) and will be referred to as "Higher-order Beyond Zel'dovich". The second form also contains the k^4 terms in (4.18) and will be referred to as "Full higher-order Beyond Zel'dovich". The new k^2 terms could cancel with other terms that are causing the breakdown of our approximation on small-scales and at low redshifts.

In Figure 4.15 the calculated dimensionless higher-order Beyond Zel'dovich power spectrum (purple dashed lines) is shown for six redshifts $z = 0,\ 1,\ 2,\ 3,\ 4$ and 5 and for three ϵ values. The higher-order Beyond Zel'dovich power spectrum is calculated with $\epsilon = 1$ in the first row, $\epsilon = 0.1$ in the middle row and $\epsilon = 0.01$ in the bottom row. The dimensionless power spectrum for linear theory (black solid lines), Beyond Zel'dovich approximation (with $\epsilon = 1$ and $k_c = 6$ h Mpc^{-1}) in orange dashed-dot lines and the EUCLID EMULATOR (pink dotted lines) are also plotted.

For high ϵ values we are plagued by numerical issues. The new k^2 terms are proportional to A^2B^2 which is a factor of 10^3 larger than B^2. Therefore for either large ϵ values or small ϵ values at low redshifts the new k^2 terms become too large and cause numerical oscillations. However for $\epsilon = 0.01$ the higher-order Beyond Zel'dovich approximation outperforms the lower order version at redshifts $z = 0$ and 1. At redshift $z = 1$ the solution for $\epsilon = 0.1$ also beats the lower order Beyond Zel'dovich power spectrum. In all other cases either the numerical artefacts are too large or the value of ϵ is too low and the higher-order terms have no effect on the solution.

In Figure 4.16 the results are the same as in Figure 4.15 but the full higher-order Beyond Zel'dovich approximation is shown in the purple dashed lines. The higher-order Beyond Zel'dovich in this figure is the full numerical solution to Equation (4.18). Again we encounter numerical issues due to the size of the higher-order terms and the spherical Bessel function summed over is now j_{n+4} resulting in large oscillations in the solution. These numerical oscillations can be seen in the calculated power spectrum when $\epsilon = 1$ and when $\epsilon = 0.1$. The k^4 terms do not appear to improve the Beyond Zel'dovich results at any redshift or for any ϵ value.

The percentage differences between the full higher-order Beyond Zel'dovich (dotted lines), higher-order Beyond Zel'dovich (dashed lines) and Beyond Zel'dovich (solid lines) power spectra and the emulator are shown in Figures 4.17 and 4.18. The full and higher-order Beyond Zel'dovich power spectra in these figures are calculated either with $\epsilon = 0.01$ or $\epsilon = 0.1$. The higher-order Beyond Zel'dovich power spectra in Figure 4.18 are calculated with a Gaussian damped initial power spectrum with a cutoff value of $k_c = 6$ h Mpc^{-1}. In both figures the Beyond Zel'dovich results are calculated using $\epsilon = 1$ and $k_c = 6$ h Mpc^{-1}. When $\epsilon = 0.01$ there is no noticeable difference between the full and higher-order Beyond Zel'dovich for the damped and undamped power spectra. This is

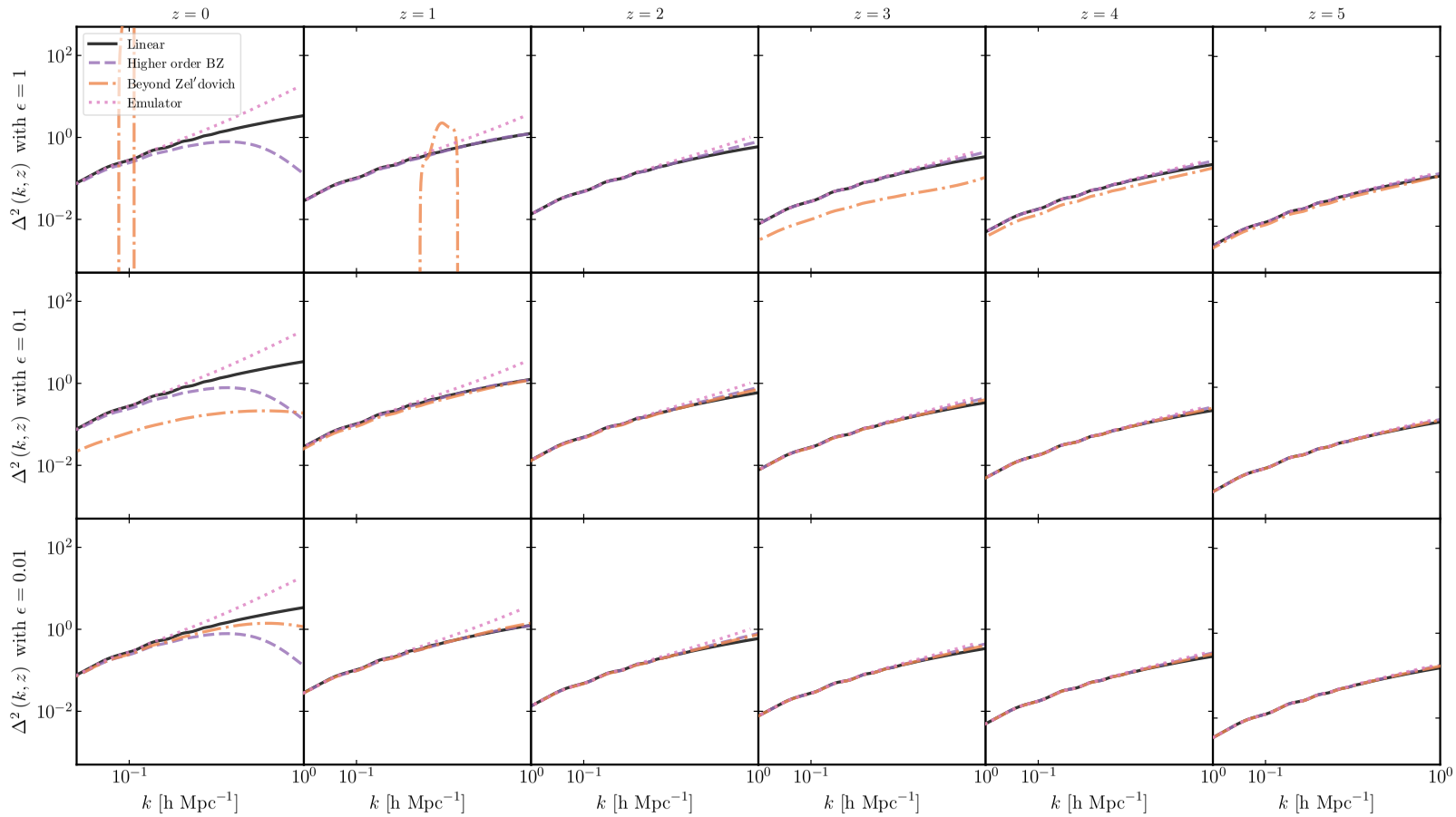

Figure 4.15 *In this Figure the dimensionless power spectra are shown for six redshifts. The black solid line is the linear dimensionless power spectrum, the orange dashed-dot line is the Beyond Zel'dovich approximation with* $\epsilon = 1$ *and* $k_c = 6$ h Mpc^{-1}*, the purple dashed line is the undamped higher-order Beyond Zel'dovich approximation with* $\epsilon = 0.01, 0.1$ *or* 1 *and finally the pink dotted line is the emulator result.*

likely due to the k^4 terms being too small to result in a difference. However there is a small difference between the full and higher-order Beyond Zel'dovich results when $\epsilon = 0.1$. The full higher-order Beyond Zel'dovich does not perform as well at lower redshifts which is likely due to numerical issues caused by the higher-order terms becoming too large. It is only at redshifts $z = 0$ and $z = 1$ that the undamped and damped full and higher-order Beyond Zel'dovich power spectra performs better than the lower order power spectrum with $\epsilon = 0.01$.

Although our hope was that these higher-order corrections to the power spectrum would fix the breakdown of the Beyond Zel'dovich approximation on small-scales, it appears there is too much numerical noise for most redshifts and values of ϵ. These higher-order terms could improve our results if the full power spectrum (3.63) could be calculated. This is not currently numerically feasible but a full inclusion of all of the terms could result in the cancelling out of the effects that cause the breakdown of the Zel'dovich approximation. We will not investigate the higher-order expansion of the power spectrum further as we cannot overcome the numerical issues yet.

4.7 Conclusions

In this chapter, we have introduced the Beyond Zel'dovich approximation which is an application of the CTM. We began by defining the time-dependent functions $A(z)$ and $B(z)$ for this approximation and our motivations. The Beyond Zel'dovich approximation aims to reproduce the linear power spectrum on large-scales without any need for re-normalisation. We also removed the acceleration term that should appear in the trajectory and expressed the tidal field in terms of the trace and trace-less parts to reduce the breakdown of the Zel'dovich approximation. We hoped that the addition of the tidal field to the Zel'dovich approximation would allow us to model structure formation more accurately on small-scales.

In Section 4.2 we calculated the power spectrum in Equation (3.79) with the Beyond Zel'dovich approximation time dependence for different redshifts, ϵ values and z_i values. We showed that at high redshifts the Beyond Zel'dovich approximation power spectrum converges to the Zel'dovich power spectrum for small values of ϵ. This is exactly the behaviour we expected as at high redshifts as the tidal field term should be small and ϵ controls the size of the gravitational

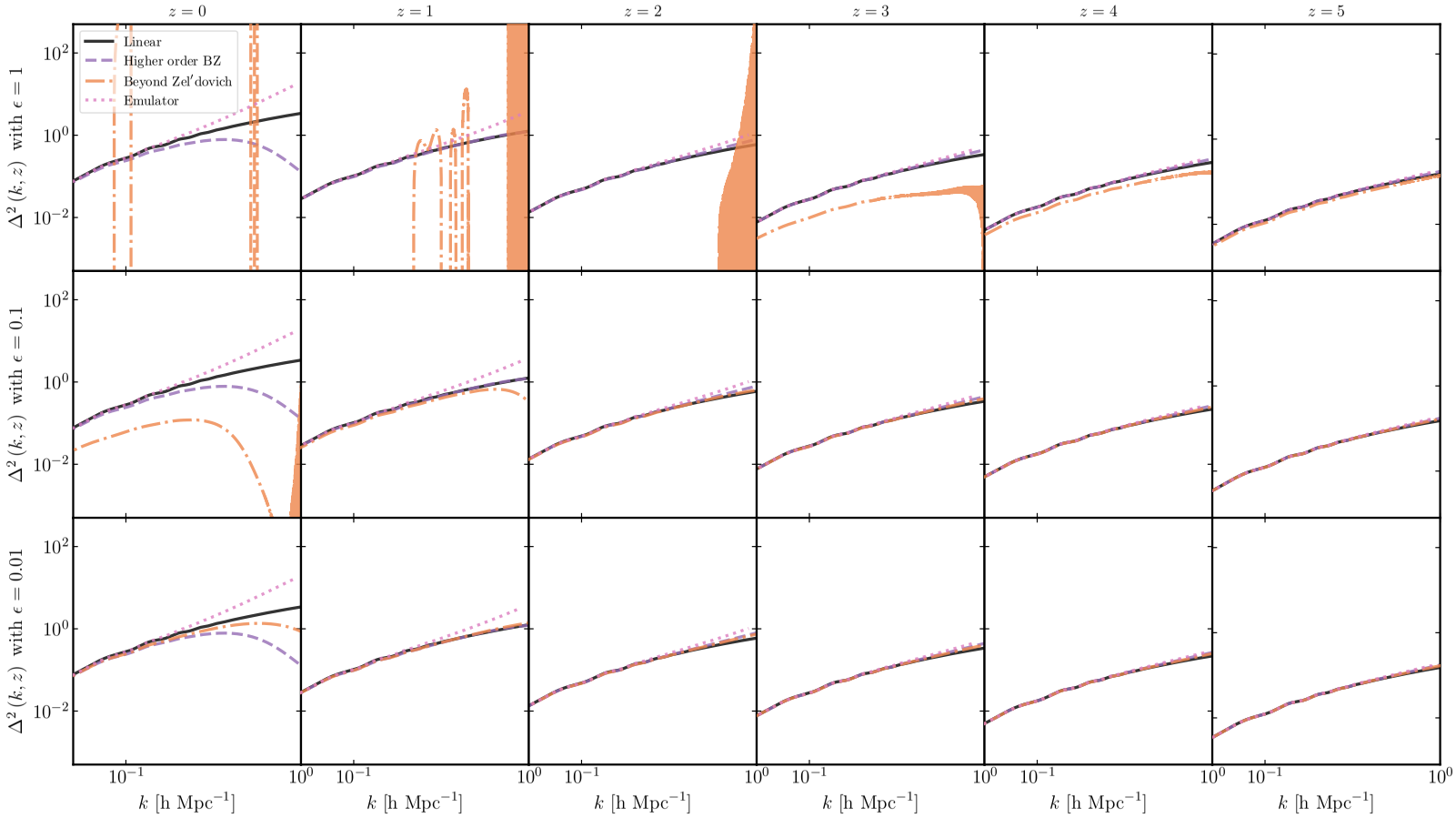

Figure 4.16 *The black solid line is the linear dimensionless power spectrum, the orange dashed-dot line is the Beyond Zel'dovich approximation with* $\epsilon = 1$ *and* $k_c = 6$ h Mpc^{-1}*, the purple dashed line is the full undamped higher-order Beyond Zel'dovich approximation with* $\epsilon = 0.01, 0.1$ *or* 1 *and finally the pink dotted line is the emulator result.*

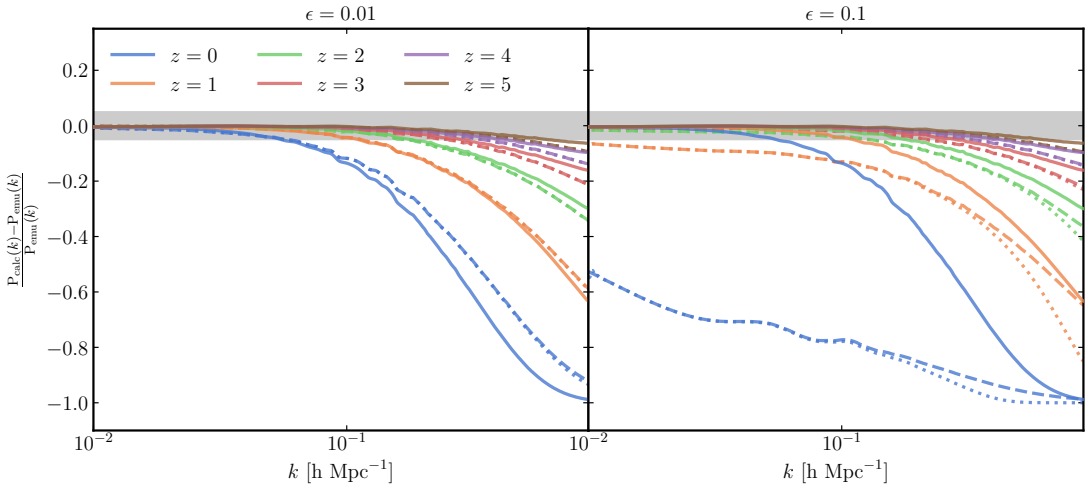

Figure 4.17 *The percentage difference between the full higher-order Beyond Zel'dovich (dotted lines), the higher-order Beyond Zel'dovich (dashed lines) power spectra and the emulator for* $\epsilon = 0.01$ *is shown in the left-hand panel and* $\epsilon = 0.1$ *in the right-hand panel. The solid lines are the percentage difference between the Beyond Zel'dovich power spectra with* $\epsilon = 1$ *and* $k_c = 6$ h Mpc^{-1} *and the emulator.*

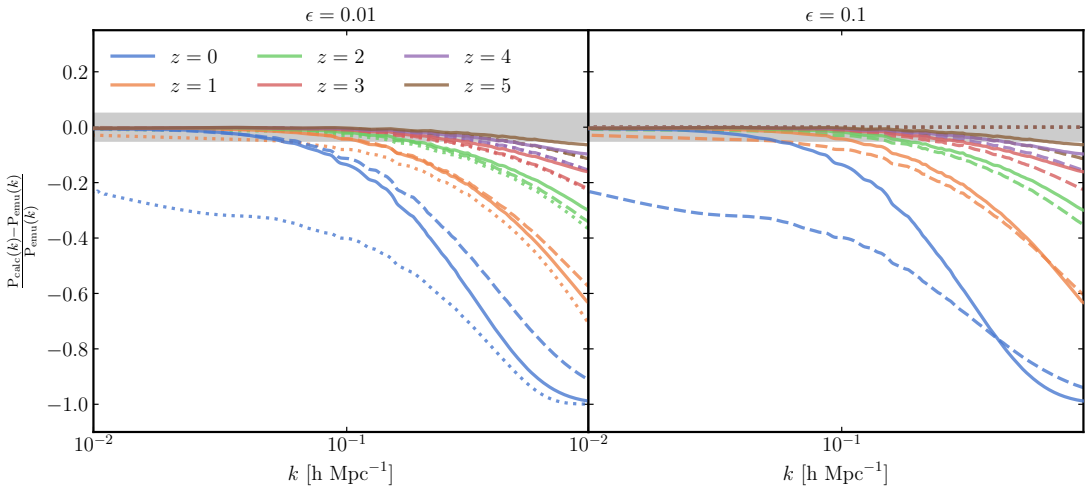

Figure 4.18 *The percentage difference between the full higher-order Beyond Zel'dovich (dotted lines), the higher-order Beyond Zel'dovich (dashed lines) power spectra and the emulator for* $\epsilon = 0.01$ *shown in the left-hand panel and* $\epsilon = 0.1$ *in the right-hand panel. Both of the higher-order power spectra have been calculated using a Gaussian damped initial power spectrum with* $k_c = 6$ h Mpc^{-1}*. The solid lines are the percentage difference between the Beyond Zel'dovich power spectra with* $\epsilon = 1$ *and* $k_c = 5$ h Mpc^{-1} *and the emulator.*

interaction. Therefore the smaller the value of ϵ the smaller the non-linear correction to structure formation on small-scales. The computation of Beyond Zel'dovich for different redshifts and ϵ values resulted in the conclusion that we should choose $\epsilon = 1$ for the tidal term to affect all redshifts. The effect of the tidal term at low redshifts for $\epsilon = 1$ is unfortunately destructive as the Zel'dovich approximation and numerics begin to breakdown on small-scales. Before beginning to find a solution to this breakdown of the approximation at low redshifts we investigated the initial redshift chosen in the cosmological trajectory. There was little difference between suitably high initial redshifts however if one chose an extreme example of $z_i = 50$ then the impact could be seen on the final power spectrum result. We chose to keep $z_i = 100$ because it is more physically motivated than a lower redshift value.

We introduced a Gaussian cutoff in the initial power spectrum and used it to calculate the Beyond Zel'dovich approximation in Section 4.3. This cutoff in the initial power spectrum was determined by a cutoff k_c value. We first chose three cutoff values of $k_c = 50,\ 5$ and 0.5 h Mpc^{-1}. We found that a value of $k_c = 50$ h Mpc^{-1} was too large and that it was not damping down the breakdown of the Zel'dovich approximation on small enough scales. Similarly a value of $k_c = 0.5$ h Mpc^{-1} was too small and erased all structure at high redshifts. The value of $k_c = 6$ h Mpc^{-1}, which corresponds physically to the size of a galaxy cluster (it is at these scales that non-linear effects cause the Zel'dovich approximation to be no longer valid), allowed us to push to lower redshifts. The small-scale effects were successfully damped down for the all redshifts above $z = 1$ and we outperformed the Euclid Emulator at redshifts $z = 4$ and $z = 5$. As this cutoff value could depend on the cosmology chosen we tested whether there was a difference between the largest k-value we could calculate the power spectrum up to before we dropped 5% below the emulator results. We found that there was a noticeable difference, however, we were limited in our choice of alternative cosmology. We leave it to future work to obtain N-body results for a large range of cosmological parameters to stringently test this dependence.

The Beyond Zel'dovich approximation was found to perform best when it was calculated using a Gaussian damped initial power spectrum with $k_c = 6$ h Mpc^{-1} and $\epsilon = 1$. We found that at high redshifts i.e. above $z = 1$ we performed competitively compared to results from an emulator. We also briefly discussed how the Beyond Zel'dovich approximation could be applied to Lyman-α observations and how these observations can be used to constrain cosmological

parameters and new physics related to dark energy. In this chapter, we also investigated another approximation we called "LPT like" in Section 4.4. This approximation did not perform as well as Beyond Zel'dovich but it demonstrated that the CTM can be easily applied to a wide range of theories including KFT.

After determining the best values for the free parameters in our theory and discovering a method to damp down the breakdown on small-scales of the Zel'dovich approximation we began to compare Beyond Zel'dovich to other methods. The first method we investigated was SPT 1-loop. We found that although this method outperformed ours when calculating the power spectrum we captured the non-linear evolution of the BAO peak in the correlation function more accurately. This is not surprising as the Zel'dovich approximation is known to model the BAO peak very well compared to SPT. We also found that another method CLPT approximated the power spectrum on non-linear scales more accurately than Beyond Zel'dovich. The correlation functions for both methods were practically identical but both showed more precise modelling of the BAO peak. The CLPT method also breaks down for high redshifts, therefore Beyond Zel'dovich could be more applicable to future cosmological observations in the mildly non-linear regime. Finally, B14 and AH15's method (also referred to as KFT) produced less accurate small-scale results for the power spectrum. As KFT requires a normalisation of the power spectrum we believe that our method is more intuitive and is more general allowing its application to a wider range of scenarios.

Finally, we expanded our CTM power spectrum so that it included new k^2 terms and terms proportional to k^4. We hoped that the new k^2 terms would cancel with some of the lower order terms to remedy the breakdown of the approximation on small-scales. These higher-order terms were proportional to A^2B^2 and thus proved too large causing numerical issues for large ϵ and low redshift values. There was a small improvement over lower-order Beyond Zel'dovich approximation at redshifts $z = 0$ and $z = 1$. This is promising as it hints that if the full power spectrum could be calculated numerically we could model structure formation in the non-linear regime precisely.

The accuracy of the Beyond Zel'dovich approximation in modelling the correlation function and the ease of comparison with methods such as CLPT, which are designed to model redshift space distortions, will be utilised in the next chapter. In Chapter 5 we will calculate the redshift space version of our power spectrum.

Chapter 5

The Cosmological Trajectories Method: The Beyond Zel'dovich approximation and its applications in redshift space

> Math. It's just there...you're either right or you're wrong. That's what I like about it.
>
> *Katherine Johnson*

5.1 Overview

In Chapters 3 and 4 we introduced the Cosmological Trajectories Method (CTM) as a perturbative technique that can be used to model dark matter structure formation in our Universe. Modelling the formation of large-scale structure and features like the BAO peak (see Section 4.5 for a review of the BAO) can give insight into how the cosmic web formed. The clustering of matter can be studied by measuring the galaxy power spectrum and correlation function from redshift surveys (Percival & White, 2009, Taruya et al., 2011, Blake et al., 2011, Beutler et al., 2014, Howlett et al., 2015, Collaboration et al., 2016). However, when

using such observational data the line-of-sight distance discrepancies, caused by the mapping between real space and redshift space, can lead to an error in the positioning of objects. These distortions are called Redshift-Space Distortions (RSD) and a brief introduction is given in Section 5.2. Biases are also introduced when determining the underlying dark matter field from the galaxy surveys. Measurements of these bias factors can help to narrow down parameter spaces for alternate gravity and dark energy models (Guzzo et al., 2008, Jennings et al., 2012, Raccanelli et al., 2013, Hellwing et al., 2014, Valogiannis et al., 2020) and can be incorporated into RSD models to more accurately determine the underlying density field. We will not focus on biases and their measurements in this thesis.

As with the matter power spectrum the linear perturbation theory techniques used to model redshift-space statistics (Kaiser, 1987, Heavens & Taylor, 1995, Hamilton & Culhane, 1996, Szapudi, 2004, Pápai & Szapudi, 2008, Taruya et al., 2011, Castorina & White, 2019) break down on small scales. Phenomenological models as described in Heavens et al. (1998), Scoccimarro (2004), Percival & White (2009), Kazin et al. (2011) and Zheng & Song (2016) have been discussed in the literature as a way to accurately model RSD. A wide range of non-linear extensions (Mann et al., 1993, Vlah et al., 2016a, Chen et al., 2020) also exist including the TNS model (Taruya et al., 2010, Valageas, 2011) which will be introduced in Section 5.2.2, streaming models (Uhlemann et al., 2015, Kopp et al., 2016, Vlah et al., 2016b, Kuruvilla & Porciani, 2018), distribution function models (Seljak & McDonald, 2011, Okumura et al., 2012b,a, Vlah et al., 2012, 2013, Okumura et al., 2015), EFT models (Senatore & Zaldarriaga, 2015, Fonseca de la Bella et al., 2017, Lewandowski et al., 2018) and the bispectrum (Scoccimarro et al., 1999, Gil-Marín et al., 2014).

Cosmological simulations can accurately model redshift-space distortions (Hatton & Cole, 1998, Scoccimarro & Sheth, 2002, Raccanelli et al., 2010, Hellwing et al., 2016). If one wishes to examine a large range of cosmologies and modified gravity models then again multiple large simulations must be run. This, as was discussed in Section 3.1, is both time and cost expensive. Lyman-α observations can also allow us to measure redshift-space distortions (Seljak et al., 2005a, Seljak, 2012, Givans & Hirata, 2020) and as we have seen in Section 4.3 these observations are usually at high redshifts and are therefore in the mildly non-linear regime (where perturbative methods are applicable and accurate). Hence, if one wishes to narrow down a wide parameter space one could use perturbative methods in combination with Lyman-α observations rather than simulations.

Lagrangian Perturbation Theory (LPT) can model structure formation more accurately than Standard Perturbation Theory (SPT) as it is less susceptible to caustics and shell-crossing (Vlah et al., 2015a). These characteristics have resulted in LPT (Matsubara, 2008a,b, Matsubara, 2014, Vlah & White, 2019) and methods based on LPT being used extensively to model RSD. The Zel'dovich approximation (first-order LPT) redshift-space power spectrum has been calculated in Couchman & Bond (1988), Hivon et al. (1995), Taylor & Hamilton (1996), Sugiyama (2014) and Castorina & White (2018). Other techniques based on LPT include IR-resummation schemes (Ivanov & Sibiryakov, 2018), Zel'dovich reconstruction methods (Nadathur et al., 2019, Chen et al., 2019), Convolved Lagrangian Perturbation Theory (CLPT) (Carlson et al., 2013, Wang et al., 2014, Vlah et al., 2016b) and a Lagrangian-space Gaussian ansatz in Valageas & Nishimichi (2020).

The CTM is based on the Zel'dovich approximation and can be computed for a wide range of cosmologies. The method also can be applied to modified gravity and alternative dark energy models. Extending our method to redshift space will allow it to be used with a wider range of observational data. In Section 4.3 the Beyond Zel'dovich approximation power spectrum computed with an initial damped Gaussian power spectrum was demonstrated to outperform the Zel'dovich approximation (for $z = 1$ to 5) and the EUCLID EMULATOR (for $z = 4$ and 5). These results, as well as those for the correlation function, implying that the approximation could be used to model RSD and used in combination with Lyman-α and other high redshift observations.

In this chapter, we will give a brief introduction to RSD and provide an example of a linear and non-linear method. In Section 5.3 we will calculate the redshift-space power spectrum for the CTM analytically and then compute it numerically for the Beyond Zel'dovich approximation. We will then compare the results to other methods and simulation data in Section 5.5. Finally, we will present our conclusions in Section 5.6.

5.2 Redshift-space distortions (RSD)

In this section we will give a brief introduction to RSD. For a more in depth review we refer the reader to Peebles (1980), Hamilton (1998), Bernardeau et al.

(2002), Percival et al. (2011), Vlah & White (2019) and the online notes [1].

The observed redshift of an object, $z_{\rm obs}$, with a radial peculiar velocity along the line-of-sight $v_\parallel$ and peculiar relativistic redshift, z_p , is given by

$$1 + z_{\rm obs} = (1 + z)\left(1 + z_p\right) = (1 + z)\left(1 - \frac{v_\parallel}{c}\right)^{-1} \tag{5.1}$$

and as the peculiar velocity is small compared to the Hubble flow the observed redshift can be expanded as

$$z_{\rm obs} \approx z + (1 + z)\,\frac{v_\parallel}{c}. \tag{5.2}$$

Then the physical co-moving distance to an object, taking into account the peculiar velocity, is

$$s\,(z) = c\int_0^z \frac{dz'}{H\,(z')} + c\int_z^{z(1+z)\frac{v_\parallel}{c}} \frac{dz'}{H\,(z')} = cx\,(z) + \frac{v_\parallel}{caH\,(z)} \tag{5.3}$$

and in 3D space (setting $c = 1$)

$$\mathbf{s} = \mathbf{x} + \frac{\hat{\mathbf{x}}\cdot\mathbf{v}}{aH}\hat{\mathbf{x}} \tag{5.4}$$

where $\mathbf{s}$ is the redshift-space position and $\mathbf{x}$ is the real-space position. The second term in (5.4) is usually ignored as it is small, however it has an impact on clustering statistics. This is because the peculiar velocity induces anisotropies in the clustering of matter, these are RSD.

In Figure 5.1 these effects are shown for a range of scales and scenarios. The solid red dots represent objects, such as galaxies, the arrows are the peculiar velocities of the objects and there is a spherical overdensity at the centre of each circle.

[1] https://wwwmpa.mpa-garching.mpg.de/ komatsu/lecturenotes/Shun_Saito_on_RSD.pdf

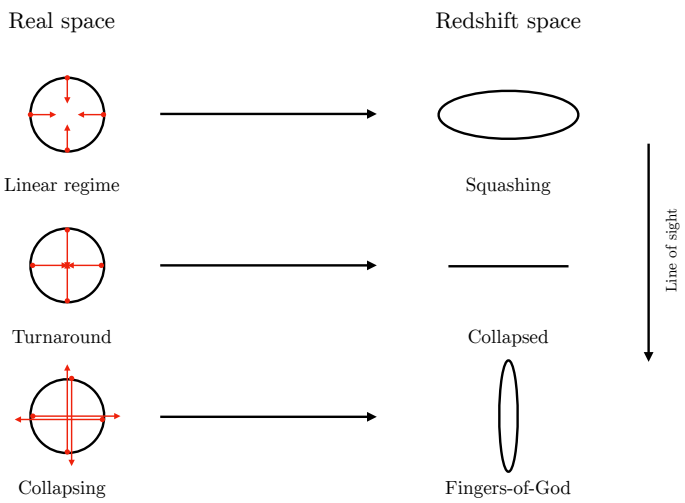

Figure 5.1 *Diagram showing how a spherical region with a central overdensity and objects at the solid red points appear in real space and redshift space. The top row of the diagram represents the largest scales and the lower row represents the smallest scales.*

On large scales, labelled as the linear regime, the objects are gravitationally attracted to the overdense region in the centre causing the region to appear squashed in redshift space. This is also known as the Kaiser effect (Kaiser, 1987). On turnaround scales, the peculiar velocities of the objects are larger and as the objects are in the centre of the sphere this causes the region to appear collapsed. Finally on small scales, labelled as collapsing in the diagram, the objects are virialised and random motions cause the region to appear stretched. This stretching effect is also referred to as the Fingers-of-God (Jackson, 1972).

In order to study RSD there are three approximations that are usually applied:

- **Distant observer and plain parallel approximations** - these allow us to replace $\hat{\mathbf{x}}$ with a global line-of-sight direction $\hat{\mathbf{z}}$. There can of-course be wide angle effects introduced (Szapudi, 2004, Pápai & Szapudi, 2008, Castorina & White, 2019, Taruya et al., 2020) and other effects (Heavens & Taylor, 1995, Hamilton & Culhane, 1996) if these approximations are not taken.

- **No velocity bias** - This implies that the matter velocity field, $\mathbf{v}_m$, is equal to the galaxy velocity field, $\mathbf{v}_g$. The only bias taken into account is the density field bias. Assuming that there is no velocity bias is not strictly true and this is investigated in Biagetti et al. (2014) and Baldauf et al. (2015b).

5.2.1 Linear RSD Example - Kaiser formula

Recall that the linear perturbation equations (see Section 2.2.1) are

$$\theta(\mathbf{x}) = -\frac{\nabla \cdot \mathbf{v}(\mathbf{x})}{aH} \tag{5.5a}$$

$$\delta_{\mathrm{m}}^{\mathrm{L}}(\mathbf{x}) = \frac{1}{f}\theta(\mathbf{x}) \tag{5.5b}$$

with $f = \frac{d\ln D_1}{d\ln a} \approx \Omega_m^{0.6}$ (Sargent & Turner, 1977, Lahav et al., 1991).

The mass conservation from real to redshift space is given by,

$$\delta_{\mathrm{m}}^{\mathrm{s}}(\mathbf{s}) = \left|\frac{d\mathbf{s}}{d\mathbf{x}}\right|^{-1} (1 + \delta_{\mathrm{m}}(\mathbf{x})) - 1 \tag{5.6}$$

and the Jacobian can be approximated (where v_z is the velocity in the line-of-sight direction) as

$$J = \frac{d\mathbf{s}}{d\mathbf{x}} \approx 1 + \frac{\partial v_z}{\partial z}. \tag{5.7}$$

Fourier transforming Equation (5.6) yields,

$$\delta_{\mathrm{m}}^{\mathrm{s}}(\mathbf{k}) \approx \int d^3x \left[\delta_{\mathrm{m}}^{\mathrm{L}}(\mathbf{x}) - \frac{1}{aH}\frac{\partial v_z}{\partial z}\right] \mathrm{e}^{i\mathbf{k}\cdot\mathbf{x} + ik\mu_k \frac{v_z}{aH}} \tag{5.8}$$

and truncating to linear order results in

$$\delta_{\mathrm{L}}^{\mathrm{s}}(\mathbf{k}) = \left(1 + f\mu_k^2\right) \delta_{\mathrm{m}}^{\mathrm{L}}(\mathbf{k}). \tag{5.9}$$

This is the Kaiser formula (Kaiser, 1987) and the redshift-space power spectrum

is

$$\mathrm{P}_{\mathrm{m}}^{\mathrm{s,L}}\left(\mathbf{k}\right)=\left(1+f\mu_{k}^{2}\right)^{2}\mathrm{P}_{\mathrm{m}}^{\mathrm{L}}\left(\mathbf{k}\right) \tag{5.10}$$

with $\mu_k = \hat{\mathbf{k}}\cdot\hat{\mathbf{z}}$.

5.2.2 Non-linear RSD Example - TNS model

In Taruya et al. (2010) the power spectrum at next to leading order was obtained. This model is called the Taruya, Nishimichi, Saito (TNS) model. Beginning with Equation (5.8) and defining $u_z = -\frac{v_z}{aHf}$ for ease, the power spectrum in redshift space is

$$\mathrm{P}^{\mathrm{s}}\left(\mathbf{k}\right)=\int d^{3}r\ \mathrm{e}^{i\mathbf{k}\cdot\mathbf{r}}\langle\mathrm{e}^{-ik\mu_{k}f\Delta u_{z}}\left[\delta\left(\mathbf{x}_{1}\right)+f\nabla_{z}u_{z}^{1}\right]\left[\delta\left(\mathbf{x}_{2}\right)+f\nabla_{z}u_{z}^{2}\right]\rangle. \tag{5.11}$$

In the above expression $\mathbf{r} = \mathbf{x}_2 - \mathbf{x}_1$ and $\Delta u_z = u_z\left(\mathbf{x}_2\right) - u_z\left(\mathbf{x}_1\right)$. We will apply the cumulant expansion theory to evaluate the $\langle\cdots\rangle$ term. The expression we wish to apply is

$$\langle\mathrm{e}^{J_{1}A_{1}}A_{2}A_{3}\rangle=\mathrm{e}^{\langle\mathrm{e}^{J_{1}A_{1}}\rangle}\left[\langle\mathrm{e}^{J_{1}A_{1}}A_{2}A_{3}\rangle+\langle\mathrm{e}^{J_{1}A_{1}}A_{2}\rangle\langle\mathrm{e}^{J_{1}A_{1}}A_{3}\rangle\right] \tag{5.12}$$

where $J_1 = -ik\mu_k f$, $A_1 = \Delta u_z$, $A_2 = \delta\left(\mathbf{x}_1\right) + f\nabla_z u_z^1$ and $A_3 = \delta\left(\mathbf{x}_2\right) + f\nabla_z u_z^2$. Hence, the TNS power spectrum is

$$\mathrm{P}_{\mathrm{m,TNS}}^{\mathrm{s}}\left(\mathbf{k}\right)=\mathrm{e}^{-k^{2}\mu_{k}^{2}f^{2}\sigma_{\psi}^{2}}\left[\mathrm{P}_{\delta\delta}+2f\mu_{k}^{2}\mathrm{P}_{\delta\theta}+f^{2}\mu_{k}^{4}\mathrm{P}_{\theta\theta}+A\left(k,\mu_{k}\right)+B\left(k,\mu_{k}\right)\right] \tag{5.13}$$

with

$$A\left(k,\mu_k\right) = J_1 \int d^3r\ \mathrm{e}^{i\mathbf{k}\cdot\mathbf{r}}\langle A_1 A_2 A_3\rangle \tag{5.14}$$

$$B\left(k,\mu_k\right) = J_1^2 \int d^3r\ \mathrm{e}^{i\mathbf{k}\cdot\mathbf{r}}\langle A_1 A_2\rangle\langle A_1 A_3\rangle. \tag{5.15}$$

The TNS model is one of the most popular models and is often used in conjecture with observations such as in the SDSS survey (Beutler et al., 2016). For more details on RSD models we refer the reader to Peebles (1980), Hamilton (1998), Bernardeau et al. (2002), Percival et al. (2011) and Vlah & White (2019).

5.3 Calculating the Cosmological Trajectories Method power spectrum in redshift space

5.3.1 Calculating the redshift-space Zel'dovich power spectrum

In this subsection we will compute the redshift-space power spectrum for the Zel'dovich approximation in order to demonstrate an alternate method (Taylor & Hamilton, 1996) to that presented in subsection 5.3.2. Recall, that the redshift-space position is given by

$$s_i = x_i + \frac{\hat{z}_j v_j}{aH}\hat{z}_i \tag{5.16}$$

where $v_j = a\dot{x}_j = a\frac{\dot{D}_1(t)}{D_1(t_i)}\Psi_j^{(0)}\left(\mathbf{q},t_i\right)$ for the Zel'dovich approximation. The redshift-space position is therefore

$$s_i = q_i + \frac{D_1\left(t\right)}{D_1\left(t_i\right)}\Psi_j^{(0)}\left(\mathbf{q},t_i\right)\left[\delta_{ij} + f\hat{z}_i\hat{z}_j\right] = q_i + \frac{D_1\left(t\right)}{D_1\left(t_i\right)}R_{ij}\Psi_j^{(0)}\left(\mathbf{q},t_i\right) \tag{5.17}$$

where $f = \frac{d\ln D_1}{d\ln a}$. Following the same procedure as was used to calculate the

real-space Zel'dovich power spectrum in Section 3.2.3, the power spectrum is

$$\mathrm{P}\left(k,\mu_k\right) = \int d^3q \; \mathrm{e}^{i\mathbf{k}\cdot\mathbf{q}} \mathrm{e}^{-\frac{1}{2}k_k k_l R_{ik} R_{jl} A_{ij}(\mathbf{q})}. \tag{5.18}$$

Now we will introduce a new vector $K_i = k_k R_{ik}$ and re-write (5.18) as

$$\mathrm{P}\left(k,\mu_k\right) = \int dq d\mu \; \mathrm{e}^{ikqc\mu} \mathrm{e}^{-\frac{1}{2}K^2\left(X+Y\mu^2\right)} \mathrm{e}^{-ikqs\sqrt{1-\mu^2}\cos\phi} \tag{5.19}$$

with $\mu = \hat{\mathbf{K}} \cdot \hat{\mathbf{q}}$, $\mu_k = \hat{\mathbf{k}} \cdot \hat{\mathbf{z}}$, $c = \frac{1+f\mu_k^2}{\sqrt{1+f(2+f)\mu_k^2}}$ and $s = \frac{f\mu_k\sqrt{1-\mu_k^2}}{\sqrt{1+f(2+f)\mu_k^2}}$. The azimuthal angle (integral over ϕ) and the μ integrals can be performed analytically

$$\mathrm{P}\left(k,\mu_k\right) = 4\pi \int dq \; q^2 \mathrm{e}^{-\frac{1}{2}K^2(X+Y)} \sum_{m=0}^{\infty} \left(\frac{-2}{kq}\right)^m G_m\left(kqc, -\frac{1}{2}K^2Y, kq\right) j_m\left(kq\right) \tag{5.20}$$

where the function G_m is defined as

$$G_m\left(kqc, -\frac{1}{2}K^2Y, kq\right) = \sum_{n=m}^{\infty} \frac{\Gamma\left(m+n+1/2\right)}{\Gamma\left(m+1\right)\Gamma\left(n+1/2\right)\Gamma\left(1-m+n\right)} \left[-\frac{1}{2}K^2Yc^2\right]^n \; {}_2F_1\left(\frac{1}{2}-n; -n; -\frac{1}{2}-m-n; \frac{1}{c^2}\right). \tag{5.21}$$

The functions X and Y are equal to those defined in (3.25) and j_m are spherical Bessel functions. In Section 5.5 we will compute the Zel'dovich power spectrum for a range of μ_k and redshift values using an alternate integration method. In Vlah & White (2019) and Chen et al. (2020) both methods were tested and were both found to converge to within a sub-percent level.

5.3.2 Analytic computation of the CTM redshift-space power spectrum

The real-space position $\mathbf{x}$ for the CTM is given in Equation (3.47) and its derivative is

$$\dot{x}_j = aH\Psi_i^{(0)}\left(\mathbf{q}, t_i\right)\left[A\left(z\right) f_1\delta_{ij} + B\left(z\right) f_2 E_{ij}\left(\mathbf{q}, t_i\right) + \frac{1}{3}B\left(z\right) f_2\delta^{(0)}\left(\mathbf{q}, t_i\right)\delta_{ij}\right]. \tag{5.22}$$

The functions $f_1 = \frac{d\ln A}{d\ln a}$ and $f_2 = \frac{d\ln B}{d\ln a}$ are analogous to the function f introduced in Equation (5.5). Following Taylor & Hamilton (1996), Vlah & White (2019) and Chen et al. (2020) the redshift-space position (5.16) can be written as

$$s_i = q_i + A\left(z\right) R_{ij}^1\Psi_j^{(0)}\left(\mathbf{q}, t_i\right) + B\left(z\right) R_{ij}^2\Psi_k^{(0)}\left(\mathbf{q}, t_i\right) E_{jk}\left(\mathbf{q}, t_i\right) + \frac{1}{3}B\left(z\right) R_{ij}^2\Psi_j^{(0)}\left(\mathbf{q}, t_i\right)\delta^{(0)}\left(\mathbf{q}, t_i\right) \tag{5.23}$$

with $R_{ij}^1 = \delta_{ij} + f_1\hat{z}_i\hat{z}_j$ and $R_{ij}^2 = \delta_{ij} + f_2\hat{z}_i\hat{z}_j$. The redshift-space CTM power spectrum is,

$$\begin{aligned} \mathrm{P^s}\left(k, z\right) = \int d^3q\ \mathrm{e}^{i\mathbf{k}\cdot\mathbf{q}}\Bigg[\Big\langle \mathrm{e}^{\mathrm{ik_i}\left[\mathrm{AR^1_{ij}\Psi_j + BR^2_{ij}\Psi_k E_{jk} + \frac{1}{3}BR^2_{ij}\Psi_j\delta^{(0)}}\right]} \\ \mathrm{e}^{-\mathrm{ik_i}\left[\mathrm{AR^1_{ij}\Psi'_j + BR^2_{ij}\Psi'_k E'_{jk} + \frac{1}{3}BR^2_{ij}\Psi'_j\delta^{(0)\prime}}\right]}\Big\rangle - 1\Bigg] \end{aligned} \tag{5.24}$$

which can be calculated exactly like the real space power spectrum in Section 3.4. This leads to

$$\mathrm{P^s}\left(k, z\right) = \int d^3q\ \mathrm{e}^{i\mathbf{k}\cdot\mathbf{q}}\left[\left(\left|\det 1 + \mathbf{MC}\right|\right)^{-1/2}\mathrm{e}^{-\frac{1}{2}\mathbf{K}^T\mathbf{C}\left[1+\mathbf{MC}\right]^{-1}\mathbf{K}} - 1\right] \tag{5.25}$$

with $\mathbf{K} = \left(Ak_\alpha R^1_{\alpha\beta}, -Ak_\alpha R^1_{\alpha\beta}, 0, 0, 0, 0\right)$, the covariance matrix, $\mathbf{C}$, as in (3.51) and

$$\mathbf{M} = R^2_{\alpha\delta} \begin{bmatrix} 0 & 0 & -iBk_\alpha\delta_{\beta\gamma} & 0 & -\frac{1}{3}iBk_\alpha & 0 \\ 0 & 0 & 0 & iBk_\alpha\delta_{\beta\gamma} & 0 & \frac{1}{3}iBk_\alpha \\ -iBk_\alpha\delta_{\beta\gamma} & 0 & 0 & 0 & 0 & 0 \\ 0 & iBk_\alpha\delta_{\beta\gamma} & 0 & 0 & 0 & 0 \\ -\frac{1}{3}iBk_\alpha & 0 & 0 & 0 & 0 & 0 \\ 0 & \frac{1}{3}iBk_\alpha & 0 & 0 & 0 & 0 \end{bmatrix}. \quad (5.26)$$

Again as the full expression in Equation (5.25) is numerically too challenging to currently calculate we again expand to order ϵ^2. Hence the expanded redshift-space power spectrum is

$$\mathrm{P^s}\left(k, z\right) \approx \int d^3q \; \mathrm{e}^{i\mathbf{k}\cdot\mathbf{q}} \left[\mathrm{e}^{-\frac{1}{2}A^2(z)k_k k_l R^1_{ik} R^1_{jl} A'_{ij}(\mathbf{q})} \mathrm{e}^{B^2(z)k_k k_l R^2_{ik} R^2_{jl} B'_{ij}(q)} - 1\right] \quad (5.27)$$

where $A'_{ij}\left(\mathbf{q}\right) = X'\left(q\right)\delta_{ij} + Y'\left(q\right)\hat{q}_i\hat{q}_j$ and $B'_{ij}\left(\mathbf{q}\right) = W'\left(q\right)\delta_{ij} + Z'\left(q\right)\hat{q}_i\hat{q}_j$. The functions X', Y', W' and Z' are defined and calculated in Sections 3.2.4 and 3.4.4. We wish to calculate (5.27) numerically. In order to achieve this we follow the method presented in Vlah & White (2019) and Chen et al. (2020). We refer the reader in particular to Vlah & White (2019) for a derivation of the Zel'dovich power spectrum in redshift space using this method which is a simplified case of the calculation carried out here. The method used in Section 5.3.1 cannot easily be applied to the cosmological trajectories power spectrum as we have f_1 and f_2.

We begin by expanding the exponents in (5.27)

$$k_i k_j R^1_{ij} R^1_{jm} A'_{lm} = k^2 X' \left(1 + f_1^2\mu_k^2 + 2f_1\mu_k\right) + k^2 Y' \left(\mu^2 + f_1^2\mu_k^2\left(\hat{\mathbf{z}}\cdot\hat{\mathbf{q}}\right)^2 + 2f_1\mu_k\mu\left(\hat{\mathbf{z}}\cdot\hat{\mathbf{q}}\right)\right) \quad (5.28a)$$

$$k_i k_j R^2_{ij} R^2_{jm} B'_{lm} = k^2 W' \left(1 + f_2^2\mu_k^2 + 2f_2\mu_k\right) + k^2 Z' \left(\mu^2 + f_2^2\mu_k^2\left(\hat{\mathbf{z}}\cdot\hat{\mathbf{q}}\right)^2 + 2f_2\mu_k\mu\left(\hat{\mathbf{z}}\cdot\hat{\mathbf{q}}\right)\right) \quad (5.28b)$$

where $\mu = \hat{\mathbf{k}} \cdot \hat{\mathbf{q}}$ and $\mu_k = \hat{\mathbf{k}} \cdot \hat{\mathbf{z}}$. The value of μ_k dictates the angle between the $\hat{\mathbf{k}}$ direction and the line-of-sight i.e. if $\mu_k = 0$ the line-of-sight is perpendicular to the $\hat{\mathbf{k}}$ vector. The cosine of the angle between the line-of-sight $\hat{\mathbf{z}}$ vector and the vector $\hat{\mathbf{q}}$ can be expressed using spherical coordinates as

$$\hat{\mathbf{z}} \cdot \hat{\mathbf{q}} = \mu\mu_k + \sqrt{1-\mu_k^2}\sqrt{1-\mu^2}\cos\phi. \tag{5.29}$$

Let us define the following functions; $\alpha_0 = 1 + f_1\mu_k^2\,(2+f_1)$, $\alpha_0^1 = 1 + f_2\mu_k^2\,(2+f_2)$,$\alpha_1 = \left(1+f_1\mu_k^2\right)^2$, $\alpha_1^1 = \left(1+f_2\mu_k^2\right)^2$, $\alpha_2 = 2f_1\mu_k\sqrt{1-\mu_k^2}\left(f_1\mu_k^2+1\right)$, $\alpha_2^1 = 2f_2\mu_k\sqrt{1-\mu_k^2}\left(f_2\mu_k^2+1\right)$, $\alpha_3 = f_1^2\mu_k^2\left(1-\mu_k^2\right)$ and $\alpha_3^1 = f_2^2\mu_k^2\left(1-\mu_k^2\right)$. The α functions with no superscript correspond to those used in Vlah & White (2019) for the Zel'dovich power spectrum. Now extracting the azimuthal angle from the power spectrum integral we must calculate

$$\begin{aligned}\mathrm{P^s}\left(k,\mu_k,z\right) \approx \int d^3q\; \mathrm{e}^{i\mathbf{k}\cdot\mathbf{q}}\mathrm{e}^{-\frac{1}{2}k^2\left(A^2X'\alpha_0-2B^2W'\alpha_0^1\right)}\mathrm{e}^{-\frac{1}{2}k^2\mu^2\left(A^2Y'\alpha_1-2B^2Z'\alpha_1^1\right)} \\ \times\left[\int_0^{2\pi}\frac{d\phi}{2\pi}\mathrm{e}^{-\frac{1}{2}k^2\left(A^2Y'\alpha_3-2B^2Z'\alpha_3^1\right)\left(1-\mu^2\right)\cos^2\phi} \right. \\ \left. \mathrm{e}^{-\frac{1}{2}k^2\left(A^2Y'\alpha_2-2B^2Z'\alpha_2^1\right)\mu\sqrt{1-\mu^2}\cos\phi}\right].\end{aligned} \tag{5.30}$$

In order to use the following integral identity (Chen et al., 2020)

$$\int_0^{2\pi}\frac{d\phi}{2\pi}\mathrm{e}^{\alpha\mu\sqrt{1-\mu^2}\cos\phi+\beta\left(1-\mu^2\right)\cos^2\phi} = \sum_{l=0}^{\infty}F_l\left(\alpha,\beta\right)\frac{\alpha^2\mu^2}{\beta}^l \tag{5.31}$$

where

$$\begin{aligned}F_l\left(\alpha,\beta\right) = \sum_{m=0}^{l}\frac{\Gamma\left(m+\frac{1}{2}\right)}{\pi^{1/2}\Gamma\left(m+1\right)\Gamma\left(1+2m-l\right)\Gamma\left(2l-2m+1\right)}\left(-\frac{\beta^2}{\alpha^2}\right)^m \\ \times\; M\left(l-2m;l-m+\frac{1}{2};\frac{\alpha^2}{4\beta}\right)\; M\left(m+\frac{1}{2};m+1;\beta\right)\end{aligned} \tag{5.32}$$

and $M(a;b;c)$ is a hypergeometric function of the first kind to evaluate the azimuthal integral we will re-write the exponents functions. These re-written functions are

$$A^2X'\alpha_0 - 2B^2W'\alpha_0^1 = A^2X'\alpha_0\left[1 - 2\left(\frac{B}{A}\right)^2\frac{W'}{X'}\frac{\alpha_0^1}{\alpha_0}\right] = A^2X'\alpha_0\xi = A^2X'\alpha_0^{\rm BZ} \tag{5.33a}$$

$$A^2Y'\alpha_1 - 2B^2Z'\alpha_1^1 = A^2Y'\alpha_1\left[1 - 2\left(\frac{B}{A}\right)^2\frac{Z'}{Y'}\frac{\alpha_1^1}{\alpha_1}\right] = A^2Y'\alpha_1\kappa = A^2Y'\alpha_1^{\rm BZ} \tag{5.33b}$$

$$-\frac{1}{2}\left(A^2Y'\alpha_3 - 2B^2Z'\alpha_3^1\right) = -\frac{1}{2}k^2A^2Y'\alpha_3\left[1 - 2\left(\frac{B}{A}\right)^2\frac{Z'}{Y'}\frac{\alpha_3^1}{\alpha_3}\right] = C\alpha_3\sigma = C\alpha_3^{\rm BZ} \tag{5.33c}$$

$$-\frac{1}{2}\left(A^2Y'\alpha_2 - 2B^2Z'\alpha_2^1\right) = -\frac{1}{2}k^2A^2Y'\alpha_2\left[1 - 2\left(\frac{B}{A}\right)^2\frac{Z'}{Y'}\frac{\alpha_2^1}{\alpha_2}\right] = C\alpha_2\gamma = C\alpha_2^{\rm BZ}. \tag{5.33d}$$

Now the redshift-space power spectrum is,

$$\begin{aligned}{\rm P^s}(k,\mu_k,z) \approx & \int d^3q\ {\rm e}^{i\mathbf{k}\cdot\mathbf{q}}{\rm e}^{-\frac{1}{2}k^2A^2X'\alpha_0^{\rm BZ}}{\rm e}^{-\frac{1}{2}k^2A^2Y'\alpha_1^{\rm BZ}} \\ & \times\left[\int_0^{2\pi}\frac{d\phi}{2\pi}{\rm e}^{C\alpha_3^{\rm BZ}\left(1-\mu^2\right)\cos^2\phi + C\alpha_2^{\rm BZ}\mu\sqrt{1-\mu^2}\cos\phi}\right]\end{aligned} \tag{5.34}$$

and computing the azimuthal integral using (5.32) gives

$$\begin{aligned}{\rm P^s}(k,\mu_k,z) \approx & \int d^3q\ {\rm e}^{i\mathbf{k}\cdot\mathbf{q}}{\rm e}^{-\frac{1}{2}k^2A^2X'\alpha_0^{\rm BZ}}{\rm e}^{-\frac{1}{2}k^2A^2Y'\alpha_1^{\rm BZ}} \\ & \times\sum_{l=0}^{\infty}F_l\left(2C\sqrt{\alpha_0\alpha_1}\left(\frac{\xi}{\kappa}\right)^{1/2}\frac{\gamma^2}{\sigma}, C\alpha_0\frac{\gamma^2\xi}{\sigma\kappa}\right)\left(C\alpha_1\mu^2\right)^l\left(\frac{\gamma}{\sigma}\right)^l.\end{aligned} \tag{5.35}$$

The only integral left to compute analytically is the integral over μ this is carried

out using a specific case of the integral formula in (3.27),

$$\frac{1}{2}\int_{-1}^{1} d\mu\, \mu^{2l} \mathrm{e}^{i\mu E+\mu^2 D} = \frac{(-1)^l\, \mathrm{e}^D}{D^l} \sum_{n=0}^{\infty} U\left(-l; n-l+1; -D\right) \left(\frac{-2D}{E}\right)^n j_n\left(E\right), \quad (5.36)$$

where $U\left(a; b; c\right)$ is a confluent hypergeometric function of the second kind. The analytic redshift-space power spectrum for the CTM is hence given by

$$\begin{aligned} \mathrm{P}^{\mathrm{s}}\left(k, \mu_k, z\right) \approx 4\pi \sum_{n=0}^{\infty} \int_0^{\infty} dq\; \mathrm{e}^{-\frac{1}{2}k^2A^2X'\alpha_0^{\mathrm{BZ}}} \mathrm{e}^{-\frac{1}{2}k^2A^2Y'\alpha_1^{\mathrm{BZ}}} \left(\frac{kA^2Y'\alpha_1^{\mathrm{BZ}}}{q}\right)^n j_n\left(kq\right) \\ \sum_{l=0}^{\infty} \left(-1\right)^l F_l\left(C\alpha_1\right)^l \left(C\alpha_1^{\mathrm{BZ}}\right)^{-l} \left(\frac{\gamma^2}{\sigma}\right)^l U\left(-l; n-l+1; -C\alpha_1^{\mathrm{BZ}}\right). \end{aligned} \quad (5.37)$$

The power spectrum (5.37) can be re-expressed such that all higher-order gravitational terms and redshift-space corrections are contained in a function $K_n\left(q, z, \mu_k\right)$

$$\mathrm{P}^{\mathrm{s}}\left(k, \mu_k, z\right) \approx 4\pi \sum_{n=0}^{\infty} \int_0^{\infty} dq\; \mathrm{e}^{-\frac{1}{2}k^2A^2\left(X'+Y'\right)} \left(\frac{kA^2Y'}{q}\right)^n j_n\left(kq\right) K_n\left(q, z, \mu_k\right) \quad (5.38)$$

with

$$\begin{aligned} K_n\left(q, z, \mu_k\right) = \mathrm{e}^{-\frac{1}{2}k^2A^2X'\left[f_1\mu_k^2\left(2+f_1\right)-2\left(\frac{B}{A}\right)^2\frac{W'}{X'}\alpha_0^1\right]} \mathrm{e}^{-\frac{1}{2}k^2A^2Y'\left[f_1\mu_k^2\left(2+f_1\mu_k^2\right)-2\left(\frac{B}{A}\right)^2\frac{Z'}{Y'}\alpha_1^1\right]} \\ \times \sum_{l=0}^{\infty} F_l\left(2C\sqrt{\alpha_0\alpha_1}\left(\frac{\xi}{\kappa}\right)^{1/2}\frac{\gamma^2}{\sigma}, C\alpha_0\frac{\gamma^2\xi}{\sigma\kappa}\right)\left(-1\right)^l \alpha_1^n\kappa^{n-l}\left(\frac{\gamma^2}{\sigma}\right)^l U\left(-l; n-l+1; -C\alpha_1\kappa\right). \end{aligned} \quad (5.39)$$

In the next section we will compute both the Zel'dovich and Beyond Zel'dovich power spectra using (5.38).

5.4 Calculating the Beyond Zel'dovich redshift-space power spectrum at different redshifts and investigating the free parameters

In this section we will compute the Beyond Zel'dovich redshift-space power spectrum at multiple redshifts and line-of-sight angle values in order to investigate the free parameter ϵ. We again use CLASS to generate the initial power spectrum and CLASSYLSS to calculate the linear growth function and Hubble parameter. All of the power spectra shown in this section were calculated using 1000 k-values, *Planck18* cosmology and with $n = 32$ and $l = 10$.

We tested the convergence of the power spectrum and found that there was no significant difference between 1000 and 5000 k-values as there was in real space. The convergence issue in real space was caused by the oscillations in the functions X and Y on small scales. In redshift space we do not expect to reach these scales as the Zel'dovich approximation breaks down at a smaller k-value due to peculiar velocities i.e. the fingers-of-God effect. The CTM MODULE takes around one hour to run for one redshift value and six μ_k values on a standard computer.

5.4.1 Different ϵ values

In Section 4.2.1 we investigated the effect of the free parameter ϵ on the Beyond Zel'dovich power spectrum. This parameter controls the size of the higher-order gravitational terms and the size of the over and under densities. We saw in Figure 4.1 that the larger the ϵ value the larger the impact of the higher-order terms and the smaller the ϵ value the smaller the impact. In fact, for small ϵ values the Beyond Zel'dovich power spectrum tended to the Zel'dovich result in real space. In this subsection we will calculate the redshift-space Beyond Zel'dovich power spectrum for multiple redshifts and ϵ values in order to choose the most suitable ϵ value as we did in real space.

In Figure 5.2 the dimensionless redshift-space Beyond Zel'dovich power spectrum is shown for four redshifts ($z = 0,\ 1,\ 2$ and 3). Three angles of sight are shown: $\mu_k = 0$ (purple lines), $\mu_k = 0.5$ (orange lines) and $\mu_k = 1$ (blue lines) and three ϵ values: $\epsilon = 0.01$ (dotted lines), $\epsilon = 0.1$ (dashed lines) and $\epsilon = 1$ (solid lines). For all ϵ values and redshifts the Beyond Zel'dovich power spectrum tends to

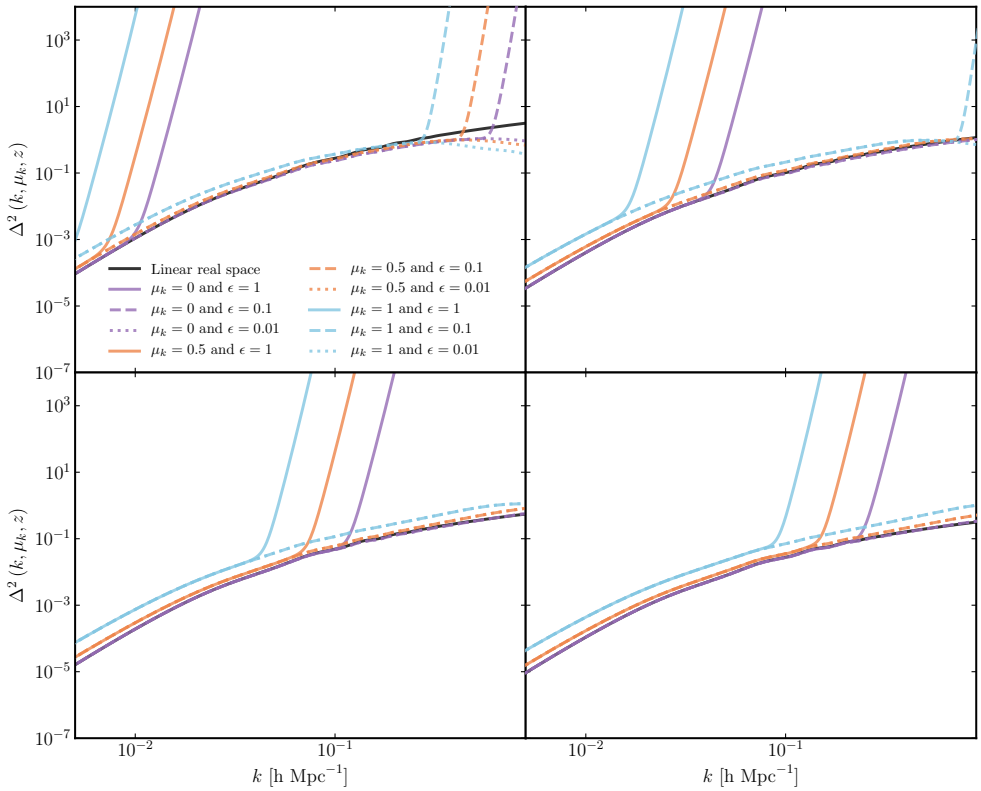

Figure 5.2 *In this figure the dimensionless linear real space (black solid line) and Beyond Zel'dovich power spectra are shown. The four panels are $z = 0$ (upper left), $z = 1$ (upper right), $z = 2$ (lower left) and $z = 3$ (lower right). The Beyond Zel'dovich redshift-space power spectra are calculated for three μ_k values: $\mu_k = 0$ in purple, $\mu_k = 0.4$ in orange and $\mu_k = 1$ in blue and three ϵ values: $\epsilon = 0.01$ in dotted lines, $\epsilon = 0.1$ in dashed lines and $\epsilon = 1$ in solid lines.*

the linear real-space power spectrum on large scales for $\mu_k = 0$ (when $\hat{\mathbf{k}}$ is perpendicular to the line-of-sight $\hat{\mathbf{z}}$) as expected. On small scales and low redshifts there is a wave-like feature as was the case in real space. Again this feature is more prominent for larger ϵ values and is partly caused by the breakdown of the Zel'dovich approximation and random velocities of virialised structures on small scales. The higher-order gravitational terms are proportional to B^2 which becomes very large for high k-values and at low redshifts. This causes the numerical tool used to calculated the spherical Bessel integrals to fail. We leave it to future work to investigate this further. The divergence of the Beyond Zel'dovich power spectrum is more pronounced as μ_k approaches one (when $\hat{\mathbf{k}}$ is parallel to the line-of-sight $\hat{\mathbf{z}}$). This effect is shown in the diagram 5.1 as the Fingers-of-God.

When $\epsilon = 0.01$ the Beyond Zel'dovich power spectrum appears to converge to the Zel'dovich power spectrum at all redshifts and for all μ_k values. In Figure 5.3

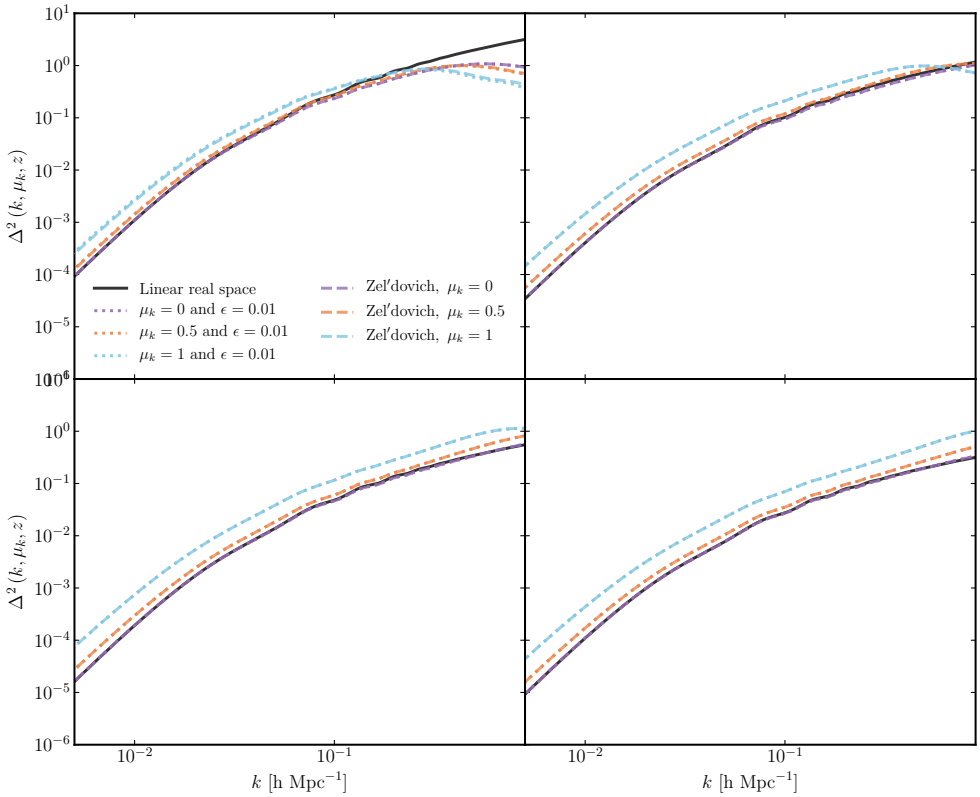

Figure 5.3 *Figure demonstrating the convergence of the Beyond Zel'dovich (dotted lines) redshift space to the Zel'dovich (dashed lines) redshift-space power spectrum for small ϵ values. Again three μ_k values are shown $\mu_k = 0$ in purple, $\mu_k = 0.4$ in orange and $\mu_k = 1$ in blue and the four panels are redshifts $z = 0,\ 1,\ 2$ and 3 from upper left to lower right.*

the dimensionless Beyond Zel'dovich power spectrum with $\epsilon = 0.01$ (dotted lines) is shown for four redshifts ($z = 0,\ 1,\ 2$ and 3) and three μ_k values ($\mu_k = 0,\ 0.5$ and 1) in purple, orange and blue lines respectively. It is clear that the Beyond Zel'dovich power spectrum converges to the Zel'dovich power spectrum (dashed lines) at all redshifts and for all μ_k values. This validates our method and the hypothesis that when the higher-order gravitational terms are small the Zel'dovich approximation is recovered. This is precisely the result obtained in real space in Figure 4.1.

In the above figures the Beyond Zel'dovich approximation broke down at a smaller k-value than in real space. This is to be expected as it is well known that perturbation theory breaks down faster in redshift space due to the random motions of virialised structures. On large scales for $\mu_k = 0.5$ and $\mu_k = 1$ there is an enhancement of power compared to the linear power spectrum. This is due to the infall of matter into collapsing structures (squashing effect). On small scales

there is a damping of power compared to the linear power spectrum. This is as a result of the random motion of virialised structures (Fingers-of-God). We will choose the value of $\epsilon = 1$ in order to capture the non-linear gravitational element of the Beyond Zel'dovich approximation at the most redshifts.

5.4.2 Calculating a Gaussian damped Beyond Zel'dovich redshift-space power spectrum at different redshifts

In Section 4.3 we introduced a Gaussian cutoff in the initial power spectrum as a method to reduce the impact of the small-scale breakdown on the Beyond Zel'dovich power spectrum at larger scales. This damped initial power spectrum is given by

$$\mathrm{P}_{\mathrm{damped}}\left(k, z_i\right) = \mathrm{e}^{-\left(\frac{k}{k_c}\right)^2} \mathrm{P}_{\mathrm{lin}}\left(k, z_i\right). \tag{5.40}$$

where k_c is the cutoff scale. Any non-linear effects after this cutoff value should be damped down and should reduce the impact of the small-scale breakdown on larger scales. In this section we will calculate the redshift-space Beyond Zel'dovich with a Gaussian damped initial power spectrum. We will also investigate whether the cutoff value, k_c, depends on the cosmology chosen.

Different k_c values

In Figure 5.5 the maximum $k-$value, k_{max}, reached before the Beyond Zel'dovich power spectra has a larger difference of $\Delta^2_{\mathrm{diff}} = \pm 5\%$ from the simulation results is shown versus ten cutoff values. The simulated redshift-space power spectra in this chapter have been computed using NBODYKIT[2] (Hand et al., 2018). The software uses PMESH[3] to generate a particle mesh in order to grid the data. The linear overdensity, $\delta_{\mathrm{L}}\left(\mathbf{k}\right)$, and velocity field given by,

$$\mathbf{v}\left(\mathbf{k}\right) = i f a H \delta_{\mathrm{L}}\left(\mathbf{k}\right) \frac{\mathbf{k}}{k^2}, \tag{5.41}$$

[2]https://nbodykit.readthedocs.io/en/latest/
[3]https://github.com/rainwoodman/pmesh

are then calculated in Fourier space. These fields are inverse Fourier transformed and used as the initial conditions. The next step is to generate a log-normal catalog of objects. In Coles & Jones (1991) and Agrawal et al. (2017) it is shown that on large to mildly non-linear scales the distribution of galaxies can be approximated using a log-normal distribution. The transformed overdensity field is

$$\delta\left(\mathbf{x}\right) = \mathrm{e}^{-\sigma^2 + b_L \delta_{\mathrm{L}}(\mathbf{x})} \tag{5.42}$$

where σ^2 ensures that the average overdensity field vanishes and b_L is the Lagrangian bias factor given by $b_L = b_1 - 1$ with b_1 being the linear bias factor. The positions of the objects are determined by Poisson sampling each cell of the mesh. The linear overdensity field is then evolved by applying the Zel'dovich approximation and redshift-space distortions are added along the line-of-sight using the velocity offset ($f\Psi$). Finally, the catalog is converted to a mesh using Cloud In Cell (CIC, Hockney & Eastwood (1981), Jing (2005)) interpolation and the output is Fourier transformed to obtain the power spectrum.

The simulated power spectra were computed with a box size of 2048 Mpch^{-1}, a mesh size of 512 Mpch^{-1} and $b_L = 1$. We computed the simulated power spectra with redshift-space distortions in the x, y and z axes and then averaged these results to obtain the simulated power spectra shown. This was in order to average out the spread on large scales as discussed in Jennings et al. (2010). The simulations were run for the following lines-of-sight μ_k = 0, 0.1, 0.2, 0.3, 0.4, 0.5, 0.6, 0.7, 0.8, 0.9, 1 and the k_{max} values shown in Figures 5.4 and 5.5 have been averaged over all μ_k values.

In Figure 5.4, the effect of different cutoff values (k_c = 50, 5 and 0.5 h Mpc^{-1}) is shown for redshifts z = 0, 1, 2, 3, 4 and 5. One can see that small cutoff-values have a large effect at low redshifts but do not effect high-redshift results. This was the case in real space. Similarly a large cutoff-value has a detrimental effect at low redshifts, this was again observed in real space. We conclude from Figure 5.4 that a cutoff value of around k_c = 5 h Mpc^{-1} is optimal. Therefore, in Figure 5.5 we test a wider range of cutoff values of the same order k_c = 1, 2, 3, 4, 5 6, 7, 8, 9, 10 h Mpc^{-1} at z = 0, 1, 2, 3, 4 and 5. In Figure 5.5, the detrimental effect of k_c = 1 h Mpc^{-1} at high redshifts and the ineffectiveness of

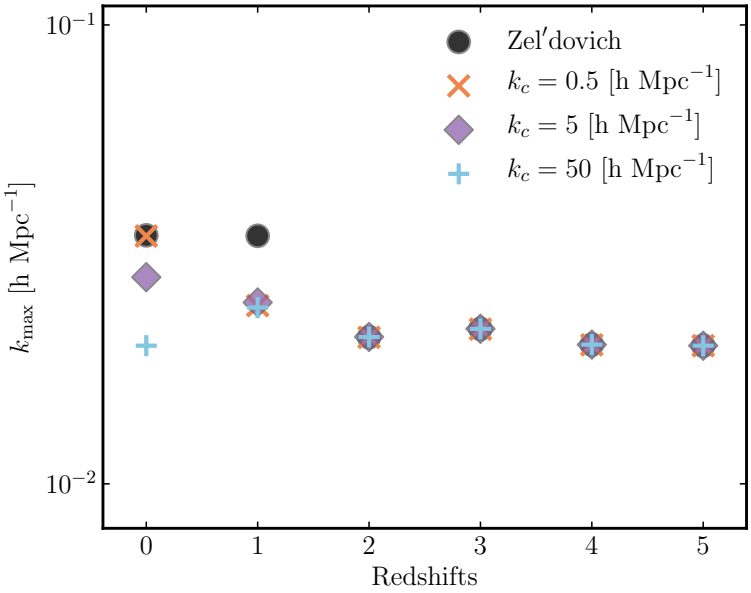

Figure 5.4 *Figure showing the maximum k-value, $k_{\max}$, reached before the percentage difference between the damped Beyond Zel'dovich and the simulation data becomes larger than ±5% versus a range of cutoff values. The black dots show the $k_{\max}$ for the undamped Zel'dovich approximation, the orange crosses show the $k_{\max}$ for the Beyond Zel'dovich approximation with $k_c = 0.5$ h Mpc^{-1}, the purple diamonds show the $k_{\max}$ for the Beyond Zel'dovich approximation with $k_c = 5$ h Mpc^{-1} and the blue plus signs show the $k_{\max}$ for the Beyond Zel'dovich approximation with $k_c = 50$ h Mpc^{-1}.*

large cutoff values at low redshifts can be clearly seen. Overall, a cutoff value of $k_c = 4$ h Mpc^{-1} has the greatest desired effect for all redshifts and μ_k values. In all future figures any result labelled as Beyond Zel'dovich will be calculated with $\epsilon = 1$ and $k_c = 4$ h Mpc^{-1}.

We discussed the possibility of k_c depending on the cosmology used in Section 4.3.1. In real space we found that there was a weak dependence on both cosmology and redshift, however we could only test our results against those from the EUCLID EMULATOR. This resulted in having a narrow range of $\boldsymbol{\Omega}_m$ values to choose from. As we are only concentrating on *Planck18* cosmology in this Thesis and cannot obtain accurate enough simulation data in real or redshift space we will not investigate this further. However, in future work when we hope to apply the CTM to modified gravity models we will carry out a full exhaustive study of these dependencies. Currently, we will assume that in redshift space there is also a mild dependence of the cutoff scale on cosmology and redshift.

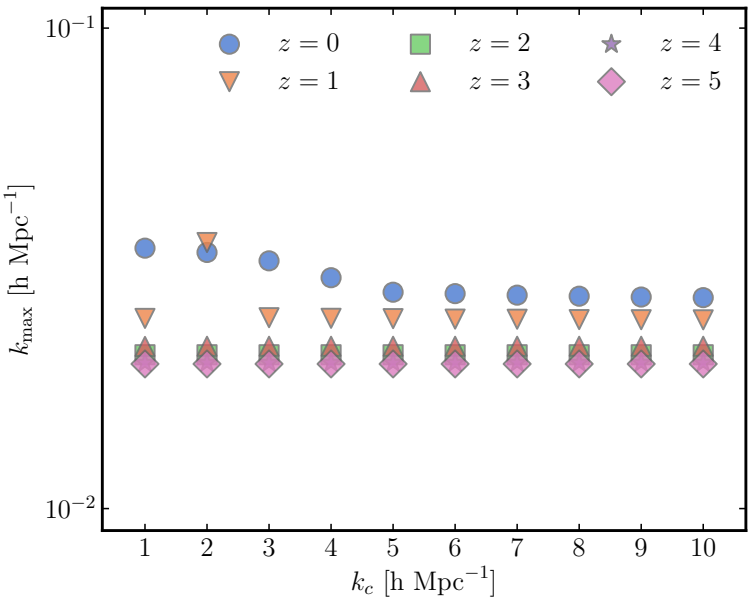

Figure 5.5 *Figure showing the maximum k-value, $k_{\max}$, reached before the percentage difference between the damped Beyond Zel'dovich and the simulation data becomes larger than $\Delta^2_{\text{diff}} = \pm 5\%$ versus a range of cutoff values. The results for $z = 0$ are shown in blue dots, $z = 1$ in orange downward pointing triangles, $z = 2$ in green squares, $z = 3$ in red upward pointing triangles, $z = 4$ in purple stars and $z = 5$ in pink diamonds.*

5.5 Comparing Beyond Zel'dovich to other methods in redshift space

In this section we will assess the performance of the Beyond Zel'dovich approximation. The Zel'dovich and Beyond Zel'dovich results have been computed using 5000 k-values, $\epsilon = 1$ and $k_c = 4$ h Mpc^{-1}.

In Figure 5.6 the dimensionless linear real space, Zel'dovich and Beyond Zel'dovich power spectra are shown at six redshifts ($z = 0,\ 1,\ 2,\ 3,\ 4$ and 5). At all redshifts the Zel'dovich and Beyond Zel'dovich power spectra converge to the linear theory for $\mu_k = 0$ as expected. The Beyond Zel'dovich power spectrum breaks down due to mostly numerical issues at redshifts $z = 0$ and $z = 1$. This breakdown requires further investigation which will be discussed in Section 6.2. Again due to coherent peculiar velocities on large scales and incoherent peculiar velocities on small scales we expect an enhancement of power on large scales and a damping of power on small scales. This can be seen in the Zel'dovich and the Beyond Zel'dovich approximation (after $z = 1$). In order to assess the performance of the Beyond Zel'dovich approximation further we will compare these results to simulation data.

The percentage difference between the Zel'dovich (dashed lines) and Beyond Zel'dovich (solid lines) approximations and the simulation data is shown in Figure 5.7. The dark and light grey bands show the percentage difference values of 5% and 10% respectively. At all redshifts we approximately lie within 10% of the simulation results for $\mu_k = 0$ and $\mu_k = 0.5$. The large difference for the smallest k-value considered is due to the scattering effect described in Jennings et al. (2010) and numerical issues. The Zel'dovich approximation outperforms Beyond Zel'dovich at $z = 0$ for $\mu_k = 0.5$ and $\mu_k = 1$. However, both approximations breakdown as we approach $\mu_k = 1$ with some improvement at higher redshifts. In general the Beyond Zel'dovich approximation performs as well as Zel'dovich at all redshifts.

The 2-point correlation function for linear theory in real space (solid black line) and the Zel'dovich (purple dashed line) and Beyond Zel'dovich (orange dashed-dot line) approximations in redshift space at $z = 0$ are shown in Figure 5.8. We would expect there to be more smearing of the BAO (see Figure 4.9 for a demonstration of this effect in real space) along the line-of-sight due to the Fingers-of-God effect. The Beyond Zel'dovich correlation function at $\mu_k = 0$ has a stretched BAO signal

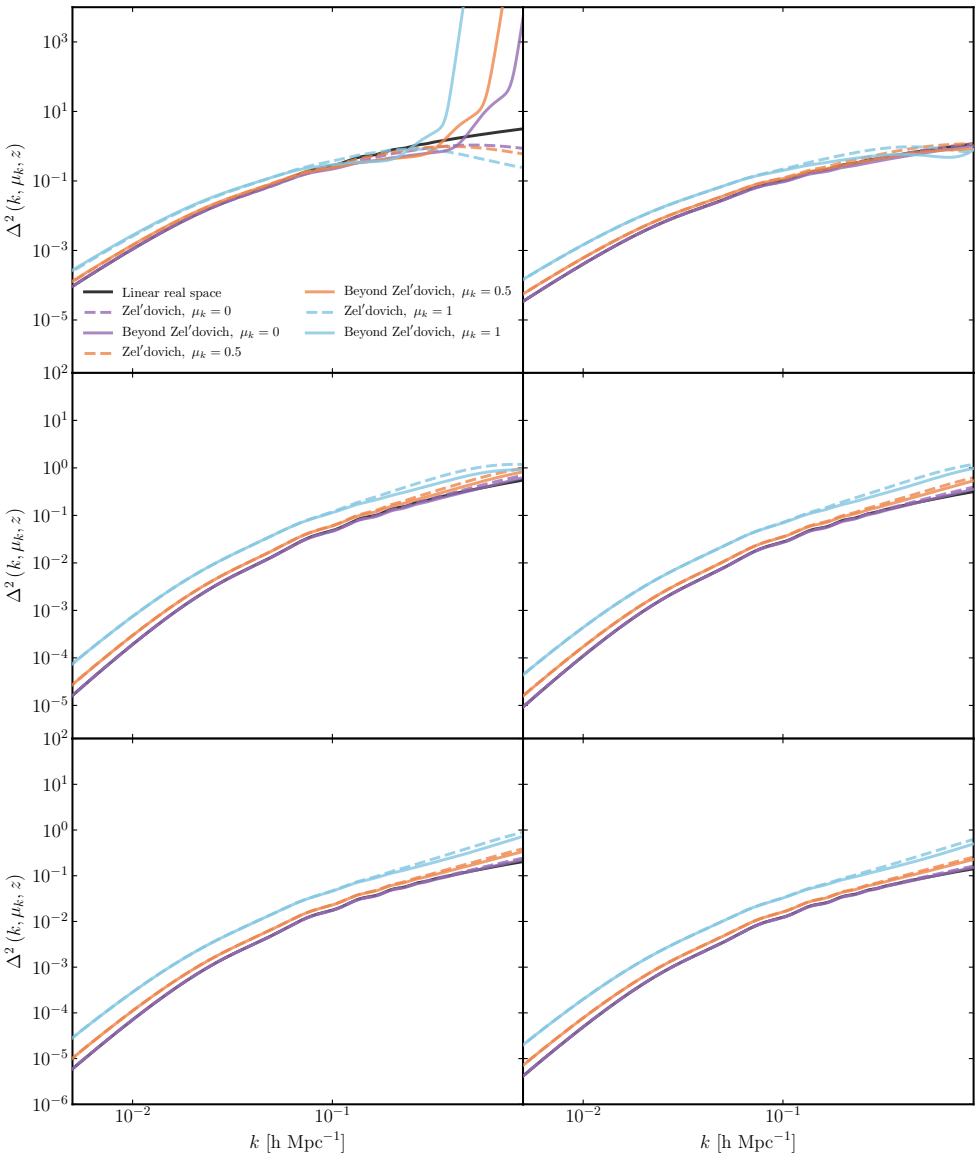

Figure 5.6 *The dimensionless real space linear (solid black lines), Zel'dovich (dashed lines), Beyond Zel'dovich (solid lines) power spectra in redshift space for three* $\mu_k = 0,\ 0.5,\ 1$ *values in purple, orange and blue respectively. The panels show six redshifts* ($z = 0,\ 1,\ 2,\ 3,\ 4$ *and* 5) *with the upper left panel being* $z = 0$ *and the lower right panel being* $z = 5$.

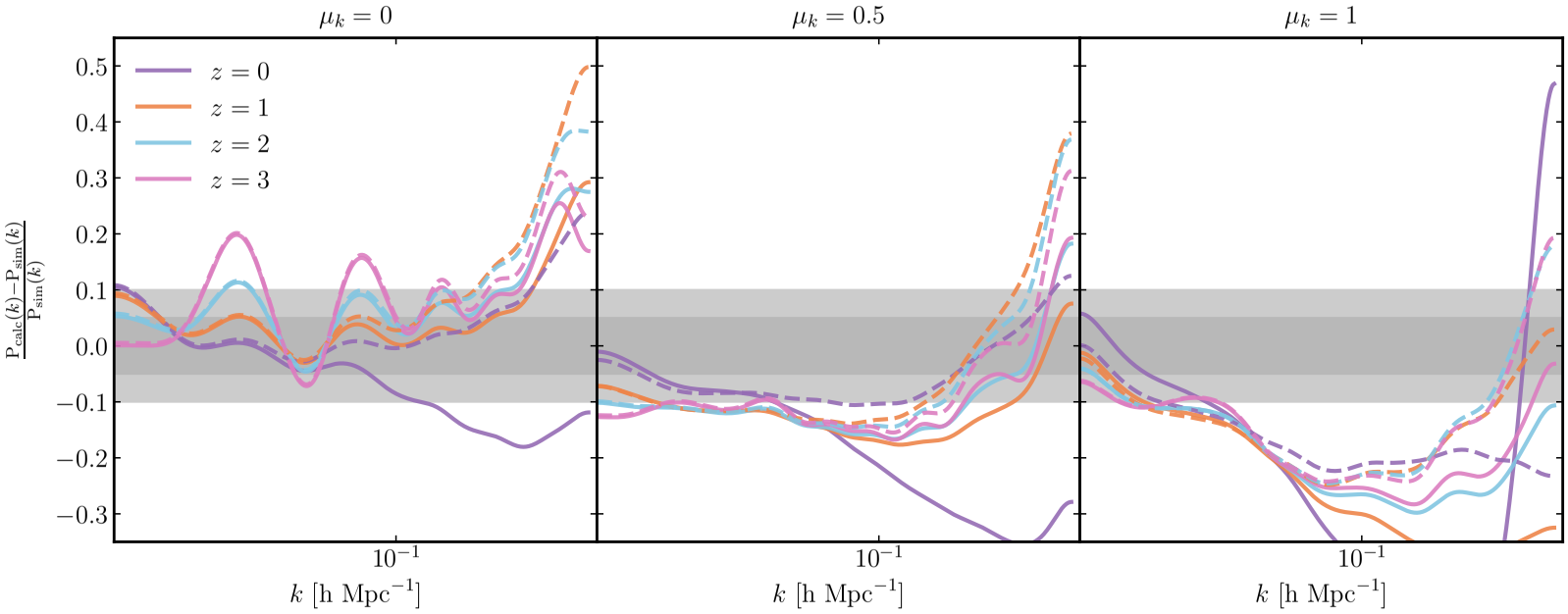

Figure 5.7 *Figure shown the percentage difference (4.4) between the Beyond Zel'dovich and simulation power spectra in solid lines and the Zel'dovich and simulation power spectra in dashed lines. The three panels are* $\mu_k = 0$, $\mu_k = 0.5$ *and* $\mu_k = 1$. *The dark grey shaded region is* $\Delta^2_{\text{diff}} = \pm 0.05$ *and the light grey shaded region is* $\Delta^2_{\text{diff}} = \pm 0.1$.

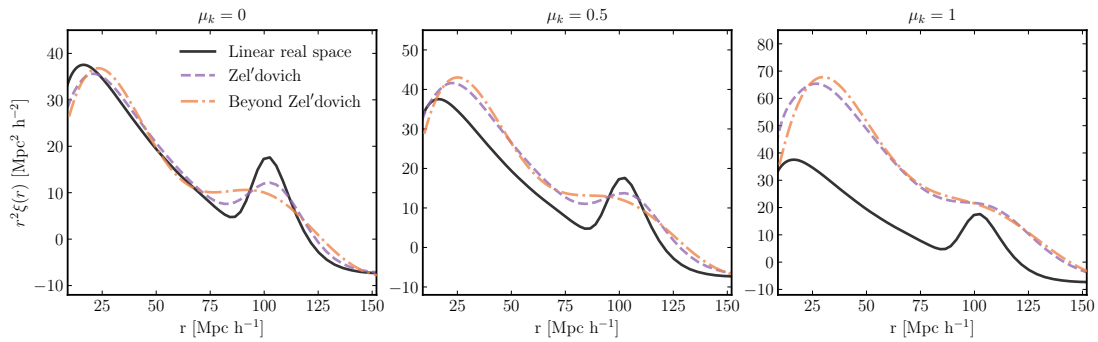

Figure 5.8 *The 2-point correlation function, $r^2\xi(r)$ at $z = 0$ is shown for linear linear in real space (black solid lines), Zel'dovich redshift space (purple dashed lines) and Beyond Zel'dovich redshift space (orange dot-dashed lines). The three panels are $\mu_k = 0$, $\mu_k = 0.5$ and $\mu_k = 1$.*

implying that the peculiar velocities are being modelled more accurately on mildly non-linear scales.

Although we have simulation data for the power spectrum we could not obtain accurate enough results for the correlation function due to limitations on box size. We therefore cannot determine whether the Beyond Zel'dovich approximation works as well or better than the Zel'dovich approximation when computing the correlation function. We leave this to future work.

5.5.1 Kaiser

The Kaiser formula used to compute power spectra in this section is given in Equation (5.10). The accuracy of the Kaiser formula compared to N-body simulations has been investigated in Heavens et al. (1998), Scoccimarro (1998), Matsubara (2008b), Carlson et al. (2009), Jennings et al. (2010) and Kwan et al. (2012). In Jennings et al. (2010) Kaiser was found to be accurate for $k < 0.03$ h Mpc^{-1}. This inaccuracy is shown in the left-hand column of Figure 5.9 for $z = 0$ to 3 from top to bottom row. The Kaiser formula is simply a scaling of the linear power spectrum. It therefore does not capture the small-scale Fingers-of-God effect at low redshifts.

Despite this failure to model mildly non-linear scales the Kaiser formula is widely used in observational surveys at low redshifts. It is for this reason that we perform a comparison of Kaiser with Beyond Zel'dovich. In Figure 5.10 the percentage difference between Kaiser, Beyond Zel'dovich and the simulation results is shown for redshifts $z = 0$ to 3. For redshifts above $z = 1$ we perform as well as Kaiser

for $\mu_k = 0$. Again at $\mu_k = 1$ Kaiser appears to overestimate the power spectrum and Beyond Zel'dovich underestimates the power spectrum.

Contour plots of the Kaiser, Zel'dovich and Beyond Zel'dovich power spectra at $z = 0$ are shown in Figure 5.12. The components $k_\parallel$ and $k_\perp$ are parallel and perpendicular to the line-of-sight $\hat{\mathbf{z}}$. If there were no RSD effects then the contour rings would be circles. However in redshift space, we expect to see stretching of the contours along the $k_\perp = 0$ direction and a squashing along the line-of-sight. The squashing is due to the Kaiser effect (caused by the infall of matter into collapsing structures) and the stretching is due to the random motions of virialised motions (Fingers-of-God). An example of this is shown in Figure 5.11 which was measured by the BOSS collaboration (Alam et al., 2017). The stretching and squashing of the contours can be seen in the left panel of Figure 5.12 clearly. The Kaiser effect is also visible for the Zel'dovich and Beyond Zel'dovich approximations which is encouraging. The squashing effect (large-scale effect) is more pronounced than the stretching effect. This suggests that on large scales we are capturing the Kaiser effect but are failing to fully capture the Fingers-of-God. This is to be expected as we saw both the Zel'dovich and Beyond Zel'dovich approximations breakdown as μ_k approaches $\mu_k = 1$ in Figure 5.7. The Fingers-of-God effect also captures physical behaviour that occurs after shell-crossing, which is exactly when perturbative schemes breakdown. We therefore do not expect to capture the Fingers-of-God effect at all. Figure B.1 shows preliminary results for the simulation power spectrum contours.

The scaled correlation functions for linear real-space, Kaiser (purple dashed lines) and Beyond Zel'dovich (orange dashed-dot lines) are shown in Figure 5.13 at $z = 0$. The Kaiser correlation lies on top of the linear real-space result for $\mu_k = 0$. We know this is not accurate as there should be smearing of the BAO peak even in real space due to non-linear effects discussed in Section 1.3.4. We therefore conclude that the Beyond Zel'dovich approximation is more accurate on BAO scales. This was to be expected as the Zel'dovich approximation is more accurate than linear theory when modelling the correlation function and the Kaiser formula is a scaling of the linear result.

Contours of the scaled correlation function $r^2\xi(r_\parallel, r_\perp)$ with respect to $r_\parallel$ (real-space position parallel to the line-of-sight) and $r_\perp$ (real-space position perpendicular to the line-of-sight) for the Kaiser, Zel'dovich and Beyond Zel'dovich approximations at $z = 0$ are shown in Figure 5.14. The white spaces are masked regions due to the $k_{\max}$ that can be reached before the Beyond Zel'dovich result

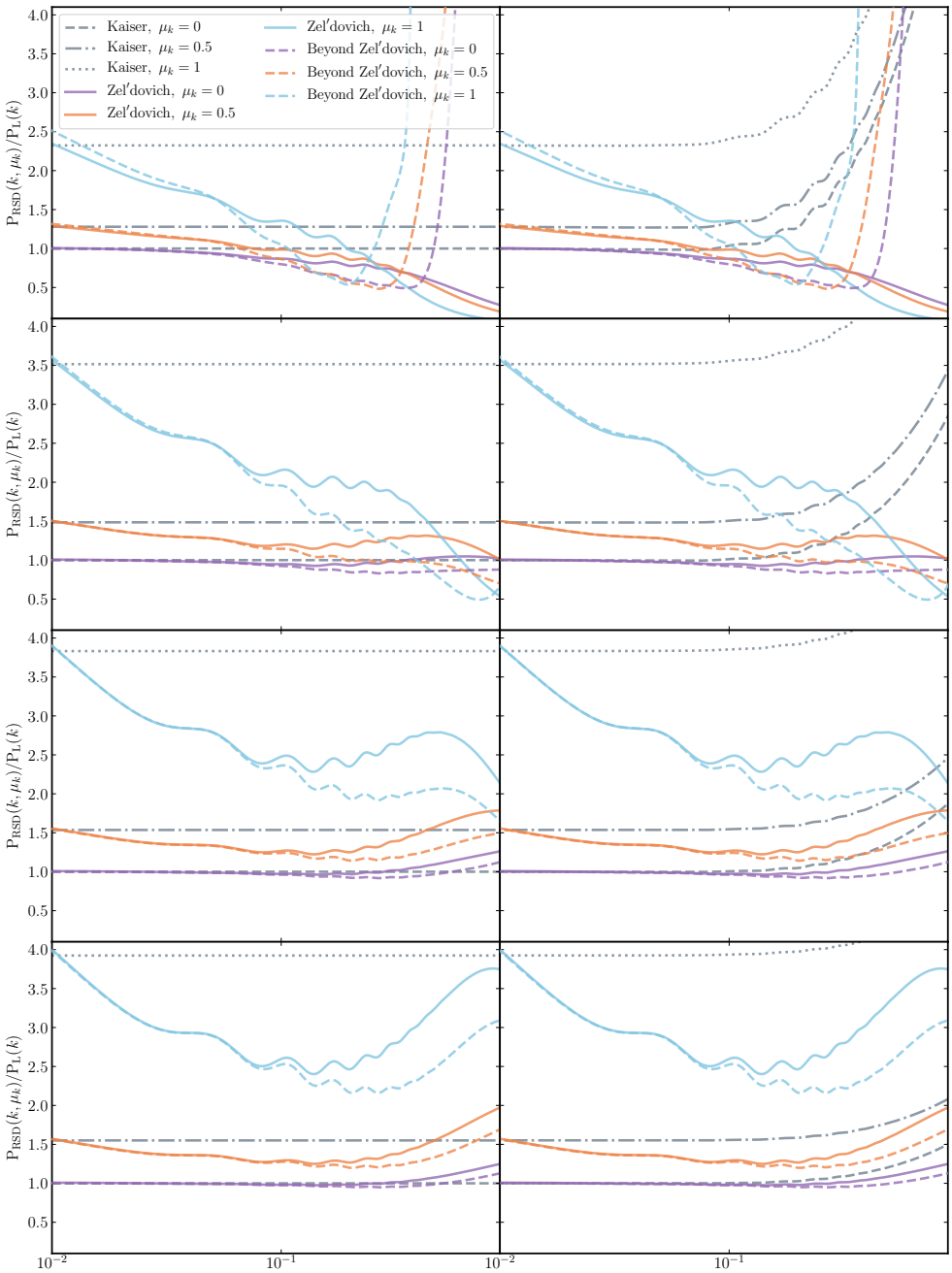

Figure 5.9 *The ratio between* $\mathrm{P_{RSD}}(k, \mu_k)$ *and* $\mathrm{P_L}(k)$ *in real space is shown for three* $\mu_k = 0,\ 0.5$ *and* 1. *The rows are the redshifts* $z = 0 - 3$ *respectively and the grey lines in left-hand column show* $\mathrm{P_{Kaiser}}/\mathrm{P_L}$ *and the right-hand column show* $\mathrm{P_{SPT}}/\mathrm{P_L}$.

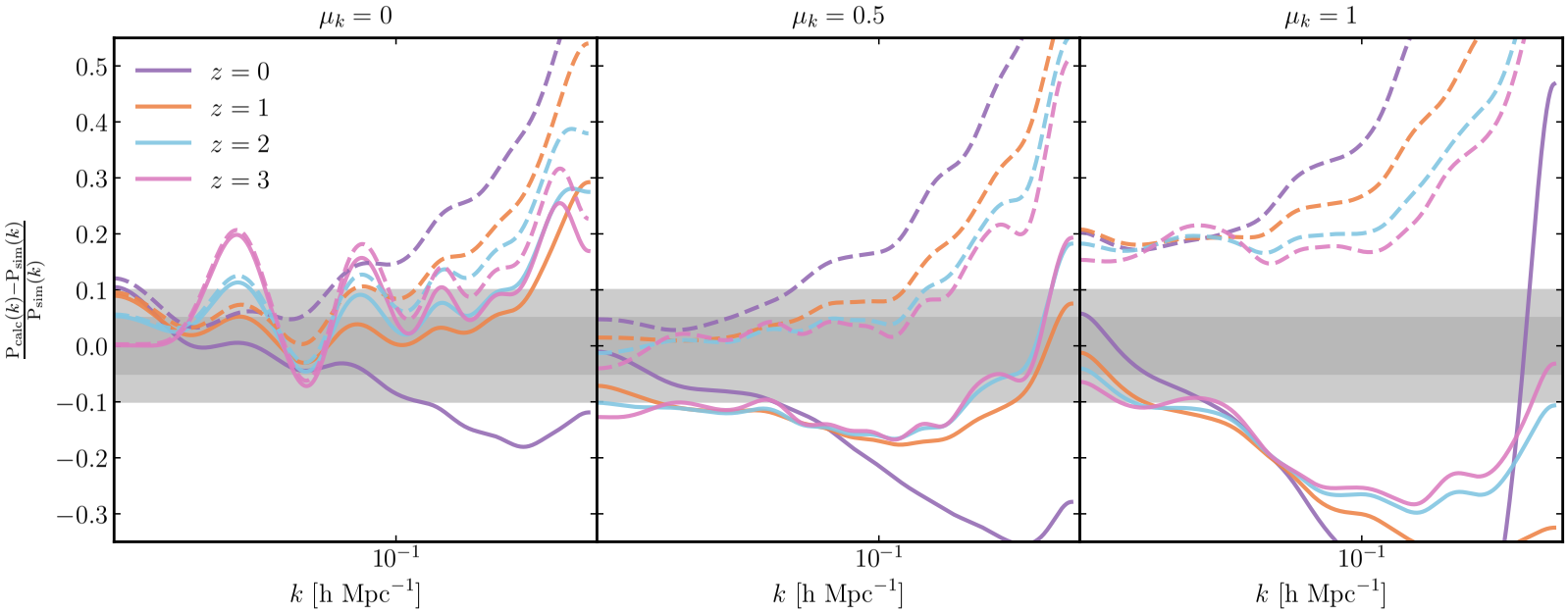

Figure 5.10 *Percentage difference between Beyond Zel'dovich (solid lines) and the simulation power spectra and Kaiser (dashed lines) and the simulation power spectra for* $\mu_k = 0,\ 0.5$ *and* 1. *The dark grey shaded region is* $\Delta^2_{\rm diff} = \pm 0.05$ *and the light grey shaded region is* $\Delta^2_{\rm diff} = \pm 0.1$.

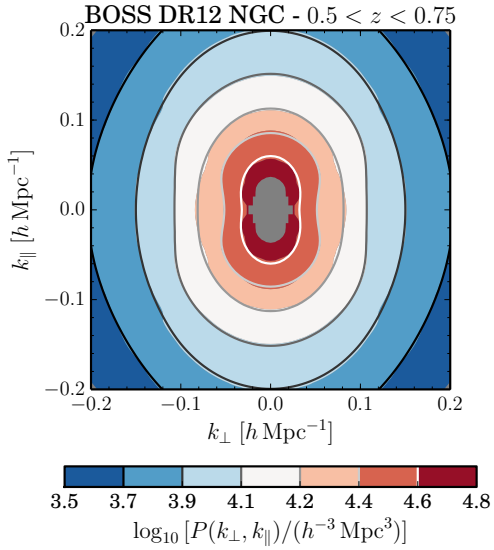

Figure 5.11 *Pre-reconstructed power spectrum measured by BOSS in Alam et al. (2017) for* $0.5 < 5 < 0.75$ *for the NGC (Northern Galactic Caps) sample. The contours show the best fit model and the colour scale shows the data.*

diverges to infinity. The BAO ring at $r \approx 100$ Mpch^{-1} can be clearly seen in all three panels. There is also squashing of the contours in all three panels. This is more promising news about the applicability of the Beyond Zel'dovich approximation.

5.5.2 SPT 1-loop

In Heavens et al. (1998), Scoccimarro et al. (1999) , Matsubara (2008b) and Kwan et al. (2012) the SPT 1-loop redshift-space result is derived. This is analogous to Equation (2.63) and the derivation follows similar logic to the one presented in Section 2.4.2. The SPT 1-loop redshift-space power spectrum is

$$\mathrm{P}_{1-\mathrm{loop}}(k, \mu_k) = \left(b + f\mu_k^2\right)^2 \mathrm{P}_{\mathrm{L}}(k) + \left(b + f\mu_k^2\right) \mathrm{P}_{13}(k) + \mathrm{P}_{22}(k) \tag{5.43}$$

where b is the linear bias (in this thesis $b = 1$) and P_{13} and P_{22} are given in (2.64). The applicability of SPT 1-loop in redshift space has been studied in previous works (Scoccimarro et al., 1999, Jennings et al., 2010) and again was found to be accurate for $k < 0.01$ h Mpc^{-1}. In the right-hand column of Figure 5.9 one can

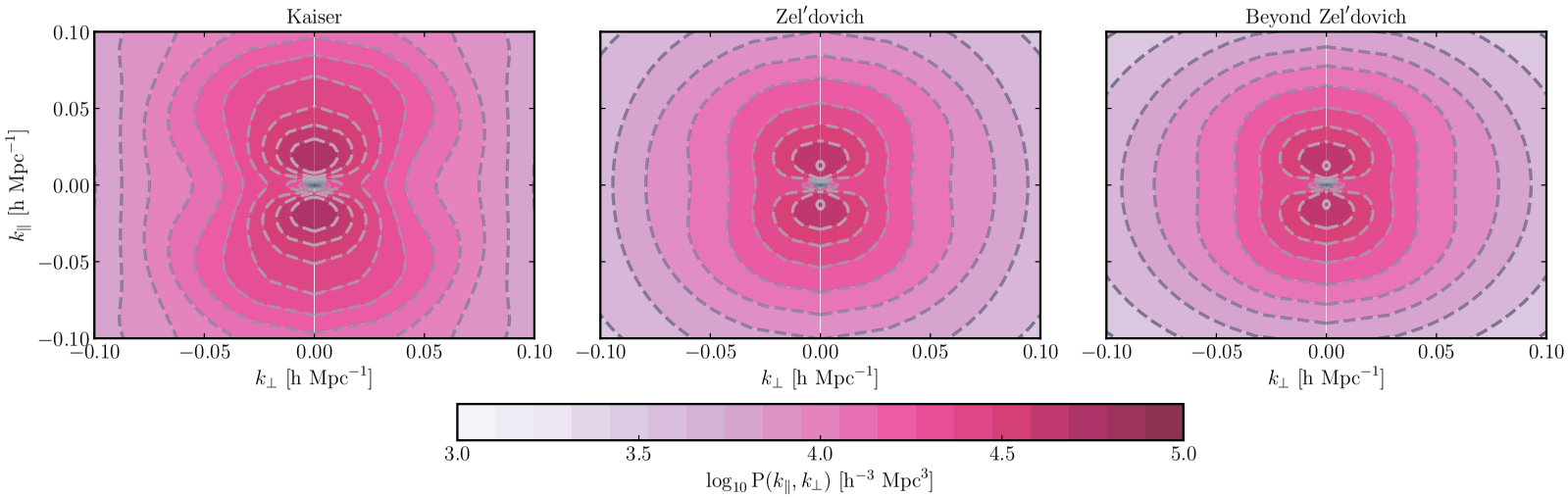

Figure 5.12 *Contour plot showing the power spectrum* $\log_{10} \mathrm{P}(k_\parallel, k_\perp)$ *at* $z = 0$ *for the Kaiser formula, damped Zel'dovich approximation and Beyond Zel'dovich approximation.*

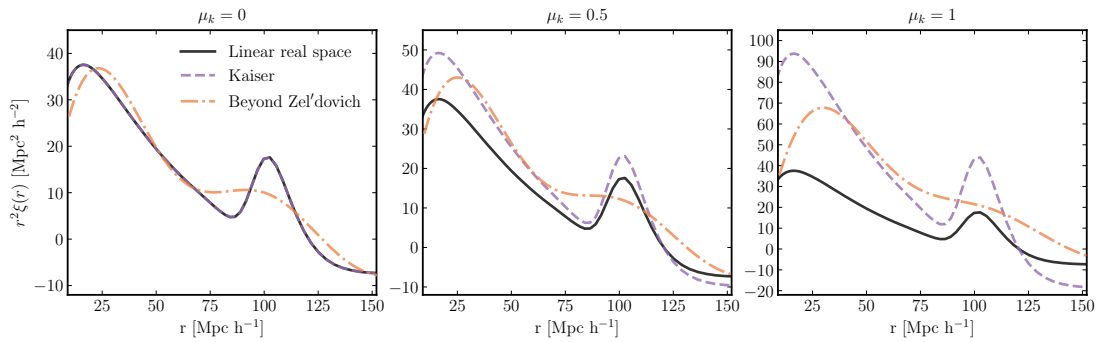

Figure 5.13 *The 2-point correlation function, $r^2\xi(r)$ at $z = 0$ is shown for linear linear in real space (black solid lines), Kaiser (purple dashed lines) and Beyond Zel'dovich redshift space (orange dot-dashed lines). The three panels are $\mu_k = 0$, $\mu_k = 0.5$ and $\mu_k = 1$.*

see SPT 1-loop predicts an increase in power on small scales. Physically there should be damping on small scales for the reasons discussed previously.

The percentage difference between SPT 1-loop and Beyond Zel'dovich and the simulation results is shown in Figure 5.15. At $z = 0$ and for $\mu_k = 0$ the Beyond Zel'dovich approximation performs as well as SPT 1-loop for small k-values and outperforms SPT 1-loop for $k > 0.1$ h Mpc^{-1}. For redshifts above $z = 1$ the Beyond Zel'dovich approximation performs as well as SPT 1-loop for $\mu_k = 0$ and $\mu_k = 0.5$ again for small k-values.

The scaled correlation functions $r^2\xi(r)$ for linear real space, SPT 1-loop and the Beyond Zel'dovich approximation at $z = 0$ are shown in Figure 5.17. As was the case in real space SPT 1-loop again fails to accurately model the BAO peak and there is no smearing of the peak for higher μ_k values. This suggests that the Beyond Zel'dovich approximation more accurately models the BAO peak compared to SPT 1-loop.

The contour plots in Figure 5.16 and 5.18 show the Kaiser effect. As was the case with comparisons to the Kaiser approximation we cannot make any strong statements about the behaviour of the Zel'dovich or Beyond Zel'dovich approximations. In Appendix B a preliminary comparison with the simulation data contours is shown for the power spectrum contour plot. In future work we aim to obtain more accurate simulation data for a larger range of μ_k and redshift values in order to perform a more stringent comparison.

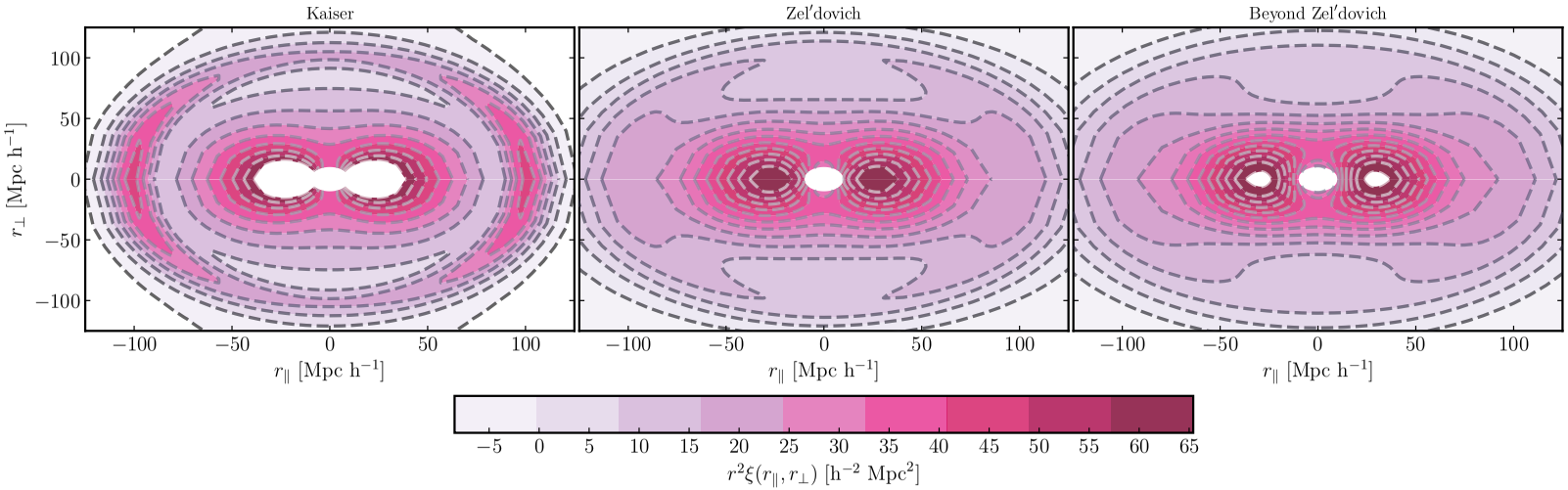

Figure 5.14 *Contour plot showing the two-point correlation function $r^2\xi(r_\parallel, r_\perp)$ at $z = 0$ for the Kaiser formula, damped Zel'dovich approximation and Beyond Zel'dovich approximation.*

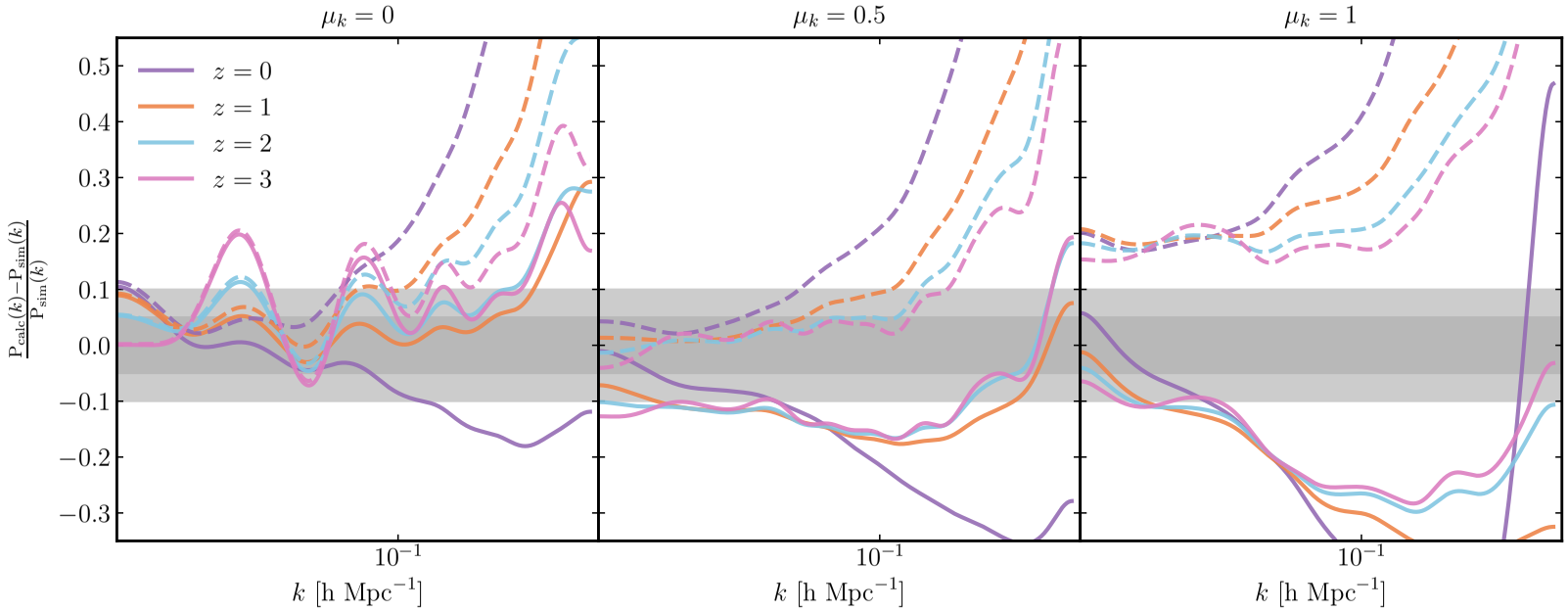

Figure 5.15 *Percentage difference between Beyond Zel'dovich (solid lines) and the simulation power spectra and SPT 1-loop (dashed lines) and the simulation power spectra for* $\mu_k = 0,\ 0.5$ *and* 1. *The dark grey shaded region is* $\Delta^2_{\text{diff}} = \pm 0.05$ *and the light grey shaded region is* $\Delta^2_{\text{diff}} = \pm 0.1$.

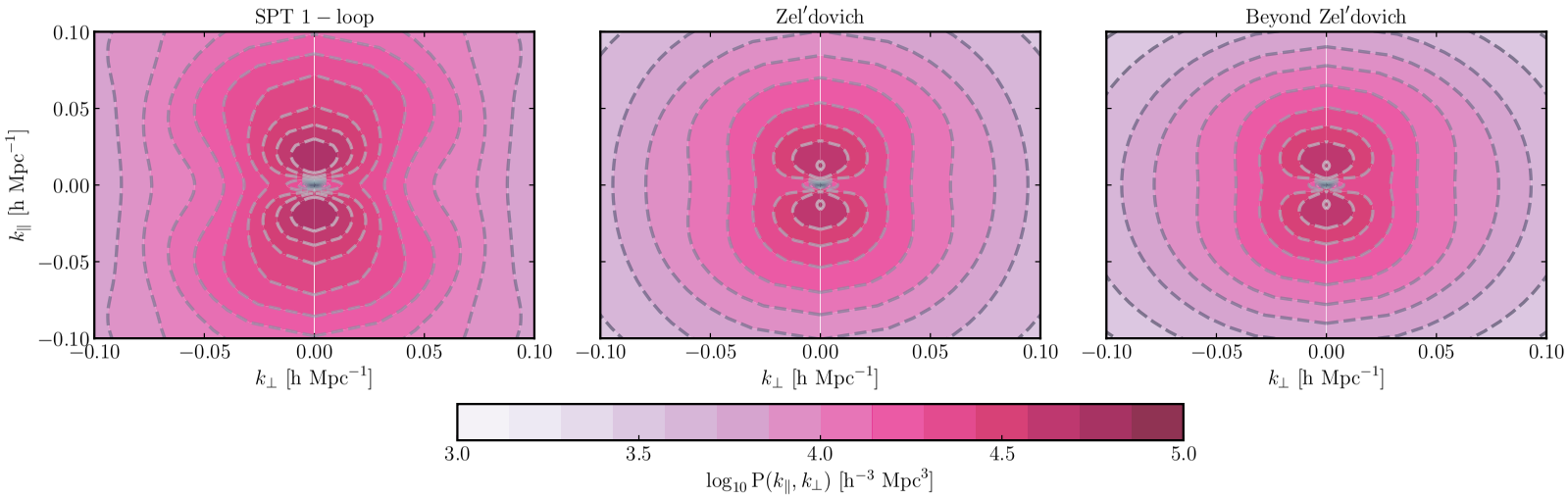

Figure 5.16 *Contour plot showing the power spectrum* $\log_{10} \mathrm{P}(k_\parallel, k_\perp)$ *at* $z = 0$ *for SPT 1-loop, damped Zel'dovich approximation and Beyond Zel'dovich approximation.*

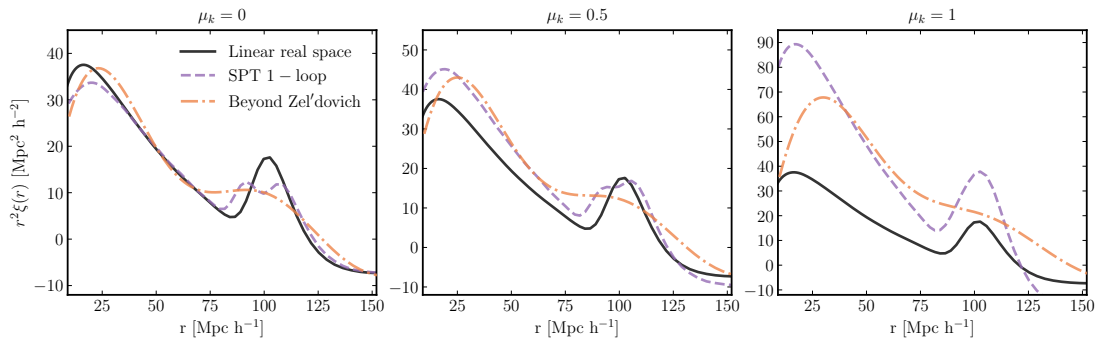

Figure 5.17 *The 2-point correlation function, $r^2\xi(r)$ at $z = 0$ is shown for linear linear in real space (black solid lines), SPT 1-loop (purple dashed lines) and Beyond Zel'dovich redshift space (orange dot-dashed lines). The three panels are $\mu_k = 0$, $\mu_k = 0.5$ and $\mu_k = 1$.*

5.6 Conclusions

In this chapter we began by introducing redshift-space distortions. These distortions arise due to an additional peculiar velocity term along the line-of-sight. This additional term has non-negligible effects on the overdensity field and makes the clustering of matter anisotropic. On large scales RSD cause an excess of power when modelling the power spectrum due to matter falling into collapsing structures (Kaiser effect) and on small scales RSD cause damping due to random velocities of virialised objects (Fingers-of-God). A linear and non-linear RSD method was introduced in Section 5.2.

In Section 5.3.2 we computed the redshift-space power spectrum for the CTM (3.47). Again we expanded the full power spectrum formula in order to compute it numerically. Using methods presented in this section we added an extension to the CTM MODULE that computed the redshift-space power spectrum for a range of μ_k values. This code was tested thoroughly and was shown to converge. We computed the Beyond Zel'dovich redshift-space power spectrum for a range of ϵ values and μ_k values as we did in real space. Recall, that the ϵ parameter controls the size of the higher-order gravitational term. We found that for small ϵ values the Beyond Zel'dovich power spectrum converged to the Zel'dovich approximation result. By observing this for all redshifts and μ_k values we validated the redshift-space extension to the CTM. We decided to calculate all future Beyond Zel'dovich power spectra with $\epsilon = 1$ as we did in real space to capture non-linear gravitational effects at all redshifts.

The Beyond Zel'dovich approximation power spectrum diverges on small scales.

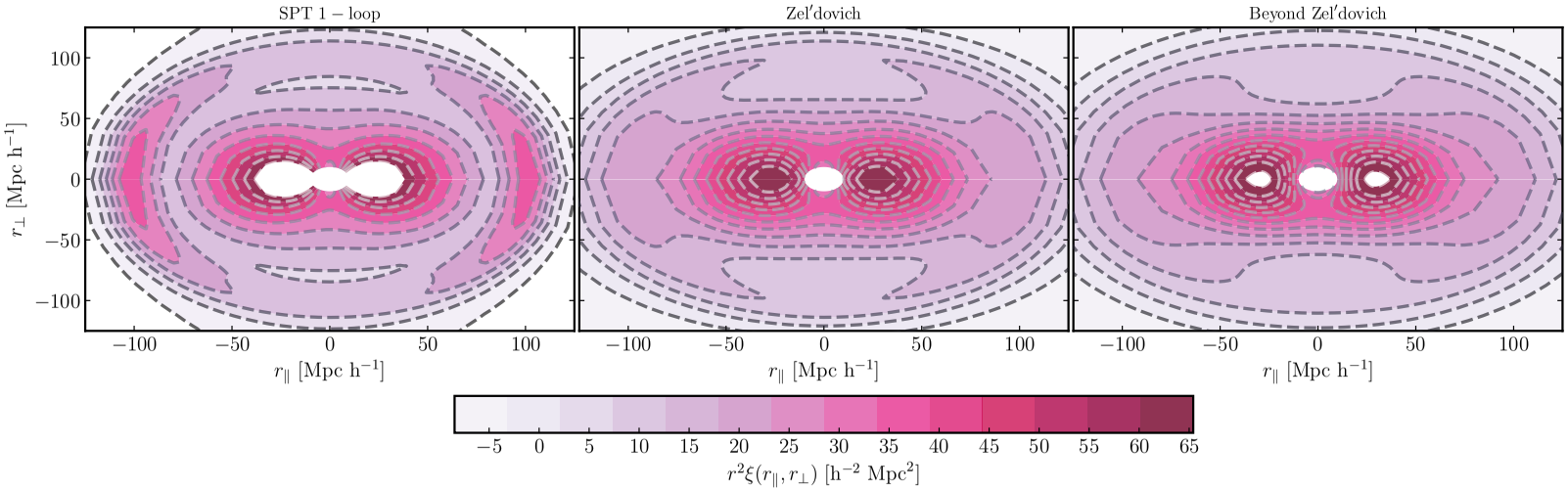

Figure 5.18 *Contour plot showing the two-point correlation function $r^2\xi(r_\parallel, r_\perp)$ at $z = 0$ for SPT 1-loop, damped Zel'dovich approximation and Beyond Zel'dovich approximation.*

This is due to numerical issues caused by the large higher-order gravitational terms and partly due to the breakdown of the Zel'dovich approximation. In order to remedy this we introduced a Gaussian cutoff in the initial power spectrum as we did in real space. In redshift space we expect the power spectrum to breakdown at a larger scale than in real space. We computed the Beyond Zel'dovich approximation power spectrum for a lower range of cutoff values $k_c = 1 - 10$ h Mpc^{-1} and compared these results to simulation data. For large cutoff values we saw a large improvement at high redshifts and for small cutoff values we observed detrimental effects at high redshifts. This is exactly the behaviour we saw in real space. After computing the maximum k-value that can be reached with each cutoff value we decided to use $k_c = 4$ h Mpc^{-1} when computing the Beyond Zel'dovich power spectrum.

In Section 5.5 we compared the redshift-space Beyond Zel'dovich power spectrum computed with $\epsilon = 1$ and $k_c = 4$ h Mpc^{-1} with simulation results. We found that for low μ_k values and low redshifts we performed as well as the Zel'dovich approximation when comparing the power spectra. At high redshifts we performed as well as the Zel'dovich approximation for $\mu_k = 0$ and 0.5. The Beyond Zel'dovich approximation also captured the smearing of the BAO peak in the correlation function marginally better than the Zel'dovich approximation. This was also observed in real space. The Beyond Zel'dovich approximation outperformed the Kaiser method at low redshifts and performed as well as the Kaiser method at high redshifts when computing the power spectrum. We discussed the range of applicability of the Kaiser method. Previous works concluded that the Kaiser method is applicable at low redshifts only for $k < 0.01$ h Mpc^{-1}. This suggests that the Beyond Zel'dovich approximation could be used in observational surveys in place of the Kaiser method. The Kaiser method also did not model the smearing of the BAO peak in the correlation function. Comparisons with SPT 1-loop yielded similar results.

The Beyond Zel'dovich approximation did not perform well when $\mu_k = 1$, in other words when $\mathbf{k}$ was perpendicular to the line-of-sight, at any redshift. This indicates that the Beyond Zel'dovich approximation is not accurately modelling the small-scale Fingers-of-God effect, this is expected as the CTM breaks down after shell-crossing occurs. We computed contour plots showing the power spectrum and correlation function in relation to parallel and perpendicular lines-of-sight at $z = 0$. Although we captured the squashing of the contours due to the Kaiser effect we did not capture the stretching of the contours due to the Fingers-

of-God effect, as expected. In Appendix B two further Figures are presented with preliminary simulated contours. These add more evidence to the conclusion that the Beyond Zel'dovich approximation is not modelling peculiar velocities on small scales accurately.

Overall, the Beyond Zel'dovich approximation power spectrum consistently lies within 10% simulation data for $\mu_k = 0$ and $\mu_k = 0.5$. There is evidence that suggests the small-scale Fingers-of-God effect is not accurately modelled. This is a symptom of the breakdown of the Beyond Zel'dovich approximation physically due to shell-crossing. It is hoped that with further investigation the applicability of the Beyond Zel'dovich approximation in redshift space can be more stringently determined.

Chapter 6

Conclusions and future work

I would like to be remembered as someone who used whatever talent she had to do her work to the very best of her ability.

Ruth Bader Ginsburg

6.1 Conclusions

The aim of the work presented in this thesis was to introduce a perturbative method for calculating 2-point dark matter statistics in the non-linear regime. We aimed to produce a method that was general i.e. it could be applied to a wide range of cosmologies and redshifts and that could be used in conjunction with a number of approximations. As the most accurate techniques we have for computing these statistics are N-body and hydrodynamical simulations we also desired our method to be competitive both in accuracy and computation time. Our final goal was that our method was applicable to small-scale data from current and upcoming surveys.

6.1.1 The Cosmological Trajectories Method

In Chapter 3 we introduced the Cosmological Trajectories Method (CTM). This method is based on the Kinetic Field Theory (KFT) method and its trajectories derivation. We expanded the full gravitational term given in previous work in order to investigate how the method functioned and to easily compute the power spectrum and correlation function. This expansion resulted in us writing down a generalised particle trajectory that consisted of an initial position, a displacement and a tidal term (a term which takes into account the gravitational potential). This general trajectory could be applied at any redshift, for any cosmology and the time dependent functions could be replaced with those from a range of theories including KFT and Lagrangian Perturbation Theory (LPT).

The general trajectory presented in Section 3.3.1 contains fields evaluated at some suitable initial time. This allowed us to compute the power spectrum using multivariate Gaussians. Unfortunately, the expression obtained was too difficult to calculate numerically with current computational power. We therefore expanded the full power spectrum expression to second-order in the gravitational terms. We were then able to construct a PYTHON code to compute the CTM power spectrum called the CTM MODULE. We tested the convergence of this code and found that with 5000 $k-$values we could compute the Zel'dovich approximation to within a few percent of other publicly available codes. The CTM code can compute the power spectrum for 5000 $k-$values at one redshift value in around 20 minutes on a standard computer. The CTM method allows us to calculate a general power spectrum with a higher-order gravitational term. The method is also intuitive as the trajectory itself can be easily related to numerical simulations. We concluded Chapter 3 by applying CTM to the KFT approximation. We discovered that in order to obtain linear power on large scales we had to introduce a re-normalisation factor. This lead us to postulate a new approximation and in the remaining thesis chapters we used the CTM to compute 2-point statistics for this approximation and others in both real and redshift space.

6.1.2 The Beyond Zel'dovich approximation in real space

Investigating the free parameters of the CTM in real space

In Chapter 4 we introduced the Beyond Zel'dovich approximation. This approximation used ideas from KFT but was set up such that we obtained linear power on large scales. This approximation is the Zel'dovich approximation (which is accurate at high redshifts and on large scales until shell-crossing) with an additional tidal term. We also removed the acceleration term that should appear in the CTM trajectory as we demonstrated that it enhanced the breakdown of the Beyond Zel'dovich approximation in Figure **??**.

The CTM has two free parameters: the initial time (z_i) and the expansion parameter (ϵ). The expansion parameter controls the size of the higher-order gravitational term. It dictates the size of the gravitational potential and hence the non-linearity of the density field. In Sections 4.2.2 and 4.2.1 we investigated a range of values for the initial time and expansion parameter. We found that there was little difference between early initial times i.e. $z_i = 150$ or $z_i = 99$. However, when a more extreme initial time of $z_i = 10$ was chosen it significantly improved the performance of the Beyond Zel'dovich approximation at low redshifts. At higher redshifts it did not have a positive effect as there was not enough time to allow the gravitational term to take effect. In order to compare our method to KFT we chose $z_i = 100$ however any redshift around $z_i = 100$ could be used.

Next we tested a range of ϵ values and found that small ϵ values caused the Beyond Zel'dovich power spectrum to converge to the Zel'dovich approximation. This was exactly as we expected and as we discussed previously without the higher-order gravitational term we recover the Zel'dovich approximation. We chose a value of $\epsilon = 1$ in order to benefit from the higher-order gravitational effects on small scales at a large range of redshifts. This high ϵ value has a detrimental effect at low redshifts ($z \leq 2$) and a wave feature is introduced on small scales ($k \approx 1$ h Mpc^{-1}). This is partly due to the integration method breaking down as a result of the higher-order gravitational terms becoming large. It is also unclear without further investigation whether the breakdown of the Zel'dovich approximation is also significant in causing this feature.

The breaking down of the Beyond Zel'dovich approximation at low redshifts could also be a indication that we are pushing the approximation to too late a time.

In an attempt to remedy this breakdown we introduced a Gaussian cutoff in the initial power spectrum. In Section 4.3 we implemented the Gaussian cutoff with a range of cutoff values (k_c). We calculated the non-linear power spectrum using the EUCLID EMULATOR and used it to assess the accuracy of the CTM. Smaller cutoff values had a negative effect at high redshifts as the Gaussian cutoff was erasing too much structure. Similarly larger cutoff values had a negligible effect at low redshifts as a result of not damping the effect of the non-linear breakdown. We concluded that a value of $k_c = 6$ h Mpc^{-1} damped down the breakdown of the Beyond Zel'dovich approximation sufficiently at redshifts $z \geq 2$. The dependence of the cutoff value on the cosmological parameters was also tested and there was found to be no dependence. However, the `Euclid Emulator` does not allow for a wide range of Ω_m values therefore we cannot conclude there would be no dependence for a larger difference between the cosmologies chosen.

Comparison of the Beyond Zel'dovich approximation to other methods

The investigation of the free parameters in the CTM resulted in the initial redshift of $z_i = 100$, the expansion parameter being $\epsilon = 1$ and a Gaussian cutoff value of $k_c = 6$ h Mpc^{-1}. Using these parameters the Beyond Zel'dovich approximation was found to outperform the damped Zel'dovich approximation (also calculated with $k_c = 6$ h Mpc^{-1}) above redshift $z = 2$ and the EUCLID EMULATOR above redshift $z = 4$. SPT 1-loop outperformed the Beyond Zel'dovich approximation when calculating the power spectrum at all redshifts. In contrast the Beyond Zel'dovich approximation modelled mildly non-linear scales (BAO scales) more accurately. This was demonstrated in Figure 4.11 where the SPT 1-loop correlation function was shown alongside results from the emulator. We additionally compared the Beyond Zel'dovich approximation to Convolution Lagrangian Perturbation Theory (CLPT). Again we found that CLPT modelled non-linear scales more accurately. However, the method broke down at higher redshifts which is one disadvantage of CLPT compared to Beyond Zel'dovich. The performance of the Beyond Zel'dovich approximation at high redshifts suggests it could be used in the analysis of Lyman-α as well as other high redshift observations.

We also investigated another approximation, LPT-like, in which the higher-order gravitational term time dependence was an ansatz based on second-order LPT. As the higher-order time dependence factor was very large at low redshifts we had to

implement it with $\epsilon = 10^{-4}$. This approximation outperformed Beyond Zel'dovich for redshifts below $z = 2$ but at higher redshifts it did not perform as well. This was due to the small ϵ value; hence we did not pursue this approximation further.

Finally, in Chapter 4 we calculated the next order CTM power spectrum term (proportional to ϵ^4). This was motivated by the hypothesis that higher-order terms may cancel out the terms causing the breakdown of the method on small scales. The time dependence of these higher-order terms was too large to calculate the Beyond Zel'dovich power spectrum with $\epsilon = 1$ without destructive numerical issues. Therefore we could not test whether the wave feature in the power spectrum was removed at low redshifts with the full impact of the higher-order gravitational term. Unfortunately we could not overcome the numerical issues yet but hope that if the full power spectrum formula could be computed we could cancel out the damaging terms effectively.

6.1.3 The Beyond Zel'dovich approximation in redshift space

The performance of the Beyond Zel'dovich approximation in real space on mildly non-linear scales suggested that the approximation could be applied to redshift-space distortions. As the CTM is based on LPT the mathematics involved in calculating the redshift-space statistics has already been studied extensively in the literature. In Chapter 5 we calculated the CTM redshift-space power spectrum to the same order as in Chapter 3. We implemented an add-on to the CTM code that computes the redshift-space power spectrum for a range of redshifts and μ_k values (angle between $\mathbf{k}$ and the line-of-sight). The code takes approximately 1.8 hours to compute the redshift-space power spectrum for 5000 $k-$values and one μ_k value or 10 minutes to compute the redshift-space power spectrum for 1000 $k-$values and one μ_k value on a standard machine.

Investigating the free parameters of the CTM in redshift space

As was the case in real space there are two free parameters in CTM in redshift space. We did not test the dependence of the power spectrum on the initial redshift and used the value of $z_i = 100$. We did test the impact of ϵ on the Beyond Zel'dovich power spectrum and found that it converged to the Zel'dovich approximation as was the case in real space. We encountered similar numerical issues and as a result could not model scales smaller than $k = 0.1$ h Mpc^{-1} or

$\mu_k = 1$. We predicted the Beyond Zel'dovich approximation would breakdown at a larger scale in real space and for μ_k values tending to one due to the peculiar velocities that cause the Fingers-of-God effect. Despite this we chose a value of $\epsilon = 1$ for maximum impact of the higher-order gravitational terms.

Since CTM in redshift space suffered a similar breakdown on small scales as in real space, we again introduced a Gaussian cutoff in the initial power spectrum. We compared the Beyond Zel'dovich approximation to simulation results. This resulted in the cutoff parameter $k_c = 4$ h Mpc^{-1} being chosen. The Gaussian cutoff again had no cosmological dependence.

Comparison of the Beyond Zel'dovich approximation to other methods in redshift space

We used NBODYKIT to simulate redshift-space distortions along the x, y and z axes with a box size of $L_{\text{box}} = 2048$ Mpch^{-1} and a mesh size of $L_{\text{mesh}} = 256$ Mpch^{-1}. We then averaged these results to reduce the scatter on large scales. We compared the Zel'dovich, Beyond Zel'dovich, linear Kaiser approximation and SPT 1-loop to these simulation results. We found that the Zel'dovich approximation (computed with $k_c = 4$ h Mpc^{-1}) outperformed Beyond Zel'dovich by a marginal amount at $z = 0$ for $\mu_k = 0.5$ and $\mu_k = 1$. Both approximations broke down as we approached $\mu_k = 1$ with some improvement for higher redshifts. This indicated that we were modelling the Kaiser effect (infall of matter into collapsing structures) accurately but not the Fingers-of-God (random motion of virialised structures).

Previous work suggests that the linear Kaiser approximation and SPT 1-loop are not accurate beyond $k \approx 0.01$ h Mpc^{-1}. In both cases the Beyond Zel'dovich approximation performed better that the Kaiser and SPT 1-loop methods at low redshifts but broke down as we approached $\mu_k = 1$. As the linear Kaiser approximation is a scaling of the linear real-space result we also found that it did not model the smearing of the BAO peak in the correlation function, whereas the Beyond Zel'dovich approximation did. Similarly, SPT 1-loop did not model the mildly non-linear scales accurately as was the case in real space.

Finally, we computed the 2D contour plots for the power spectrum and correlation function with respect to $k_\parallel$ ($r_\parallel$) and $k_\perp$ ($r_\perp$). If there were no RSD effects the contours would be circular. However, the infall of matter into collapsing structures

on large scales and the incoherent motion of matter on small scales results in squashing and stretching along the line-of-sight respectively. We demonstrated that we captured the squashing of the contours well at $z = 0$ but did not accurately capture the stretching effect. This was due to the Beyond Zel'dovich approximation breaking down on small scales. This will be investigated further in future work.

In conclusion, we demonstrated that the CTM can be applied to a wide range of redshifts and used with multiple approximations. One approximation we chose to investigate, Beyond Zel'dovich, outperformed the Zel'dovich approximation and the Euclid Emulator at high redshifts and low redshifts on mildly non-linear scales in real space. The Beyond Zel'dovich approximation can also be applied at higher redshifts than CLPT which could prove useful for future high redshift surveys. We also derived the CTM in redshift space and again found that it could be applied to data at high redshifts and mildly non-linear scales. We hope that the CTM can be used to place even tighter statistical constraints on viable dark matter, dark energy and modified gravity theories. Leading to answering some of Astronomy's biggest questions about structure formation in the Universe.

6.2 Future work

In this thesis we investigated the applicability of a new perturbative technique, the CTM and the Beyond Zel'dovich approximation. We compared the real-space results for the power spectrum and correlation function to results from the Euclid Emulator. As a result we could not test a wider range of redshifts and cosmologies. Therefore we aim to obtain N-body simulation data for a larger range of redshifts and cosmologies. This will allow us to more accurately assess the performance of the Beyond Zel'dovich approximation. Along similar lines we also wish to compare the Beyond Zel'dovich approximation to second-order LPT and IR-resummation schemes.

We observed that the numerical integration technique used to calculate the CTM power spectrum broke down on small scales; as a result of the higher-order gravitational term becoming too large. In order to determine whether this breakdown is entirely due to numerics we wish to use alternative techniques, such as Legendre polynomials, to calculate the power spectrum.

With respect to the redshift-space results for the Beyond Zel'dovich approximation we plan to compare our results to TNS, IR-resummation schemes and CLPT-GSRSD. This will likely result in the need for more accurate N-body simulation data, which we hope to obtain. Another objective is to add the ability to calculate multipoles with the CTM Module. This will allow the user to compare results more easily with previous work and observational data.

Lastly there has been much interest in whether the CTM can be applied to modified gravity and alternate dark energy theories. In future work, we aim to investigate whether we can apply the CTM to Horndeski theory, dark energy models and perhaps dark matter theories such as Self-Interacting Dark Matter (SIDM). Our initial goal was to create a general perturbative technique that could be applied to a range of scenarios. It is therefore a high priority to attempt to incorporate modified gravity into the CTM and to eventually make the code publicly available.

Appendix A

Differential Geometry

A.1 Derivation of Lorentz tensor

Let us derive and prove that a Lorentz transformation is indeed the most general transformation to preserve the line element (Weinberg, 1972) in an inertial frame. Let us begin with two inertial observers one with coordinate system x^μ and the other with coordinate system x'^μ. Assuming the following relationship

$$dx'^\mu = \frac{\partial x'^\mu}{\partial x^\alpha} dx^\alpha \tag{A.1}$$

and using the fact we know the line element is invariant gives

$$g_{\mu\nu} \frac{\partial x'^\mu}{\partial x^\alpha} \frac{\partial x'^\nu}{\partial x^\beta} = g_{\alpha\beta}. \tag{A.2}$$

Differentiation with respect to x^α yields

$$g_{\mu\nu} \frac{\partial^2 x'^\mu}{\partial x^\gamma \partial x^\alpha} \frac{\partial x'^\nu}{\partial x^\beta} + g_{\mu\nu} \frac{\partial^2 x'^\nu}{\partial x^\gamma \partial x^\beta} \frac{\partial x'^\mu}{\partial x^\alpha} = 0 \tag{A.3}$$

adding one permutation of the indices (α, β, γ) and subtracting another allows

us prove the condition needed for the non-singularity of the transformation. The equation we must now solve is

$$g_{\mu\nu}\frac{\partial^2 x'^{\mu}}{\partial x^{\gamma}\partial x^{\alpha}}\frac{\partial x'^{\nu}}{\partial \partial x^{\beta}} = 0. \tag{A.4}$$

Both the metric $g_{\mu\nu}$ and the first-order derivative have inverses. Applying these inverses leaves us with the second derivative being zero which we can solve for

$$x'^{\mu} = L^{\mu}{}_{\alpha}x^{\alpha} + A^{\mu} \tag{A.5}$$

where $L^{\mu}{}_{\alpha}$ is the Lorentz matrix and A^{μ} are constants. This Equation (A.5) is an inhomogenous Lorentz transformation. We usually use the homogeneous transformation where $A^{\mu} = 0$.

A.2 Manifolds and tangent spaces

We aim to be able to describe trajectories through curved spacetime. Vectors cannot be manipulated in curved-space in the same way as in flat-space. Spacetime globally is a topological space called a manifold. Manifolds are objects that look locally like $\mathbb{R}^4$ in our case (Riemannian manifold). The manifold of spacetime is a differentiable manifold or a Hausdorff topological space. This means it satisfies the following criteria:

- Space is viewed as an open set and the empty set , $\emptyset$, is viewed as open.
- The intersection of two open sets is open.
- The union of open sets is open.
- If p and p' are two distinct points $\exists$ an open set $O \ni p$ and an open set $O' \ni p'$ such that $O \cap O' = \emptyset$.

In Figure A.1 a diagram of a manifold is shown. The red circle is an open set, O, on the manifold which contains some point, p, which can be mapped to a point

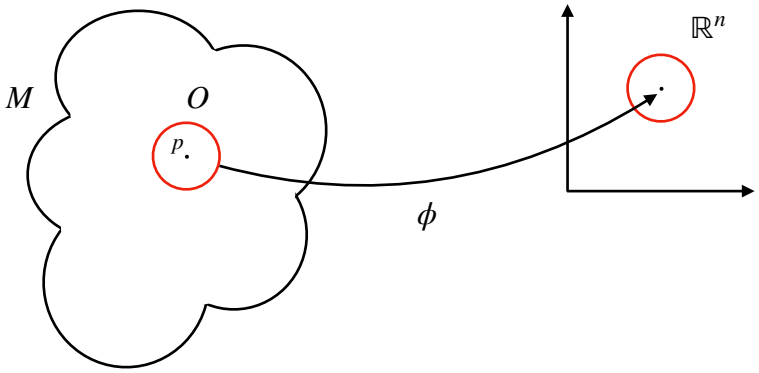

Figure A.1 *Diagram of a manifold where O is an open set containing some point p. This point can be mapped onto a point in $\mathbb{R}^n$ with a chart called ϕ.*

in $\mathbb{R}^n$ by a chart ϕ. This may seem abstract, but a simple example is the Earth. The Earth is a sphere, but locally to humans, it appears to be flat.

Defining some flat spaces on the manifold where we could easily visualise and manipulate vectors would allow us to calculate the separation of points and acceleration of objects. These flat vector spaces are called tangent spaces defined formally in A.2.1. A cotangent space, $T_p^*(M)$, is a dual vector space and is the space of all linear maps of the vectors in the tangent space. We will need cotangent spaces to carry out maps from vectors to scalars etc..

Definition A.2.1. Let M be some spacetime at any point $p \in M$ there is a space of vectors called the tangent space, $T_p(M)$.

We now have our global spacetime defined as a manifold and locally we have tangent and cotangent spaces. We will now use these to define the other necessary tools needed to describe gravity.

Tensors

There are many ways to define a tensor, which are crucial objects in special and general relativity. In general relativity, they will usually be introduced as multidimensional arrays or objects that transform like tensors (we will see this later). In differential geometry, they are defined as multilinear maps as in A.2.2. From the definition, one may notice that it is a combination of tangent and

cotangent spaces. Thus a tensor provides a way to linearly map between objects like matrices, vectors and scalars.

Definition A.2.2. A tensor of type (r, s) is a multilinear map
$T : \underbrace{T_p^*(M) \times \cdots \times T_p^*(M)}_{r} \underbrace{\times T_p(M) \times \cdots \times T_p(M)}_{s}$.

Some examples of tensors are:

- type $(0, 0)$ is a scalar
- type $(0, 1)$ is a covariant vector
- type $(1, 0)$ is a contravariant vector.

An example of a tensor is the metric tensor which takes two vectors as an input and returns a real number. The metric tensor has many uses in differential geometry. It can be used to convert covariant to contravariant vectors i.e. $u_\mu = g_{\mu\nu}u^\nu$, it is symmetric and $g^{\mu\alpha}g_{\mu\beta} = \delta^\alpha_\beta$. It is defined as A.2.3.

Definition A.2.3. Let $\mathbf{g}$ be a tensor of type $(0, 2)$, $\mathbf{g} : T_p(M) \times T_p(M) \to \mathbb{R}$. Then if $\mathbf{u}, \mathbf{v} \in T_p(M)$ then $\mathbf{g}(\mathbf{u}, \mathbf{v}) \in \mathbb{R}$.

Appendix B

Additional redshift-space figures

The figures in this appendix show preliminary results for power spectrum contour plots in redshift-space. The red solid contours represent data obtained from a simulation. The simulations were carried out using NBODYKIT using log-normal mock catalogues and Fast Fourier Transforms (FFTs). For a more in-depth discussion of the simulations see Section 5.5.

The components $k_{\parallel}$ and $k_{\perp}$ are parallel and perpendicular to the line-of-sight $\hat{\mathbf{z}}$. As was discussed in Chapter 5 if there were no RSD effects then the contour rings would be circles. However, in redshift-space, we expect to see squashing of the contours along the line-of-sight in the centre and stretching along the line-of-sight. The squashing is due to the Kaiser effect (caused by the infall of matter into collapsing structures) and the stretching is due to the random motions of virialised motions (Fingers-of-God).

In Figure B.1 and B.2 the Kaiser and SPT 1-loop methods appear to capture the squashing of the contours more effectively (large-scale behaviour). In general, the Zel'dovich and Beyond Zel'dovich approximations match the simulation results which is promising. In future work, we aim to acquire more accurate simulation data for a larger range of μ_k values to remove the large uncertainties and roughness of the contours.

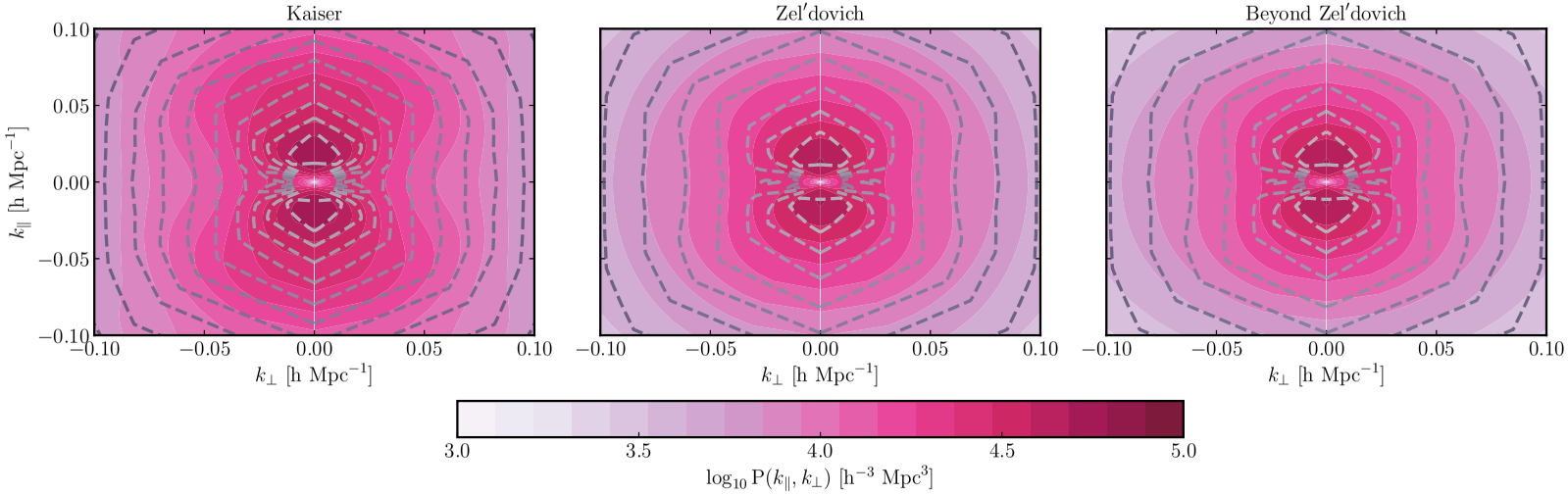

Figure B.1 *Contour plot showing the power spectrum* $\log_{10} \mathrm{P}(k_\parallel, k_\perp)$ *at* $z = 0$ *for Kaiser, damped Zel'dovich approximation and Beyond Zel'dovich approximation. The grey dashed lines show the contours produced from the simulation data described in Section 5.5.*

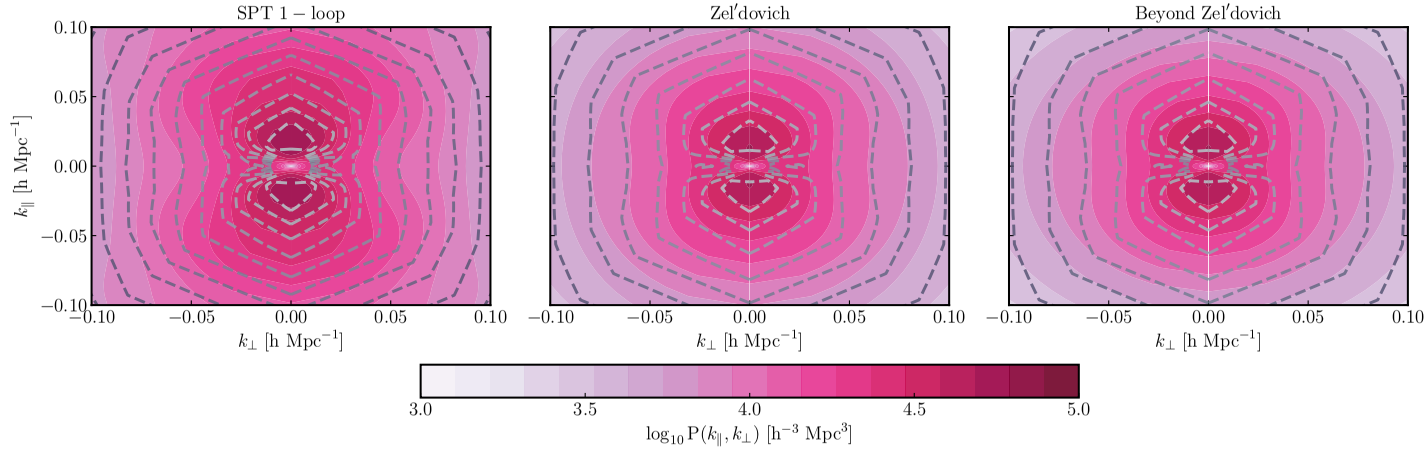

Figure B.2 *Contour plot showing the power spectrum* $\log_{10} \mathrm{P}(k_\parallel, k_\perp)$ *at* $z = 0$ *for SPT 1-loop, damped Zel'dovich approximation and Beyond Zel'dovich approximation. The grey dashed lines show the contours produced from the simulation data described in Section 5.5.*

Bibliography

Abbott T. M. C., et al., 2018, MNRAS, 480, 3879

Agrawal A., Makiya R., Chiang C.-T., Jeong D., Saito S., Komatsu E., 2017, Journal of Cosmology and Astroparticle Physics, 2017, 003–003

Alam S., et al., 2017, Monthly Notices of the Royal Astronomical Society, 470, 2617–2652

Ali-Haïmoud Y., 2015, Phys. Rev. D, 91, 103507

Amendola L., et al., 2013, Living Reviews in Relativity, 16

Anand S., Chaubal P., Mazumdar A., Mohanty S., 2017, J. Cosmology Astropart. Phys., 2017, 005

Baldauf T., Mirbabayi M., Simonović M., Zaldarriaga M., 2015a, Phys. Rev. D, 92, 043514

Baldauf T., Desjacques V., Seljak U., 2015b, Physical Review D, 92

Bardeen J. M., 1980, Phys. Rev. D, 22, 1882

Bardeen J. M., Bond J. R., Kaiser N., Szalay A. S., 1986a, ApJ, 304, 15

Bardeen J. M., Bond J. R., Kaiser N., Szalay A. S., 1986b, ApJ, 304, 15

Bartelmann M., Fabis F., Berg D., Kozlikin E., Lilow R., Viermann C., 2014a, arXiv e-prints, p. arXiv:1411.1153

Bartelmann M., Fabis F., Berg D., Kozlikin E., Lilow R., Viermann C., 2014b, arXiv e-prints, p. arXiv:1411.1502

Bartelmann M., Fabis F., Kozlikin E., Lilow R., Dombrowski J., Mildenberger J., 2017, New Journal of Physics, 19, 083001

Bartelmann M., et al., 2019, arXiv e-prints, p. arXiv:1905.01179

Bernal J. L., Verde L., Riess A. G., 2016, Journal of Cosmology and Astroparticle Physics, 2016, 019–019

Bernardeau F., 2000, Nuclear Physics B Proceedings Supplements, 87, 13

Bernardeau F., 2013, arXiv e-prints, p. arXiv:1311.2724

Bernardeau F., Colombi S., Gaztañaga E., Scoccimarro R., 2002, Phys. Rep., 367, 1

Bernardeau F., Crocce M., Scoccimarro R., 2008, Phys. Rev. D, 78, 103521

Bernardeau F., Crocce M., Scoccimarro R., 2012, Phys. Rev. D, 85, 123519

Bernardeau F., Taruya A., Nishimichi T., 2014, Phys. Rev. D, 89, 023502

Bertschinger E., 1995, Technical report, Cosmological dynamics

Beutler F., et al., 2014, MNRAS, 443, 1065

Beutler F., et al., 2016, Monthly Notices of the Royal Astronomical Society, 466, 2242–2260

Biagetti M., Desjacques V., Kehagias A., Riotto A., 2014, Physical Review D, 90

Bird S., Viel M., Haehnelt M. G., 2012, Monthly Notices of the Royal Astronomical Society, 420, 2551–2561

Blake C., et al., 2011, MNRAS, 418, 1725

Blas D., Garny M., Konstandin T., 2014, Journal of Cosmology and Astro-Particle Physics, 2014, 010

Blas D., Floerchinger S., Garny M., Tetradis N., Wiedemann U. A., 2015, J. Cosmology Astropart. Phys., 2015, 049

Blas D., Floerchinger S., Garny M., Tetradis N., Wiedemann U. A., 2018, in Bianchi M., Jansen R. T., Ruffini R., eds, Fourteenth Marcel Grossmann Meeting - MG14. pp 2376–2383, doi:10.1142/9789813226609_0278

Bouchet F. R., 1996, in Bonometto S., Primack J. R., Provenzale A., eds, Dark Matter in the Universe. p. 565 (`arXiv:astro-ph/9603013`)

Bouchet F. R., Colombi S., Hivon E., Juszkiewicz R., 1995, A&A, 296, 575

Bousso R., 2007, General Relativity and Gravitation, 40, 607–637

Boylan-Kolchin M., Bullock J. S., Kaplinghat M., 2011, MNRAS, 415, L40

Brax P., Valageas P., 2019, J. Cosmology Astropart. Phys., 2019, 049

Buchert T., 1992, MNRAS, 254, 729

Buchert T., Ehlers J., 1993, MNRAS, 264, 375

Carlson J., White M., Padmanabhan N., 2009, Phys. Rev. D, 80, 043531

Carlson J., Reid B., White M., 2013, MNRAS, 429, 1674

Carrasco J. J. M., Hertzberg M. P., Senatore L., 2012, Journal of High Energy Physics, 2012, 82

Carrasco J. J. M., Foreman S., Green D., Senatore L., 2014a, Journal of Cosmology and Astro-Particle Physics, 2014, 056

Carrasco J. J. M., Foreman S., Green D., Senatore L., 2014b, Journal of Cosmology and Astro-Particle Physics, 2014, 057

Carroll S. M., Leichenauer S., Pollack J., 2014, Phys. Rev. D, 90, 023518

Castorina E., White M., 2018, MNRAS, 479, 741

Castorina E., White M., 2019, arXiv e-prints, p. arXiv:1911.08353

Catelan P., 1995, MNRAS, 276, 115

Catelan P., Porciani C., Kamionkowski M., 2000, MNRAS, 318, L39

Chen S.-F., Vlah Z., White M., 2019, J. Cosmology Astropart. Phys., 2019, 017

Chen S.-F., Vlah Z., White M., 2020, arXiv e-prints, p. arXiv:2005.00523

Clifton T., Ferreira P. G., Padilla A., Skordis C., 2012, Physics Reports, 513, 1–189

Coles P., Jones B., 1991, MNRAS, 248, 1

Coles P., Lucchin F., 1996, Astronomische Nachrichten, 317, 14

Collaboration D., et al., 2016, The DESI Experiment Part I: Science,Targeting, and Survey Design (`arXiv:1611.00036`)

Collaboration P., et al., 2018, Planck 2018 results. VI. Cosmological parameters (`arXiv:1807.06209`)

Couchman H. M. P., Bond J. R., 1988, in Kaiser N., Lasenby A. N., eds, Post-Recombination Universe. pp 263–265

Crittenden R. G., Natarajan P., Pen U.-L., Theuns T., 2001, ApJ, 559, 552

Crocce M., Scoccimarro R., 2006a, Phys. Rev. D, 73, 063519

Crocce M., Scoccimarro R., 2006b, Phys. Rev. D, 73, 063520

Crocce M., Scoccimarro R., 2008, Phys. Rev. D, 77, 023533

Croft R. A. C., 2004, The Astrophysical Journal, 610, 642–662

Del Popolo A., Le Delliou M., 2017, Galaxies, 5, 17

Dodelson S., 2003, Modern cosmology

Dvali G., 2004, Infrared Modification of Gravity (`arXiv:hep-th/0402130`)

Einstein A., de Sitter W., 1932, Proceedings of the National Academy of Sciences, 18, 213

Eisenstein D. J., Hu W., 1998, ApJ, 496, 605

Eisenstein D. J., et al., 2005, ApJ, 633, 560

Eisenstein D. J., Seo H.-J., White M., 2007a, ApJ, 664, 660

Eisenstein D. J., Seo H.-J., Sirko E., Spergel D. N., 2007b, ApJ, 664, 675

Euclid Collaboration et al., 2019, MNRAS, 484, 5509

Fabis F., Berg D., Kozlikin E., Bartelmann M., 2014, arXiv e-prints, p. arXiv:1412.2572

Fang X., Blazek J. A., McEwen J. E., Hirata C. M., 2017, J. Cosmology Astropart. Phys., 2017, 030

Floerchinger S., Garny M., Tetradis N., Wiedemann U. A., 2016, in European Physical Journal Web of Conferences. p. 03018 (arXiv:1609.03466), doi:10.1051/epjconf/201612503018

Fonseca de la Bella L., Regan D., Seery D., Hotchkiss S., 2017, J. Cosmology Astropart. Phys., 2017, 039

Font-Ribera A., SDSS-III Collaboration 2015, in American Astronomical Society Meeting Abstracts #225. p. 125.03

Friedman A., 1922, Z. Phys., 10, 377

Friedrich P., Prokopec T., 2018, Phys. Rev. D, 98, 025010

Friedrich P., Prokopec T., 2019, arXiv e-prints, p. arXiv:1909.10049

Gil-Marín H., Wagner C., Noreña J., Verde L., Percival W., 2014, Journal of Cosmology and Astroparticle Physics, 2014, 029–029

Givans J. J., Hirata C. M., 2020, arXiv e-prints, p. arXiv:2002.12296

Goroff M. H., Grinstein B., Rey S. J., Wise M. B., 1986, ApJ, 311, 6

Gorski K., 1988, ApJ, 332, L7

Guth A. H., 1981, Phys. Rev. D, 23, 347

Guzzo L., et al., 2008, Nature, 451, 541

Hahn O., Porciani C., Carollo C. M., Dekel A., 2007a, MNRAS, 375, 489

Hahn O., Carollo C. M., Porciani C., Dekel A., 2007b, MNRAS, 381, 41

Halle A., Nishimichi T., Taruya A., Colombi S., Bernardeau F., 2020, arXiv e-prints, p. arXiv:2001.10417

Hamilton A. J. S., 1998, Linear Redshift Distortions: a Review. p. 185, doi:10.1007/978-94-011-4960-0_17

Hamilton A. J. S., Culhane M., 1996, MNRAS, 278, 73

Hand N., Feng Y., Beutler F., Li Y., Modi C., Seljak U., Slepian Z., 2018, The Astronomical Journal, 156, 160

Hatton S., Cole S., 1998, MNRAS, 296, 10

Heavens A. F., Taylor A. N., 1995, Monthly Notices of the Royal Astronomical Society, 275, 483–497

Heavens A. F., Matarrese S., Verde L., 1998, Monthly Notices of the Royal Astronomical Society, 301, 797–808

Hellwing W. A., Barreira A., Frenk C. S., Li B., Cole S., 2014, Phys. Rev. Lett., 112, 221102

Hellwing W. A., Schaller M., Frenk C. S., Theuns T., Schaye J., Bower R. G., Crain R. A., 2016, MNRAS, 461, L11

Hildebrandt H., et al., 2017, MNRAS, 465, 1454

Hivon E., Bouchet F. R., Colombi S., Juszkiewicz R., 1995, A&A, 298, 643

Hobson M. P., Efstathiou G. P., Lasenby A. N., 2006, General Relativity, doi:10.2277/0521829518.

Hockney R. W., Eastwood J. W., 1981, Computer Simulation Using Particles

Howlett C., Lewis A., Hall A., Challinor A., 2012, J. Cosmology Astropart. Phys., 1204, 027

Howlett C., Ross A. J., Samushia L., Percival W. J., Manera M., 2015, MNRAS, 449, 848

Ivanov M. M., Sibiryakov S., 2018, J. Cosmology Astropart. Phys., 2018, 053

Jackson J. C., 1972, MNRAS, 156, 1P

Jain B., Bertschinger E., 1994, ApJ, 431, 495

Jennings E., Baugh C. M., Pascoli S., 2010, Monthly Notices of the Royal Astronomical Society, p. no–no

Jennings E., Baugh C. M., Li B., Zhao G.-B., Koyama K., 2012, MNRAS, 425, 2128

Jing Y. P., 2005, The Astrophysical Journal, 620, 559

Kaiser N., 1987, MNRAS, 227, 1

Kazin E. A., Sánchez A. G., Blanton M. R., 2011, Monthly Notices of the Royal Astronomical Society, 419, 3223–3243

Klypin A., Kravtsov A. V., Valenzuela O., Prada F., 1999, ApJ, 522, 82

Kolb E. W., Turner M. S., 1990, The early universe. Vol. 69

Kopp M., Uhlemann C., Achitouv I., 2016, Phys. Rev. D, 94, 123522

Kozlikin E., Fabis F., Lilow R., Viermann C., Bartelmann M., 2014, arXiv e-prints, p. arXiv:1412.2715

Kuruvilla J., Porciani C., 2018, MNRAS, 479, 2256

Kwan J., Lewis G. F., Linder E. V., 2012, The Astrophysical Journal, 748, 78

Lahav O., Lilje P. B., Primack J. R., Rees M. J., 1991, MNRAS, 251, 128

Laureijs R., et al., 2011, Euclid Definition Study Report (`arXiv:1110.3193`)

Lesgourgues J., 2011, The Cosmic Linear Anisotropy Solving System (CLASS) I: Overview (`arXiv:1104.2932`)

Lewandowski M., Senatore L., Prada F., Zhao C., Chuang C.-H., 2018, Physical Review D, 97

Lewis A., , CAMB Notes, `https://cosmologist.info/notes/CAMB.pdf`

Lewis A., Challinor A., Lasenby A., 2000, ApJ, 538, 473

Liddle A. R., 1999, An introduction to cosmological inflation (`arXiv:astro-ph/9901124`)

Liddle A. R., Lyth D. H., 1993, Phys. Rep., 231, 1

Lilow R., Fabis F., Kozlikin E., Viermann C., Bartelmann M., 2019, Journal of Cosmology and Astro-Particle Physics, 2019, 001

Ma C.-P., Bertschinger E., 1995, ApJ, 455, 7

Mann R. G., Heavens A. F., Peacock J. A., 1993, MNRAS, 263, 798

Matsubara T., 2008a, Phys. Rev. D, 77, 063530

Matsubara T., 2008b, Phys. Rev. D, 78, 083519

Matsubara T., 2014, Physical Review D, 90

McDonald P., Vlah Z., 2018, Phys. Rev. D, 97, 023508

McEwen J. E., Fang X., Hirata C. M., Blazek J. A., 2016a, J. Cosmology Astropart. Phys., 2016, 015

McEwen J. E., Fang X., Hirata C. M., Blazek J. A., 2016b, Journal of Cosmology and Astroparticle Physics, 2016, 015–015

McQuinn M., 2016, Annual Review of Astronomy and Astrophysics, 54, 313–362

McQuinn M., White M., 2016, Journal of Cosmology and Astro-Particle Physics, 2016, 043

Meiksin A. A., 2009, Reviews of Modern Physics, 81, 1405–1469

Misner C. W., Thorne K. S., Wheeler J. A., 1973, Gravitation

Moore B., Ghigna S., Governato F., Lake G., Quinn T., Stadel J., Tozzi P., 1999, ApJ, 524, L19

Moutarde F., Alimi J. M., Bouchet F. R., Pellat R., Ramani A., 1991, ApJ, 382, 377

Mukhanov V., 2005, Physical Foundations of Cosmology, doi:10.2277/0521563984.

Nadathur S., Carter P., Percival W. J., 2019, MNRAS, 482, 2459

Okumura T., Seljak U., McDonald P., Desjacques V., 2012a, Journal of Cosmology and Astroparticle Physics, 2012, 010–010

Okumura T., Seljak U., Desjacques V., 2012b, Journal of Cosmology and Astroparticle Physics, 2012, 014–014

Okumura T., Hand N., Seljak U., Vlah Z., Desjacques V., 2015, Physical Review D, 92

Padilla A., 2015, Lectures on the Cosmological Constant Problem (`arXiv:1502.05296`)

Papastergis E., Shankar F., 2016, Astronomy & Astrophysics, 591, A58

Peacock J. A., 1999, Cosmological Physics

Peebles P. J. E., 1980, The large-scale structure of the universe

Peebles P. J. E., 1987, ApJ, 317, 576

Peebles P. J. E., Harrison E., 1994, American Journal of Physics, 62, 381

Penzias A. A., Wilson R. W., 1965, ApJ, 142, 419

Percival W. J., White M., 2009, MNRAS, 393, 297

Percival W. J., Samushia L., Ross A. J., Shapiro C., Raccanelli A., 2011, Philosophical Transactions of the Royal Society of London Series A, 369, 5058

Planck Collaboration et al., 2016a, A&A, 594, A13

Planck Collaboration et al., 2016b, A&A, 594, A13

Planck Collaboration et al., 2018, arXiv e-prints, p. arXiv:1807.06205

Polchinski J., 2006, The Cosmological Constant and the String Landscape (arXiv:hep-th/0603249)

Popolo A. D., Delliou M. L., 2017, Galaxies, 5, 17

Porto R. A., Senatore L., Zaldarriaga M., 2014, Journal of Cosmology and Astro-Particle Physics, 2014, 022

Prokopec T., Friedrich P., 2017, arXiv e-prints, p. arXiv:1704.03340

Pápai P., Szapudi I., 2008, Monthly Notices of the Royal Astronomical Society, 389, 292–296

Raccanelli A., Samushia L., Percival W. J., 2010, Monthly Notices of the Royal Astronomical Society, 409, 1525–1533

Raccanelli A., et al., 2013, MNRAS, 436, 89

Rampf C., Buchert T., 2012, Journal of Cosmology and Astroparticle Physics, 2012, 021

Riess A. G., et al., 1998, The Astronomical Journal, 116, 1009–1038

Riess A. G., et al., 2016, The Astrophysical Journal, 826, 56

Rubin V. C., Ford W. Kent J., 1970, ApJ, 159, 379

Sachs R. K., Wolfe A. M., 1967, ApJ, 147, 73

Sargent W. L. W., Turner E. L., 1977, ApJ, 212, L3

Schneider P., Bartelmann M., 1995, MNRAS, 273, 475

Schneider A., Trujillo-Gomez S., Papastergis E., Reed D. S., Lake G., 2017, Monthly Notices of the Royal Astronomical Society, 470, 1542–1558

Schutz B. F., 1985, A First Course in General Relativity

Scoccimarro R., 1998, MNRAS, 299, 1097

Scoccimarro R., 2004, Physical Review D, 70

Scoccimarro R., Sheth R. K., 2002, MNRAS, 329, 629

Scoccimarro R., Couchman H. M. P., Frieman J. A., 1999, The Astrophysical Journal, 517, 531–540

Seljak U., 2012, Journal of Cosmology and Astroparticle Physics, 2012, 004–004

Seljak U., McDonald P., 2011, Journal of Cosmology and Astroparticle Physics, 2011, 039–039

Seljak U., Vlah Z., 2015, Phys. Rev. D, 91, 123516

Seljak U., et al., 2005a, Physical Review D, 71

Seljak U., et al., 2005b, Phys. Rev. D, 71, 103515

Senatore L., Zaldarriaga M., 2015, Journal of Cosmology and Astro-Particle Physics, 2015, 013

Shandarin S. F., Zeldovich Y. B., 1989, Reviews of Modern Physics, 61, 185

Silk J., 1968, ApJ, 151, 459

Sorini D., 2017,] https://doi.org/10.11588/heidok.00023691

Starobinskii A. A., 1979, ZhETF Pisma Redaktsiiu, 30, 719

Sugiyama N. S., 2014, ApJ, 788, 63

Sunyaev R. A., Zeldovich Y. B., 1970, Ap&SS, 7, 3

Sunyaev R. A., Zeldovich Y. B., 1972, Comments on Astrophysics and Space Physics, 4, 173

Sunyaev R. A., Zeldovich I. B., 1980a, ARA&A, 18, 537

Sunyaev R. A., Zeldovich I. B., 1980b, MNRAS, 190, 413

Szapudi I., 2004, The Astrophysical Journal, 614, 51–55

Taruya A., Colombi S., 2017, MNRAS, 470, 4858

Taruya A., Hiramatsu T., 2008, ApJ, 674, 617

Taruya A., Nishimichi T., Saito S., 2010, Physical Review D, 82

Taruya A., Saito S., Nishimichi T., 2011, Physical Review D, 83

Taruya A., Saga S., Breton M.-A., Rasera Y., Fujita T., 2020, MNRAS, 491, 4162

Tatekawa T., 2004, Lagrangian perturbation theory in Newtonian cosmology (arXiv:astro-ph/0412025)

Taylor A. N., 1993, in Bouchet F., Lachieze-Rey M., eds, Cosmic Velocity Fields. p. 585

Taylor A. N., Hamilton A. J. S., 1996, MNRAS, 282, 767

Taylor A. N., Watts P. I. R., 2000, MNRAS, 314, 92

Uhlemann C., Kopp M., Haugg T., 2015, Phys. Rev. D, 92, 063004

Uhlemann C., Rampf C., Gosenca M., Hahn O., 2019, Phys. Rev. D, 99, 083524

Valageas P., 2011, A&A, 526, A67

Valageas P., Nishimichi T., 2020, Lagrangian-space Gaussian ansatz for the matter redshift-space power spectrum and correlation function (arXiv:2004.14011)

Valogiannis G., Bean R., Aviles A., 2020, J. Cosmology Astropart. Phys., 2020, 055

Verde L., Treu T., Riess A. G., 2019, Nature Astronomy, 3, 891–895

Viel M., 2005, Proceedings of the International Astronomical Union, 1, 255–260

Viel M., Haehnelt M. G., Springel V., 2004, Monthly Notices of the Royal Astronomical Society, 354, 684–694

Viel M., Lesgourgues J., Haehnelt M. G., Matarrese S., Riotto A., 2005, Physical Review D, 71

Viermann C., Fabis F., Kozlikin E., Lilow R., Bartelmann M., 2015, Phys. Rev. E, 91, 062120

Vlah Z., White M., 2019, J. Cosmology Astropart. Phys., 2019, 007

Vlah Z., Seljak U., McDonald P., Okumura T., Baldauf T., 2012, Journal of Cosmology and Astroparticle Physics, 2012, 009–009

Vlah Z., Seljak U., Okumura T., Desjacques V., 2013, Journal of Cosmology and Astroparticle Physics, 2013, 053–053

Vlah Z., Seljak U., Baldauf T., 2015a, Phys. Rev. D, 91, 023508

Vlah Z., White M., Aviles A., 2015b, Journal of Cosmology and Astro-Particle Physics, 2015, 014

Vlah Z., Seljak U., Yat Chu M., Feng Y., 2016a, Journal of Cosmology and Astro-Particle Physics, 2016, 057

Vlah Z., Castorina E., White M., 2016b, Journal of Cosmology and Astro-Particle Physics, 2016, 007

Wang L., Reid B., White M., 2014, MNRAS, 437, 588

Weinberg S., 1972, Gravitation and Cosmology: Principles and Applications of the General Theory of Relativity

Weinberg D. H., 2003, AIP Conference Proceedings

Weinberg S., 2005, Living in the Multiverse (arXiv:hep-th/0511037)

Weinberg S., 2008, Cosmology

Weinberg D. H., Bullock J. S., Governato F., Kuzio de Naray R., Peter A. H. G., 2015, Proceedings of the National Academy of Sciences, 112, 12249–12255

White M., 2014, MNRAS, 439, 3630

Wong K. C., et al., 2019, H0LiCOW XIII. A 2.4% measurement of H_0 from lensed quasars: 5.3σ tension between early and late-Universe probes (arXiv:1907.04869)

Zaroubi S., Viel M., Nusser A., Haehnelt M., Kim T.-S., 2006, Monthly Notices of the Royal Astronomical Society, 369, 734–750

Zel'dovich Y. B., 1970, A&A, 5, 84

Zheng Y., Song Y.-S., 2016, Journal of Cosmology and Astroparticle Physics, 2016, 050–050

Zwicky F., 1937, ApJ, 86, 217

van de Weygaert R., Bertschinger E., 1996, MNRAS, 281, 84